EXPLORING THE USE OF SMARTPHONE, WIRELESS SENSORS, AND 3D-PRINTING FOR LOW-COST MEDICAL TECHNOLOGY—DIAGNOSIS, TREATMENT, AND REHABILITATION

By

Rui Li

(Under the Direction of Zion Tsz Ho Tse)

ABSTRACT

This dissertation studies the design principles of low-cost scalable medical devices for diagnosis, treatment, and rehabilitation via smartphone, wireless sensors, and 3D-printing technologies.

Image-guided therapy (IGT) combines medical imaging and robotic devices for diagnostic and therapeutic procedures in an accurate and minimally invasive manner. Compared to conventional open surgery, potential benefits of the IGT include targeted diagnosis and treatment, minimally invasiveness, shorter hospitalization, lower surgical risks, and, therefore, faster recovery times for the patients. To enhance dexterity and visualization during the procedures, technologists have developed robotic systems as a way to provide targeting precision. However, robotic surgeries could be limited by its prolonged workflow, extended training requirements, and the high capital and maintenance costs. In comparison, small assistive devices have advantages over the cost, usability, and adaptation to the clinical environment.

The aim of this dissertation is to explore the use of smartphone applications, wireless sensors, and 3D-printing to develop low-cost scalable medical devices for diagnosis, treatment,

and rehabilitation. The research outcome would balance the technology scalability, clinical usability, and technical novelty that optimize the cost, accuracy, and user experience.

In this study, five medical devices were designed in different versions as case studies of low-cost scalable medical technologies that spanned in a wide range of clinical applications and shared the design principles: 1) 3D-printing reduces fabrication cost for medical devices and provides a customized solution for individual patients; 2) smartphone applications provide real-time tracking and visualization information of the medical instruments; 3) wireless sensors and the supported setup allow synchronous, remote data acquisition, transfer, and analysis.

Anthropomorphic organ phantoms, animal cadaver, live animal, and human studies were conducted to evaluate and validate the performance of the developed devices. The design presents only a small fraction of the costs of their robotic counterparts while delivering comparable accuracy, efficacy, and a streamlined workflow. This dissertation presents knowledge in the field of medical devices by offering low-cost scalable solutions for designs used for diagnosis, treatment, and rehabilitation.

INDEX WORDS: Image-guided Therapy, Percutaneous, 3D-printing, Micro-Electromechanical System (MEMS), Smartphone Application, Inertial Measurement Unit (IMU), Rehabilitation

EXPLORING THE USE OF SMARTPHONE, WIRELESS SENSORS, AND 3D-PRINTING FOR LOW-COST MEDICAL TECHNOLOGY—DIAGNOSIS, TREATMENT, AND REHABILITATION

by

RUI LI

M.E., Imperial College, London, 2009

A Dissertation Submitted to the Graduate Faculty of The University of Georgia in Partial

Fulfillment of the Requirements for the Degree

DOCTOR OF PHILOSOPHY

ATHENS, GEORGIA

2020

ProQuest LLC
789 East Eisenhower Parkway
P.O. Box 1346
Ann Arbor, MI 48106 - 1346

EXPLORING THE USE OF SMARTPHONE, WIRELESS SENSORS, AND 3D-PRINTING FOR LOW-COST MEDICAL TECHNOLOGY—DIAGNOSIS, TREATMENT, AND REHABILITATION

by

RUI LI

Major Professor:	Zion Tsz Ho Tse
Committee:	Leidong Mao
	Javad Mohammadpour Velni
	Kent Ronald Nilsson

Electronic Version Approved:

Ron Walcott
Interim Dean of the Graduate School
The University of Georgia
August 2020

ACKNOWLEDGMENTS

I would like to express my deepest gratitude to my supervisor and lifelong mentor, Dr. Zion Tsz Ho Tse, for his invaluable guidance on my research and future career path. From day one in the lab, I have been offered many great research opportunities to explore the unknown in the field of image-guided therapy. I could not make this far without his immense support on supervising my daily research activities and developing my lifelong research skills. His supervision has driven me to become a capable academic researcher. It is whole-heartedly to say that learning in the Medical Robotics Laboratory is a forever important milestone in my career development.

I would like to give my special regards to my Ph.D. committee members, Dr. Leidong Mao, Dr. Kent Ronald Nilsson, and Dr. Javad Mohammadpour Velni. Their invaluable advice has not only significantly improved the quality of my research work but also greatly broaden the knowledge base of my dissertation.

I would like to sincere appreciation to the collaborators Dr. Sheng Xu and Dr. Bradford Wood in the National Institute of Health, Dr. Hongliang Ren, at the National University of Singapore, and Dr. WenZhan Song and Dr. Christopher Modlesky at the University of Georgia. Their expert knowledge has dramatically broadened my perspective on clinical medicine, medical devices, wireless communication, and physical rehabilitation.

I also would like to thank all the administrative staff in the College of Engineering for their invaluable support in this journey, especially Ms. Margaret Sapp. I also really appreciated the collaborative work from my lab colleagues Zhuo Zhao, Brian Boland, Kevin Wu, Julian Moore,

and Austin Taylor. In particular, I am grateful for Sierra Hovet for giving me writing comments for my research work.

Last but not least, I wish to express my gratitude to my beloved wife, Xia Wang, and my parents on both sides: Shuping Liu, Enjie Li, Bin Wang, and Qiulong Zhang, my two brothers: Zhi Li, and Zilong Zhang, and Uncle Dong. I want to thank my two angels William Li and Anna Li, for giving me so much happy momentum and allow me optimistically and persistently to tackle challenging problems. The name list for appreciation is non-exhaustive. Their spritual support has helped me going through this epic journey.

TABLE OF CONTENTS

Page

ACKNOWLEDGEMENTS IV

LIST OF TABLES VIIV

LIST OF FIGURES IXV

CHAPTER

1 INTRODUCTION 1

Objective of the Study 1

Novelty of the Study 1

Impact of the Study 2

Outline of the Dissertation 2

2 LITERATURE REVIEW 5

Introduction 5

Precision Surgical Planning 7

Precision Surgical Tracking 9

Precision Diagnosis 14

Precision Surgical Treatment 15

Precision Physical Rehabilitation 23

3 LANDSCAPE OF PRECISION MEDICINE IN CLINICAL APPLICATIONS 32

Abstract 33

Introduction....33
Materials and Methods....36
Results....44
Discussion....47
Summary....52
4 A WEARABLE SMART DIAGNOSTIC DEVICE FOR HEATSTROKE PREVENTION....53
Abstract....54
Introduction....54
Materials and Methods....56
Results....63
Discussion....67
Summary....70
5 A LOW-COST, MRI-VISIBLE, AND 3D-PRINTED FLEXIBLE TEMPLATE FOR PRECISION TUMOR TARGETING....71
Abstract....72
Introduction....72
Materials and Methods....76
Results....83
Discussion....87
Summary....92
6 A LOW-COST PATIENT-MOUNTED NEEDLE LOCALIZER FOR IN-PLANE RF THERMAL ABLATION....93

Abstract 94
Introduction 94
Materials and Methods 98
Results 102
Discussion 107
Summary 109
7 A LOW-COST, SMARTPHONE-BASED, AND MEMS IMU-ENABLED HANDHELD TRACKER FOR CT-GUIDED INTERVENTION 110
Abstract 111
Introduction 112
Materials and Methods 113
Results 121
Discussion 126
Summary 129
8 A HUMAN STUDY OF LOW-COST, SMARTPHONE-BASED AND MEMS IMU-ENABLED BODY TRACKER 130
Abstract 131
Introduction 131
Materials and Methods 136
Results 147
Discussion 150
Summary 152
9 CONCLUSION AND FUTURE WORK 154

Conclusion 154

Future Work 158

REFERENCES 164

APPENDICES 205

Journal Publications 205

Conference Publications 206

LIST OF TABLES

Table 1-1: Five smartphone-based and 3D-printed devices presented in this dissertation 3

Table 2-1: Clinical workflow for an image-guided procedure 10

Table 2-2: Commercially available navigation system in interventions 10

Table 2-3: The working principle and performance metrics of selected devices..... 19

Table 2-4: Commercially available surgical robotic system for interventions 20

Table 2-5: Current commercially available or under-developed IMU systems 25

Table 2-6: Current commercially available or developing robotic-assisted rehabilitation systems 27

Table 2-7: Current commercially available or developing VR rehabilitation systems 30

Table 3-1: Shows some commercially available optical tracking systems (OTS) 34

Table 3-2: The tool tracking parameters used in this study 37

Table 3-3: Shows the Symbols used for equations in **Table 3-4** (The coordinate system is shown in **Figure 3(d))**. 39

Table 3-4: The results summary of the three tests in this study, ABS means absolute values 46

Table 4-1: Calibration process of obtaining a color map 59

Table 4-2: Conditions of simulation..... 63

Table 5-1: Existing assistive needle guidance systems 74

Table 5-2: Commercially available needle guidance systems 75

Table 5-3: Design criteria and descriptions of an ideal needle template 77

Table 6-1: The comparison between other devices and the presented device in this study..... 96

Table 6-2: Design specifications for the presented device..... 98

Table 6-3: Definition of Symbols used in the image analysis..... 103

Table 7-1: Specifications of hardware elements shown in **Figure 7-1**. 115

Table 7-2: Definitions of symbols..... 119

Table 7-3: Statistical analysis between two insertion methods..... 125

Table 8-1: Comparison of functionality between our system and existing ones 135

Table 8-2: Head-to-head comparison between the IMU and NDI optical tracking system..... 137

Table 8-3: Variable definitions for kinematic equations..... 141

Table 8-4: Motion analysis using NDI optical tracking system..... 143

Table 8-5: Motion analysis using IMU tracking system..... 144

LIST OF FIGURES

Figure 2-1: Three commonly used imaging modalities in Image-guided therapy, (a) shows the CT scanner—Philips CT 6000 iCT[35], (b) shows the Ultrasound system—GE Voluson S10[36], (c) shows the MRI scanner—Simens Avanto, which has a closed bore size of approximately 60 cm[37]. 8

Figure 2-2: Some of the currently available navigation systems, (a) shows Shwartz et al.'s research work[60], (b) shows Fichtinger et al.'s research work[65], (c) shows Mauri et al.'s research work[62], and (d) shows Dixon et al.'s research work[63]. 14

Figure 2-3: Show some commercially available devices. (a) LeVeen needle electrodes by Boston scientific [112], (b) StarBurst XL & semi-flex RFA device by Angiodynamics [113], (c) Valleylab Cool-tip RF ablation system by Covidien [114], (d) Visualase MRI-guided ablation system by Medtronic [115]. 19

Figure 2-4: Shows (a) Micro Hand S system, which was developed by Tianjin University, China, has a three-arm operation cart [124], (b) Revo-i robotic system, which was developed by Mere company, South Korea, has a four-arm operation cart [80], (c) da Vinci robotic system, which was developed by Intuitive Surgical, has a four-arm operation cart, a surgeon console, and vision cart [123]. 23

Figure 2-5: Different types of IMU motion tracking systems. (a) Xsens system [145], (b) Muller et al.'s self-calibrating elbow angle device [146], (c) Chang et al.'s developed finger device [144], and (d) Bakhshi et al.'s body joint angle measurement system [147]..... 26

Figure 2-6: Shows the systems of (a) Rewalk developed by Argo Medical Technologies Ltd [159], (b) ALEX developed by University of Delaware [161], (c) HAL developed by Cybernic s [160], (d) I-Pam developed by University of Leeds [157]..... 28

Figure 2-7: Different types of VR rehabilitation systems, (a) Crosbie et al.'s experimental set up [176], (b) Gokeler et al.'s experimental setup [177], and (c) Slobounov et al.'s experimental setup [174]. 31

Figure 3-1: Overall test design for assessing the accuracy of the OTS. 36

Figure 3-2: Shows the experimental and tool setup, (a) displays the working principle of NDI OTS, UR 10, and relevant hardware, (b) shows the tracking volume of the NDI OTS, (c) shows how the tool was held by the UR10, (d) shows the needle positioning and the needle used was 17G and has a length of 200 mm, (e) shows the tool dimensions. 38

Figure 3-3: Experimental setup for testing: (a) the marker orientation, (b) the marker occlusion, (c) the environmental reflection, and (d) shows the global coordinate system of the NDI OTS. The optical tracking system was mounted on the wooden board in a fixed position to the needle tool within the tracking distance of 2400 mm. A vacuum base vise was used to hold the marker coverage tool.r..... 41

Figure 3-4: Tracking errors generated when the tool was oriented in the (a) yaw direction, and (b) pitch direction..... 45

Figure 3-5: (a) Tracking errors generated when increasing the marker occlusion from 10% to 40%. At 40%, the tool tracking was lost, (b) tracking error generated when rotating the stainless-steel panel..... 46

Figure 3-6: NDI software interface showed phantom points (in black color) appeared during the experiment when reflections had a significant influence on the tracking quality. The coordinate system was previously defined in **Figure 3-3 (d)**..... 47

Figure 4-1: (a) The working principle of the device, (b) Chemical transformation of Leuco dyes[245, 246]..... 56

Figure 4-2: Proposed workflow of the application 59

Figure 4-3: Temperature sensor development and operating demonstration: (a) the resin used to create the temperature sensor, (b) bracelet-shaped sensor model, (c) 3D-printed sensor, (d) demonstration of sensor changing color with skin temperature, (e) and using the smartphone to take a picture (f) to measure the temperature and alert..... 60

Figure 4-4: (a) The thickness of the device, (b) Color transition of one thermochromic sample under the heating temperature of 38 ºC. The purple color means the temperature of the circular block reached 30 °C. The white color means the temperature of the circular block reached 38 °C. This was a quantitative test that can measure both the rate and the extension of the color change. 62

Figure 4-5: Open-air test setup and simulation layout. As for the simulation, the dimensions of the block and the heat source were identical to the real thermochromic block and heat source in the open-air test. The separation distance C between the blocks was proportional to the distance A in the open-air test. The separation distance D between the block to the center of heat source was proportional to the distance B in the open-air test..... 63

Figure 4-6: (a) Shows the time taken for a thin block made from thermochromic material to change from dark purple to completely white. The linear relationship indicates that there is a positive correlation between the time taken for the color change to occur and the thickness of the

object, (b) Shows the time taken for the complete color change, which includes two states, the color transition period (t = 0-80 s) and steady-state (after t = 80 s). 64

Figure 4-7: (a) Comparison between the temperature readings from our device and conventional laser thermometer, which has an accuracy of ±0.1°C. The average error of these two devices is 0.06°C. Each data point is the average value of twenty repetitions of trials. (b) The Bland-Altman plot is used to evaluate the accuracy of the device. 65

Figure 4-8: the experimental and simulation result for heat transfer between the thermochromic circular blocks and round heat source underneath. (a) shows the color image from the experiment, which shows the color changes from purple to white as the heat transfer happens between the heat source and thermochromic blocks, (b) is the processed grayscale image using Matlab 2017b® (Natick, MA) with the color bar on the side indicating the temperature distribution ranging from 25 °C to 40 °C. (c) is the simulation result using Energy 2D®(Concord, MA), the dotted red line is the isotherm line of 30 °C. As time elapses, the isotherm line expands outwardly, which matches consistently with both the color appearance and temperature analysis in (a) and (b)..... 66

Figure 5-1: The presented template-guided system for minimally invasive interventional procedure..... 76

Figure 5-2: (a) shows the design of the template, (b) shows the 3D print result from the formlabs®, (c) shows the template flexibility test, the template was able to bend and make full contact with the arch. (d) shows the cap design for sealing the contrast agent, (d) shows the final assembly result of the template, (f) shows the MR image (T1-weighted)..... 78

Figure 5-3: Detailed design information on optimization..... 79

Figure 5-4: Two different types of test blocks were CAD designed, and 3D printed for optimizing both the Gd concentration and container size. (a) shows the circular containers with a constant diameter of 4mm but the concentration of Gd-water solution increases from 0.9mg/ml to 42.6mg/ml and pure water as a control reference is placed at the bottom right corner, (b) shows a series of containers with gradual decreasing size, optimal Gd concentration is applied to all the containers in this case. 80

Figure 5-5: (a) shows the registration user interface, the blue dots are manually identified markers, the yellow circles are where the software thinks the MRI contrast should be located, the red dot is the projection of the target on the template, (b) shows the virtual needle generated by the software goes through the interval between fiducial markers..... 81

Figure 5-6: (a) shows a template placed inside the CT scanner, (b) shows the typical CT image, (c) how the distance is measured and analyzed, LR is the left-right distance error, SP is the superior-posterior distance error. 82

Figure 5-7: The clinical workflow of template application 82

Figure 5-8: (a) shows MRI images of different concentrations of Gd solutions, (b) shows the signal intensity versus the Gd concentrations 84

Figure 5-9: (a) shows MRI images of different test container diameter, (b) shows the signal intensity versus the test container diameter 85

Figure 5-10: shows the 9 out of 13 insertions on the prostate phantom are displayed and analyzed. (a)—(c) is on Tumor A, (d)— (f) is on Tumor B, and (g)—(I) is on Tumor C. 86

Figure 5-11: Shows a comparison of absolute values of SP, LR, and TD errors for 13 insertions. 87

Figure 5-12: Shows the Bland-Altmann plot for SP and LR respectively. 87

Figure 6-1: shows the description of the procedure, there are three main steps involved: at first, the presented device measures the needle angle and displays the angular data on the smartphone. The angular information assists the physician to decide the skin entry angle for ablation biopsy. The device could continuously provide real-time angular information during needle advancement. After one ablation is done, the device could be used repeatably for multiple ablations. 97

Figure 6-2: shows (a) CAD design, (b) Needle release and Remote Center of Motion (RCM) mechanism, (c) final device assembly using biocompatible material, and (d) Bluetooth communication with the mobile platform, which shows the real-time needle angle..... 99

Figure 6-3: presented clinical workflow, which has six steps. Step 1, Step 2-4, and Step 5-6 are the planning step, the target acquiring steps, and the treatment steps, respectively. 101

Figure 6-4: shows the results of the benchtop test. The number of trials is listed underneath, along with the absolute errors in each trial. 102

Figure 6-5: One example of needle insertion from the stage of planning to completion, (a) shows pre-inserted CT visible targets (0.5mm-BB beads), (b) shows pre-planned insertion pathway, (c) shows the final scan of the actual pathway. 103

Figure 6-6: shows all the CT images of insertions for 6 targets. On each row, the first image presents the overall needle pathway. The second image displays the needle and tumor location. Besides the images, there are four parameters, PDS (planned insertion distance from skin entry point), ADS (actual insertion distance from skin entry point), TTD (needle tip-to-target distance error), and AE (needle angular error). The red line is the planned insertion with a circle end indicating the tumor position. The yellow line is the actual insertion with a square end indicating the actual needle position. 105

Figure 6-7: Results of six insertions for the in-vivo study, (a) shows the comparison between the actual and planned insertion distance, (b) shows the TTD errors, (c) shows the comparison between the actual and planned insertion angle, (d) shows the AE errors. The mean accuracy, measured as the minimum needle path to the target, was 5.2 mm. The average tip to target distance was 7.4 mm. The average puncture time was 25.5 s. Only one of the punctures required an intermediary CT scan, and none of the insertions required any needle drawback or repositioning. 106

Figure 7-1: Overview of the system design architecture and tracker design, (c) showing its use (1) and the needle channel (2). The description of each part in (3) is shown in **Table 7-1**..... 114

Figure 7-2: 3D printed station for calibration of the tracker reading. 117

Figure 7-3: Comparison between conventional and tracker-assisted CT-guided clinical workflow. (a) shows the conventional procedure. More intermittent CT scans (steps 3–5, as shown in the orange arrows) are likely required in this workflow, lengthening the procedure. Treatments that require multiple needle insertions for multiple targets repeat steps 3–7 (green arrows). (b) Tracker-assistance shows the alternative method for step 4, in which online monitoring of needle position provides instant feedback, potentially reducing the number of confirmatory CT scans for positioning and improving the efficiency of CT in guiding needle placement. 118

Figure 7-4: Interpretation of the CT image. The yellow line shows the planned pathway, and the red line shows the actual insertion pathway. The blue lines indicate each parameter. 119

Figure 7-5: Comparison of the angular measurement (a) using the phantom, (b) In-axial plane angle measured by CT compared to (c) the smartphone application's reading. In (c), the smartphone displays: (1) X, Y, Z as angles of rotation about the roll, pitch and yaw, (2) Time

function enables the creation of a needle time log/event, (3) Acceleration of the angular movement, (4) Velocity of the angular movement, (5) Output function logs out the file and data can be transferable to a computer. The schematic diagram of beeping vs. angle deviation is shown in (d), and needle alignment and insertion are shown in (e). 120

Figure 7-6: Statistical analysis between the measured angle and actual angle. (a) shows the data analysis on the benchtop test, (b) shows the data analysis on the abdominal phantom study. ... 122

Figure 7-7: (I) shows three examples of needle insertions performed in the phantom: (a), (b), and (c) show relative positions of needles with respect to the target; (d), (e), and (f) are the quantitative analysis of needle trajectories. (II) and (III) shows the results from the tracker-assisted and cognitive guided freehand needle insertion, respectively. The yellow lines show the planned needle trajectory, and the red lines show the actual insertion pathway. The yellow squares show the position of the target, and the red circles show the position of the needle tip. On the right-hand side of each image, the six parameters are displayed: PD, AD, RE, AE, TTE, and ARE..... 124

Figure 7-8: In (a), (1) shows the comparison between the PD and AD; (2) shows the comparison between the AE and RE; (3–4) show the trends of TTE and ARE. (b) shows the comparison of ARE and TTE between the tracker-assisted and freehand procedures. 126

Figure 8-1: (a) shows the overview of the tracking system with reflective markers, and (b) suggested mounting locations on the hip, knees, and ankles of end-users. The IMU modules were placed on the outer surface of the hip, knees, and ankles. 138

Figure 8-2: (a) shows the interior structure of the IMU sensor, which has a gyroscope, an accelerometer, a microprocessor, a battery, a Bluetooth module, and a switch. All the components were placed in a 3D-printed case, (b) shows the coordinate system of the IMU

sensor, (c) shows the experimental set up for human trials. The blue lines on the floor are the measuring distance, and the IMU sensor was mounted on human participants using flexible bands. The NDI equipment was set on the table at a detectable distance to the participants. The control console was placed nearby for data recording. 139

Figure 8-3: Smartphone interface 139

Figure 8-4: (a) shows NDI lower-limb kinematic analysis and NDI segmented kinematics analysis for each NDI marker on the (b) hip, (c) knee, and (d) ankle. Each segment was defined based on the joint region between the waist and the thigh, the thigh and the leg, the leg and the foot, respectively. 142

Figure 8-5: (a) shows NDI lower-limb kinematic analysis and NDI segmented kinematics analysis for each NDI marker on the (b) hip, (c) knee, and (d) ankle. 144

Figure 8-6: Shows the analysis of (a) scatter plot and (b) Bland-Altman plot. 147

Figure 8-7: Gait comparison between the NDI optical tracking and our tracking system for one participant 148

Figure 8-8: The walking, jogging, and fencing lunging results for 10 participants. The solid line is the IMU data, and the dashed line is the NDI data. Taking one graph of the hip movement of subject 1 as an example, $\mu = 4.40$, $\sigma = 4.70$, cc= 0.81 means the mean of differences is 4.40º, the average standard deviation is 4.70º, and the cross-correlation is 0.81. The two lines were artificially separated from each other by adding an offset of 40º for better presentation. 149

Figure 8-9: shows cross-correlation, standard deviation, and average difference for walking, jogging, and fencing lunging for 10 participants. 150

Figure 9-1: Illustration of the proposed template 160

Figure 9-2: Shows a developed prototype using the MPD concept 161

Figure 9-3: Shows a future trend for fencing analytics: (a) conventional coaching technique for fencing, (b) common fencing injuries-knee problem, (c) new training practice using sensors and smartphone application 163

CHAPTER 1

INTRODUCTION

Objective of the Study

This dissertation studies the design principles of low-cost scalable medical devices for diagnosis, treatment, and rehabilitation via smartphone, wireless sensors, and 3D printing technologies.

Novelty of the Study

The novelty of this work lies in developing low-cost, fast-deployable, and scalable medical devices in the challenging CT and MRI environments. The design presents only a small fraction of the costs of their robotic counterparts. The previous efforts have been put into developing state-of-art medical devices or robotic systems for precision medicine, but the high-cost limits their use in environments such as small clinics or homes. The presented devices demand significantly less training and can be easily fit into the current clinical workflow. One of the devices developed—the angular localizer—significantly shortens the time for surgical planning and treatment. In addition, the medical devices are scalable, which means the design is customizable to different clinical requirements and production needs. One example is the flexible template can cut into smaller size for young patients. Last but not least, the developed devices have comparable accuracy and efficacy to those systems which are commercially available.

Impact of the Study

Image-guided therapy (IGT) is to use state-of-art technologies such as wireless sensors for disease diagnosis and treatment in a fast, accurate, and minimally invasive manner. It is hypothesized that using appropriate design principles and precision technologies, the low-cost image-guided medical devices could achieve comparable accuracy to the existing commercial robotic systems.

In the phantom studies, the distance errors of all the presented devices were generally within the range of 1.0—2.0 mm and angular errors were within the range of 1.0—2.0°. In the animal studies, one of the device—the patient-mounted localizer—showed a mean tip-to-target distance errors of 5.2 mm. In comparison, the tip-to-target distance errors of the robotic systems were 2.0 — 5.0 mm. The cost of fabricating this medical device was significantly lower than the robotic systems.

Outline of the Dissertation

In the first part of this dissertation, a literature review presents the current development of precision medicine in different areas: diagnosis, surgical tracking, and treatment as well as physical rehabilitation. The second part of the dissertation describes a list of medical devices being developed for image-guided therapy and rehabilitation (**Table 1-1**). First, the limitations of the current system were thoroughly investigated. Second, a smartphone-based and wearable medical device was fabricated via 3D printing technology, aiming to provide an accurate diagnosis for heatstroke. Then, three low-cost, fast-deployable, and disposable medical devices were fabricated for needle biopsy and ablation. Then, a motion tracking system was developed to track the human joint movement accurately. A group of volunteers was recruited to carry out three different

exercises: walking, jogging, fencing lunge in order to verify the functionality of the systems. The final part of the dissertation summarizes the overall research outcomes and future research directions.

Table 0-1: Five smartphone-based and 3D-printed devices presented in this dissertation

Chapter	4	5	6	7	8
Device	Low-cost, smartphone-based, wearable diagnostic device for heatstroke prevention	Low-cost, MRI visible and flexible template	Patient-mounted needle tracker for in-plane needle insertion	Smartphone-based, MEMS handheld tracker for needle insertion	Low-cost, smartphone-based, 3D printed, MEMS sensor-enabled body tracker
Sensor type	Chemical	Chemical	MEMS IMU	MEMS IMU	MEMS IMU
Detail	The device measures real-time skin temperature using a smartphone camera and alerts the people of the risk of heatstroke.	The MRI-visible flexible template was 3D printed. It assists needle biopsy for cancer diagnosis.	A patient-mounted, and smartphone-based MEMS angular localizer assists the radiofrequency ablation.	A compact MEMS- angular handheld tracker provides angular needle guidance.	A smartphone-based, wearable system consists of seven MEMS IMU sensors, which could accurately track the joint movements for lower limbs.
Targeted disease	Heatstroke	Cancer	Cancer	Cancer	Movement Disorder
Performance metric	The accuracy of our device is comparable to the laser thermometer. The average error was 1.3 ºC.	The mean total distance error between planned and actual insertion is 2.7 mm, the maximum error is 4.78 mm, and the standard	In the live swine study, the mean tip-to-target distance error, was 5.2 mm, with a standard deviation of ± 1.3 mm. The mean tip-to-target angular error was 4.2°, with a	The animal experiment resulted in a mean angular error of 6.6 mm with an SD of ± 1.9 mm and a mean tip-to-target distance error of 8.7 mm	The average cross-correlation value is 0.85, the mean difference of joint angles is 2.00°, and the standard deviation of

		deviation is ± 1.1 mm.	standard deviation of ± 2.6°.	with an SD of ± 3.1 mm.	joint angles is ± 2.65°.
Limitation	Environmental lighting could influence the performance.	The template has a duration limit (approx. 30 days).	Currently, the device can only perform the in-plane insertions.	Benchtop calibration is required.	The system only analyzes the two-dimensional joint movement.

CHAPTER 2

LITERATURE REVIEW

2.1 Introduction

Precision medical technology is referring to use state-of-art technologies such as CT or MRI imaging to provide precise surgical planning, diagnosis, and treatment. For example, the minimally invasive surgery (MIS), which includes laparoscopic or robotic surgery, only requires small incisions for surgical operation [1, 2]. Compared to open surgery, the MIS has better surgical outcomes in treating small, early-stage malignancies, such as fewer surgical site infections, less pain, and shorter hospital stays [3, 4]. Image-guided therapy (IGT) is the use of any form of medical imaging to help with planning, performing and evaluating surgical procedures and therapeutic interventions. It further improves the efficacy and reduces the surgical risk of MIS [5].

J.H. Clayton used the bromide print of an x-ray to remove an industrial sewing needle from a worker's hand, which was widely regarded as the first IGT [6]. Since then, the physicians rely primarily on the different imaging modalities such as ultrasound, computer tomography, and magnetic resonance imaging to acquire visual data for target guidance. However, in a clinical setting, IGT creates multiple challenges to the physician, such as the disturbing hand-eye coordination [7, 8] and impaired depth perception [9]. To overcome these challenges, navigational technologies such as optical tracking [10, 11], IMU tracking [12], and electromagnetic tracking [12, 13] are served as important informational supports to the physicians. This not only enhances the spatial perception during the surgery but also allows better decision making in the stages of

pre-surgical and intermittent planning. It is widely recognized that the use of navigational technologies greatly reduces surgical risk and time[14-16].

On the other hand, precision medical technology could also be applied to assisting post-operative rehabilitation and treating neurodegenerative diseases. For example, movement disorders could significantly reduce the patient's quality of life by affecting their performance of basic activities of daily living (ADL). Physical therapy is regarded as one of the most effective approaches to assist the patient in restoring the movement functionalities [17]. Conventional rehabilitation training programs typically involve intense repetition of coordination exercises and require physical therapists to observe and assess the training outcome. A popular trend is to use real-time motion tracking modalities such as optical tracking for more quantitative assessment of patients' physical activities [18].

This literature review provides detailed information about the current practice of precision medical technology in four major areas: surgical planning, tracking, diagnosis, treatment, and physical rehabilitation.

2.2 Precision Surgical Planning

Surgical planning is the pre-operative method of defining surgical steps by pre-visualizing the surgical operating site [19]. In recent years, a fast advancement of image modalities enabled physicians to tackle the challenge of accurate surgical planning. Nowadays, Ultrasound (US) imaging [20-22], magnetic resonance imaging (MRI) [23, 24], computed tomography (CT) scanning [25, 26], cone-beam CT [27], and X-ray imaging [28] are commonly used image modalities for preoperative surgical planning.

2.2.1 Computed Tomography

Computed Tomography (CT) uses computer-processed combinations of X-ray measurements taken from different angles to produce tomographic images on the areas of

interest on the scanned objects (**Figure 2-1 (a)**). It provides fast guidance for image-guided needle biopsy of various interventional applications. The advantage of CT over X-ray imaging is that CT can present the anatomy on a slice-by-slice basis for the more exact localization of the tumors. A diagnostic biopsy is the most widely used CT procedure, the main area of application is head, neck, thorax, liver, pancreas, adrenal glands, kidney, pelvis, retroperitoneum, and prostate [29, 30].

The major disadvantages of CT are it uses ionizing radiation, which may have safety issues, and it provides less tissue information compared to MRI and Ultrasound imaging. Hence, CT is mainly sensitive to anatomic rather than direct physiological changes. CT may be used, for example, in a gated test or electron beam, to gather information on myocardial wall movement[31]. In contrast, it is not sensitive to changes in temperature, diffusion coefficient, or perfusion as the MRI and unable to give the physician an early warning of a change in a disease condition. Moreover, compared to MRI, CT is less capable of providing detailed information such as the lesion boundaries or margins.

2.2.2 Ultrasound

Ultrasound imaging (US) has been widely used in interventional radiology as a non-invasive way to obtain real-time images under low operation costs (**Figure 2-1 (b)**). The US is generally the method of choice for a procedure such as peripheral joints[32] and soft tissue injections[33]. However, as the contrast of the scanned images is relatively low compared to those obtained with CT and MRI, the US can only be used in less-selective surgical procedures.

2.2.3 Magnetic Resonance

Magnetic resonance imaging (MRI) has unique advantages including good tissue discrimination between various organs[34]; superior definition of lesions and distinction between the lesions and normal tissue in order to improve the therapy targeting accuracy; great indicator

for providing accurate trajectory definition with submillimeter spatial resolution; good selection of image acquisition protocols such as echo-planar imaging (EPI), fast spin-echo imaging, and gradient-echo imaging, enabling real-time visualization and characterization of physiological changes. Due to the above merits, MRI is the gold standard imaging acquisition tool for percutaneous surgical procedures (**Figure 2-1 (c)**). However, the working principle of MRI poses great challenges in designing medical devices to work in the MR environment. If the medical device has an electronic component, it will induce an electromagnetic field inside the scanner, which results in a reduced signal-to-noise ratio (SNR) of the images. Moreover, the limited workspace inside the scanner bore (approximately 60 cm) means the device has to be designed as compact as possible, considering the patient's body has occupied at least half of the space.

(a) CT scanner (b) Ultrasound (c) MRI scanner

Figure 2-1: Three commonly used imaging modalities in Image-guided therapy, (a) shows the CT scanner—Philips CT 6000 iCT[35], (b) shows the Ultrasound system—GE Voluson S10[36], (c) shows the MRI scanner—Simens Avanto, which has a closed bore size of approximately 60 cm[37].

2.2.4 Image Registration

The image-to-image registration is a process to integrate the pre-operative image data with the intra-operative image data of the patient [38]. It plays an important role in the image navigation procedure as it links the scanned images with the body of the patient on a shared coordinate system [39], especially the images from different modalities such as MRI or ultrasound. Xu et al. have

successfully developed an MRI-TRUS fusion system for targeted prostate biopsy. The accuracy of the systemin phantom studies was shown to be 2.4 ± 1.2 mm [40].

In general, there are two different methods to facilitate image registration: frame or frameless registration [41]. In frame registration, such as the N-localizer developed by Brown et al., each CT-visible fiducial marker is placed in a predefined position, and image registration is completed via the known geometry of the fiducial markers [42]. Another method is to use radiopaque markers for frameless registration, or frameless stereotaxis. The radiopaque markers include pellets, crosshairs, and grids [43]. The Radiopaque markers have been shown to provide information that helps find the tumor location and offer ease of use.[44-49] Different types of CT-visible templates have been reported in past studies. Specifically designed skin-mounted marker-based templates, such as the Fast Find grid, assist in determining the skin entry point.[50, 51] Marker patterns, including but not limited to pre-manufactured patterns on dots, grids, and lines, may provide enhanced capabilities in surgical navigation. Possibilities include designs that can guide the needle's skin entry angle and subsequent insertion, which conventional markers cannot offer.

2.3 Precision Surgical Tracking

Imaging modalities can provide pre-operative anatomical and physiological information for surgical planning, but the challenges remain as the physicians would need more information on the surgical planning stage to decide the location of the skin-entry points, the angle, and depth of insertion. The physician would also need real-time positional and orientational information of the interventional devices. Therefore, surgical tracking devices, also known as the localizer, become an essential component of the surgical procedure to increase the accuracy of the minimally invasive surgery, and, more importantly, patient safety.

The continuous advancement of tracking devices has led to the new development of image-guided systems. These devices were deployed to track the relative positions of instruments to the patient's anatomy. Early devices were mostly based on mechanical tracking. In some of the earliest cases, Klopotek developed a mechanical tracking system for laser surgery[52]. Later, the optical tracking systems were then quickly adopted because of their high accuracy and large field of view[53]. Apart from that, electromagnetic trackers have been available on the market for over two decades[54]. A typical clinical workflow of the image-guided and tracking-aided procedure is shown in **Table 2-1**.

Table 2-1: Clinical workflow for an image-guided procedure

Steps	Details
1	Preoperative images are acquired (typically tomographic images).
2	The surgical instruments are tracked using a localizer.
3	The patient's anatomy is registered to the preoperative image.
4	The position of the surgical instruments is displayed on this image relative to the patient anatomy.
5	The physician uses this virtual display to manipulate the instruments to accomplish the procedure.
6	A confirming image is obtained upon procedure completion.

Until now, there are many tracking devices have been commercialized, such as Polaris optical tracking system (NDI, Waterloo, ON, Canada) and from the NOCTN150 system (Philips, Amsterdam, Netherlands). Research on the feasibility of using these products in interventions has been conducted (**Table 2-2**).

Table 2-2: Commercially available navigation system in interventions

Company name	System type	System name	Performance metrics	References
NDI medical	Electromagnetic tracking system (EM tracking)	Aurora system	Positional accuracy: RMS: 1.20 mm, 95% Confidence Interval: 1.80 mm Orientational accuracy: RMS: 0.5°, 95% Confidence Interval: 0.7°	[55]

NDI medical	Optical tracking system	Polaris Vega	Positional accuracy: RMS: 0.12 mm (pyramid), RMS: 0.15 mm (extended pyramid) 95% Confidence Interval: 0.20 mm (pyramid), 0.30 (extended pyramid)	[56]
Philips	Image fusion and needle navigation	NOCTN150	The accomplished Euclidean distances were 4.42±1.33 mm, 4.26±1.32 mm, and 4.46±1.56 mm at a slice thickness of 1, 3, and 5 mm, respectively. The mean lateral positional errors were 3.84±1.59 mm, 3.84±1.43 mm, and 3.81±1.71 mm, respectively	[57]
Medtronic	Electromagnetic Navigation	Stealth Station AxiEM	The Euclidean distances were 3.86±2.28 mm, 3.74±2.1 mm, and 4.81±2.07 mm at a slice thickness of 1, 3, and 5 mm, respectively. The mean lateral positional errors were 3.29±1.52 mm, 3.16±1.52 mm, and 3.93±1.68 mm, respectively.	[57]
Amedo	Laser navigation system	LNS	Target point accuracy of 5.0 ± 1.2 mm, entrance point accuracy of 2.0 ± 1.5 mm, needle angulation accuracy of 1.5 ± 0.3°, intervention time of 12.08 ± 3.07 minutes, and used 5.7 ± 1.6 CT-images for the first experience with patients.	[58]
CAScination	An optical stereotactic navigation system	CAS-One IR	Performance data could be evaluated for 17 patients with 25 lesions (mean [± SD] lesion diameter, 14.9 ± 5.9 mm; mean lesion location depth, 87.5 ± 27.3 mm). The antennae were placed with a mean lateral error of 4.0 ± 2.5 mm, a depth error of 3.4 ± 3.2 mm, and a total error of 5.8 ± 3.2 mm in relation to the intended target.	[59]

Meanwhile, there are many preclinical and clinical studies relating to electromagnetic tracking. Shwartz et al. published the first preclinical study on electromagnetic bronchoscopy (ENB)[60]. Peripheral lung lesions were created in four swine models by insertion of a metal tube

(1 x 10 mm) via a transthoracic approach. An electromagnetic field was created by placing the animal on an electromagnetic location board. A position sensor incorporated into the distal tip of a dedicated tool was used to navigate to the various target lesions (**Figure 2-1 (a)**). Information gathered in real-time during a bronchoscopy was presented on a monitor simultaneously by displaying previously acquired CT images. The registration accuracy expressed by the fiducial target registration error, expressing both the registration quality and the stability of fiducial (registration) points, was 4.5 mm on average.

Folch et al. performed electromagnetic navigation bronchoscopy (ENB) for pulmonary lesions in 1215 subjects[61]. The equipment used is named NAVIGATE— a multicenter, global, single-arm, pragmatic cohort study of ENB using the superDimension® navigation system, version 6.0 or higher (Medtronic, Minneapolis, Minnesota). Biopsy tools used by the NAVIGATE investigators were aspirating needles, biopsy forceps, cytology brushes, needle-tipped cytology brushes, the superDimension® triple-needle cytology brush (Medtronic), the GenCut core biopsy system (Medtronic), and bronchoalveolar lavage (considered a tool for this analysis). Among the 1157 lung lesion biopsy cases, navigation was successful, and tissue was obtained in 94.4%.

Mauri at al. uses electromagnetic tracking together with the CT/MRI fused image to develop a virtual-navigation system[62]. Hardware included a magnetic field transmitter, fixed to the operation table and placed close to the right upper quadrant of the patient abdomen (Ascension Technology Corporation, Burlington, USA) and two electromagnetic sensors, one applied to the US probe and one attached to the handle or, from 2010, secured to the hub (VirtuTrax, CIVCO Medical Solutions, Kalona, IA) of the ablation applicator (**Figure 2-1 (c)**). Successful ablation was achieved in 266 of 295 (90.2 %) tumors. Sixteen of 295 (5.4 %) tumors were correctly targeted,

but the necrosis volume size was insufficiently large to cover the whole tumor volume and the ablative margin, resulting in incomplete ablation.

Dixon et al. developed a localized intraoperative virtual endoscopy in a preclinical setting before deployment in the operating room[63]. Optical IGS reflective markers were attached to the head, the 0° endoscope (Hopkins II telescope and IMAGE1 camera; Karl Storz, Tuttlingen, Germany), and the drill (M4 hand-piece; Medtronic, Jacksonville, FL). Registration of the head to the imaging data was then undertaken with an optical tracking system (Polaris; NDI, Waterloo, Ontario, Canada). Skull base procedures were performed on 14 cadaver specimens by seven fellowship-trained skull base surgeons. All seven participants completed the two clivus ablation exercises. Fiducial registration errors were consistent with current clinical practice (between 1 mm and 1.8 mm for all cases).

Some researchers have developed novel navigation based on a smartphone. Xu et al. develop an iOS-based iPhone (Apple) app, OncoGuide (National Institutes of Health), with Xcode (version 8.3.3, Apple) using Objective-C (Apple)[64]. The accuracy and efficacy of smartphone-guided needle angle selection were evaluated using commercial phantoms. The accuracy was 0.4° ± 0.3° across ten trials.

Figure 2-1 shows the devices being used in preclinical or clinical studies.

Figure 2-2: Some of the currently available navigation systems, (a) shows Shwartz et al.'s research work[60], (b) shows Fichtinger et al.'s research work[65], (c) shows Mauri et al.'s research work[62], and (d) shows Dixon et al.'s research work[63].

2.4 Precision Diagnosis

Precision diagnosis is a procedure that can detect and check the disease condition of the patients using either external physiological signals or internal biological samples.

2.4.1 Diagnosis Based on External Physiological Signals

As for the external physiological signals, the skin temperature, the pulse rate as well as breath rate can all be used as essential references for detecting anomaly on human bodies. Bovenzi proposed a finger skin temperature measurement for the evaluation of peripheral vascular reactivity[66]. There are factors that could potentially influence the diagnostic significance, such as room temperature, season, and food intake [67].

2.4.2 Diagnosis Based on Internal Tissue Samples

As for the internal biological samples, a needle biopsy was commonly used to extract tumor samples in a minimally invasive way to determine the stage of cancers. For example, the needle biopsy is a frequently used method to acquire tissue samples for histological analysis.

There are approximately 1 million prostate biopsy procedures conducted in the US each year [68, 69] for the diagnosis of prostate cancer. One popular approach is to use prostate biopsy, for which Transrectal Ultrasound (TRUS) or Magnetic Resonance Imaging (MRI) serves as the imaging tool [70-72]. MRI, especially multi-parametric MRI, is currently the most promising imaging modality for detecting prostate cancer with great accuracy [73, 74]. An early investigation by D'Amico A.V. et al. performed a transperineal MRI-guided prostate biopsy in an open configuration 0.5 Tesla MRI scanner [75]. Nowadays, high-precision robotic systems have been applied to overcome the problem of limited patient access inside the bore of the MRI scanner. Fichtinger et al. designed one of the first manually powered platforms for prostate interventions in a closed MR system. The system was reported to have a size of a carry-on suitcase, and have a 7-DoF, passive mounting arm with a motorized end effector. In the phantom study, the average distance error between the needle tip and the target was 2 mm [76]. Alternatively, some studies have been focusing on assistive medical devices. Tokuda et al. developed a rigid acrylic template for a transperineal needle biopsy. The distance errors (root-mean-square) between the needle and the planned targets were 4.9 mm [77].

2.5 Precision Surgical Treatment

Minimally Invasive or percutaneous Surgery (MIS) has been regarding as an important milestone in modern surgery. It is a surgical procedure that involves small cut openings, miniaturized instruments, and anatomic imaging guidance. Bozzini developed the first endoscope for minimally invasive surgery in 1806 [78]. Since then, thanks to the constantly evolutionary advancement, the surgical instruments used in MIS has transformed from simple and bulky devices to sophisticated and automated instruments. During the past decade, the MIS has significantly influenced many surgical specialties, such as thoracic surgery[79], gastrointestinal tract[80],

cardiac surgery[81], oral and maxillofacial surgery[82], and nephrectomy[83]. It is foreseeable that major surgical procedures will be leaning towards a minimally invasive approach[84, 85].

However, as to the physicians, MIS were both new opportunities and challenges for them as MIS could potentially reduce surgical accuracy and introduce unexpected complications[86]. The procedure poses a learning curve risk for physicians to operate new instruments in the OR. Another problem is that indirect vision and manipulation of soft tissues could disturb hand-eye coordination as well as the perception of depth. In order to overcome the above challenges, one current trend is to integrate the MIS with image-guided intervention technologies.

One typical MIS procedure—thermal energy-based tumor ablation is referring to the destruction of human tissue via extreme temperature (high or low). Percutaneous energy-based ablation has been applied for the treatment of many types of malignancies, such as liver[87], kidney[88], lung[89], and bone cancers[90]. In order to control the level of energy deposition, either multiple temperature probes[91] or specialized temperature-sensitive imaging methods (particularly MRI) are employed[92]. In the ideal thermal therapy procedure, the targeted tissue volume is heated to 57-60°C for protein denaturing[93]. The application of thermal surgery has gradually increased due to the improvement of imaging guidance and monitoring. MR imaging is sensitive to temperature changes, and recent advances have made it possible to obtain MR images in less than 1 second, thus making it feasible to obtain and update three-dimensional temperature change "maps" of the tissue under consideration in times matched to the temporal resolution of the thermal changes so as to avoid artifacts [29]. This feature allows MRI thermometry to be used to guide, monitor, and control the thermal ablation [94].

2.5.1 Radiofrequency Ablation

One of the most commonly used thermal ablation technique is called radiofrequency ablation (RFA). RFA was primarily developed for the treatment of aberrant cardiac pathways and has now been increasingly used for renal masses and prostate hyperplasia [[95]. The main mechanism of RFA depends primarily on the principle of heat conduction caused by high frequency alternating RF current. Many clinical cases have reported using RFA procedures under image guidance, such as CT [96] and ultrasound [97], but not MRI due to the interference.

2.5.2 Laser Ablation

Interstitial Laser Therapy (ILT) is another minimally invasive technique that uses image-guided needle probes, which delivers focused laser energy and destroys tumor cells[98]. MRI monitoring of interstitial laser therapy has been suggested [99]. ILT has shown to treat many tumor-specific pathologies such as radiation necrosis [100] and pediatric brain tumors [101]. ILT has proved useful for cases in which the tumor locations are difficult to access or high-risk surgical patients involved[102].

However, ILT has the drawback of a wide range of temperature profiles across the optical fiber, which could create a non-uniform thermal lesion through the ablation site. Image guidance has helped to mitigate the drawback of this procedure. Baccaria et al. have conducted a study of brachytherapy of malignant lung lesions using MRI images together with interstitial laser therapy. The results showed the technique is safe to operate [103].

2.5.3 Cryoablation

A number of studies have suggested cryotherapy could destroy tumors using extreme cold. This would allow for the implementation of MIS treatment without damaging collagenous tissue structures[104]. Cryoablation is a promising technology due to its relatively low cost, effective cellular necrosis, and anesthetic effect due to cell cooling[105]. Current cryosurgical

procedures are either open (oral) or percutaneous (prostate). Image guidance and continuous monitoring are required [106]. Recent technological developments in the cryoprobes have made MRI guidance possible[107].

2.5.4 Ultrasound Ablation

Focused ultrasound (FUS) evolved from lithotripsy and has affinities to localized hyperthermia techniques pioneered in the 1940s and 1950s. FUS uses an ultrasound transducer to create a point source of heat at its focus[108]. High-aperture ultrasound transducers are able to create a converging beam for focal treatment. The ablation temperature is between 70°C and 100°C. The point source of heat could generate a uniform cylindrical shape (Diameter:1—3 mm and Length: 2—5 mm). The advantage of using FUS is that it destroys only the target without affecting the surrounding tissues. However, the lack of appropriate localization and temperature-monitoring techniques has made it difficult to achieve clinically useful applications. Both Ultrasound and MRI has been suggested as the optimal technique for spatially localizing, targeting, and controlling heat deposition and has been tested by various research groups[109-111]. The rapid MRI image acquisition can offer instant feedback to the physicians, which significantly reduces the risk of damaging to normal structures. **Figure 2-3** shows four examples of commercially available surgical treatment devices.

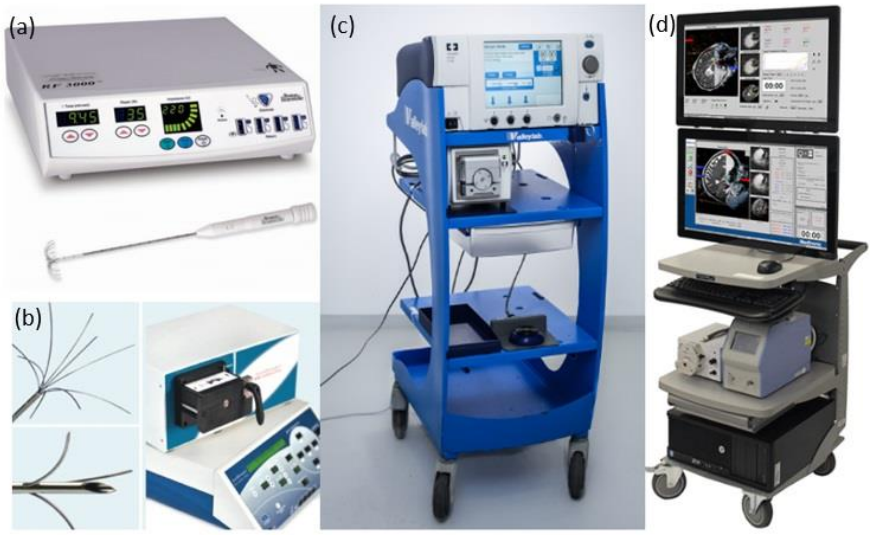

Figure 2-3: Show some commercially available devices. (a) LeVeen needle electrodes by Boston scientific [112], (b) StarBurst XL & semi-flex RFA device by Angiodynamics [113], (c) Valleylab Cool-tip RF ablation system by Covidien [114], (d) Visualase MRI-guided ablation system by Medtronic [115].

Table 2-3 shows the details of the medical devices mentioned in **Figure 2-3**.

Table 2-3: The working principle and performance metrics of selected devices.

Company	Commercial System	Working Principle	Performance metric	Reference
Boston Scientific (Natick, MA)	LeVeen Needle Electrode	Radiofrequency ablation (RFA)	This method enabled safe ablation without complications. The mean follow-up period was 13.5 month (range, 9–18 months). No local recurrence was observed at the follow-up points.	[112]
AngioDynamics (Queensbury, NY)	StarBurst XL	RFA	The largest diameter of ablation was 25.6 ± 3.7 mm, the smallest diameter 21.9 ± 2.9 mm, and the ablation volume was 7.20 ± 2.38 cm^3	[113]
Covidien (Mansfield, MA)	Valleylab Cool-tip RFA system	RFA	Long- and short-axis diameters of the ablation areas by RFA were 30.9 ± 1.1 mm, and 26.8 ± 2.9 mm, respectively.	[114]

Medtronic	Visualase	Laser Ablation	The ablation ares was 0.30 ± 0.18 cm^2 in kidney samples and 0.69 ± 0.41 cm^2 in liver.	[115]

2.5.5 Robotic-assisted Ablation

The da Vinci robotic surgical system (Intuitive Surgical, Sunnyvale, CA) has been proved to be one of the most prominent robotic surgical systems. It has been applied in for a wide range of procedures, such as lung interventions. The da Vinci system has two major units—the physician's console unit and manipulator units. The physician's console unit is basically the user display and interacting system, which can provide the physician with the virtual in-vivo operational information. Apart from that, there a variety of manipulator units, including telemanipulators and endoscopic cameras. The physician sits at the console look at the binocular display of the operational field while controlling the manipulator unit to carry out different surgical tasks. Hubens et al. reported a performance study and showed that the inexperienced user was able to complete the task with fewer mistakes and faster speed[116]. Park et al. also used this system for a clinical trial of 34 patients, and the study approved the system was feasible and safe for video-assisted thoracic surgeries[117]. **Table 2-4** shows typical examples of commercialized robotic systems.

Table 2-4: Commercially available surgical robotic system for interventions

Company	Commercial System	Type of surgery	Performance metric	Reference
Renishaw	NeuroMate	Neurosurgical procedure	(1) with the robot in a frame-based configuration, the RMS error was 0.86 ± 0.32 mm; (2) with the robot in the frameless configuration. The RMS error was 1.95 ± 0.44 mm; (3) in a standard stereotactic (ZD) frame-based approach. The RMS error was 1.17 ± 0.25 mm; (4) with an infrared tracking system using the	[118]

			frame for fiducial registration. The RMS error was 1.47 ± 0.45 mm; (5) with an infrared tracking system using screw markers for registration. The RMS error was 0.68 ± 0.26 mm.	
Prosurgics	Pathfinder	Neurosurgical procedure	A total of 140 targets were tested with an average of 3—4 targets per patient. The mean application accuracy was less than 1 mm, and the application accuracy was consistent in all targets in the same patient.	[119]
Maxor Robotics	Renaissance	Spinal surgery	The average distance of the screws from the facets was 5.2 ± 2.1 mm and 2.7 ± 1.6 mm in the Robot-PLIF and Freehand-PLIF groups, respectively ($P < 0.001$).	[120]
Curexo Technology Corp	THINK Surgical TSolution-One	Knee surgery	The mean surgical duration for our robotic-assisted TKA patients was 91 min. The robotic-assisted TKA can be performed by one surgeon, one assistant, and one scrub nurse. One additional THINK Surgical staff is required on-site to control the robot, provide technical assistance, and rectify intraoperative workspace errors as required.	[121]
MAKO	Robotic Interactive Arm (RIO)	Knee surgery	RMS errors were within 3° for all femoral component alignments. The mean tibial RMS error was 1.5°, and the mean femoral RMS error was 2.6°.	[122]
Intuitive Surgical	da Vinci	Lung surgery	The operating time was 46 —300 min, averaged at 91.51 ± 30.80 min.	[123]

Micro Hand S (Tianjin University, China) consists of a surgeon console as well as a slave cart, which was claimed to require less maintenance work and adjustable sensitivity level of the robotic operation. The first clinical trial was reported recently [124]. The Flex robotic system (Medrobotics, Raynham, MA, USA), which received the US FDA in 2015, provides surgeons with single-site access visualization of hard-to-reach anatomical locations. Remacle *et al*. reported the first surgical application of the Flex robotic system on humans by performing three

procedures of transoral robotic surgery [125]. Titan Medical (Toronto, ON, Canada), a public company, has developed the Single Port Orifice Robotic Technology (SPORT™ surgical system). The system contains two articulating instruments with disposable and replaceable tips and a 3D high-definition camera. The incision can be as small as 25 mm [126].

Revo-i (Meere Company Inc., Yongin, Republic of Korea) includes a surgeon control console, a four-arm robotic operation cart, a high-definition vision cart, and reusable endoscopic instruments. A preclinical study of Revo-i was completed on the porcine model in 2016. Chang et al. and Kang et al. performed human clinical trials of robotic prostatectomy and cholecystectomy, respectively, using Revo-I [127, 128].

The multiport surgical robotic ALF-X system (SORAR SpA, Milan, Italy) was firstly designed for gynecological surgery. Fanfani et al. reported that 146 cases of hysterectomy were carried out with the ALF-X system for benign and malignant diseases [129]. Compared to the da Vinci system, each arm of ALF-X can be positioned independently from the others in the surgical field. The system has incorporated haptic feedback and a remote 3D vision with an eye-tracking system. However, one of the limitations is the lack of wristed instruments such as needle drivers used in the da Vinci system.

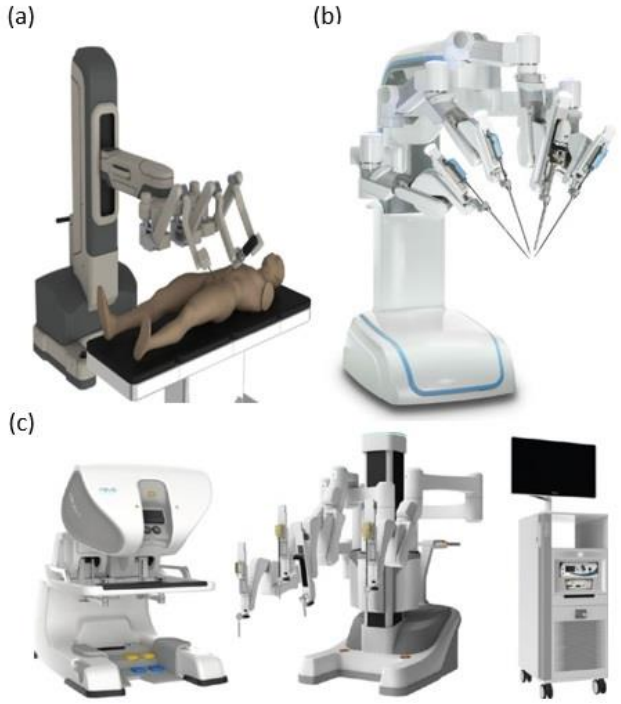

Figure 2-4: Shows (a) Micro Hand S system, which was developed by Tianjin University, China, has a three-arm operation cart [124], (b) Revo-i robotic system, which was developed by Mere company, South Korea, has a four-arm operation cart [80], (c) da Vinci robotic system, which was developed by Intuitive Surgical, has a four-arm operation cart, a surgeon console, and vision cart [123].

2.6 Precision Physical Rehabilitation

Physical rehabilitation, or physical medicine, aims to enhance and restore functional ability to those whose activities of daily life (ADL) has been significantly impacted by physical impairment and disabilities. In another words, it is a set of interventions required when a person is experiencing or is likely to experience limitations in daily functioning due to aging or a health condition, including chronic diseases or disorders, injuries or traumas. It is a highly person-centered health strategy that may be delivered through specialized rehabilitation programs. There is one specific type of rehabilitation called neurorehabilitation. It aims at treating conditions such as movement disorders. The patients have to repetitively move their limbs so that functional patterns can be produced. Common movement disorders include but are not limited to

Friedreich's ataxia [130], cervical dystonia [131], Huntington's disease [132], and Parkinson's disease [133-135]. For example, Parkinson's disease has affected 1 million people in the US and 5 million people worldwide [136]. Rehabilitative locomotor training is very labor intensive, and requires three or four physical therapists for one patient intervention. In recent years, new technologies have been applied to enhance the efficacy of neurorehabilitation. Significant breakthroughs have occurred in the fields of wearable IMU sensors, rehabilitation robots, and virtual reality (VR)–based physical therapy.

2.6.1 IMU-assisted Rehabilitation

The micro-electro-mechanical systems (MEMS) IMUs has given a new surge to motion tracking research [137-140]. These devices are cost-effective for accurate, non-invasive, and portable motion tracking. The major point of interest in these devices is that they can overcome the limitations of optical systems and mechanical trackers. The use of inertial sensors has become a common practice in ambulatory rehabilitation [141, 142]. In order to increase the accuracy and attain drift-free orientation estimation, several works of literature reported combining the signals from 3D gyroscopes, accelerometers, and magnetometers. Kong et al. have developed an IMU-based motion capture system. The WB-4R sensor composed of a 3-axis gyroscope and a 3-axis magnetometer. The results showed the accuracy of motion tracking is comparable to a commercially optical system Optitrack[143]. However, other researches have reported potential interference on the accelerator as well as magnetometer due to the presence of vibration and ferromagnetic material. Chang et al. developed a new logarithm based on the Direction Cosine Matrix (DCM), only use the input from a gyroscope. The result approved the feasibility of measuring human joint angles via IMU sensors[144]. **Table 2-5** summarizes some of the major commercialized and under-developed systems.

Table 2-5: Current commercially available or under-developed IMU systems

Companies or research group	System	No. of sensors	Main body area	Detail	Reference
Xsens Technologies	MVN	17	Full body	Xsens MVN consists of 17 inertial and magnetic sensor modules. Data is transmitted by a wireless connection to the laptop computer on which the processing is performed and visualized. A suit is used for quick and convenient placement of sensors and cables.	[145]
Muller et al.	Xsens-MTs Awinda	2	Upper limbs	The device is alignment-free and self-calibrating using arbitrary movements of the user and an initial zero reference arm pose	[146]
Chang et al.	Custom	2	Upper limbs	It is a device for angle measurement method through the IMU sensor, which can be mounted on the fingers and have the ability to measure each angle of each finger.	[144]
Kong et al.	WB-4R	7	Lower Limbs	The IMU sensing system is composed of seven WB-4R IMUs. One placed on the subject on the lumbar spine, one on each upper leg, one on each lower leg, and one on each forefoot. Each IMU was positioned roughly in the middle of the segments considered in the kinematic model.	[143]
Bakhshi et al.	Custom	2	Lower limbs	It is a device to measure knee angle using two IMU sensors mounted on the body shank and thigh. The measurements are transmitted to a computer via Bluetooth protocol for further data analysis and evaluation.	[147]

Figure 2-6 shows some developed IMU motion tracking systems. The Xsens system has 17 sensors, which can track full-body movement (**Figure 2-6 (a)**). Muller et al. developed a self-

calibrating elbow angle device (**Figure 2-6 (b)**). Chang et al. developed a device for finger rehabilitation (**Figure 2-6 (c)**). Bakhshi et al. developed a device to track knee movement (**Figure 2-6 (d)**).

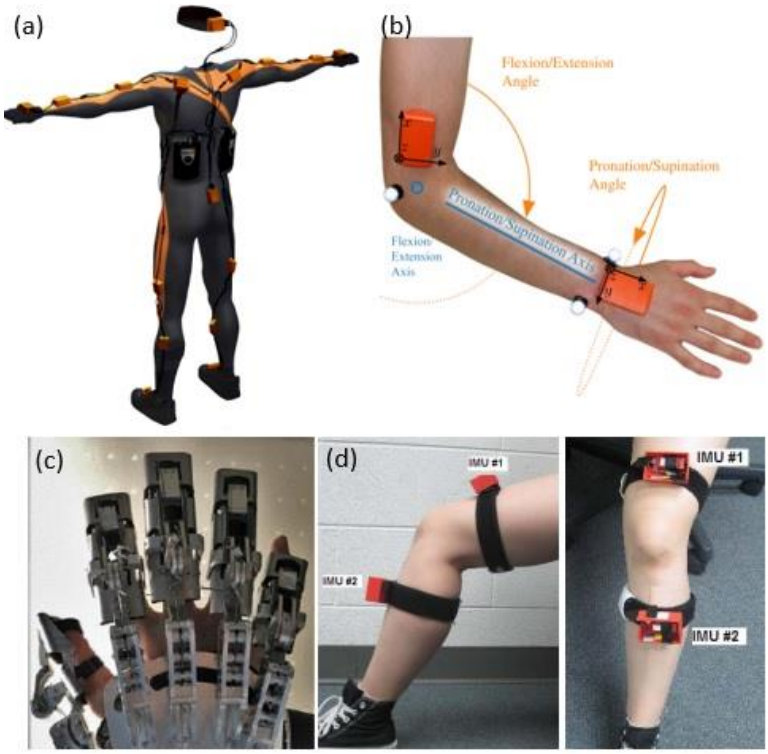

Figure 2-5: Different types of IMU motion tracking systems. (a) Xsens system [145], (b) Muller et al.'s self-calibrating elbow angle device [146], (c) Chang et al.'s developed finger device [144], and (d) Bakhshi et al.'s body joint angle measurement system [147].

2.6.2 Robotic-assisted Rehabilitation

Robotic rehabilitation is currently regarded as a rapidly developing field, which is considered as a complementary technology to the therapist's work [148-151]. One of the major advantages of using robots is that they can deliver highly intensive training [152]. Assistive robotic systems are designed to allow patients to have more autonomy with a wider range of exercise tasks. The use of robotic devices has been reported to be an effective additional therapeutic treatment and motor learning [153], including the effectiveness of repetitive grasp and

release exercises [154], constraint-induced therapy for the paretic limb [155], and feasibility of high-intensity exercise [156]. **Table 2-6** shows some more robotic systems for rehabilitation.

Table 2-6: Current commercially available or developing robotic-assisted rehabilitation systems

Institute	System name	Types	Application	Detail	Reference
University of Leeds	iPam	Single point of contact	Upper limb	This system uses two symmetric arms with three active degrees of freedom in each robotic arm. The main drawback of this iPam system is that the free space usually needed by the therapist to assist the patient	[157]
University of California, Irvine	Pneu-WREX (Pneumatic-Wilmington RoboticEXoskeleton)	Exoskeleton	Upper limb	The wearable 4-DoF exoskeleton using pneumatic muscles. 1 DoF at shoulder, one at the elbow, one at the forearm and one at the wrist	[158]
Argo Medical Technologies Ltd	Rewalk	Exoskeleton	Lower limb	It comprised a motorized exoskeleton, a battery unit, and a computer-based controller contained in a backpack, a wireless mode selector, and an array of sensors that measure the upper-body tilt angle, joint angles, and ground contact.	[159]
Cybernics	HAL	Exoskeleton	Full body	It is an exoskeletal robot for humans with joints designed to fit those of the wearer. It can move several, computer-controlled, electromotor driven joints, called power units, to assist the wearer's motor function	[160]
University of Delaware	Active Leg Exoskeleton (ALEX)	Treadmill-based exoskeleton	Lower body	ALEX is a motorized orthosis. The overall setup has five main components. (i) Walker, which supports the weight of the device; (ii) The main body part; (iii) Thigh segment of the orthosis has two DOFs with respect to trunk of the orthosis; (iv) The shank (v) Foot segment.	[161]

Handy 1 (Rehab Robotics, Keele, UK) was the first commercial assistive robot for rehabilitation [162]. It is controlled by a single switch input to select the desired actions as it was designed to assist a young patient. Another early task-specific rehabilitation system is the Neater Eater (Neater Solutions, Buscton, UK), a modular device assist patient's eating recovery and can be controlled either by hand or via head or foot switches [163]. Other research mainly focuses on robotic arms with more degrees of freedom. Exact Dynamics' iARM had a robotic arm and two-fingered grasper. The robot can be mounted to electric wheelchairs and accessible via multiple ways such as a keypad, joystick, or single button [164]. The Mobility System (Myomo, Cambridge, MA, USA) is designed to be a wearable device that can achieve patient arm movement activated by biosignals [165].

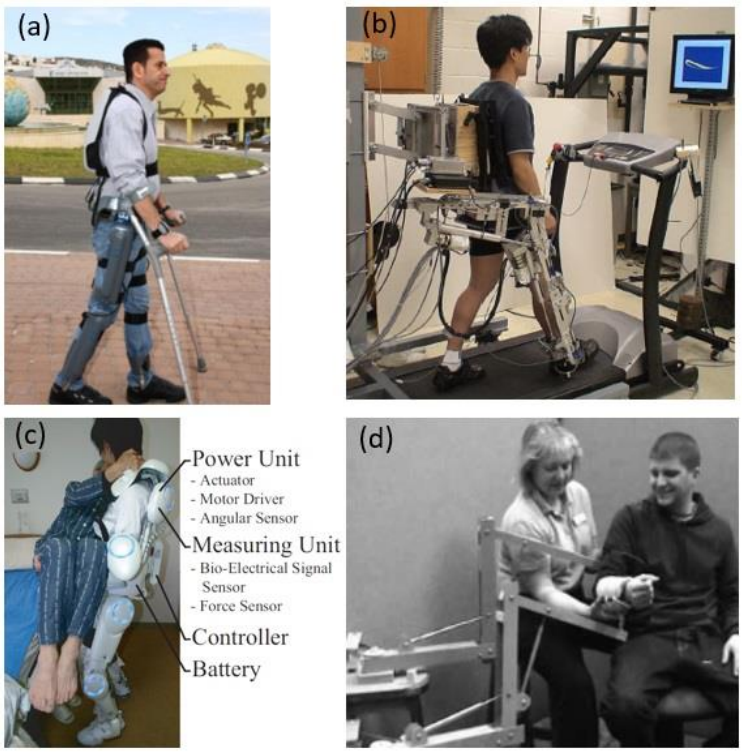

Figure 2-6: Shows the systems of (a) Rewalk developed by Argo Medical Technologies Ltd [159], (b) ALEX developed by University of Delaware [161], (c) HAL developed by Cybernic s [160], (d) I-Pam developed by University of Leeds [157].

2.6.3 VR-based Rehabilitation

Virtual reality (VR) in neurorehabilitation is an emerging approach that shows great promise to enhance the motor learning of the patients, resulting in more effective motor recovery. VR Rehabilitation is defined as a "group of all forms of clinical intervention (physical, occupational, cognitive, or psychological) that are based on, or augmented by, the use of virtual reality, augmented reality, and computing technology" [166]. The range of virtual rehabilitation includes local interventions or telerehabilitation. VR therapies or interventions are conducted using real-time motion tracking as well as computer graphic technologies to display the patients' physiological behavior during assigned specific tasks in a virtual rehabilitation environment.

VR rehabilitation has been applied in Stroke [167], Cerebral palsy[168], Parkinson's [169], and many other conditions. Using VR as a tool for healthcare has the advantage of real-time feedback and modification and flexible training programs [170]. Moreover, VR offers personalized treatment and further standardizes the assessment and training protocols [171].

The features of immersion and interactive engagement enables VR to offer the patients with unique experiences that are extensive, surrounding, inclusive, vivid, and matching [172]. This will improve the assessment outcome of neurorehabilitation. The current development of VR rehabilitation can be divided into three different categories: non-immersive, semi-immersive, and fully immersive. Subramanian et al. studies of the upper extremity movement patterns of the patients with a fully immersive system. They use a head-mounted device (HMD) with a FOV of 50°, a rear-projection system, and a motion tracking system (Optotrak Certus, NDI, Ontario Canada) [173]. Slobounov et al. compared the postural stability and navigation success rates between 3D VR (fully immersive system) and 2D projection screen (semi-immersive system) in spatial navigation tasks. The test results reported that the fully immersive system enables the patients to focus more on cognitive and motor training. The

successful rate of navigational tasks was statistically significantly higher using the fully immersive system [174]. **Table 2-7** shows some more recent developed VR-based rehabilitation systems.

Table 2-7: Current commercially available or developing VR rehabilitation systems

Research group	VR model	Type of patients	Body area	Detail	Reference
Subramanian et al.	Kaiser 150	Stroke	Upper	To compare shoulder movement patterns when performed in a head-mounted display (HMD or screen projection system	[173]
Lloréns et al.	N/A	Stroke	N/A	To study mobility variables of a VR-based balance rehabilitation system for patients with acquired brain injury	[175]
Slobounov et al.	3D Glasses	Asymptomatic	N/A	To examine the effect of immersive 3D presentations and less immersive VR environments	[174]
Bailenson et al.	CAVE	Asymptomatic	N/A	To study the effect of interactivity on learning physical actions in VR	[176]
Gokeler et al.	CAREN	ACL (knee)	Full body	To study if the VR will improve the movement pattern of patients with ACL.	[177]

Figure 2-7 shows three rehabilitation systems, Figure 2-7 (a) shows a fully immersive system designed by Crosbie et al. Figure 2-7 (b) and (c) shows two semi-immersive systems.

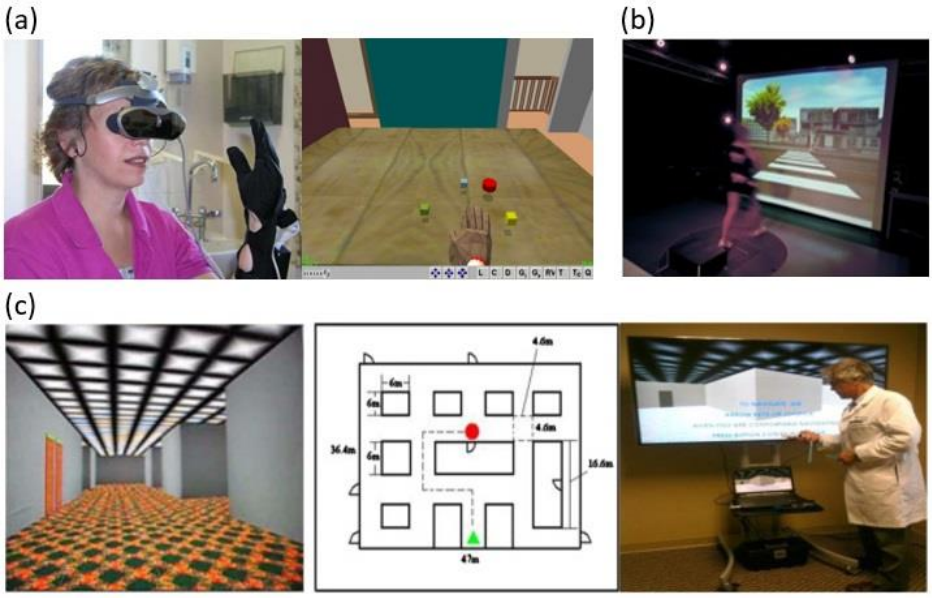

Figure 2-7: Different types of VR rehabilitation systems, (a) Crosbie et al.'s experimental set up [176], (b) Gokeler et al.'s experimental setup [177], and (c) Slobounov et al.'s experimental setup [174].

CHAPTER 3

LANDSCAPE OF PRECISION MEDICINE IN CLINICAL APPLICATIONS[1]

[1] Li, R., Jumet, B., Ren, H.L., Song, W.Z. and Tse, Z.T.H. To be submitted to *Minially Invasie Therapy & Allied Technolgies.*

3.1 Abstract

An optical tracking system (OTS) is one of the most popular surgical navigation tools for training in neurosurgery. However, OTSs can encounter errors while operating in various clinical environments. The purpose of this paper is to quantitatively evaluate the accuracy as well as potential limitations of the NDI tracking system in a lab setting. In this paper, we tested three potential error sources: the marker orientation, the marker occlusion affected by the blood during surgery, and the environmental reflection. These experiments generated a maximum error of 2.63°, 4.88 mm, and 0.55 mm for the marker orientation, the marker occlusion, and the environmental reflection, respectively. During the reflection test, there were many phantom points generated to make the tracking impossible. In the discussion, we suggested guidelines for using OTSs for reducing medical errors and thus improving patient safety.

3.2 Introduction

Tracking systems are essential components for minimally invasive surgery, which can perform operations in small areas, which reduces bleeding, relieves pain, and shortens recovery time[1]. There are many tracking systems available, such as Electromagnetic (EM)[2] and optical tracking[3]. An optical tracking system (OTS) is a universal and well-accepted system for surgeries [4-7] with high accuracy. An OTS utilizes high-precision hardware and algorithms integrated with a purposely developed software such as NDI 6D Architect® to track the exact position and rotation of a surgeon's tool down to the sub-millimeter level[8]. There are two different types of OTS. One is active optical tracking, where a camera captures the light emitted by infrared markers fixed on the surgical instruments. The other is passive optical tracking, where illuminators emit light, and a camera captures the light reflected by retro-reflective markers attached to the instruments.

There are many commercial OTSs on the market, such as the Polaris optical measurement system by Northern Digital Inc. (Ontario, Canada) [56, 193], Certus, and Certus HD by Optotrak, Micron Tracker Hx60 by ClaroNav Inc, FusionTrack 500 by Astrasys Interactive SA (**Table 3-1**).

Table 4-1: Shows some commercially available optical tracking systems (OTS)

Model	Company	Reported Accuracy (RMS)	Tracking volume (radius × width × height) (mm)
Polaris Vega [193]	NDI	Pyramid (measurement volume): 0.20 mm	Pyramid: 1566 × 1312 × 2400
		Extended pyramid (extended measurement volume): 0.30 mm	Extended pyramid: 1856 × 1470 × 3000
Polaris Spectra [56]	NDI	Pyramid: 0.25 mm	Pyramid: 1566 × 1312 × 2400
		Extended pyramid: 0.30 mm	Extended pyramid: 1856 × 1470 × 3000
Polaris Vicra [56]	NDI	0.25 mm	Volume: 1336 × 938 × 887
Certus [194]	Optotrak	0.10 mm	Volume: 7000 × 4200 × 3000
Certus HD [195]	Optotrak	0.10 mm	Volume: 7000 × 4200 × 3000
Micron Tracker Hx60[196]	ClaroNav Inc	0.35 mm	Volume: 2000 × 1300 × 1000
FusionTrack 500[197]	Astracsys Interactive SA	0.09 mm	Volume: 2000 × 1327 × 976

However, the use of an OTS is limited by the operating environment in which it is used. Such limitations can be from line-of-sight issues; background noise (e.g., reflection and refraction of infrared light); visibility of the passive markers from various types of biohazardous waste (e.g., blood); orientation of the surgical tool and its markers; and other interferences commonly seen in an operating room environment.

Previous studies have mainly focused on investigating the accuracy of OTSs rather than studying their limitations [188, 198-207]. In one study of a surgical tracking system, Ma et al.

reported Micron Tracker (ClaroNav Inc, Toronto, Canada) is sensitive to illumination and fail to track two or more surgical tools. However, they did not quantitatively analyze the errors[208]. Kral et al. claimed the accuracy of one OTS—Stealth Station S7 (Medtronic SNT, Louisville, CO) was 0.22 mm and also mentioned the problem of line-of-sight. However, the authors did not quantify the tracking error [209].

The purpose of this study is to fill the knowledge gap left from the previous studies and provide an in-depth assessment of the inaccuracies of an OTS due to interferences from a clinical environment. The novelty of this work is to use a high-precision robotic system in a purposely created environment to exam possible limitations of NDI OTS in detail and give quantifiable error reports. It is hypothesized that there are three major factors introducing errors to OTSs. The first factor is the optical distances between the markers. Marker orientation becomes an issue when the tool is rotated to an extreme angle such that two markers eclipse each other. This causes the system to have difficulty in differentiating between the two markers, determining a center point of each marker, and thus locating the tip of the tool inside the patient. The second factor is the partial occlusion of markers. As the marker gets covered by blood splatter or surface marks during one single procedure, the reflective surface is no longer an ideal reflective sphere that the OTS uses to determine the marker location. The third factor is environmental reflection. The stainless-steel tools, trays, and other reflective materials omnipresent in surgical settings are bound to redirect infrared waves undesirably and thus interfere with the abilities of the OTS. This paper aims to quantify the magnitudes of errors that result from these factors and provide quickly implementable solutions to reduce or prevent these errors and ultimately provide suggestions for training.

3.3 Materials and Methods

Figure 3-1 shows a detailed description of tracking methods, environment, and assessment. In the section of tracking methods, it shows reflective markers are continuously tracked by the NDI OTS. In the section of the environment, a 3D-printed tool was used to hold the needle in position. There are three experiments performed to assess the accuracy of the NDI OTS: marker orientation, maker occlusion, and environmental reflection.

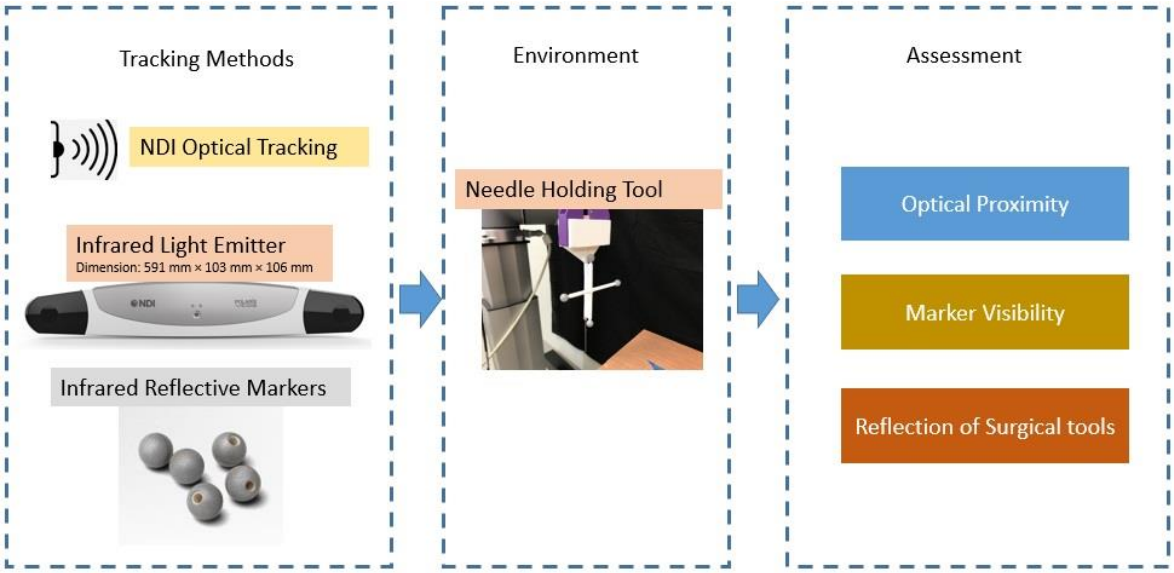

Figure 4-1: Overall test design for assessing the accuracy of the OTS.

The working principle of NDI OTS, as well as the tracking volume of the NDI, are shown in **Figure 3-2**. OTS often employ infrared sensing through two or more cameras to triangulate a position in three dimensions. The sensors often use passive markers that are attached to the surgical tool and employ a reflective surface to reflect infrared light from emitters surrounding the camera lenses back to the cameras. NDI Polaris Vega® (NDI OTS) (Ontario, Canada) was used in this study for accurate tracking of a training tool. The tool, as shown in **Figure 3-2(c)**, was designed as a rigid body according to the NDI tool design guideline[210], and 3D printed using MakerBot Replicator® (Kowloon, Hong Kong). The tool was to hold the biopsy needle as

well as the infrared (IR) reflective markers. The markers were configured to be seen as normal to the NDI. Therefore, although the markers were position to be orthogonal to the typical normal direction, they were correctly observed by the NDI.

All the tool tracking parameters of the NDI software shown in **Table 3-2**. The maximum 3D angle means the marker can be facing away from the position sensor. The maximum 3D error means the maximum difference between the marker's expected and measured positions. The minimum spread means the system is checking the minimum distance requirement between the markers for tool transformation. However, the marker spread check is not implemented for passive Polaris.

Table 4-2: The tool tracking parameters used in this study	
Maximum 3D angle	90°
Maximum 3D error	2
Minimum spread	0

The Universal Robot 10® (Odense, Denmark), hereafter referred to as the UR10, allows precise movement of the designed tracking tool and mitigates additional human errors. The movement precision for the UR 10 is ± 0.05 mm. Thus, the UR10 was used to manipulate a needle in the OTS assessments conducted in this study. Finally, the software used was 6D Architect® developed by NDI. This software allows the user to create a rigid body and track the rigid body using the optical sensors. Additionally, Microsoft Excel was used as the processing software to analyze the exported data from 6D Architect®.

(a) The experimental workflow

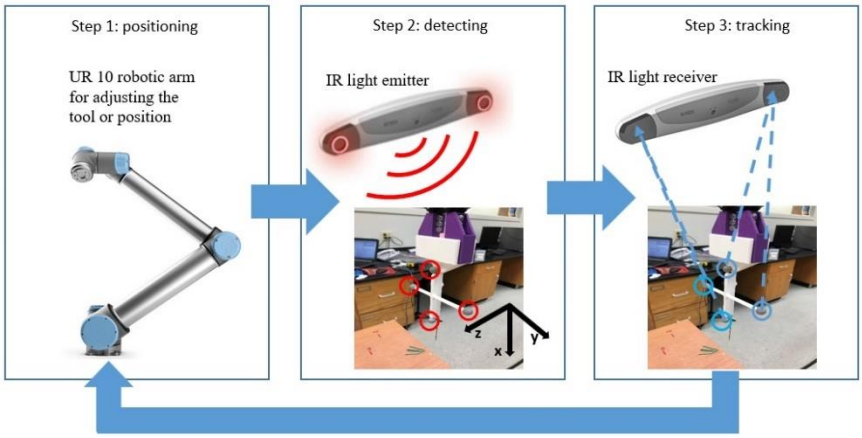

(b) Tracking volume of the NDI OTS

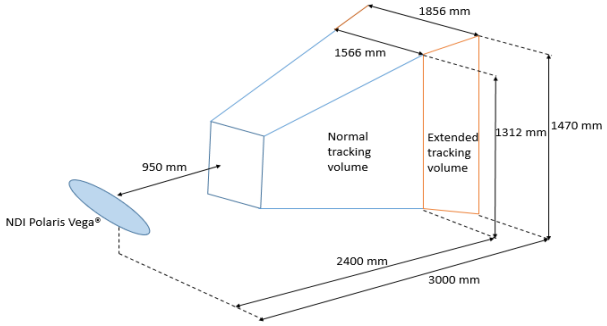

(c) Tool dimensions

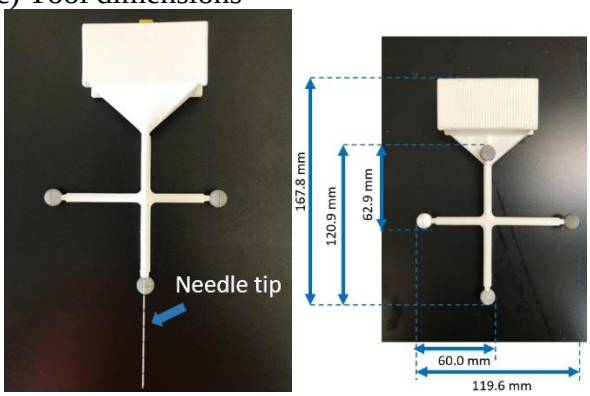

Figure 4-2: Shows the experimental and tool setup, (a) displays the working principle of NDI OTS, UR 10, and relevant hardware, (b) shows the tracking volume of the NDI OTS, (c) shows the tool dimensions.

Each experiment was run five times and **Eqs. (1) — (11)** were used to quantify the movements and errors of the needle. **Table 3-2** defines all the symbols used in the equations; the coordinate system referred to was shown in **Figure 3-3 (d)**.

Each experiment used the middle 50% of the time elapsed. The experiments lasted 10—20 seconds at each orientation or position. The first 25% of each orientation or position were avoided for analysis due to the induced frequency of a sudden start and stop. The last 25% of each orientation or position were excluded because the frame rate and thus, time tracking of the NDI was not consistent and would deviate further from the actual elapsed time throughout each experiment. For consistent analysis, the middle 50% of each actual ten-second window was used.

These specific time allotments were qualitatively observed to be sufficient to avoid both problematic situations.

The marker orientation experiment analyzed the orientation accuracy when subjecting the tool to the rotation. These calculations used the incremental difference in marker orientation. This theoretical difference would be 1° at every measurement. (**Eqs. (1) – (2)**). The other two experiments (marker occlusion and reflective interference from the surgical tool) used a translational analysis of the needle tip. These experiments analyzed the difference between the control experiment with no interference and the same movements with the interference introduced. The control experiment was also conducted twice: once before the interference, and once after. That would make sure that no perturbations had occurred during the process of the recorded interference experiments. These two controls were averaged and compared relative to the trials with the interference introduced. Further, if the deviation of measurements between the prior and post control experiments is more than 5%, the experiment data would not be included for analysis.

Table 4-3: Shows the Symbols used for equations in **Table 3-4** (The coordinate system is shown in **Figure 3(d))**.

Optical Proximity		
Variable	Definition	Unit
R_x	Rotation in NDI X-Z Plane (Around NDI Y-Axis)	Degrees
Ry	Rotation in NDI Y-Z Plane (Around NDI X-Axis)	Degrees
n	n^{th} degree	
Marker visibility and Reflection		
T_x	Translational Position in X Direction	mm
T_y	Translational Position in Y Direction	mm
T_z	Translational Position in Z Direction	mm
n	Trial Number	

$N_{1, 2, 3, 4, 5}$	Sub-trial Number	

The equations for calculating the errors are shown in **Table 3-3**:

Table 4: Equations used to calculate detection errors	
Marker Orientational Error (Yaw Direction)	
$Ry_{error} = \overline{Ry_n} - \overline{Ry_{n-1}} - 1°$	(1)
Marker Orientational Error (Pitch Direction)	
$Rx_{error} = \overline{Rx_n} - \overline{Rx_{n-1}} - 1°$	(2)
Translational Positional Error in Marker Occlusion and Environmental Reflection	
$Tx_{error,n} = \lvert \overline{Tx_n} - \overline{Tx_{Control}} \rvert$	(3)
$Tx_{control} = \frac{(Tx_{control,1}) + (Tx_{control,2})}{2}$	(4)
$\overline{Tx_n} = \frac{\overline{Tx_{n,1}} + \overline{Tx_{n,2}} + \overline{Tx_{n,3}} + \overline{Tx_{n,4}} + \overline{Tx_{n,5}}}{5}$	(5)
$Ty_{error,n} = \lvert \overline{Ty_n} - \overline{Ty_{Control}} \rvert$	(6)
$Ty_{control} = \frac{(Tc_{Control,1}) + (Ty_{control,2})}{2}$	(7)
$\overline{Ty_n} = \frac{\overline{Ty_{n,1}} + \overline{Ty_{n,2}} + \overline{Ty_{n,3}} + \overline{Ty_{n,4}} + \overline{Ty_{n,5}}}{5}$	(8)
$Tz_{error,n} = \lvert \overline{Tz_n} - \overline{Tz_{Control}} \rvert$	(9)
$Tz_{control} = \frac{(Tz_{control,1}) + (Tz_{control,2})}{2}$	(10)
$\overline{Tz_n} = \frac{\overline{Tz_{n,1}} + \overline{Tz_{n,2}} + \overline{Tz_{n,3}} + \overline{Tz_{n,4}} + \overline{Tz_{n,5}}}{5}$	(11)

Figure 3-3 shows the experimental setups for three different tests. The optical tracking system was mounted on the wooden board in a fixed position to the needle tool within the tracking distance of 2400 mm, defined in **Figure 3-3 (b)**. **Figures 3-3 (a)–(b)** show the UR10 holding the tracking tool directly, while **Figures 3-3 (c)** show the UR10 holding the reflective material.

(a) The marker orientation test

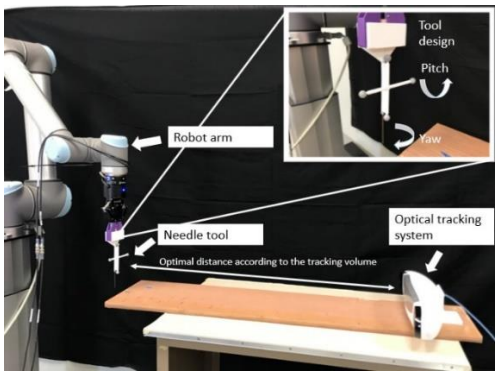

(b) The marker occlusion test

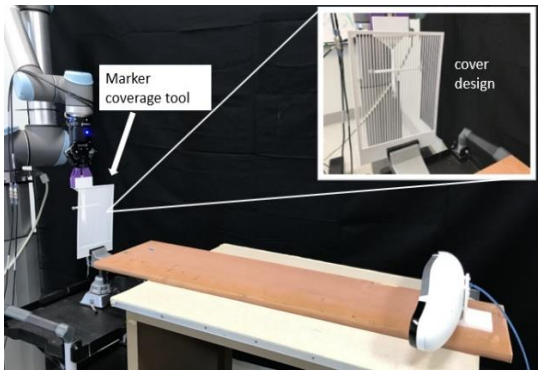

(c) The environmental reflection test

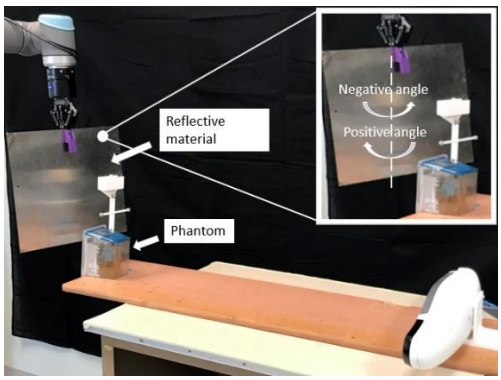

(d) The global coordinate system of the NDI Polaris Vega®

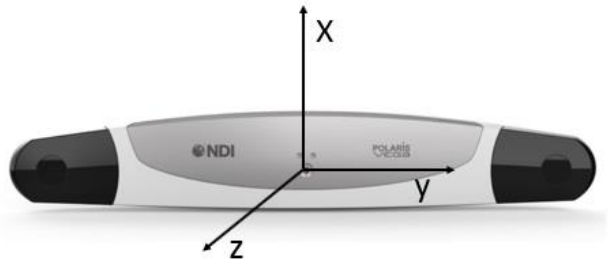

Figure 4-3: Experimental setup for testing: (a) the marker orientation, (b) the marker occlusion, (c) the environmental reflection, and (d) shows the global coordinate system of the NDI OTS. The optical tracking system was mounted on the wooden board in a fixed position to the needle tool within the tracking distance of 2400 mm. A vacuum base vise was used to hold the marker coverage tool.

3.3.1 Marker Orientation

The marker orientation test simulated the clinical environment where the biopsy needle was inserted into human skin under the guidance of NDI OTS. The NDI detected the presence of markers by IR light. The system employs four markers in total, and a minimum of three markers need to be visible simultaneously.

If the markers are too close to each other, the reflection interference will affect the process of marker detection. This is because the NDI OTS algorithm determines the location of

the tool tip by assessing the centers of each of the markers from the pre-determined tool geometry. The NDI user guideline mentioned that if the markers start to eclipse each other, the system would have difficulties determining specific marker positions and would thus lose accuracy in determining the tool tip's exact position. It is worth noting that all tools require the use of at least three markers at all times to be tracked in 3D space.

Yaw direction

The UR10 was programmed to rotate clockwise from −90° to −70° and +70° to +90° in 1° increment starting from an orthogonal view relative to the NDI OTS in the NDI Y-Z plane (**Figure 3-3 (a)**). At every increment, the needle was held in place before being rotated to the next position. Each position was recorded; the average R_x, R_y, and R_z were taken for each interval. The orientational errors were calculated using Eq. (2).

Pitch direction

The needle was again contained in the 3D-printed needle tool and held by the UR10's gripper. The UR10 was programmed to rotate the needle counter-clockwise from +60° to +90° in 1° increment in the NDI's X-Z plane. At every increment, the needle was held in position and had its rotational R_x, R_y, and R_z data averaged for each increment. The orientational errors were calculated using Eq. (2).

3.3.2 Marker Occlusion

The percentage of marker visibility test was conducted to examine the inaccuracies caused by partial coating from blood in real surgical situations. The 3D printed mesh could simulate the situation by partially blocking the marker from the NDI. The percentage of visualization was varied from 10% to 30%. This was done by using the UR10's gripper, holding the 3D-printed tool orthogonal to the NDI, and introducing different percentages of marker

visibility between the needle and NDI. Each increment started with a 20-second control experiment with no interference, allowing for the determination of a true position from which deviations were calculated. The specified mesh coverage sheet was then introduced between the needle and the NDI to a point where all four passive markers were covered but still allowed for the tool to be tracked. This was recorded for 20 seconds. The mesh was removed and then re-introduced. This was done five times. The mesh was removed for a final time before recording another 20 seconds for a secondary control. This secondary control was used to verify that no experimental procedures caused an unintended deviation from the original position. The middle 10 seconds of each data set were used. The average X, Y, and Z positions of the five tests per coverage were used for data analysis and plotted against each percentage of cover. The raw data was normalized and averaged for each mesh tested (**Eqs. (3) — (11)**).

3.3.3 Environmental Reflection

The environmental reflection test aimed to test inaccuracies introduced by using stainless-steel surgical tools and other reflective materials in the OR. A stainless-steel panel attached to the UR10 was held behind the needle and rotated from −10° to +10° in 2° increments around the vertical NDI OTS X-axis. The dimensions of the panel were 335 mm (L) × 350 mm (W) × 0.5 mm (H), and the surface finish was polished. Lights were projected onto this panel from roughly 45° and roughly 45 cm away from the panel. Each recording at the 2° increments was 20 seconds long, and the middle 10 seconds were used to reduce the noise from the panel shaking after moving positions. The resulting error was calculated similarly to the previous test. There were two controls taken: one preceding the test and one succeeding the test. These controls were averaged and subtracted from the average calculated position for each interval (**Eqs. (3) — (11)**).

3.4 Results

The results section reports the deviations of the optical tracking resulting from the three factors: optical proximity between markers, marker visibility, and reflection of surgical tools.

3.4.1 Marker Orientation

In the yaw orientation, the software consistently lost track of two or more markers around the ±76° mark and was unable to track the tool at the lost markers. Thus, the NDI was unable to track the needle before −76° and beyond +76°. This left a 152° arc in which the tool could be tracked. The overall detection range was more extensive than the manufacturer suggested. On the other hand, the rotational error of the needle was more than 1° when the needle orientation was at the orientational angle of -75° and 76°, respectively. Overall, the rotational error of the needle was less than 1° in the range from -74° to 75°. In the pitch orientation, the NDI was unable to track the needle beyond 87°, which was larger than the range mentioned by the NDI user guideline30 (**Figure 3-4 (b)**). This theoretically allows a 174° trackable arc but was unable to be tested in the other quartile (e.g., −60° to −90°) since the UR10 arm blocked the line of sight when the top of the needle was angled towards the NDI's sensors. There was a big rotational error of -0.29° when the needle orientation was at 61°. The rotational error increased dramatically to 2.63° when the needle orientation was at 83°. This was an indication about the inconsistency of the precision of the system.

(a) Yaw direction

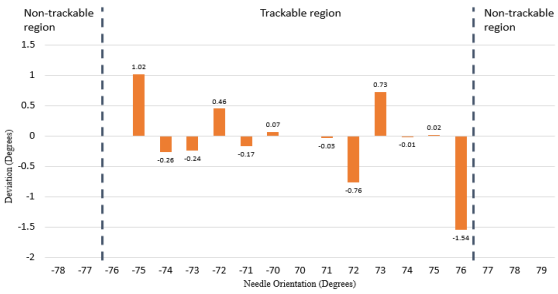

(b) Pitch direction

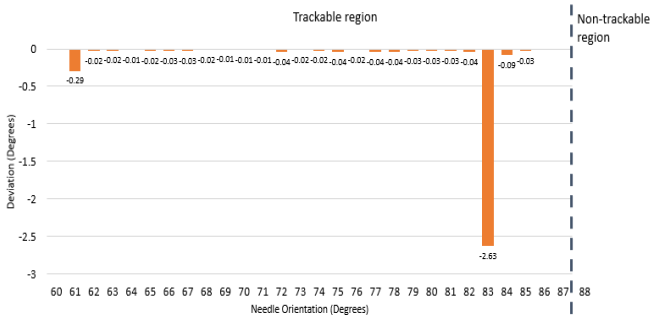

Figure 4-4: Tracking errors generated when the tool was oriented in the (a) yaw direction, and (b) pitch direction.

3.4.2 Marker Occlusion

The test results show large errors in situations that have a high potential for occurring since very little fluid is required to cover the markers to the extent being tested. The results in **Figure 3-5(a)** are 10%, 20%, 25%, 30%, and 40% of all four markers covered. The translational position Tz had a maximum error of 4.88 mm at 30%. This was more than enough to cause a significant medical error and potentially pain or death in surgeries. There was a dramatic increase in error from 25 % to 50 %, which was another indication of the inconsistency of system precision. Throughout the experiment, the positional errors of Tx and Ty were within the range of 0.05—0.8 mm, which was significantly smaller than the positional error of Tz.

3.4.3 Environmental Reflection

Figure 3-5 (b) shows the reflective material test as the stainless-steel panel was rotated around the X-axis by the robotic arm from -10° to 10°. When the orientation of the reflective surface was at 0°, the positional error of Tz was at its largest value of 0.55 mm. Throughout the experiment, the positional errors of Tx and Ty were within the range of 0.01—0.2 mm, which was much smaller than the positional error of Tz.

(a) Marker occlusion test

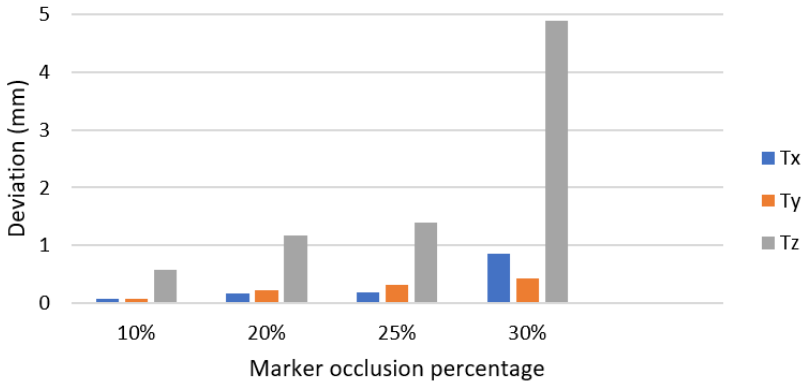

(b) Environmental reflection test

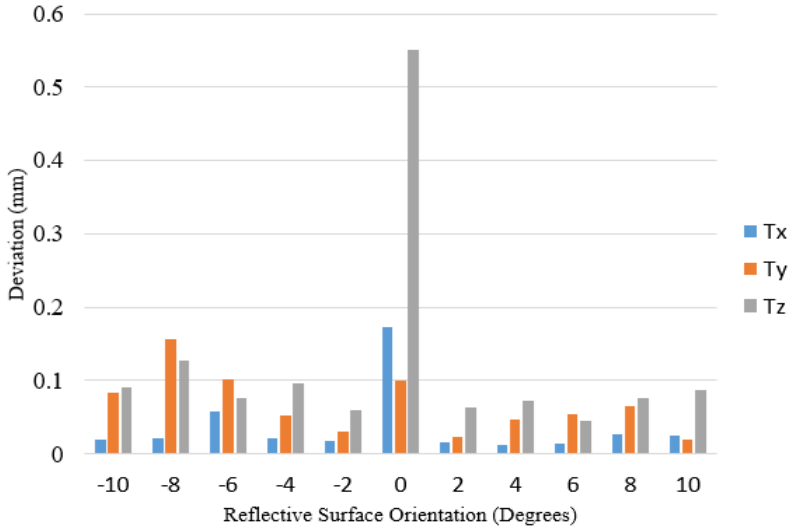

Figure 4-5: (a) Tracking errors generated when increasing the marker occlusion from 10% to 40%. At 40%, the tool tracking was lost, (b) tracking error generated when rotating the stainless-steel panel.

Table 3-5 shows the overall results of each experiment.

Table 4-4: The results summary of the three tests in this study, ABS means absolute values

Experiment type		Mean	Standard deviation	Minimum	Maximum
Marker orientation (Yaw direction)		0.44° (ABS)	± 0.48 (ABS)	0.01° (ABS)	1.54° (ABS)
Marker orientation (Pitch direction)		0.14° (ABS)	± 0.52° (ABS)	0.08° (ABS)	2.63° (ABS)
Marker occlusion	T_x	0.33 mm	± 0.36 mm	0.09 mm	0.87 mm
	T_y	0.27 mm	± 0.15 mm	0.09 mm	0.44 mm
	T_z	2.01 mm	± 1.94 mm	0.59 mm	4.88 mm
Environmental reflection	T_x	0.04 mm	± 0.05 mm	0.012 mm	0.17 mm
	T_y	0.07 mm	± 0.04 mm	0.019 mm	0.16 mm
	T_z	0.12 mm	± 0.14 mm	0.045 mm	0.55 mm

Meanwhile, during the test, many phantom points appeared when the orientation was at 0° (**Figure 3-6**). A plausible explanation was that since the software was not able to justify the correct location of the optical markers because of the background noise, it displayed all the possible locations.

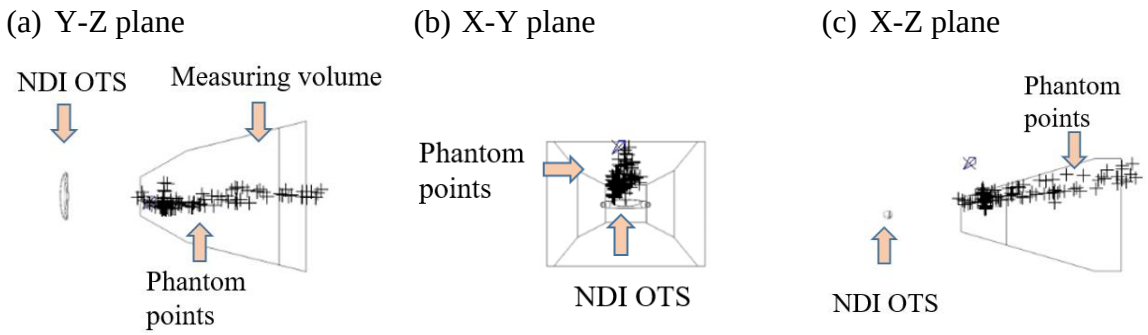

Figure 4-6: NDI software interface showed phantom points (in black color) appeared during the experiment when reflections had a significant influence on the tracking quality. The coordinate system was previously defined in **Figure 3-3 (d)**.

3.5 Discussion

The accuracy of the NDI OTS is affected by the complexity of the surgical environment, particularly the rotation of the needle into different positions, the partial occlusion of the marker with blood or other substances, and the environmental reflection.

3.5.1 Marker Orientation

The results of the optical proximity test showed the rotational errors from each interval's expected angular position. Each interval had a $\Delta 1°$ rotation performed by the UR10 coded into a loop. Thus, every angle should have a 1° difference from the previous angle. Should the errors be of significant but consistent magnitude, then the error can be attributed to either the UR10 or NDI. However, if the rotational error is inconsistent, with large jumps relative to the surrounding data, then these rotational errors can be attributed to the NDI.

From the data, it can be seen that the deviations increased as the needle tool rotated. This most likely stemmed from optical proximity and eclipsing of the passive markers, making it difficult for the NDI to distinguish between markers and determine their exact positions. The inconsistent deviations from the expected $\Delta 1°$ at each interval indicate some limitations of the NDI. As previously stated, if these deviations were consistent and small, the inaccuracies could be attributed to the UR10's ability in positioning. However, since the UR10 performed the same rotations coded in a loop, this inconsistent nature demonstrated NDI's inaccuracy. The highest magnitude was 1.54° away from the expected 1° change.

Furthermore, the NDI had a bigger accuracy issue before 87°. At 83°, the deviation from the previous position was shown to be 2.65° more than the expected 1° change. The inaccuracy at this exact angle could be attributed to an algorithm miscalculation due to the high angle of the tool and the optical proximity of the markers. There are a few other potential explanations: surgical tool reflections were only apparent at this angle due to the robot or tool not blocking them. It can also be seen as an abnormally high deviation in the pitch direction at 61°. The same previous explanations could apply for this deviation. From our findings, it seems that optical proximity has a minor effect on the NDI. However, blind spots are a problem since a commonly used tool could not be tracked beyond 76° around the vertical axis nor beyond 85° around the horizontal axis, which differed from the claimed visibility of >90°.

3.5.2 Marker Occlusion

The positional error shown in **Figure 3-5 (a)** is because the NDI sensors are not able to localize the center of each marker. Thus, the position of the tool tip cannot be correctly calculated. The NDI had difficulty tracking the tool at as little as 20% coverage, and it could not find the tool when the markers were covered 40% or more. Any percentage lower than 10%

would be difficult to spot in a clinical setting, and would cause relatively small errors in translational position. The 30% coverage condition had significant effects on the interpreted position and introduced much difficulty in keeping track of the tool; at the 40% coverage condition, the NDI could not track the tool at any time or position of the 40% mesh experiment. The reason why only the translational position T_z was closely analyzed is the positional errors of T_x and T_y were significantly smaller and under the level of submillimeter.

3.5.3 Environmental Reflection

Similarly, in this test, only the translational position Tz was closely analyzed as the positional errors of Tx and Ty were significantly smaller and under the level of submillimeter. The most significant impacts of reflection on the translational position Tz of the NDI OTS were observed at minor angles near 0°. Although most of the surgical tools are rarely large, metal panels like the panel used in the test, these findings suggest that any infrared reflection can play a significant role in affecting the NDI OTS usage. It can be seen that a relatively large positional error (~0.1 mm) occurred at most orientations except for near the 0° position. This could be due to the panel reflecting the NDI's infrared light to the NDI sensors and causing confusion about what the infrared was hitting and how to interpret the reflected infrared.

At its peak, the reflection caused an average positional error of 0.55 mm for T_z. Although the average positional errors were significantly less for T_x (0.17 mm) and T_y (0.10 mm), there was a significant increase in all directions at 0°. These errors are undesirable for surgeries with high accuracy (e.g., neurosurgery) and have the potential to cause adverse effects on patients. Given enough interference, a few other effects can occur, further reducing the NDI's ability. Occasionally, the NDI will lose track of a single marker. Most passive tools used in the NDI OTS have more markers attached than required by the tool file associated with the tool.

However, when the NDI loses one of these markers, the algorithm recalculates based on the new amount of points. This causes a new position to be determined that often differs from the previously calculated position by 0.5—1 mm. Another effect beyond losing track of a single marker is the addition of phantom points. The NDI sometimes had so many phantom points that the algorithm could no longer compute and returned an error, as seen in **Figure 3-6**. This means the tool can no longer be trackable within the detection range (2400 mm). A plausible explanation was that since the software was not able to justify the correct location of the optical markers because of the background noise, it displayed all the possible locations.

3.5.4 Limitation of the Study

Admittedly, the NDI OTS accuracy could depend on tool design. Also, a range of tool tracking parameters should be used to make the conclusion more generalizable to real-world situations.

Some other tracking errors could be potentially introduced into the experiment due to the dynamic nature of the tests. For example, the sampling rate of the NDI optical tracking was not optimized with the robotic system. This will result in some tracking data lost due to continuous robotic movement. Another limitation could include our use of a single-faced tool. Some other tracking errors could be potentially introduced into the experiment due to the dynamic nature of the tests. More realistic instruments such as hemostats, retractors, or clamps could be used to assess the accuracy of the NDI system. Moreover, in the environmental reflection test, the test ideally should happen in the OR room to best resemble the lighting condition.

In this study, there are still many influencing factors that could impact the accuracy assessment. The deviation between the test and reference measurement was only a quantitative indication of system limitation. The experimental results conducted could be impacted by

influencing factors as follows: the 3D printed model accuracy compared to tool geometry generated in the navigation software, the location-dependent accuracy of the navigation system within the tracking volume, the positional accuracy of the needle in the tool after repetitive insertion, the mesh position and mesh design, the positioning and brightness of the light source. Due to the scope of this study, the above factors are not possible to analyze and all assigned to the inaccuracy of the navigation system.

3.5.5 Operation suggestions

To minimize the orientational error, the suggested ranges for needle orientation are between -76° and 76° on the yaw direction, and between 62° and 82° on the pitch direction, respectively. The surgical environment interference should be reduced by limiting the number of polished metal tools and turning off unnecessary lights, as well as ensuring that any necessary large, metal objects are kept shielded from the direct line of sight of the NDI OTS.

A proper line of sight to the NDI OTS should be maintained with the tracking tool. Although these systems can often track with fewer than the included markers, the reliability may be reduced. Furthermore, even if the NDI OTS can track all the markers, it should have as close to an orthogonal view of the tool face as possible. A potential way to maintain a line of sight is to have a tool with multiple facets that can be tracked by the NDI OTS.

Finally, proper cleanliness of the markers should be maintained. Although similar to the line of sight issue, it is recommended that the markers need to be wholly visible by the OTS. Therefore, the markers should be adequately cleaned as soon as they become covered, being mindful of the ease with which the reflective finish can be scratched off of the markers since removing the reflective finish is the same as covering it up. Markers should be replaced as necessary when they become uncleanable or too damaged.

3.6 Summary

Overall, three tests were conducted to evaluate the impacts of three essential factors on the tracking ability of an OTS. Rotating the needle to change the optical proximity between the markers led to a maximum error of 2.63°, covering the markers to various coverage percentages led to a maximum error of 4.88 mm, and introducing a reflective material near the needle and OTS led to a maximum error of 0.55 mm. Many phantom points appeared because of a system error during the reflection test. Suggestions on how to properly use optical tracking systems were provided so that medical errors can be further reduced.

CHAPTER 4

A WEARABLE SMART DIAGNOSTIC DEVICE FOR HEATSTROKE PREVENTION[2]

[2] Li, R., Smith, A., Tadinada, H., Sierra, H., and Tse, Z.T.H. Accepted by *Proceedings of the IMechE, Part H: Journal of Engineering in Medicine*.

4.1 Abstract

Heatstroke is one of the most serious forms of heat injury and is classified as a medical emergency. It is characterized by an elevated core body temperature along with the failed body cooling mechanism in response to the sudden heat-up. People vulnerable to heatstroke are children, elders, and sports professionals. Previous efforts have emphasized exercise adjustments and post-treatments, such as environmental-based activity modification and cold-water-immersion (CWI). However, the general public, especially elders, will have difficulty to conduct such adjustments by themselves. Moreover, few studies have been done on the early preventative measurement stage. A wearable 3D printed thermochromic device presented can warn the people of a sudden rise in skin temperature and can advise them to take quick action. Combined with the smartphone applications, for both the android and iPhone platforms, the device is able to monitor real-time skin temperature and alerts the people who are vulnerable to heatstroke. The 3D printable resin developed, can change color at a specific activation temperature. The device has undergone a series of performance tests in order to optimize the color transition rate and stability of color change. The accuracy of our device is compared to the conventional thermometer. The regression analysis shows the R-square value is 0.7599, and the average error is 1.3 ºC. Future work will be to mitigate the surrounding lighting effects on the smartphone camera and further improve our device accuracy.

Keywords: Heatstroke, 3D-printing, Thermochromic, Temperature-sensitive

4.2 Introduction

Heatstroke is a life-threatening condition. An elevated core body temperature over certain specific temperature such as 40°C will result in central nervous system dysfunctions that can cause delirium, convulsions, and coma[211-215]. From 2001 to 2010, 20 states in the United

States recorded a total of about 28,000 heat-related hospitalizations[216]. Classic heat stroke primarily occurs during annual heat waves within vulnerable groups, including the elderly and children[217-219]. Moreover, exertional heat stroke (EHS) happens most often in outdoor sports enthusiasts and professionals[220-222]. The current prevention and treatment methods include heat acclimatization, environmental-based activity modification, and cold-water immersion (CWI)[223-226]. However, those who do survive a heat stroke may have permanent neurological damage[227-230]. Some studies reported that heatstroke could be monitored or predicted using physiological measures[231-233]. Measuring core body temperature is the golden standard to prevent heat stroke; however, the limitation of this approach is the accessibility and invasiveness of the measuring tool needed to obtain the internal temperature[234-236]. Alternatively, many works of literature have revealed the relationship between sharp-rising skin temperature due to outdoor activity and an indication of heatstroke[237-239]. The current methods for monitoring skin temperature are mainly electronic-based, so batteries are required[240-243]. The above literature has indicated that the skin temperature is a valuable and measurable factor that could help to prevent heatstroke. The normal skin temperature is typically ranging from 31°C to 34°C[244].

A new method is needed to inform individuals of a sharp rise in their skin temperature before heatstroke occurs. The proposed thermochromic material provides a practical solution that can transform an unseen rising skin temperature into a visible color change, which can notify the user and cause them to take quick action. Moreover, it is a cost-effective device that can be widely used in developing countries. It can be concluded that the 3D printed wearable device developed is able to detect anomalies of skin temperature at a comparable accuracy level to a conventional thermometer. This will give the users a new way to prevent time-sensitive

heatstroke before receiving any post-treatment. Moreover, the device will have a smartphone platform where physical data can be converted into digital information for network uploading and sharing.

4.3 Materials and Methods

4.3.1 System Overview

The presented system consists of two parts. Part one is to use the chemical property to detect the skin temperature change as a result of color transformation. Part two is to use the smartphone application to convert the color transformation into digital readings and alert the users of potential hazards of heatstroke. **Figure 4-1 (a)** shows the workflow of the device. The temperature device is designed to be wearable so that people can check their skin temperature on a regular basis. The smartphone application developed is not only able to provide the accurate temperature reading of the device, but also provides the location as well as the time information. The users will be alerted by the device, and they can then take quick action in order to prevent the heatstroke from happening. Moreover, the temperature data would be uploaded and shared on a local health emergency network.

(a) System architecture

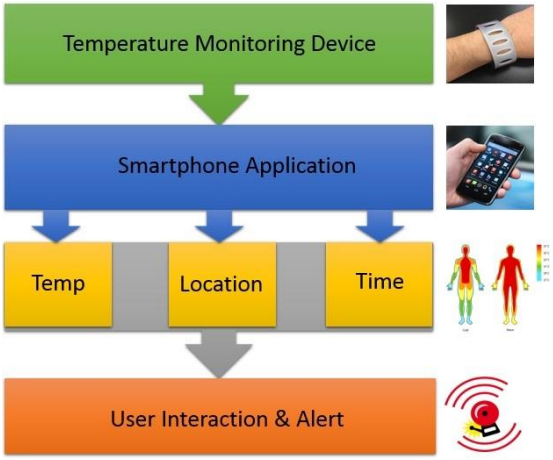

(b) Commonly used thermochromic chemical

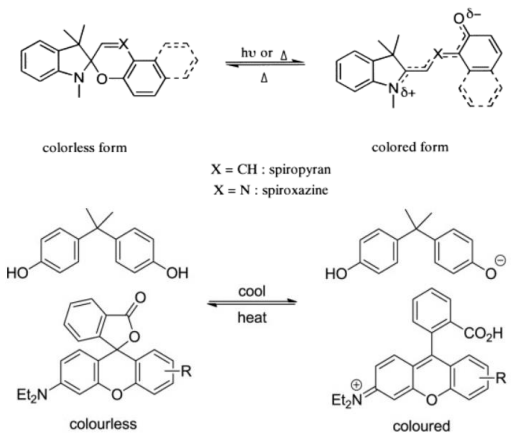

Figure 5-1: (a) The working principle of the device, (b) Chemical transformation of Leuco dyes[245, 246]

4.3.2 Thermochromic Chemicals

The concept behind the product is thermochromism, which is the result of a color change depending on a unique activation by temperature. Leuco dyes are organic chemicals that change color when heat energy makes their molecules shift back and forth between two subtly different structures, which is known as the leuco and non-leuco forms. The leuco and non-leuco forms absorb and reflect natural light in a different way. The color appearance of the product changes accordingly. Typical leuco dyes used for thermochromic mixtures are spirolactones, fluorans, spiropyran, and fulgides. Some transformations such as spiroxazine [245] and fluourans [246] are shown in their molecular structures in **Figure 4-1 (b)**.

The external temperature is acting as a stimulus that changes the structure of the leuco dye. This change of structure results in the change of light wavelength that is reflected; thus, it provides a color change. Based on these properties found in thermochromic powder, experiments were conducted to create a 3D printable resin that is characterized by sharp color contrast and rapid color transition. For example, one of the resins used to make the wearable devices will change its color from dark purple to grey, then finally to white in color.

4.3.3 Principle of Skin Temperature Monitoring Device

The assumption is that under a fixed skin temperature, the amount of heat transferred to the bracelet is constant. Since the thermochromic material can display a broad range of color based on the specific activation temperature, the final color displayed on the bracelet will be a direct indication of the user's current skin temperature. Admittedly, the ambient temperature is the main disturbance that impacts the optimal performance of the device. A bracelet design with maximum contact area to the skin will allow for the heat transfer between the device and the skin to be more predominant than between the device and the ambient environment. This will help

increase the accuracy of the temperature being monitored. The main benefit of this material is its ability to be 3D printed, which allows it to be highly customizable and inexpensive to produce.

4.3.4 Smartphone Application

The smartphone application is used to determine the temperature of the surroundings through the red-green-blue (RGB) analysis. For Android phones, the program platform used to develop the application is MIT app inventor® (Cambridge, Massachusetts). For iPhone, the program platform used in Xcode (Cupertino, California). This camera application converts the whole area of the picture into an average RGB value, which is then compared to a local color map database that correlates each RGB value to a specific temperature. The corresponding temperature is outputted from the database and displayed on the smartphone screen. This application has additional features such as a map view and a location sharing network service that is shared with local emergency departments.

The camera application is split into four user interface views, shown in **Figure 4-2**. The initial view is the camera with an outline of the thermochromic product. The second view has an analyze button that calculates the RGB value and the temperature by comparing it to a database. It then displays the picture that the user captured. The third view outputs the surrounding temperature that was calculated and had a "send to the network button," which sends the data to a local cloud server. It also has a "current location" button, which shifts the screen to the fourth view. The location view displays the coordinates, timestamp, temperature, and the map of the current location.

The program uses image-processing tactics to calculate the average RGB value of the object. Its calibration process is shown in **Table 4-1**. The region of interest (ROI) is used to

identify a specific area for color analysis. An average RGB is calculated for the ROI, which represents the entire product.

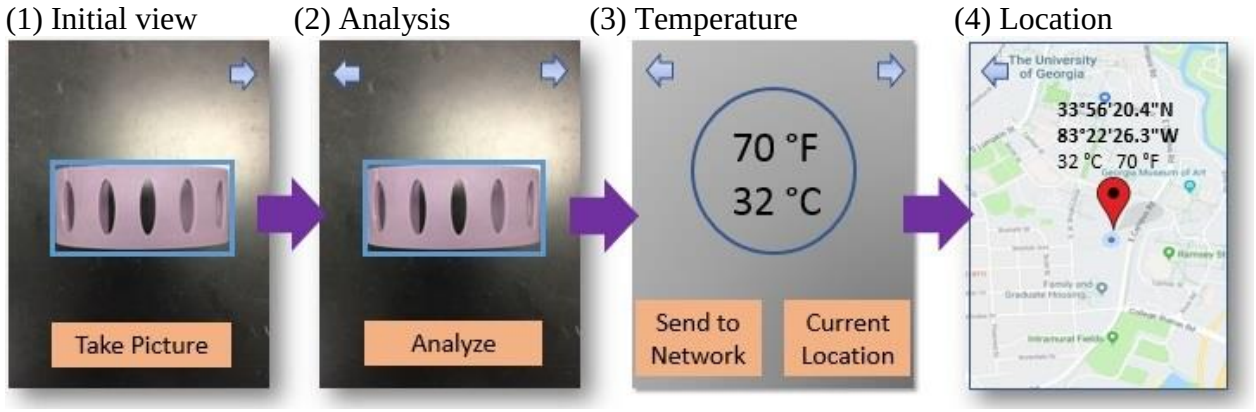

Figure 5-2: Proposed workflow of the application

The calibration process for color mapping is described in **Table 4-1**.

Table 5-1: Calibration process of obtaining a color map			
Step 1	Step 2	Step 3	Step 4
A thermochromic 3D object model, which has a size of 38mm by 38mm, was used to determine the temperature and color change.	The hot plate was heated to 25 °C and continue to increase by an incremental value of 1°C until the model color change stops. The total color change time is recorded.	A video was used to record the color transition of the model	The images were taken from the video, which is corresponding to different temperatures. The RGB value of the ROI was obtained from each image, and a color map is generated.

4.3.5 Manufacturing Process

0.5g thermochromic powder is weighed on a Mettler Toledo® analytical balance (Columbus, OH). 250ml formlabs® resin (RS-F2-GPCL-04) is poured into a 500ml chemical beaker and mixed with the thermochromic powder. A Scilogex ® overhead stirrer is used for increasing the uniformity of the thermochromic powder suspension in the clear resin. The continuous stirring process lasts for 20 minutes until the color of the clear resin turns into a similar color of the thermochromic powder. The suspension is then poured into an empty Formlabs® tank and ready for print.

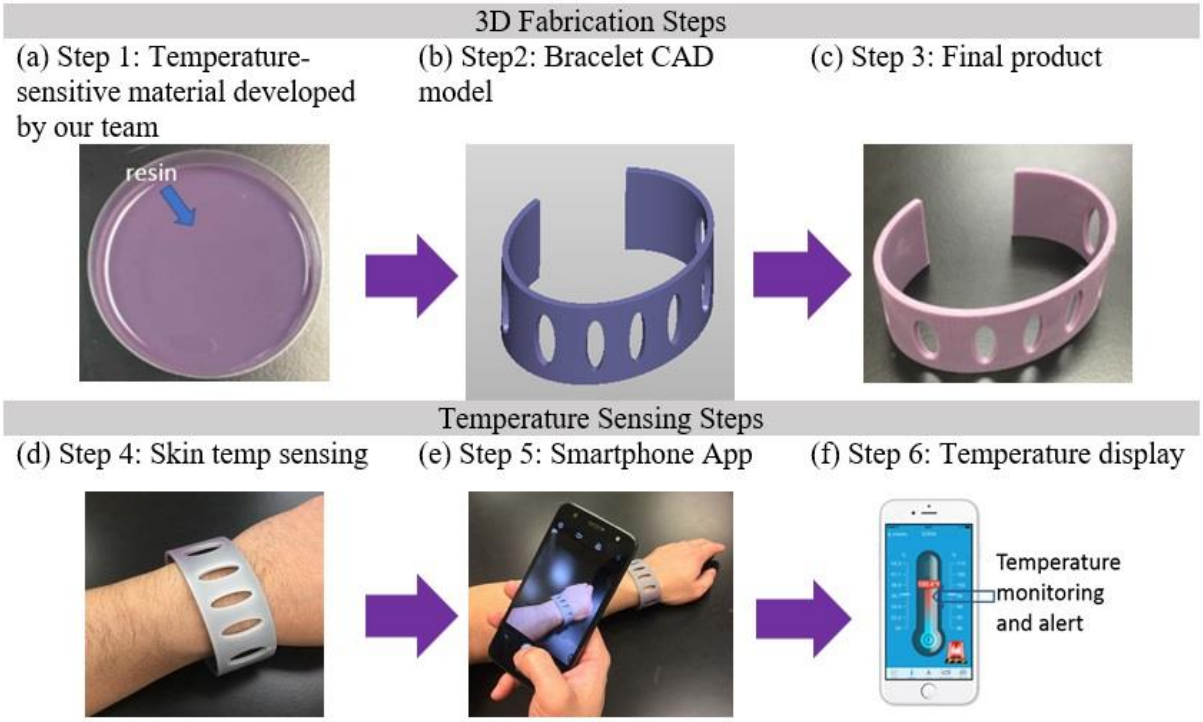

Figure 5-3: Temperature sensor development and operating demonstration: (a) the resin used to create the temperature sensor, (b) bracelet-shaped sensor model, (c) 3D-printed sensor, (d) demonstration of sensor changing color with skin temperature, (e) and using the smartphone to take a picture (f) to measure the temperature and alert.

A bracelet prototype has been printed out in order to demonstrate the feasibility of the color change as well as the temperature display. The entire fabrication process from the production of the temperature-sensitive material to a final prototype is shown in **Figure 4-3 (a) – (c)**. The temperature sensing steps show that the final prototype changed color when it was in contact with the user's skin. The corresponding temperature was displayed on the smartphone screen.

The reason for designing a device in terms of the bracket is that it can ensure the maximum skin contact with the thermochromic material so that heat transfer between the device and skin can reach maximum. This is critical for the temperature monitoring functionality of the device.

4.3.6 Performance Test

The performance test is to ensure the proposed device and thermochromic material can make accurate and reliable skin temperature predictions.

Thickness Test

The first parameter aims to ensure that the device responds fast since a heatstroke occurs very quickly. The thickness of the device will be optimized so that the rate of heat transfer, as well as the color change through our device, is fast enough for notifying users (**Figure 4-4 (a)**). A series of 3D-printed thin circular blocks have been used for tests. The purpose of this test is to determine the heat-transfer property of the thermochromic material. The heat gun is placed on the top of the wooden board.

Color Change Rate and Extension

The second parameter determines whether the temperature-monitoring device can give users a reliable signal for heatstroke prevention. The reason why using the circular block rather than the device itself is that the rate of color transition is more visible in the form of circular blocks. Hence, the color variation of the device will be tested to ensure that there is a large contrast as well as a stable final color, shown in **Figure 4-4 (b).** A temperature control system was used in this case for the purpose of adjusting the heat conduction and making quantitative analysis to color change. It can control the surface temperature of the heated board, where a circular block was placed on top. Constant heat was applied to the surface of a circular block (with a diameter of 23mm and a thickness of 2mm) while a video was taken to record the color transition of the block. The set temperature of heating was 38 °C. After using the smartphone application, three-color lines representing Red, Green, and Blue light compositions (RGB) of the

real color was applied to demonstrate the trend of color change. A graph was plotted using the RGB values versus the time it took to rise in heat.

(a) Parameter One (b) Parameter Two

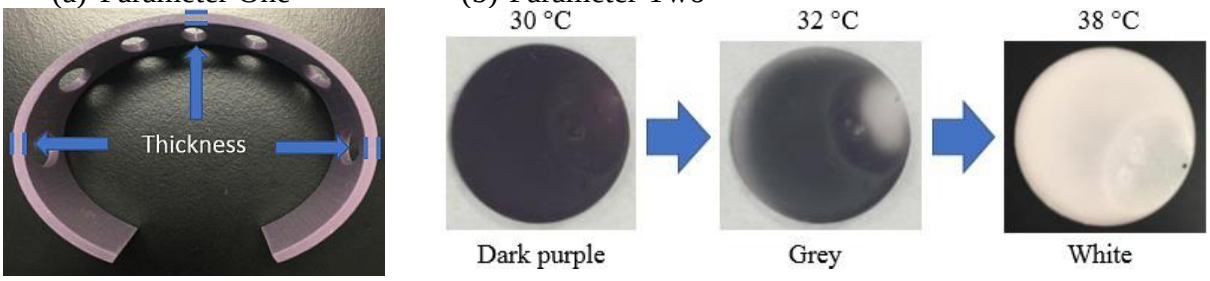

Figure 5-4: (a) The thickness of the device, (b) Color transition of one thermochromic sample under the heating temperature of 38 ºC. The purple color means the temperature of the circular block reached 30 °C. The white color means the temperature of the circular block reached 38 °C. This was a quantitative test that can measure both the rate and the extension of the color change.

Accuracy of Temperature Reading

The key to having an accurate temperature reading is a device with a distinctive color pattern for each specific temperature within the appropriate skin temperature range. An experiment will be carried out by heating a small circular thermochromic block and measuring it with a Ryobi® infrared thermometer (Anderson, SC) and our smartphone application, respectively.

The experiment of heat transfer and simulation validation

The open-air test is to verify the color change of the thermochromic blocks under the influence of temperature while the simulation is to validate there is actual heat transfer happening between the heat source and the thermochromic blocks. The separation between each block, as well as the separation between the heat source and block, is identical in the open-air test as well as the simulation (**Figure 4-5**). That is to ensure the consistency of the color and temperature change in both scenarios.

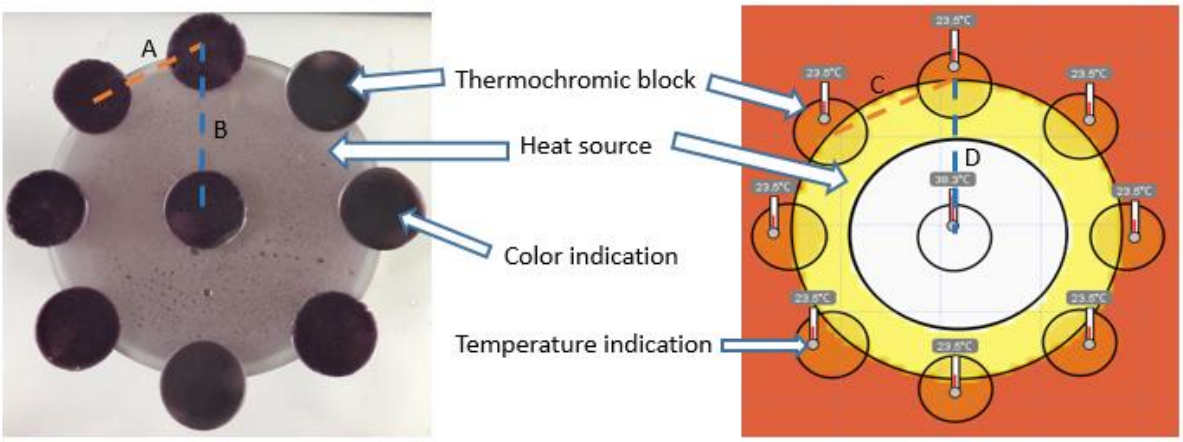

Figure 5-5: Open-air test setup and simulation layout. As for the simulation, the dimensions of the block and the heat source were identical to the real thermochromic block and heat source in the open-air test. The separation distance C between the blocks was proportional to the distance A in the open-air test. The separation distance D between the block to the center of heat source was proportional to the distance B in the open-air test.

Table 4-2 shows the conditions of the simulation. The simulation was run in the Energy 2D® (Concord, MA).

Table 5-2: Conditions of simulation	
Medium density	1200 kg/m^3
Medium thermal conductivity	0.5 W/(m·K)
Thermochromic material density	1.1 kg/m^3
Thermochromic material thermal conductivity	0.3 W/(m·K)
Initial temperature of the thermochromic blocks	23.5 °C
Diameter of the thermochromic blocks	25 mm
The final temperature of the thermochromic blocks	38 °C

4.4 Results

Key elements for a high-quality product is to use evidence-based decision-making and continuous improvements. There are three parameters for quantifying the performance of the skin temperature-monitoring device in order to determine the device's effectiveness on heatstroke detection: color change rate, the extension of color change, and the accuracy of the

temperature reading. The color change rate and extension of color change will be used to quantify the effectiveness of the device. Accuracy is quantified by comparing our device with other commercial devices. Finally, the experimental result is compared with the simulation to ensure the consistency of the heat transfer.

4.4.1 Thickness Test

An initial experiment was done on circular blocks, and preliminary data has been collected, shown in **Figure 4-6 (a)**. The data provides an important understanding of how to design a fast-responsive wearable device. The linear correlation between the color change time and the thickness indicates that the heat transfer is mainly carried out in terms of conduction. When considering the mechanical strength of the device, the optimal thickness is 2mm, which corresponds to 70 seconds for the complete color change of the device.

(a) Color change rate experiment

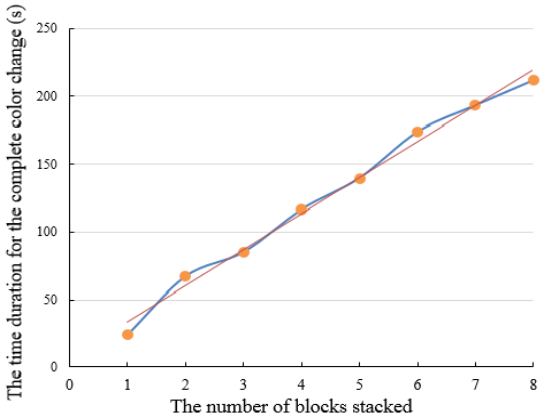

(b) Extension of color change experiment

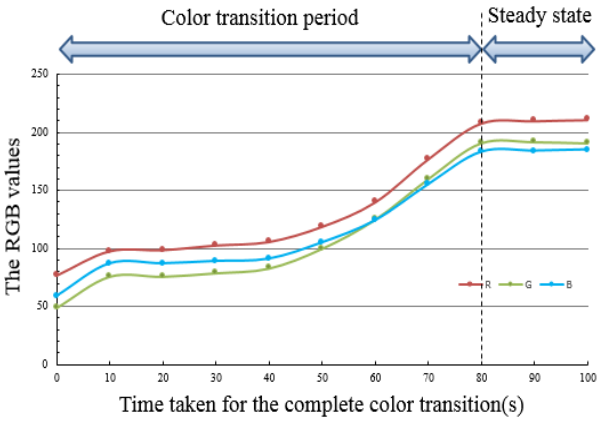

Figure 5-6: (a) Shows the time taken for a thin block made from thermochromic material to change from dark purple to completely white. The linear relationship indicates that there is a positive correlation between the time taken for the color change to occur and the thickness of the object, (b) Shows the time taken for the complete color change, which includes two states, the color transition period (t = 0-80 s) and steady-state (after t = 80 s).

4.4.2 Color Change Rate and Extension

A test has been carried out, and the results are shown in **Figure 4-6 (b)**. During the initial 80 seconds, three light compositions (RGB) increase gradually. This is indicated by the gradual

fade of the original color and formation of the white color. At this moment, heat transfer occurs between the block and its surroundings. After the RGB values have reached a steady-state, there are no obvious variations in the values, which means the final color of the material is stabilized even when the temperature of the block continues to rise. In this test, the block will remain white in color once it reaches the temperature of 38°C.

4.4.3 Accuracy of the Temperature Reading

Figure 4-7 (a) shows an accuracy test has been done; each data point was calculated as a mean value of 20 repeated trials. **Figure 4-7 (b)** shows the Bland-Altman analysis. It can be concluded there is a comparable accuracy between our device and the conventional device.

(a) Comparison between our device and conventional laser thermometer

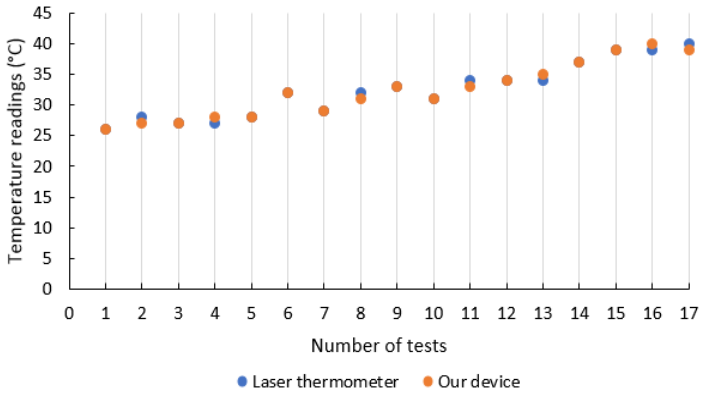

(b) The Bland-Altman analysis with the conventional device

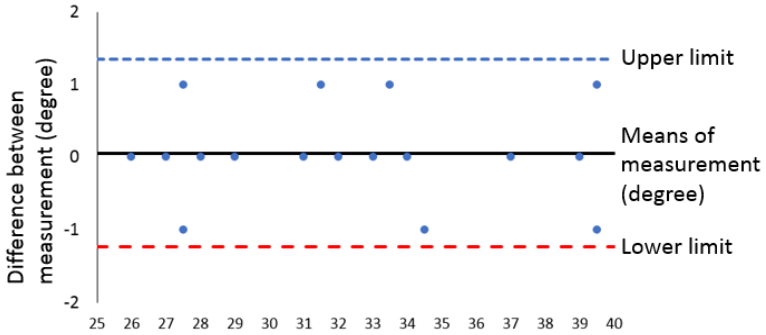

Figure 5-7: (a) Comparison between the temperature readings from our device and conventional laser thermometer, which has an accuracy of ±0.1°C. The average error of these

two devices is 0.06°C. Each data point is the average value of twenty repetitions of trials. (b) The Bland-Altman plot is used to evaluate the accuracy of the device.

4.4.4 Heat transfer experiment and simulation results

Figure 4-8 (a) —(b) shows the experimental result and temperature analysis. The temperature analysis is done in the Matlab 2017b® (Natick, MA). **Figure 4-8 (c)** shows the simulation result. The heat transfer pattern, as well as the local temperature distribution from the experimental result, is consistent with the ones from the simulation. The simulation is designed and carried out on the platform Energy 2D® (Concord, MA).

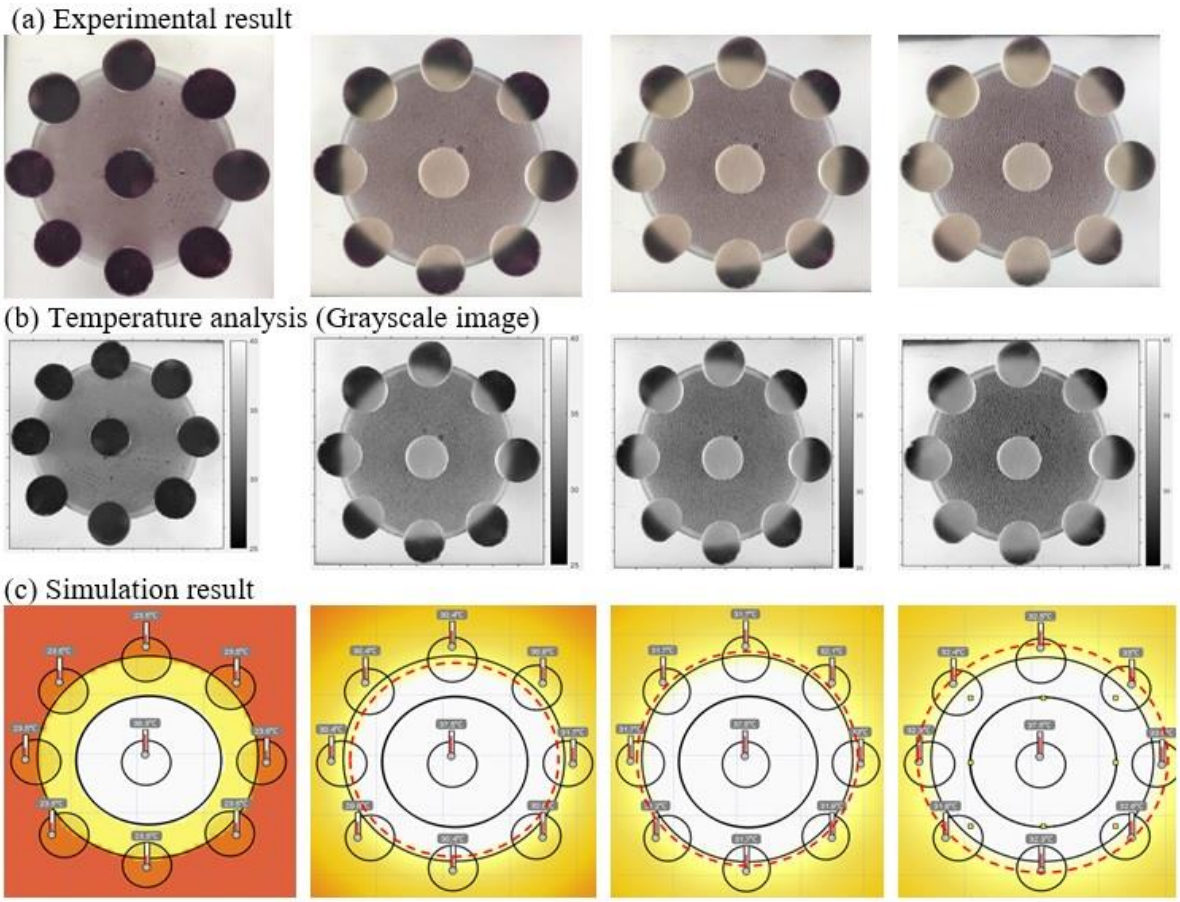

Figure 5-8: the experimental and simulation result for heat transfer between the thermochromic circular blocks and round heat source underneath. (a) shows the color image from the experiment, which shows the color changes from purple to white as the heat transfer happens between the heat source and thermochromic blocks, (b) is the processed grayscale image using Matlab 2017b® (Natick, MA) with the color bar on the side indicating the temperature distribution ranging from 25 °C to 40 °C. (c) is the simulation result using Energy

2D®(Concord, MA), the dotted red line is the isotherm line of 30 °C. As time elapses, the isotherm line expands outwardly, which matches consistently with both the color appearance and temperature analysis in (a) and (b).

4.5 Discussion

Thermochromism is a phenomenon in which the color appearance of a material change based on external hot or cold stimuli. In other words, the material will change color according to its own temperature variation. Early investigation in the application of thermochromism has begun in many industries, such as strip thermometers, battery testers, and fabric[247-249]. So far, commercial thermochromic products can only give visual information to users. There is no interaction between the users and the device. The presented device not only gives users a more accurate temperature reading via color analysis but also converts the physical temperature data into digital information, which can be uploaded and shared on a network for future reference. In this way, the users can track their history of skin temperature and receive notifications from the smartphone application about any anomalies. Moreover, the device can still indicate the rise of skin temperature without the smartphone application because the color change can be observed with the naked eye.

Admittedly, there is a small temperature difference between the inner surface of the bracelet in contact with the skin and the outer surface exposed to the ambient environment. The thickness of the device is chosen to be one of the design criteria so that the temperature difference can be minimized. The device can then adequately display the color change based on skin temperature. The purpose of using thermochromic material is that it can vary colors in a certain temperature range. The variation of normal human body temperature is within 10°C and below 35°C, so the range of the thermochromic material in this article was selected to be from 25°C to 35°C[250]. Due to its color-changing ability, this material can detect a sharp rise in skin

temperature, which is a possible indication of heatstroke. However, the small temperature range could be a limitation under certain conditions. It would be ideal to have a broader range of temperature detection so that the device would be applicable to a wider range of scenarios with various environmental, clothing, and exertion conditions.

The 3D-printed material used here is not stretchable. However, there is flexible material made by Formlabs (Somerville, MA), which can be used in the future to increase the skin contact area and improve the heat transfer efficiency between the skin and our device. 3D printing technology has many advantages of developing an optimal device for detecting heatstroke. First, it provides a way of fast-prototyping for product design optimization. Second, it can offer customized design to users, which opens up a wide range of applications such as food containers, wearable devices, and indoor thermal decors. Thirdly, the cost of 3D print operation and the raw material is very low compared with the traditional industrial manufacturing process. Before 3D printing can be used for fabricating the wearable device, two important issues need to be addressed. One is whether the mixture of thermochromic material and resin can still retain the physical property as the pure thermochromic powder after the 3D printing process. From the results, one single 3D printed thermochromic block starts the color change after 1 second and can reach a stable color appearance after 80 seconds. The performance of the newly developed resin mixture not only shares the same physical property as the original thermochromic material but also ideal for the fast detection of heatstroke. Another question is whether the resin mixture has an optimal thickness for the color change to be visible for users. Another experiment has been done here to give an optimal thickness of 2mm.

Traditional thermometers, such as mercury-in-glass thermometers, need both close contact with the skin for a long time and a stable environment in order to accurately read skin

temperatures. Meanwhile, the new-generation thermometer, such as a laser thermometer, can obtain a temperature reading in a fast manner. However, it requires the users to press the start button and initiate the temperature detection. The new type of temperature sensor proposed here offers an alternative principle of measuring temperature disregarding the surface structure and property of the material. The resin proposed here is able to be 3D-printed into any shape and can be easily integrated with smartphone cameras for instantly temperature sensing.

On the contrary, the accuracy of our device is impacted by three factors. One is the lighting condition of the background since the color of the thermochromic block will appear significantly different under bright and dim lighting backgrounds. A possible solution is to force-start the phone's camera light while taking pictures to make the light background constant under any circumstances. The second factor is the inhomogeneity of the resin during the mixing preparation, which can potentially affect the uniformity of the color density distribution. Thus, the color analysis can differ based on the location of the region of interest (ROI). More sophisticated mixing and curing equipment should be used in the future. The third factor is the contact area between the heat source and the device. As can be seen in **Figure 4-7 (b)**, the temperature discrepancy of ±1.5°C between the measured and reference values is due to the variation of the total amount of heat transfer, which correlates with the continuously changing contact area.

In secion "Heat transfer experiment and simulation results", both the experimental and simulation results are able to show there is a strong and quantifiable relationship between the color appearance of the thermochromic material and temperature variation on the contact surface. The consistent outcomes validate the proposed material as well as the device is able to detect temperature variation on the contact surface if being placed onto the human skin.

4.6 Summary

A temperature-sensitive resin combined with 3D printing can detect skin temperature in order to warn individuals of potential risk with heat-related illnesses. This product can potentially be customized to fit different age groups since children and elders are more susceptible to heatstroke. The experiments conducted are able to show that the resin can change color at a specific activation temperature in a fast and stable manner. The accuracy of our device is similar to the conventional temperature-measuring device, such as the laser thermometer. The regression analysis shows the R-square value is 0.7599, and the average error is 1.3 ºC. Combine with the smartphone application, the device combines with a smartphone application to provide monitoring of real-time skin temperatures and alerts people who are vulnerable to heatstroke.

CHAPTER 5

A LOW-COST, MRI-VISIBLE, AND 3D-PRINTED FLEXIBLE TEMPLATE FOR PRECISION TUMOR TARGETING[3]

[3] Li, R., Xu, S., Bakhutashvili, I., Turkbey, I.B., Choyke, P.L., Pinto, P.A., Wood, B.J., and Tse, Z.T.H. Accepted by *Annals of Biomedical Engineering*.

Reprinted here with permission of publisher.

5.1 Abstract

To improve the targeting accuracy and reduce procedure time in magnetic resonance imaging (MRI)-guided procedures, a 3D-printed flexible template was developed. The template was printed using a flexible photopolymer resin FLFLGR02 in Form 2 printer (Formlabs, Inc., Somerville, MA). The flexible material gives the template a unique advantage by allowing it to make close contact with human skin and provide accurate insertion with the help of the newly developed OncoNav software. At the back of the template, there is a grid comprised of circular containers filled with contrast agent. At the front of the template, the guide holes between the containers provide space and angular flexibility for needle insertion. MRI scans are initially used to identify tumor position as well as the template location. The OncoNav software then pre-selects the best guide hole for targeting a specific lesion and suggests insertion depth for the physician. A phantom study of 13 insertions in a CT scanner was carried out for assessing needle placement accuracy. The mean total distance error between planned and actual insertion is 2.7 mm, the maximum error was 4.78 mm, and the standard deviation was 1.1 mm. The accuracy of the OncoNav-assisted and template-guided needle targeting is comparable to the robot-assisted procedure. The proposed template is a low-cost, quickly-deployable, and disposable medical device. The presented technology will be further evaluated in prostate cancer patients to quantify its accuracy in needle biopsy.

Keywords: MRI-guided procedure, 3D-printed template, MRI-visible

5.2 Introduction

Prostate cancer is a common site of malignancy in men [251]. Approximately 1 million prostate biopsy procedures are conducted in the US each year [68, 69] for the diagnosis of

prostate cancer. Image-guided biopsy is able to increase the accuracy of prostate cancer diagnosis by providing physicians image-based feedback during the biopsy procedure. Transrectal Ultrasound (TRUS) and Magnetic Resonance Imaging (MRI) have been commonly used as the modalities for prostate imaging and image-guided biopsy. TRUS is widely available for guiding prostate biopsy, but prostate tumors often are not visible in ultrasound. MRI, especially multi-parametric MRI, is currently the most promising imaging modality for detecting prostate cancer with great accuracy [73, 74]. MRI-TRUS fusion for guidance of targeted prostate biopsy has been reported in the literature [252-254]. However, prostate patients without rectum are excluded from this method, and ultrasound artifacts oftentimes compromise the efficiency of the image fusion[255, 256]. An early investigation by D'Amico A.V. et al., performed transperineal MRI-guided prostate biopsy in an open configuration 0.5 Tesla MRI scanner [75]. Since then, the advancement of prostate MRI imaging and interventional devices as well the availability of wide-bore MRI scanners favorable for interventional use have enabled in-bore biopsies to be performed more easily [257-261].

Robotics is understood to be an effective method to overcome the problem of limited patient access inside the bore of the MRI scanner. Also, the high accuracy of the robotic procedure has been widely recognized. Fichtinger et al. firstly reported designs of a manually powered platform for prostate interventions in a closed MR system [262-265]. Since then, the development of prostate robots has been demonstrated in closed MRI scanners [266-269]. However, the addition of a robotic operation onto the current interventional procedure requires a significantly modified clinical workflow and extensive training. Moreover, certain parts of the robots have a negative impact on the Signal-to-Noise (SNR) in the MR image.

Alternatively, some studies have investigated the possibility of improving template biopsies without disrupting clinical workflow. Given the fact that the diagnostic outcome from this freehand approach is strongly dependent on the physician's skills and experience, repetitive biopsy insertions and sampling are very common, which increases the potential risks and complications of the procedure. Beekley Medical (Bristol, CT) has developed a fiducial marker (PinPoint®) that can improve the accuracy of freehand needle insertion [68]. But the marker provides the surgeon with limited positional guidance. The other effective approach is to use a template or grid and provide the relative positional information of the tumor to the physicians. So far, most of the templates available in the market or reported in the research can only achieve a 2-dimensional vertical insertion and have been mainly used in Ultrasound and CT modalities. **Table 5-1** and **Table 5-2** shows the current development of CT/MRI compatible assistive needle guidance system. Kokoda J. et al., has reported using a specially designed needle guidance template to perform the prostate biopsy in a 70cm bore 3T MRI [77]. The promising result shows an improved accuracy compared to the conventional freehand procedure. However, the conventional MRI marker-based registration is used, which requires the physician to manually enter the positions of the MRI markers of the Z-frame read from the scanner console.

Table 6-1:Existing assistive needle guidance systems

Lead Author	Template Type	Dimension	Function	Application
Tokuda J. et al. [77]	Acrylic block	100×120×25mm	Biopsy needle guide	Prostate biopsy
Hata N. et al. [270]	Standard template	0.0059-inch holes spaced 5mm apart		

Pinkstaff et.al[271]	Standard template	N/A		
Ayres, Benjamin E., et al[272]	Virtual template mapping	Brachytherapy template with holes at 5mm intervals		

Table 6-2: Commercially available needle guidance systems

Companies	Template Type	Size	Function	Application
Civico®[273]	N/A	N/A	Positioning and stabilizing equipment	CT-guided procedures
Noras®[274]	Biopsy unit for GE 8-channel breast coil	N/A	Lateral, medial and craniocaudal access to the breast	MRI-Breast biopsy
Webb medical ®[275]	The Fast Find Grid®	N/A	Flexible grid, fast and accurate pinpointing of area	CT-biopsies

In this paper, an innovative 3D-printed template has been developed and manufactured, which combines the advantages of both a fiducial marker and template to improve the real-time biopsy procedure. First, the template is flexible, which means it can follow the contour of the patient and lies on the skin allowing the physician to carry out freehand needle insertion without any additional training. Second, it provides MRI-visibility in both coronal and transverse planes on MRI. A phantom study has been done inside a CT scanner to test accuracy. Finally, it is low

cost and disposable because it is 3D-printed from commonly available resin as raw material. In the future, it will be tested in clinical trials to prove its effectiveness and accuracy.

5.3 Materials and Methods

The final printed version of the template will be directly mounted on the patient's body. There will be a guidance system for the physician to insert the needle at different angles and hit the tumors at different locations. (**Figure 5-1**)

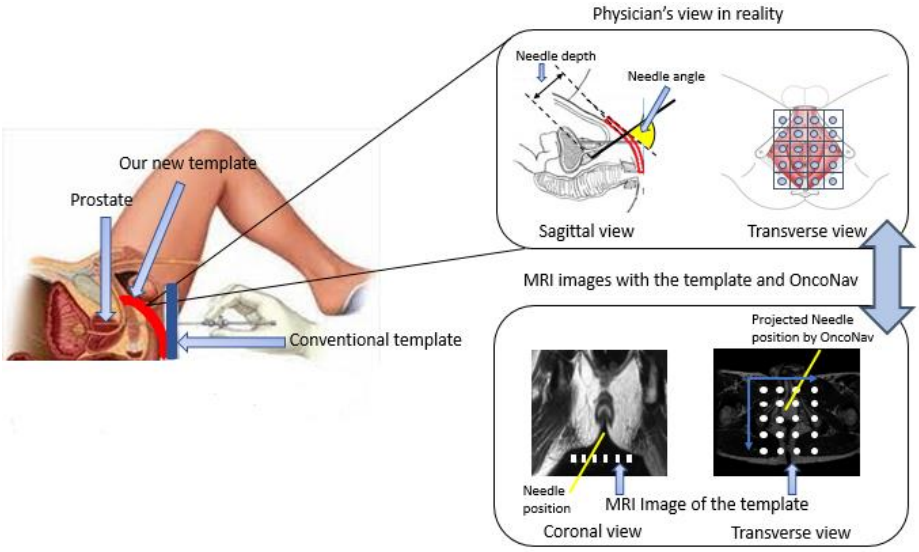

Figure 6-1: The presented template-guided system for minimally invasive interventional procedure

5.3.1 Design Criteria

Our design criteria are based on a survey of interventional radiologists who frequently perform prostate interventions. The general criteria show the features which a template should have to meet the market demand, environmental regulations, training and setup requirement, site restrictions, patient accessibility, and safety. The operational criteria show the technical

requirement for the template, such as the dimension, method of insertion, MRI visibility, and contact surface (**Table 5-3**).

Table 6-3: Design criteria and descriptions of an ideal needle template

General criteria	Descriptions
Cost	The cost should be significantly lower than the current costs of commercially available templates
MRI-compatible	The material used should be MR-compatible, the quality of scan images should not be significantly impacted by the presence of the template
Optimal SNR	The signal to noise ratio has to be adjusted to be optimum at different image sequences, primarily T1 and T2-weighted.
Environmental hazards	The material should be disposable
Training requirement	The procedure of using the template should facilitate a fast learning curve and be easy to manipulate
Set up requirement	The template should be compatible with the MRI scanner, easy to set up and be quickly adopted into the clinical environment
Site restriction	The template can be used in both a small MRI clinic and a large hospital
Patient accessibility	It should be a flexible template that can be mounted on any skin contour. It should be easily resizable with common scissors to personalize the template to each patient's dimensions.
Patient safety	The material used must be biocompatible. The template has to be properly sterilized before use.
Operational criteria	Descriptions
Size	The dimensions of the template are designed to be fit the patient's perineal region. The template size can be customized to suit specific patients.
Manual insertion	The insertion holes should be evenly distributed on the template. The separation distance is 8mm
Image contrast	Magnevist® by (Bayer HealthCare Wayne, NJ), a contrast agent used in MRI imaging, the main chemical composition being Gadopentetate Dimeglumine
Patient mounted	The flexibility of the template allows being attached to the patient's skin surface. Double-sided tape is added on one side of the template to give the adhesive nature

5.3.2 Flexible Template Design

The template was initially designed in Solidworks® (Solidworks Corporation, Waltham, MA). The template should be large enough to cover the whole perineal region. The size of the template is 80mm×80mm, which is finalized after consultation with the physician in NIH lab facilities. It has 144 Gadolinium (Gd) containers (**Figure 5-2 (a)**); each container is filled with a diluted Gd solution for MRI visualization. The material used for printing out the template is a flexible photopolymer FLFLGR02 manufactured by Formlabs® (Formlabs Inc, Somerville, MA). The advantage of using the 3D printing method over other fabrication methods is its low cost and fast-prototyping. The template is designed for 16, 17, and 18 G biopsy or treatment needles, which are commonly used needle sizes for clinical trials in NIH facilities.

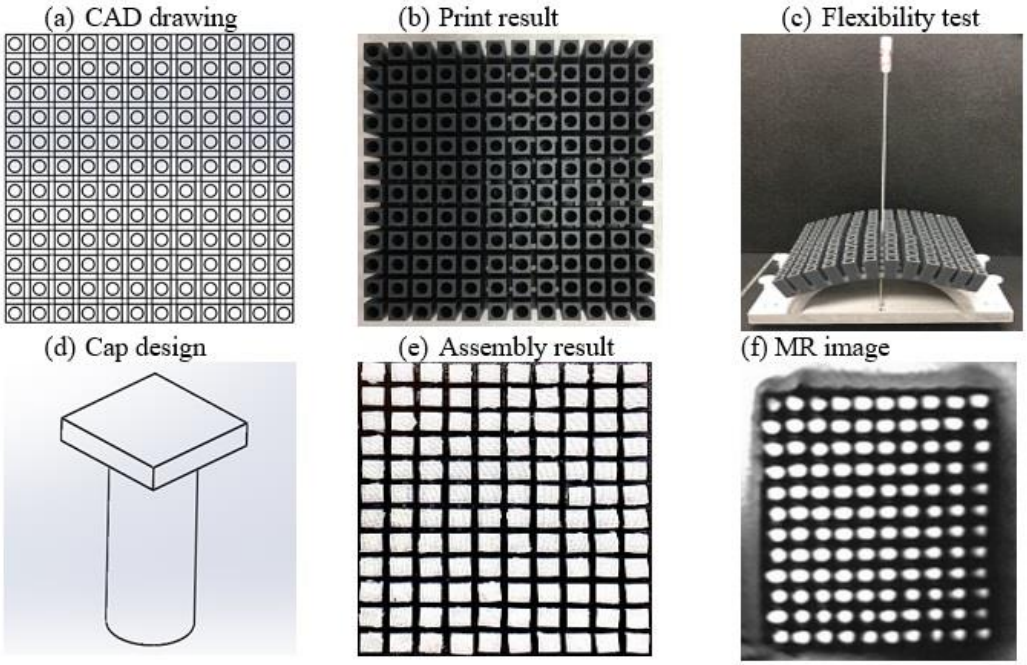

Figure 6-2: (a) shows the design of the template, (b) shows the 3D print result from the formlabs®, (c) shows the template flexibility test, the template was able to bend and make full contact with the arch. (d) shows the cap design for sealing the contrast agent, (d) shows the final assembly result of the template, (f) shows the MR image (T1-weighted).

The print was tested on a platform with maximum curvature of 120 degrees. The cap for closing the Gd containers is designed to have one insertion module. The circular-shaped module underneath is for closing the Gd container. In addition, the double-sided tape was used to firmly attach the template onto the patient's body during the operation. The mechanical design of the template has experienced systematic optimizations. The idea is to make a template that is both durable and easy-to-use. **Figure 5-3** illustrates the detailed design consideration.

(a) Top view of the template

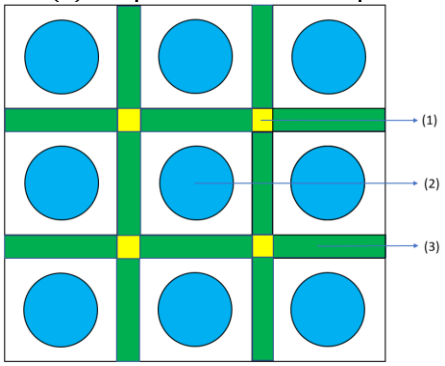

(b) Sideview of the template

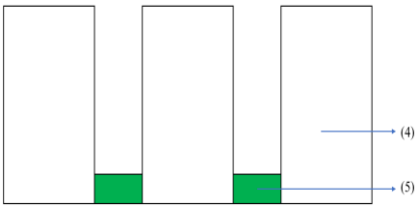

Number	Description
(1) Needle insertion point	The holes are suitable for 16, 17 and 18G needles.
(2) Container	The diameter is 4mm, the circular design is to ensure the best print result and mechanical stability. A circular cavity opening is more easily covered.
(3) , (5) Connector	It is optimized to be 2mm in length and 2mm in height, this achieves a balance between strength and flexibility.
(4) Container	The height is optimized to be 10mm to ensure the best visibility in MRI images period.

Figure 6-3: Detailed design information on optimization

5.3.3 Image Contrast

There are two factors that should be taken into consideration in order to make sure the template can be MRI visible under any circumstances: container size and the concentration of the

Gd solution. These two factors are independent of each other. The MRI scans were conducted to find out the suitable diameter for optimal MRI signal intensity.

5.3.4 Preparation of Contrast Agent

To find out the optimum concentration for Gd concentration, a test block situated with a series of containers was prepared, which has a diameter of 4mm. The Gadolinium to water ratio increased from 0 to 10% for eight containers. The MRI scans were conducted to find a suitable mixing ratio for optimal MRI signal intensity (**Figure 5-4 (a)**). It is also equally important to finding out the optimum diameter for the Gd container. A test block situated with a series of containers of gradual increasing diameters was prepared. The Gadolinium to water ratio was optimized and fixed in this case (**Figure 5-4 (b)**).

(a) Test block for Gd concentration

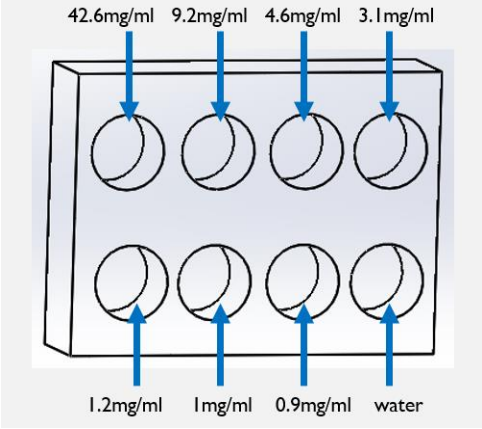

(b) Test block for diameter

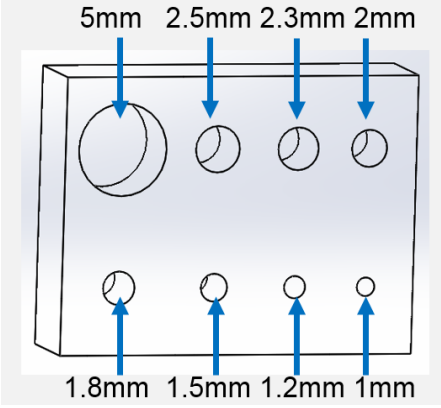

Figure 6-4: Two different types of test blocks were CAD designed, and 3D printed for optimizing both the Gd concentration and container size. (a) shows the circular containers with a constant diameter of 4mm but the concentration of Gd-water solution increases from 0.9mg/ml to 42.6mg/ml and pure water as a control reference is placed at the bottom right corner, (b) shows a series of containers with gradual decreasing size, optimal Gd concentration is applied to all the containers in this case.

5.3.5 OncoNav Software

This software provides additional guidance for the physician to use the template in the MRI environment. After the template is registered with the software, it is able to place artificial markers on the template and further enhance the functionality of projected needle pathway. The software outputs the grid location for needle insertion as well as the insertion angle and depth. (**Figure 5-5**).

(a) Registration in the OncoNav

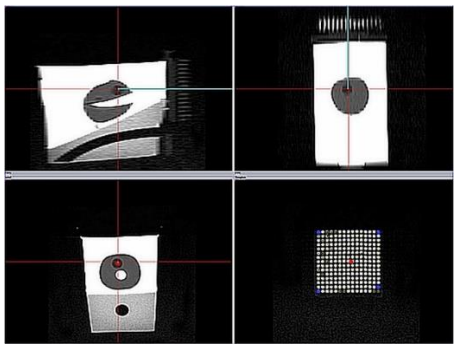

(b) A virtual needle shown on the template

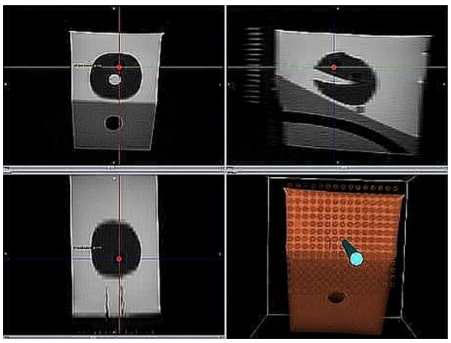

Figure 6-5: (a) shows the registration user interface, the blue dots are manually identified markers, the yellow circles are where the software thinks the MRI contrast should be located, the red dot is the projection of the target on the template, (b) shows the virtual needle generated by the software goes through the interval between fiducial markers.

5.3.6 Needle Placement Accuracy Test

Three targets were identified, and the template was placed in position on the prostate phantom through an MRI scan. Finally, the needle insertions were performed inside a CT scanner. Overall, 13 insertions were performed on three targets. **Figure 5-6 (a)** shows the template setup inside the CT scanner. The insertion accuracy is further analyzed using error bars and Bland-Altman plots.

(a) Template setup in the scanner

(b) Typical needle insertion CT image

(c) Distance illustration

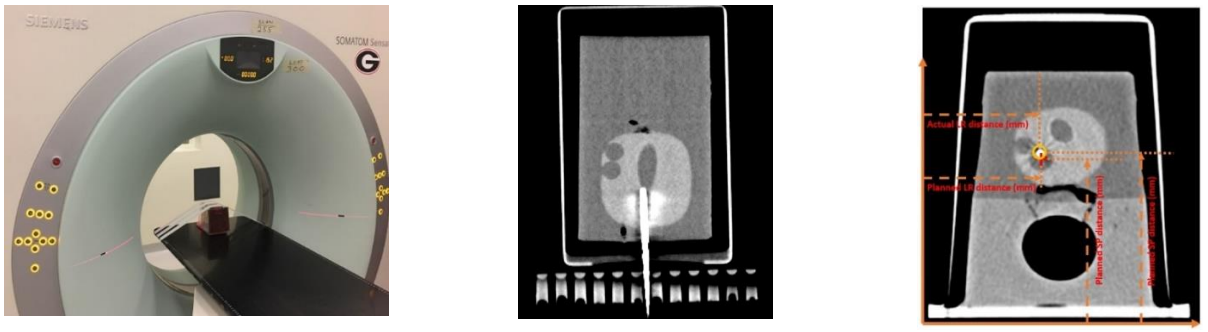

Figure 6-6: (a) shows a template placed inside the CT scanner, (b) shows the typical CT image, (c) how the distance is measured and analyzed, LR is the left-right distance error, SP is the superior-posterior distance error.

5.3.7 Clinical Workflow

The clinical workflow of the proposed template-based approach is designed to be as close to the current biopsy procedure as possible. This will enable the physician to perform the biopsy without significant additional training (**Figure 5-7**).

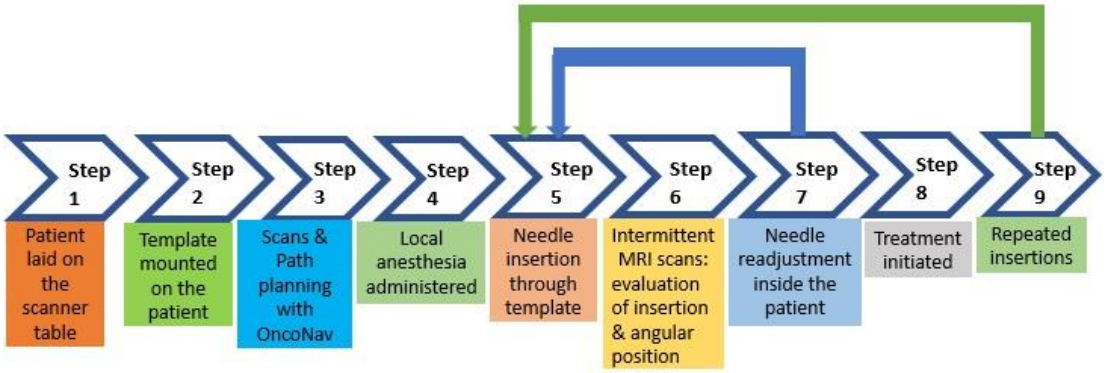

Figure 6-7: The clinical workflow of template application

The detailed workflow is as follows:

1. Place the patient on the support board with a standard Lithotomy position inside the MRI scanner.
2. Take the template out of the sterile bag and place it on the perineum of the patient.
3. Scan the prostate tumor region, register the template with the software, identify the target on the user interface of and select the best location on the template mapping for insertion with the assistance of the virtual needle function.
4. Administer local anesthesia to the area of insertion.
5. Insert the needle through the planned hole, puncture the skin, and move towards the tumor by incremental distance, followed by the projected pathway provided by the software.
6. Take intermittent MRI scans and evaluate the insertion pathway.
7. Readjust the needle position by switching to different insertion hole if the MRI images from intermediate MRI scan shows the needle will miss the tumor target significantly. Step 4 to 6 is repeated until the needle tip is moving towards the tumor on the planned pathway.
8. The treatment is started as soon as the needle tip is directly on the target tumor.
9. Steps 4-8 are repeated if multiple insertions are required.

5.4 Results

There are two different tests to validate the accuracy of the flexible template, the first one is the optimization of the image contrast, the second one is the needle placement accuracy test.

5.4.1 Image Contrast

The test block was used to determine the optimum Gadolinium (Gd) concentration for the template. As can be seen in **Figure 5-8**, both the image brightness and the signal intensity reach maximum when the concentration of Gd is 0.9 mg/ml, which corresponds to a 500:1 Gd to water ratio. The test was carried out in a 7T MRI scanner, and the sequence used was T1-weighted.

(a) MRI signal of different Gd concentrations

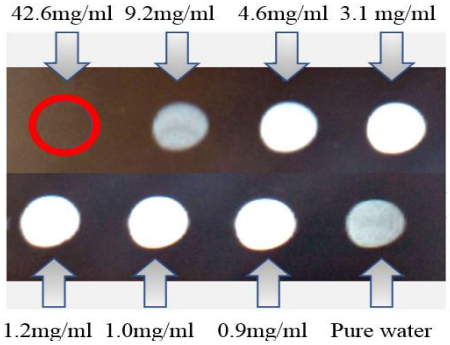

(b) MRI signal intensity versus Gd concentrations

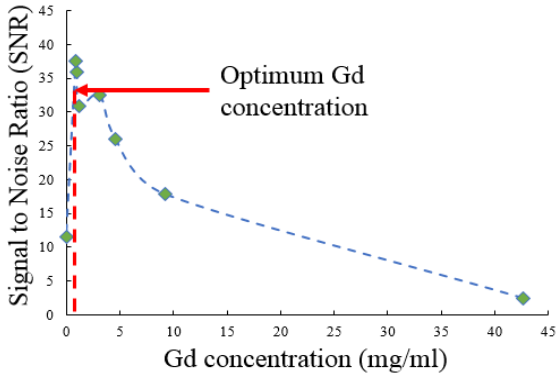

Figure 6-8: (a) shows MRI images of different concentrations of Gd solutions, (b) shows the signal intensity versus the Gd concentrations

The test block was used to find out the optimum Gd container diameter for the template. The concentration of the Gd solution is 0.9 mg/ml. As can be seen in **Figure 5-9**, the image brightness and the signal intensity are the best when the diameter is 5mm. However, due to the size constraint of the template for transperineal needle placement, the maximum container diameter was adjusted to 4mm. The test was carried out in a 7T MRI scanner, and the sequence used was T1-weighted.

(a) MRI signal of different test container

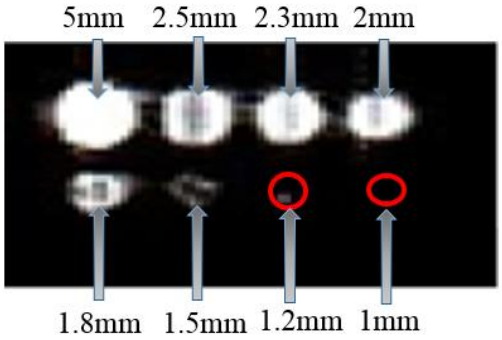

(b) MRI signal intensity versus test container

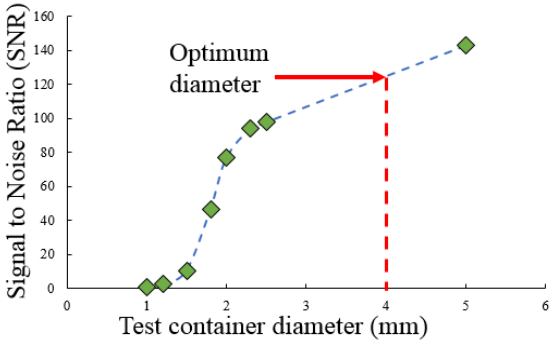

Figure 6-9: (a) shows MRI images of different test container diameter, (b) shows the signal intensity versus the test container diameter

5.4.2 Needle Placement Accuracy Test

Figure 5-10 shows 9 of the 13 insertions being conducted in the phantom study. The total distance (TD) error, superior-posterior (SP) error, and left-right (LR) error are displayed underneath each CT image. Each row shows three different insertions on one specific tumor, which is labeled as letter A, B or C in the CT images. The yellow circle is the actual point of insertion while the red circle is the planned point of insertion.

(a) Insertion #1 on Tumor A

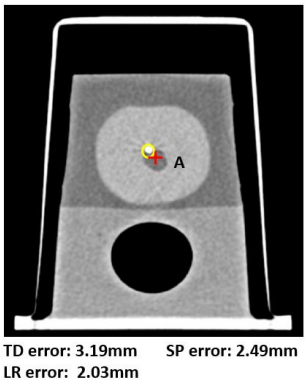

(b) Insertion #2 on Tumor A

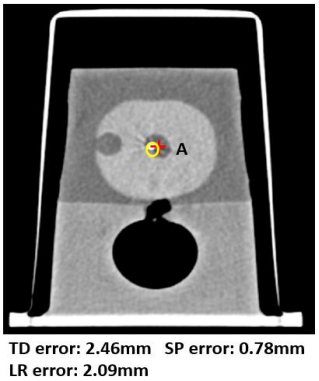

(c) Insertion #3 on Tumor A

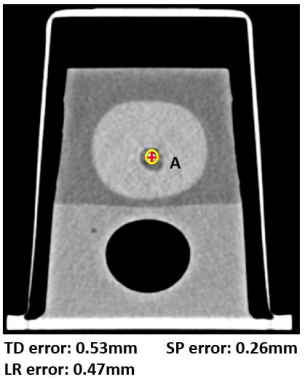

(d) Insertion #1 on Tumor B (e) Insertion #2 on Tumor B (a) Insertion #3 on Tumor B

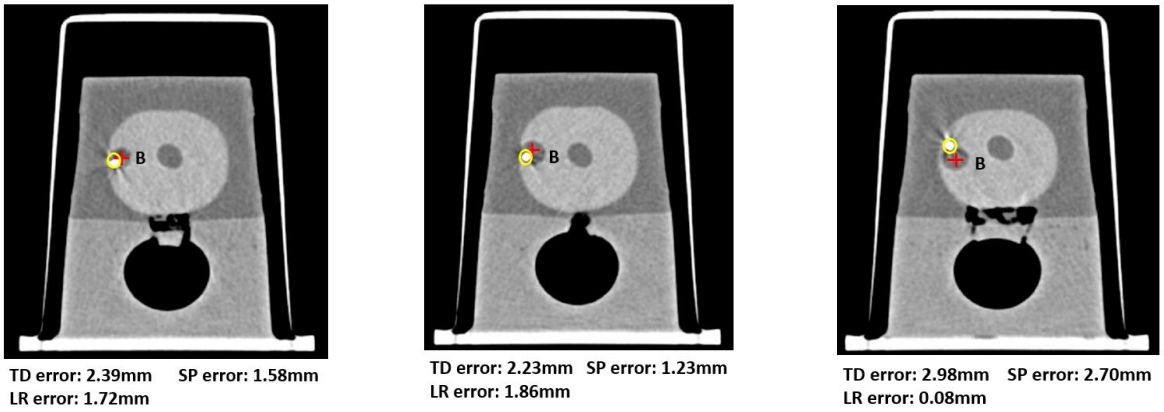

(b) Insertion #1 on Tumor C (c) Insertion #2 on Tumor C (d) Insertion #3 on Tumor C

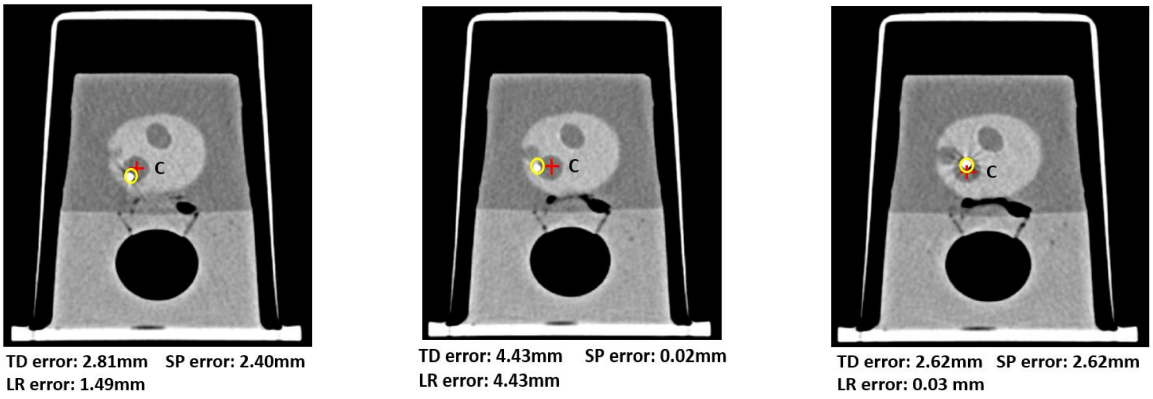

Figure 6-10: shows the 9 out of 13 insertions on the prostate phantom are displayed and analyzed. (a)—(c) is on Tumor A, (d)— (f) is on Tumor B, and (g)—(I) is on Tumor C.

The SP, LR, and overall distance errors are shown in terms of error bars in **Figure 5-11**.

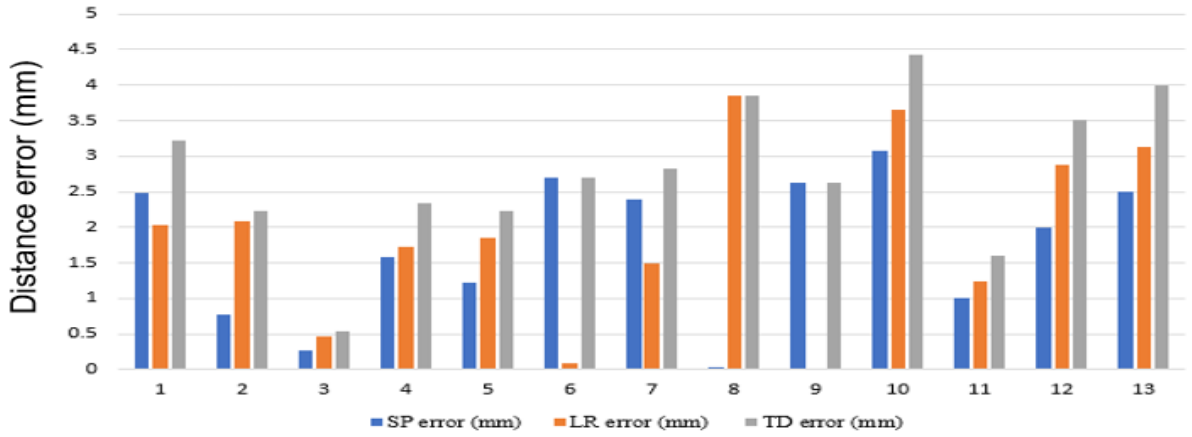

Figure 6-11: Shows a comparison of absolute values of SP, LR, and TD errors for 13 insertions.

The SP and LR errors have been analyzed, and Bland-Altman plots are in **Figure 5-12**.

(a) For the SP error

(b) For the LR error

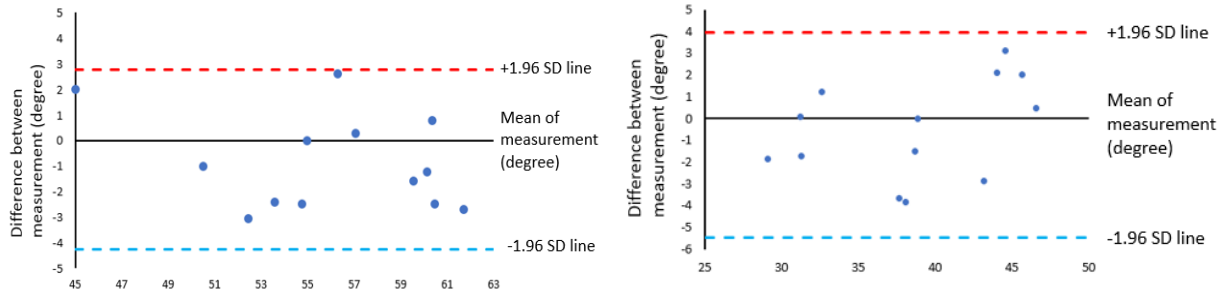

Figure 6-12: Shows the Bland-Altmann plot for SP and LR respectively.

5.5 Discussion

A new method for real-time MRI-guided biopsy is described. Although a prospective analysis of a large cohort of patients will be required to critically assess the clinical feasibility of this procedure, the ability to target simulated prostate tumors with acceptable accuracy has been demonstrated in a CT phantom study in this paper.

Since the initial development of PSA screening, the pathological diagnosis of prostate cancer has been based on the gold standard-systematic TRUS biopsy. However, the reported poor sensitivity of such biopsies shows the limitation of this conventional method and raises concerns about potentially missing significant cancer [276]. The TRUS-guided prostate biopsy has already been associated with high false-negative test results, which leads to repeated biopsies in men as their PSA levels continue to increase. MRI-guided biopsy, either using fusion biopsy or for in-bore biopsy, has been established as an alternative method of investigating suspicious lesions on MRI. Moreover, the false-negative rate of mpMRI has been significantly improved. Pepe et al. reported a 16.2% and 39.7% respective false-negative rates for targeted fusion prostate biopsy of PI-RADS 3 or greater and 4 or greater lesions[277]. The mpMRI, as well as MRI/TRUS fusion, is now widely recognized as one of the most efficient and cost-effective methods to detect significant prostate cancer [278, 279]. Recent studies showed the fusion biopsy detected 30% more high-risk cancers and 17% fewer low-risk cancers[280]. In two of the literature, the diagnostic accuracy of in-bore and MRI/TRUs fusion biopsy is 24.4% and 37%, respectively[281, 282].

The high-resolution and comprehensive image information provided by MRI has proven to be successful in diagnosing more clinically significant prostate cancers and fewer indolent cancer. Thus, it is proposed that there is an opportunity for the physician to benefit further by utilizing a guided system combining both the real-time MRI image with the actual body structure. Compared to transperineal template-guided mapping biopsy (TTMB) [283], the MRI-visible template is able to provide accurate positional and inserting depth information. Moreover,

the physicians are able to perform needle insertion on optimal skin entry point and adjust the needle pathway to reach the tumor.

The template-assisted needle biopsy insertion is done by MRI for a clinical procedure. One of the limitations of this study is that the validation test was carried out in CT instead of MRI. CT scan is not part of the clinical workflow. During the CT-guided procedure, intra-operative imaging is not used to adjust needle insertions. Therefore, CT is merely a tool to evaluate accuracy. CT is used in the accuracy test because it is more accessible than MRI and better at localizing the needle.

3D printing material is flexible and highly elastic. In addition, the Formlabs® printer can provide a high printing accuracy of 0.05mm. This allows the design of tight-fit and high-tolerance holes for specific needle sizes, such as 17 G needles, which are commonly used in clinical practice. Therefore, once the needle is positioned on the template, the orientation of the needle can be manually adjusted.

The connectors are designed to be removable so that the template not only can be easily segmented into smaller pieces and sizes for different populations but also can be flexible enough so that it can attach to the skin surface directly. Together with the MRI-visible Gd containers, the template is able to appear as a series of columns along the curvature of the skin surface in MRI images at the transverse view.

Due to the proximity of the template, the physician can have an understanding of the distance from the skin entry point to the target. Since the template appears consistently on MRI slices on both coronal and transverse views, it allows the physicians to track the needle trajectory based on the position and orientation of the template. The physician uses coronal-plane images to

determine the best skin entry point. After the needle is inserted, template images at transverse planes provide angular and depth information of the needle. One limitation of the template is that all the markers may not be shown on the single slice of the MRI image. However, a software used is able to register each marker of the template and display both existing and software simulated marker positions. During the insertion, the template stays firmly on the skin surface so that the physicians can take intermediate MRI scans, adjust the needle orientation if it deviates from the planned trajectory or any unplanned occurrences. This can ensure insertion accuracy comparable to the robot-assisted approach without dedicated training. Zandman et al. have developed a robotic device with an average error of 1.84 mm [284]. Other robotic systems like Srimathveeravalli et al. have achieved an accuracy of 2.58 mm [285]. The mean error of the proposed template is 2.7 mm.

The signal intensity is the key for the template to be visible in the scan images. There are four factors influencing the signal intensity; the first is the mixing ratio between Gd solution and pure water; the optimized value is 1ml:500ml. In **Figure 5-9**, the pure water appears darker than the rest of the Gd solutions. This is because the higher the Gd concentration, the more quickly the molecules in Gd concentration can realign its longitudinal magnetization with B_0 after RF pulse, thus shortening T1. Therefore, the image will appear brighter on T1 weighted scans. On the other hand, the concentration of 42.6 mg/ml is dark because of the profound shortening of T2. The second factor is the size of the Gd container. A larger container will have more visibility in the MRI images. However, because the overall size of the template is limited to the perineal region, a larger container will greatly increase the separation distance between the insertion holes. This will reduce the accuracy of the needle insertion process. The third factor is the

sequence used during the MRI scanning. A T1-weighted sequence is used in the MRI scan because it is a standard procedure for experimental purposes in the research institution. In the future, a T2-weighted sequence will be used so that tumors can be optimally visible. The final factor is the location of the organ. The prostate is closer to the bladder, which will lower the template visibility because of the urine storage.

The uniqueness of the procedure is that the template can be mounted to the patient with close skin contact. The template is filled with the optimal concentration of contrast agent, which is MRI-visible in both transverse and coronal planes. The physician is able to perform the needle insertion with a real-time indication of needle position. However, one of the limitations is that the contrast agent will gradually lose its MRI visibility over a month's time due to the vaporization of the solution. We will find out a better way to seal the contrast agent and retain its maximum visibility in the future. The other limitation is that the flexibility could potentially self-introduce some errors because some insertion holes on the template will be slightly stretched on the uneven surface. One solution is the intermittent scans will further guarantee the needle remains targeting towards the lesion.

In terms of economic potential, the template can be printed out in a 3D printer repeatedly with consistent quality. The print material is a flexible photopolymer resin FLFLGR02 developed by Formlabs®, which is commercially available. Finally, the template is designed to be reusable for a predetermined number of uses and then becomes disposable.

5.6 Summary

This chapter presents an innovative, flexible template that can be 3D-printed with biocompatible material. The template is designed specifically for the transperineal prostate biopsy in MRI scanners. The template can be cut into customized sizes for different age groups. Other important features are its visibility on MRI and the ability to quickly register it to standard images. The phantom study shows, with the assistance of the template and software, the accuracy of the prostate biopsy is comparable to a robotic system. It can be foreseen that the overall clinical procedure time will be reduced without significant alteration of the clinical workflow. Future work will be testing the diagnostic accuracy of the template in a human clinical study and compare the results with the standard procedure for a needle biopsy.

CHAPTER 6

A LOW-COST PATIENT-MOUNTED NEEDLE LOCALIZER FOR IN-PLANE RF THERMAL ABLATION[4]

[4] Li, R., Xu S., Wood B., Tse, Z.T.H. To be submitted to *Journal of Vascular and Interventional Radiology*.

6.1 Abstract

CT-guided percutaneous needle insertion is one of the most common guidance techniques in interventional radiology (IR) but requires experienced operators and multiples X-ray controls. We aimed to evaluate the feasibility and performance of CT-guided radiofrequency liver ablation assisted by a new angular tracker in an in-vivo animal model. A low cost, ergonomic, patient-mounted, and smartphone-based micro-electromechanical system (MEMS) angular localizer was designed, and 3D printed as a needle holder. It was first tested and calibrated in a rigid and controlled benchtop environment, followed by an in vivo experiment on a live swine. Six CT-guided percutaneous liver ablations were conducted and assisted by our novel device.

The mean tip-to-target distance error, measured as a minimum needle path to the target, was 5.2 mm, with a standard deviation of ± 1.4 mm. The average tip to target distance was 7.4 mm. The mean tip-to-target angular error was 4.2°, with a standard deviation of ± 2.6°. The average puncture time was 25.5 s. Only one of the punctures required an intermediary CT scan, and none required any needle drawback or repositioning. No major complication was noted during the procedure. This MEMS angular tracker device can reliably assist in-vivo percutaneous insertions conducted under CT-guidance.

Keywords: MEME Sensor, Cancer Ablation, In-vivo Study, Image-guided

6.2 Introduction

Primary liver cancer is the most common cancer worldwide, causing an estimated one million deaths every year [286]. For patients with inoperable or recurrent liver cancer, RFA provides a safe and successful option [287]. RFA is minimally invasive, safe, and effective and has great potential for local tumor destruction.

Recent advancements in radiofrequency thermal ablation (RFA) have opened a variety of treatment options for certain oncology patients [287-289]. Image-guided percutaneous therapy [290, 291] may now provide an effective local treatment of isolated or localized neoplastic disease, and can also be used as an adjunct to conventional surgery [292], systemic chemotherapy [293], or radiation [294]. RFA is a classic example of utilizing heat in medical applications. During the procedure, the locations of the tumors are identified with various imaging modalities such as ultrasound [294], computed tomography (CT) [295], or magnetic resonance imaging (MRI) [296]. The principle for RFA is that the patient is treated into an electrical circuit by placing grounding pads on the thigh area. The physician inserts a small needle, which has the electrode, through the skin, and then reaches the tumor target. The needle tip generates ionic vibration and leads to frictional heat.

However, in the RFA procedure, failed to target and ablate the tumor with clean edges will result in regrowth of the tumor [297]. Also, the ablation will damage all the healthy cells along the needle pathway during the retracting process at the end of the treatment session. In other words, improper path planning will result in a potential risk of thermal injury to critical structures [298].

In order to increase the insertion accuracy to avoid the above problems, various efforts have been put to improve either needle trajectory planning or tracking. Some of the research groups focused on trajectory planning. DiMaio et al. developed effective motion planning and needle steering model base on finite element analysis (FEA) [299]. The others focused more on trajectory tracking. In the category of trajectory tracking, there were two subclasses: active systems such as needle steering robots. Cleary et al. developed a “needle driver” robotic system

for minimally invasive procedures [300], where the precision results were comparable to the manual procedure. Ben-Davis et al. developed a CT-Guided Robotic system with a maximum error of 4.8 mm for liver insertion [301].

Other groups were leaning towards the development of real-time tracking devices using Electromagnetic (EM) [302]. Apart from that, commercially available needle tracking systems such as VirtuTRAX® instrument navigator [303] and NeoRad SimpliCT [304] developed hardware and software platforms to assist needle navigation.

Table 6-1 shows the recent development of tracking devices. Most of the devices have reached the stage of the clinical study.

Table 6-1: The comparison between other devices and the presented device in this study

Research groups	Technology	Year	Types of studies	Accuracy	Reference
Ben-David et al.	Xact Robotics	2018	Animal	The mean distance to target was 92.9 mm ± 19.7 (range, 64—146 mm).	[301]
Abayazid et al.	Inertial Measurement Unit	2017	Phantom	The mean errors of the experimental trials varied between 0.86 mm and 1.29 mm.	[305]
Basafa et al.	ClearPoint	2016	Phantom, animal, and human	The total systematic error was (3.99 ± 1.43) mm.	[306]
Koethe	Perfint Maxio	2014	Phantom	Mean entry-to-target distance was 11.0 ± 3.8 cm (range, 10.2—11.5 cm) for needle insertions simulating percutaneous biopsy.	[307]
Appelbaum et al.	VirtuTRAX	2013	Animal	The target accuracy was 4.0 ± 3.2 mm when an EM sensor was installed on the needle tip.	[308]
Roberts et al.	SeeStar	2006	Phantom and animal	N/A	[309]

Magnusson at al.	NeoRad SimpliCT	2005	Human	The error was 1.1°.	[310]
The presented device	IMU		Animal	9.8 mm ± 2.3mm and 2.3° ± 1.2° in vivo; the mean length of the puncture tract was 96.6 mm (± 26.6 mm).	

In this study, a small, patient-mounted, and smartphone-based MEMS angular localizer was fabricated to assist the surgical planning as well as improve the targeting accuracy. The device will optimize the needle insertion pathway by providing real-time angular information at the skin entry point. The device could be easily mounted on the patient's body with a simple sterilization procedure. Moreover, the presented device is able to stabilize the needle advancement for long-distance insertion (> 110 mm). **Figure 6-1** describes the MEMS tracker-assisted procedure.

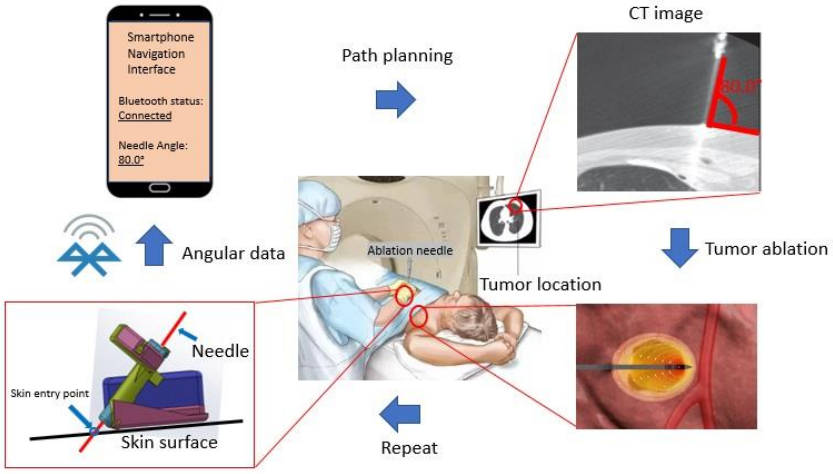

Figure 6-1: shows the description of the procedure, there are three main steps involved: at first, the presented device measures the needle angle and displays the angular data on the smartphone. The angular information assists the physician to decide the skin entry angle for ablation biopsy. The device could continuously provide real-time angular information during needle advancement. After one ablation is done, the device could be used repeatably for multiple ablations.

6.3 Materials and methods

6.3.1 Hardware Preparation

There are two critical factors in image-guided thermal ablation: surgical planning and needle targeting. The surgical planning means the pre-interventional imaging of tumor size and the number of tumors. The targeting means the placement of the RF tip into the tumor tissue. The design challenges and solutions of our device are shown in **Table 6-2**.

Table 6-2: Design specifications for the presented device

Challenges	Solutions
Needle tracking	A miniaturized MEMS IMU module was attached to the needle channel for measuring the needle angle
Continuous surgical operation	A 400 mAh lithium battery was used ensuring at least 4-hr continuous operation during the surgical operational hours
Device communication	A built-in Bluetooth module (Bluetooth 3.0) allows the device communicated with the smartphone application
Needle stabilization	A tight-locking mechanism has been developed to stabilize the needle when the treatment is happening
Hands-free operation for long-distance insertion	The device can be attached to the surface area of interest and stabilized by a double-sided type. The physician only needs to hold the needle during operation.
Skin-entry proximity	The device was designed in a way that the Rotation Center of Motion (RCM) of the needle tip is on the skin entry point. This will ensure the measured angle is the same as the skin entry angle.
Needle release mechanism	A release mechanism was designed in a way that the device can be detached quickly from the needle once the needle tip hits the tumor target
Needle traveling range	The specially-designed joint movement gives the angular measurement range of 0° — 230°
Biocompatibility	As the device is patient-mounted, it will require a high level of biocompatibility. The base of the device was 3D printed using the Formlabs® dental resin, which can be used to fabricate FDA-approved class 2 surgical devices. Moreover, the whole device will be placed into a sterilized bag during operation.

Repeatable usage	The device was designed to be mechanically robust and can be used in multiple insertions.
Low-cost solution	The total material cost of the device was less than $100, including the 3D printing material as well as the MEMS IMU sensor.

Figure 6-2 shows the overall design and fabrication process. The device was firstly designed and assembled in Solidworks®. Then the Formlabs® 3D printer was used to print out the device. The rotational joint was made with a metal rod. A white cable was used to connect the MEMS tracker with the microprocessor. Moreover, there is a Bluetooth module inside the black case, which enables the tracker to communicate with and output angular data to the smartphone application.

(a) CAD design

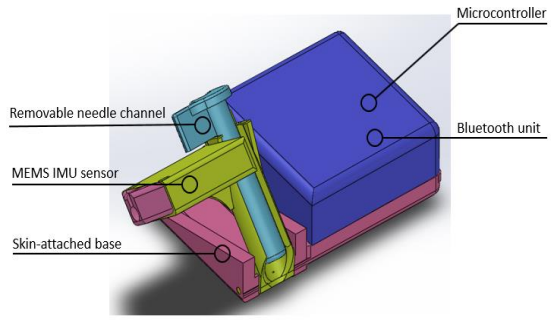

(b) Needle rotating and release mechanism

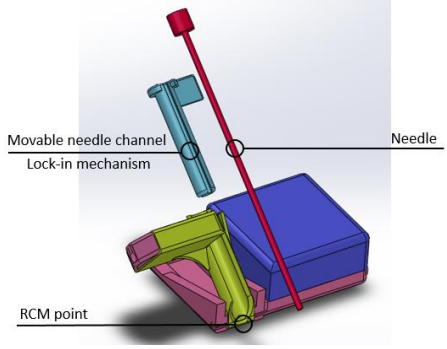

(c) Final device assembly

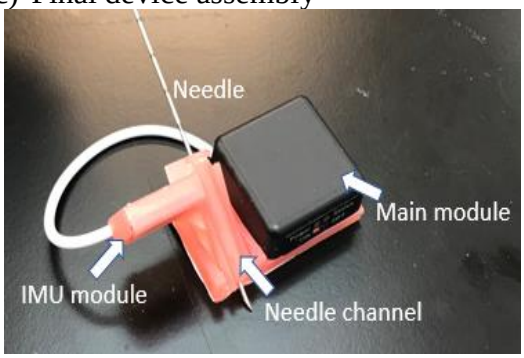

(d) Pairing with a mobile platform

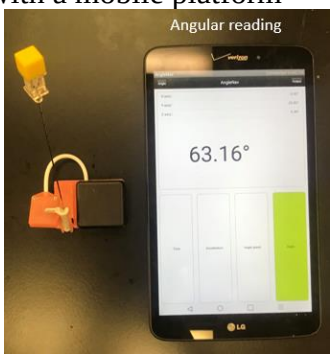

Figure 6-2: shows (a) CAD design, (b) Needle release and Remote Center of Motion (RCM) mechanism, (c) final device assembly using biocompatible material, and (d) Bluetooth communication with the mobile platform, which shows the real-time needle angle.

The device was 3D-printed using a biocompatible material RS-F2-DBOP-01 by Formlabs® (Sommerville, CA). The resin has a class II biocompatibility with high accuracy of 50 microns. Moreover, during the operation, a sterile bag was used to enclose the device and ensure the device was sterilized. The device includes a microprocessor, a battery, a Bluetooth communication module, and a measurement unit. The measurement unit includes a gyroscope, a magnetometer sensor, and an accelerometer to provide angular measurements on three axes. The Bluetooth module allows communicating with a smartphone app for angular display.

6.3.2 Clinical Workflow

Figure 6-3 shows the proposed clinical workflow for this device. It mainly breaks down into the following steps:

Step 1 Trajectory planning: intravenous conscious sedation is required. The skin area on the patient is aseptically prepared and draped. The skin entry point, as well as the planned insertion angle, was defined after the initial CT scan.

Step 2 Needle placement: the physician first places the device on the skin entry point using double-sided tape. The angle of the needle channel was set to the planned insertion angle, and the needle was locked in position on the device.

Step 3 Needle advancement and adjustment: the needle was punctured through the skin and advanced towards the tumor target. Intermediate CT evaluation allows the stepwise correction of the needle's position to the tumor target as the target may move under natural respiration.

Step 4 Needle confirmation: one final CT scan was conducted to confirm the needle position relating to the tumor target for ablation treatment.

Step 5 Treatment initialization: the physician detaches the device from the skin entry point and initiates the ablation treatment.

Step 6 Multiple sites of ablation: the physician retract the needle and reinitiate the needle insertion if multiple ablation sites are required.

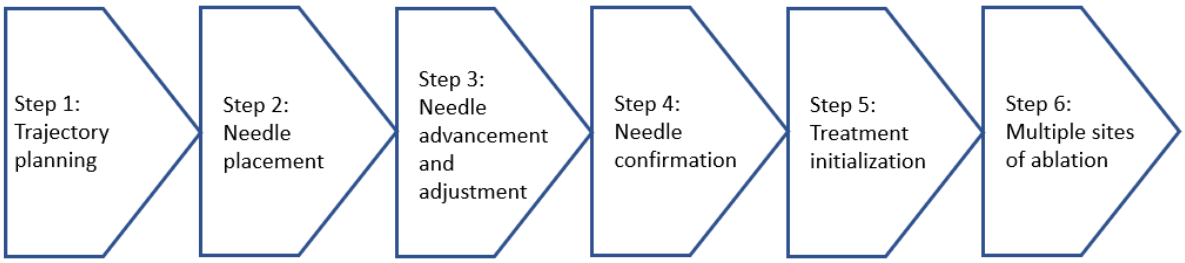

Figure 6-3: presented clinical workflow, which has six steps. Step 1, Step 2-4, and Step 5-6 are the planning step, the target acquiring steps, and the treatment steps, respectively.

6.3.3 Accuracy Test

Two tests have been carried out to test the accuracy of the device. The first one is the benchtop test, which tests the measuring accuracy of the device in an ex-vivo environment. The second test was carried out in a live swine, which validate the insertion accuracy of the device in an in-vivo surgical environment.

6.3.4 Benchtop Test

The purpose of the benchtop test is to calibrate the needle in a rigid and controlled environment. The test takes place on a flat surface, where protractor was used to measure the actual inclination angle, which was compared to the IMU measurement.

6.3.5 In-vivo Study

All procedures were performed under a protocol approved by the Institutional Animal Care and Use Committee using one healthy castrated male Yorkshire domestic swine study (70 pounds). After the test was finished, all the CT images were analyzed in the software MircoDicom viewer®.

6.4 Results

There are two different tests to validate the accuracy of the handheld tracker, the first one is the benchtop test, the second one is the live swine study.

6.4.1 Benchtop Test

Figure 6-4 shows the benchtop test. The Root-Mean-Square (RMS) error is 0.64°.

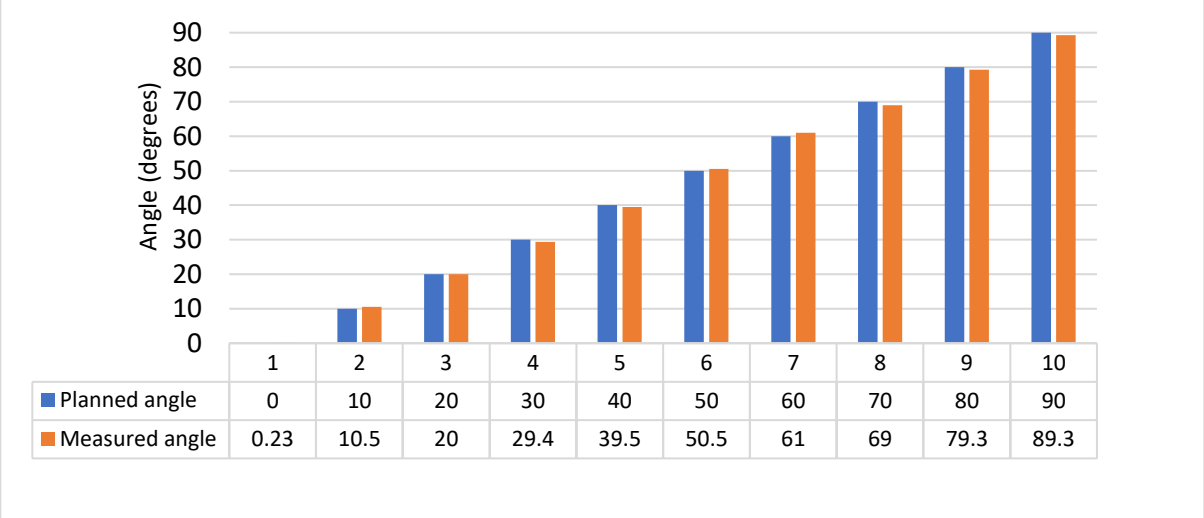

	1	2	3	4	5	6	7	8	9	10
Planned angle	0	10	20	30	40	50	60	70	80	90
Measured angle	0.23	10.5	20	29.4	39.5	50.5	61	69	79.3	89.3

Figure 6-4: shows the results of the benchtop test. The number of trials is listed underneath, along with the absolute errors in each trial.

6.4.2 In-vivo Study

Figure 6-5 shows one typical example of how the planned and actual insertion depth was obtained from the CT study. The swine was scanned on the transverse plane to locate the targets. Then the pre-planned pathway was determined and measured for one specific target, shown in a red line in **Figure 6-5 (b)**. The target was marked as a red circle. Finally, after the actual insertion was done, the pathway was scanned, measured, and highlighted in the yellow line. The needle tip was marked as a yellow square.

(a) Pre-inserted targets (b)Pre-planned pathway (c) Actual insertion pathway

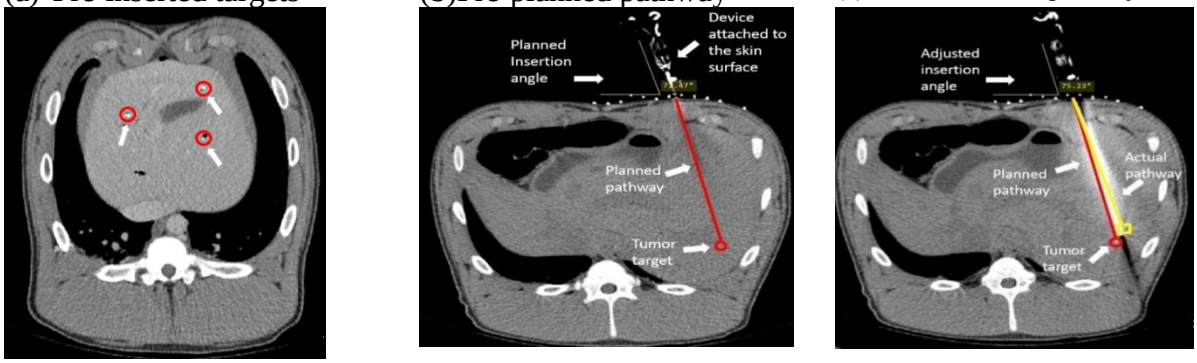

Figure 6-5: One example of needle insertion from the stage of planning to completion, (a) shows pre-inserted CT visible targets (0.5mm-BB beads), (b) shows pre-planned insertion pathway, (c) shows the final scan of the actual pathway.

Table 6-3 shows the definition of symbols used in **Figure 6-6** as the device is skin-mounted, so the planned and actual insertion depth was calculated from the skin entry point.

Table 6-3: Definition of Symbols used in the image analysis

Symbols	Meanings
PDS	Planned Insertion Depth from Skin Entry Point
ADS	Actual Insertion Depth from Skin Entry Point
TTD	Needle Tip-to-Target Distance Error
AE	Needle Angular Error between PDS and ADS

Figure 6-6 shows 6 insertion results from the in-vivo study. The average actual insertion depth is 96.2 mm (± 28.5 mm).

(a) Target 1

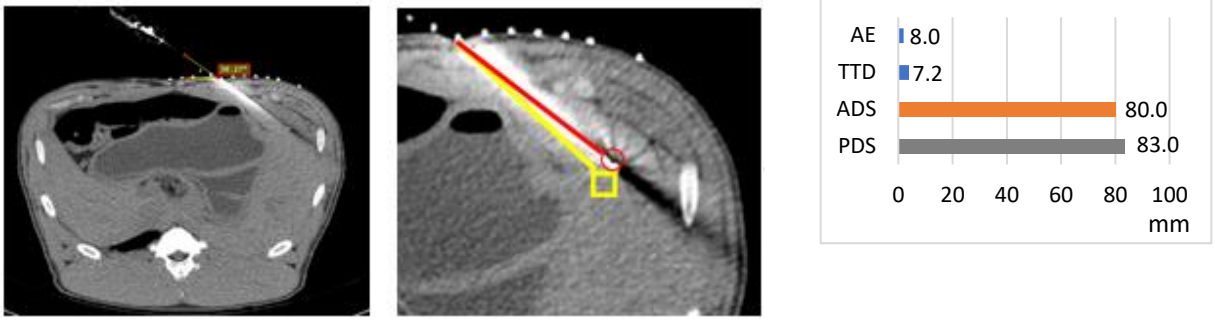

(b) Target 2

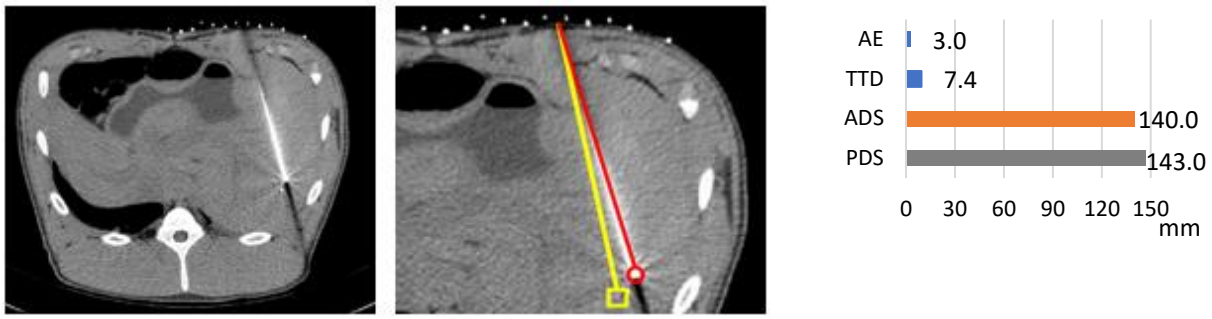

(c) Target 3

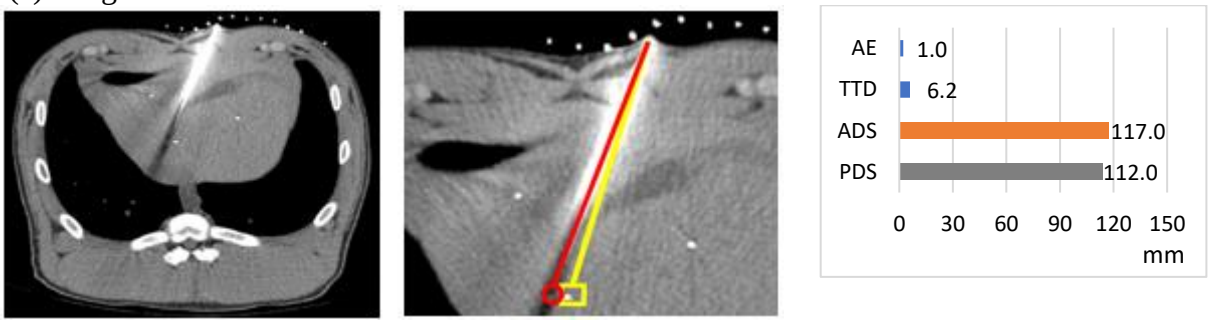

(d) Target 4

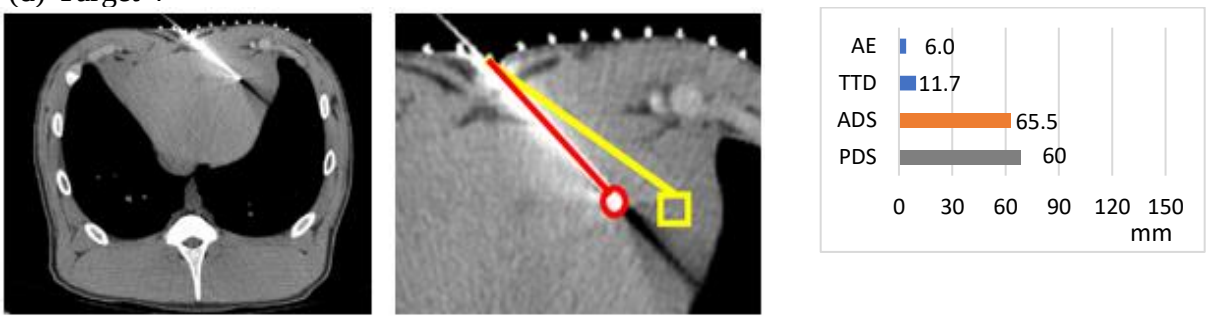

(e) Target 5

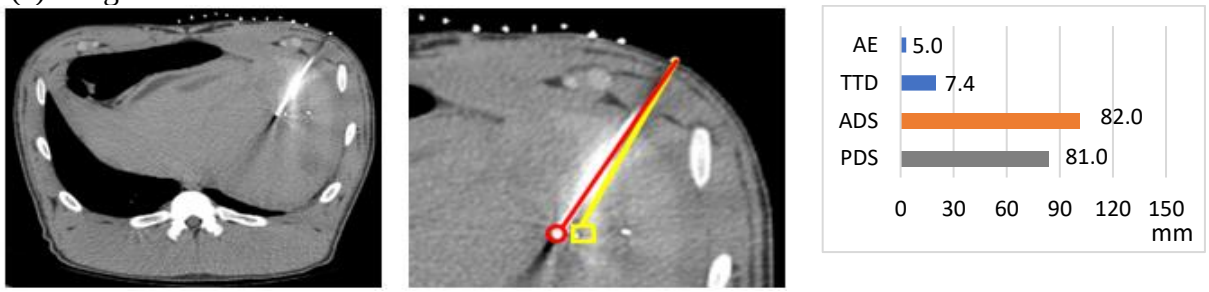

(f) Target 6

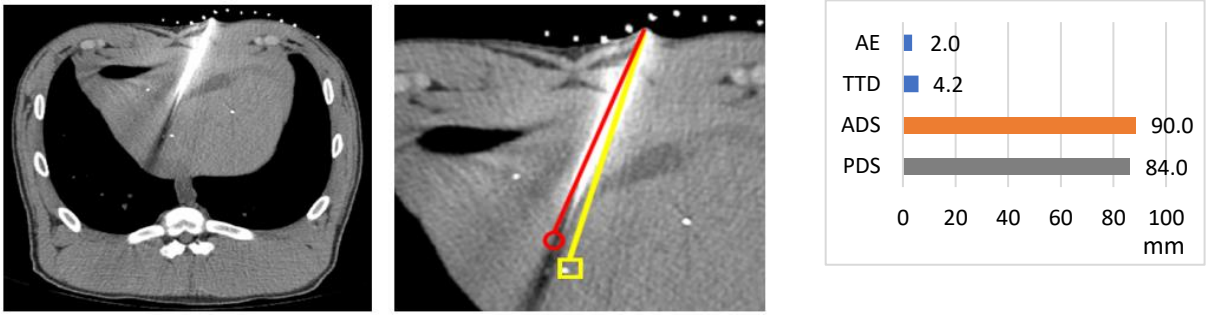

Figure 6-6: shows all the CT images of insertions for 6 targets. On each row, the first image presents the overall needle pathway. The second image displays the needle and tumor location. Besides the images, there are four parameters, PDS (planned insertion distance from skin entry point), ADS (actual insertion distance from skin entry point), TTD (needle tip-to-target distance error), and AE (needle angular error). The red line is the planned insertion with a circle end indicating the tumor position. The yellow line is the actual insertion with a square end indicating the actual needle position.

Figure 6-7 shows the comparisons between the planning pathway and the actual pathway in terms of TTD and AE. **Figure 6-7 (a)** shows the comparison between planned and actual insertion distances. **Figure 6-7 (b)** shows the corresponding tip-to-target error. **Figure 6-7 (c)** shows the comparison between planned and actual insertion angles and **Figure 6-7 (d)** shows the corresponding angular error.

(a) Comparison between planned and actual insertion distances

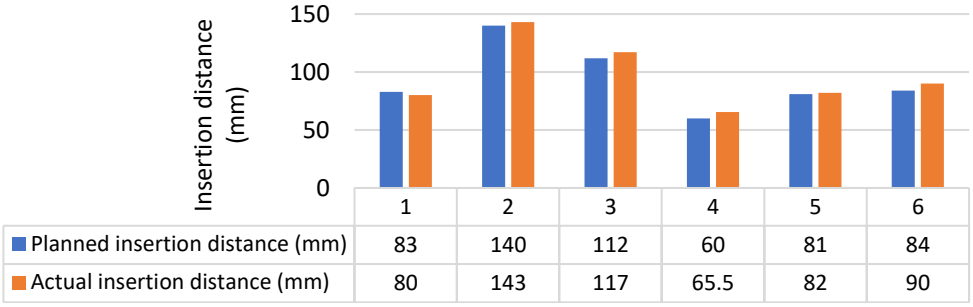

	1	2	3	4	5	6
Planned insertion distance (mm)	83	140	112	60	81	84
Actual insertion distance (mm)	80	143	117	65.5	82	90

(b) Tip-to-target Distance Error (TTD)

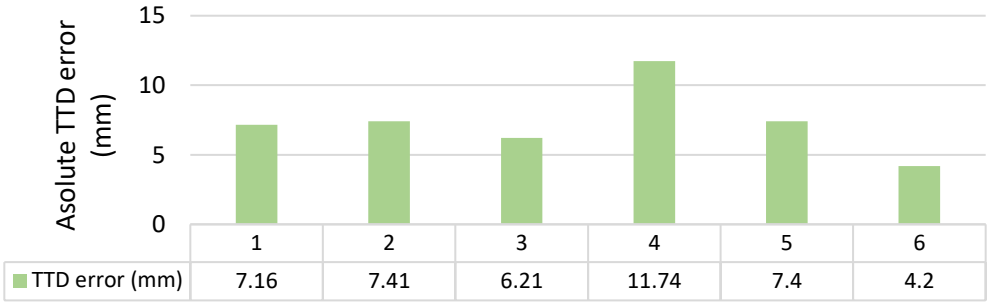

	1	2	3	4	5	6
TTD error (mm)	7.16	7.41	6.21	11.74	7.4	4.2

(c) Comparison between planned and actual insertion angles

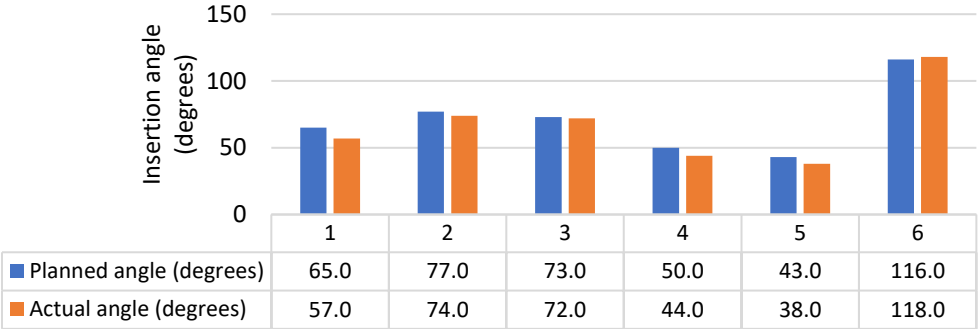

	1	2	3	4	5	6
Planned angle (degrees)	65.0	77.0	73.0	50.0	43.0	116.0
Actual angle (degrees)	57.0	74.0	72.0	44.0	38.0	118.0

(d) Angular Error (AE)

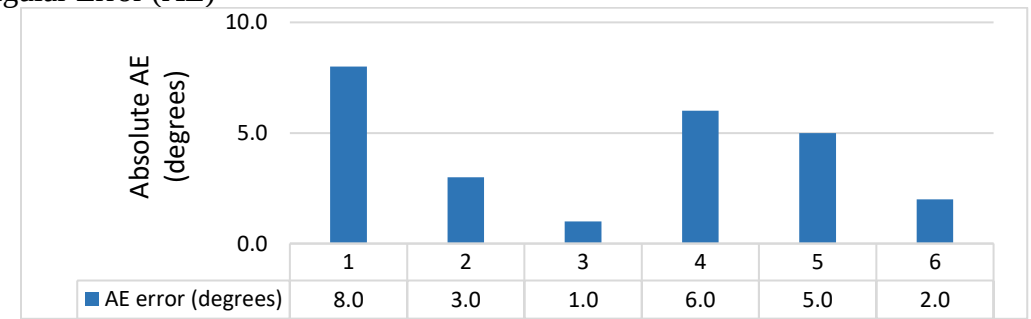

	1	2	3	4	5	6
AE error (degrees)	8.0	3.0	1.0	6.0	5.0	2.0

Figure 6-7: Results of six insertions for the in-vivo study, (a) shows the comparison between the actual and planned insertion distance, (b) shows the TTD errors, (c) shows the comparison between the actual and planned insertion angle, (d) shows the AE errors. The mean accuracy, measured as the minimum needle path to the target, was 5.2 mm. The average tip to target

distance was 7.4 mm. The average puncture time was 25.5 s. Only one of the punctures required an intermediary CT scan, and none of the insertions required any needle drawback or repositioning.

6.5 Discussion

The In-plane needle localizer could provide real-time angular information. There are many design consideration to ensure the consistent and accurate angular output. However, there are some limitations of the device which will be addressed in this section.

6.5.1 Angular Measurement

Although IMU sensors have benefits of large operation range and free of the line of sight problem compared to the optical sensors, they suffer from the drifting problem. In our case, a tri-axial accelerometer and a tri-axial magnetometer were integrated with the gyroscope inside the MEMS IMU module. The combined data from each sensor were processed via an extended Kalman filter-based data fusion algorithm. This approach can significantly reduce the measurement error and provide a more accurate angular estimation. Moreover, as the MEMS IMU sensor detects the three-dimensional position, and the device needs to output two-dimensional angular information, the tilt angle was used to calculate from the pitch and roll angles of the IMU sensor.

6.5 2 Assistive Image-guided Devices

The past literature has explored a wide range of assistive devices in different image modalities, such as CT biopsy templates [311, 312]. For those image-guided devices, the biggest issue is the lengthy image registration [39]. The current solutions were to use fiducial [313, 314] or apply computing-based methods [315]. Alternatively, devices could be designed to be close contact with the skin surface, which greatly shorten the distance to the surgical references, and

thus lower the registration difficulty. The only requirement is to align the device with the laser guide during the surgical planning, so the device is on the same image slice as the tumor target.

Moreover, the Remote Center of Motion (RCM) point was designed to overlap with the skin entry point. This means the skin entry angles measured from the CT images will be the same as the needle rotational angles measured from the MEMS IMU sensor. In other words, during the incremental needle advancement, the physician could firstly measure the skin entry angle, plan the new skin entry angle judged by the extent for targeting deviation, then set the new needle angle using the device. Admittedly, the orientation of the inserted needle tip may not be consistent with the one of outside needle shaft as the needle was likely deflected by the motion of soft tissue. The current practice of mitigating this impact was to steer the needle or manipulate the tissue manually. The tissue deflection is out of the scope of this study. In the future, another study could be conducted to combine the device with a steerable needle and evaluate the TTD and AE.

6.5.3 Other Errors in the Experiment

During the in-vivo study, the respiratory movement of the animal model could potentially deflect the needle direction. Moreover, the punctuation through the skin surface and into soft and inhomogeneous tissue will cause the needle to deviate from the planned pathway due to the curvature of the needle shaft. In the clinical setting, the accuracy of the needle placement could be largely impacted by difficult inserting approach, respiratory motion, peristalsis, and changing target location sue to mechanical pressure in soft tissues [316].

6.5.4 Limitations

Currently, the device can only carry out in-plane insertion because of its design constraints. The device has to be aligned with the laser guide so that the device can be registered with the CT image, and the measured angle is consistent with the skin entry angle. The laser line acted as a reference for in-plane insertions. The needle has to be maintained in the axial plane during insertion.

6.6 Summary

Radiofrequency thermal ablation (RFA) is a minimally invasive approach for cancer treatment that uses the images for needle path planning and applies thermal energy at the needle tip to damage cancer cells. Deviated needle pathway, however, could result in ineffective treatment while posing risks of thermal injury to healthy surrounding organ tissues. Several research groups have made substantial progress in optimizing the needle trajectory.

In this study, a 3D-printed, portable, easy-to-mount, and smartphone-based MEMS tracker was developed to assist the operation of cancer ablation. The benchtop test showed the device has an RMS error of 0.64°. The in-vivo study on a swine model demonstrated that the mean tip-to-target distance error, measured as a minimum needle path to the target, was 5.2 mm, with a standard deviation of ± 1.3 mm. The mean tip-to-target angular error was 4.2°, with a standard deviation of ± 2.6 °. The average puncture time was 25.5 s. This study prove that this device could effectively assist accurate needle insertion.

CHAPTER 7

A LOW-COST, SMARTPHONE-BASED, AND MEMS IMU-ENABLED HANDHELD TRACKER FOR CT-GUIDED INTERVENTION[5]

[5] Li, R., Xu, S., Pritchard, W.F., Karanian, J.W., Krishnasamy, V.P., Wood, B.J., and Tse, Z.T.H. Accepted by *Annals of biomedical engineering*.

7.1 Abstract

As a low-cost needle navigation system, AngleNav may be used to improve the accuracy, speed, and ease of CT-guided needle punctures. The AngleNav hardware includes a wireless device with a microelectromechanical (MEMS) tracker that can be attached to any standard needle. The physician defines the target, desired needle path, and skin entry point on a CT slice image. The accuracy of AngleNav was first tested in a 3D-printed calibration platform in a benchtop setting. An abdominal phantom study was then performed in a CT scanner to validate the accuracy of the device's angular measurement. Finally, an in-vivo swine study was performed to guide the needle towards liver targets (n = 8). CT scans of the targets were used to quantify the angular errors and needle tip-to-targeting distance errors between the planned needle path and the final needle position. The MEMS tracker showed a mean angular error of 0.01° with a standard deviation (SD) of ± 0.62° in the benchtop setting. The abdominal phantom test showed a mean angular error of 0.87° with an SD of ± 1.19° and a mean tip-to-target distance error of 4.89 mm with an SD of ± 1.57 mm. The animal experiment resulted in a mean angular error of 6.6° with an SD of ± 1.9° and a mean tip-to-target distance error of 8.7 mm with an SD of ± 3.1 mm. These results demonstrated the feasibility of AngleNav for CT-guided interventional workflow. The angular and distance errors were reduced by 64.4 and 54.8%, respectively, if using AngleNav instead of freehand insertion, with a limited number of operators. AngleNav assisted the physicians in delivering accurate needle insertion during CT-guided intervention. The device could potentially reduce the learning curve for physicians to perform CT-guided needle targeting.

Keywords: CT-guided biopsy or ablation, MEMS sensor, Tracker, Angular tracking

7.2 Introduction

In conventional needle placement procedures, the physician manually orients the needle to match the needle's physical angle with the planned computed tomography (CT) insertion angle. Needle placement errors can lead to missing the tumor or injury to vital structures. Image guidance for needle placement procedures, therefore, is highly desirable for improving accuracy.

CT -guided needle placement is one of the most common techniques in interventional radiology. It is used for many procedures, including biopsy, drainage, and ablation [317-323]. One drawback of CT-guided therapies is ionizing radiation exposure [324, 325]. Cone Beam CT (CBCT) as an option on a fluoroscopy system is an alternative method for CT guided needle placement. CBCT integrated with needle guidance systems, and fluoroscopy allows the physician to see needle locations in real-time, relative to target locations, and surrounding organs [326, 327].

Needle guidance systems could improve needle puncture procedures by providing more accurate needle targeting [328-338], reducing needle deflection [339] and the number of total needle passes [328, 329, 331, 333, 334, 337, 340-343], decreasing radiation exposure [333, 334, 337, 340-343] and procedural time [329, 330, 334, 337, 340-342], reducing the number of needle repositionings [328, 329, 331, 333, 334, 337, 340-343], and thus decreasing procedural risks [334-336, 344]. Many commercially available needle guidance systems utilize electromagnetic tracking [345, 346], optical tracking[347], mechanical tracking [348, 349], and inertial measurement tracking. Commercially available systems include Philips PercuNav, NeoRad SimpliCT, amedo-LNS, and CAScination CAS-ONE[350-355]. However, needle guidance

systems have not been widely adopted because of cost, ergonomics, and increased procedure length and complexity.

The system proposed here has the goal to improve accuracy, speed, and ease of needle placement. It is a compact angular tracker based on microelectromechanical systems (MEMS) that provides angular needle guidance to the physician. This was then transferred to the smartphone application via Bluetooth connection for the display of the angular readings.

7.3 Materials and Methods

The handheld device was fabricated using the MEMS IMU sensor as well as a 3D-printed outer case. The device was designed to be compact, wireless-operated, and can be easily fit into the existing clinical workflow. In order to assess the functionality of the design, the device was firstly calibrated on a benchtop setup, then evaluated in the CT phantom and in-vivo study.

7.3.1 MEMS-based Measurement Unit and Software

The overview of the system design architecture is shown in **Figure 7-1**. The inertial measurement unit is attached to a needle guide, which is responsible for detecting and recording the orientation of the needle. The magnetometer helps to improve the accuracy of the angular measurement. The medical image provides the positional information of the needle. The digital data of the angular information (i.e., pitch, roll, and yaw) from the inertial measurement unit is transferred into the micro-controller, wherein the data is integrated and processed into the guidance information displayed on the software smartphone platform.

(a) Flowchart of a tracker-assisted needle insertion procedure

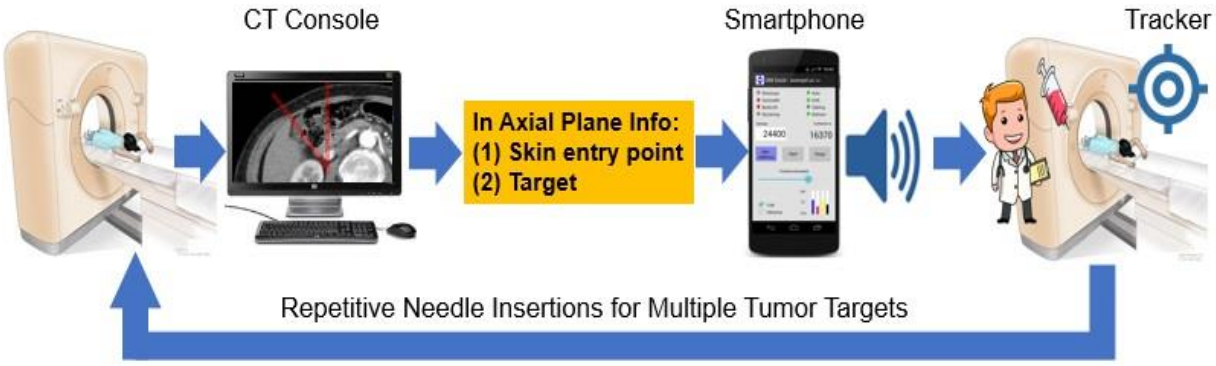

(b) A detailed description of the role and function of the tracker

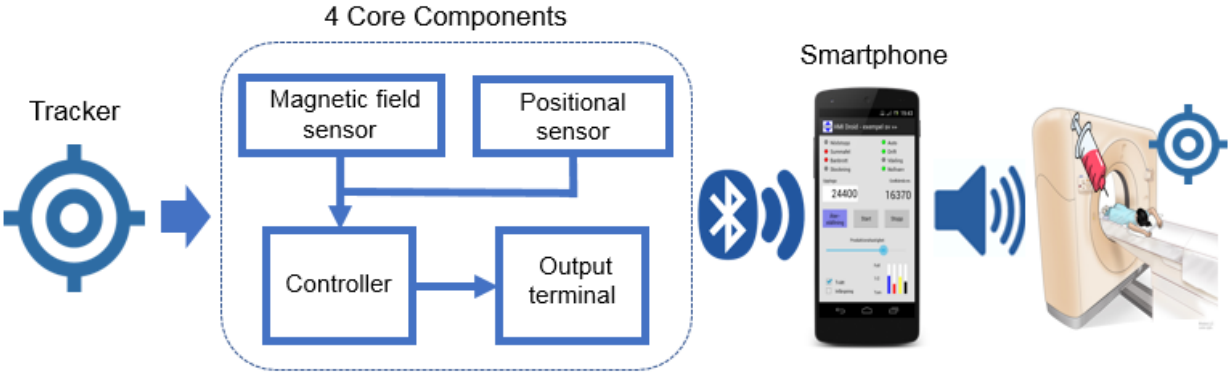

(c) Description of tacker and the needle channel

(1) Holding position (2) Needle channel (3) MEMS tracker

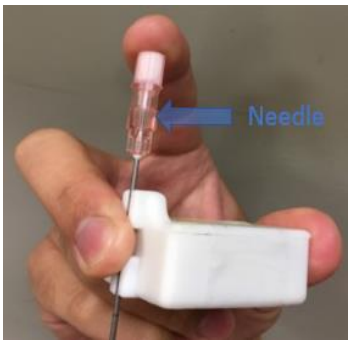

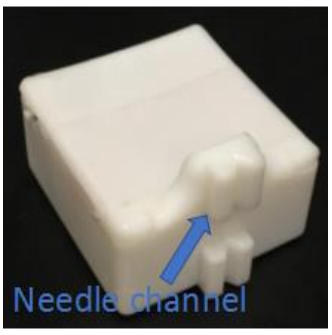

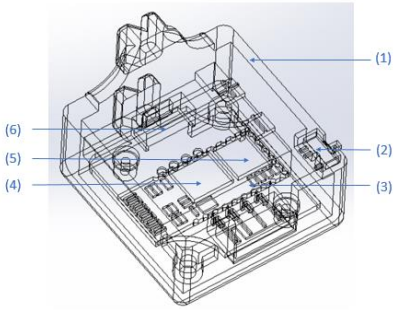

Figure 8-1: Overview of the system design architecture and tracker design, (c) showing its use (1) and the needle channel (2). The description of each part in (3) is shown in **Table 7-1**.

The tracker consists of a MEMS-based measurement unit, a microprocessor, and a Bluetooth communication module that wirelessly transmits tracking information to an external computer display (**Figure 7-1 (c)**). The MEMS-based measurement unit contains a gyroscope, a

magnetometer sensor, and an accelerometer to provide angular measurements on three axes. The microprocessor manages data fusion from different sensors, digital signal processing as well as communications between each part of the tracker. The tracker case was designed in Solidworks® (Dassault Systèmes, Vélizy-Villacoublay, France) and printed with a Form 2® 3D printer (Formlabs Inc, Somerville, MA). The case was designed with a needle channel that allows the needle to be aligned with the tracker. The rechargeable battery in the tracker provides four hours of continuous use of the tracker after one hour of charging. The tracker case was made to be disposable but can also be reusable with a sterilization cover bag.

Table 8-1: Specifications of hardware elements shown in **Figure 7-1**.

Part	Description	Specifications
(1) Tracker Case	Electronics & needle guide	37 mm (L) x 34 mm (W) x 19.7 mm (H)
(2) Switch	Microslide on/off	6.7 mm (L) ×2.9 mm (W) ×1.4 mm (H)
(3) MEMS unit	Measure angular, acceleration & magnetic info	30 mm(L) ×30 mm (W) ×1mm (H) Maximum range: Acceleration: ±16 g, Angular speed measurement: ±2000°/s, angular measurement: ±180° Accuracy of angular reading: 0.01°
(4) Bluetooth	Communicate to PC or smartphone	Effective range: 10 m
(5) Microprocessor	Digital signal processing	MPU6050, comprised of triple-axis MEMS gyroscope and triple-axis MEMS accelerometer and 9-Axis Motion Fusion by the on-chip Digital Motion Processor
(6) Battery	Lithium battery	4-hour continuous operation, 400 mAh

7.3.2 Benchtop Test

The purpose of the benchtop test is to calibrate the needle in a rigid and controlled environment. A 3D-printed evaluation platform comprised of a series of holes that point at the center cross, which is situated underneath the arch. The directions of the holes are organized so that the accuracy of the needle can be evaluated in two dimensions. The three-dimensional X-Y-Z Cartesian coordinate system is defined in **Figure 7-2(b)**. On the XZ plane, the holes are evenly distributed so that insertion angles are range from 0°to 180° (**Figure 7-2(a)**). On the XY plane, the holes are organized into four sets of rows; the first row is at 0° with respect to the XZ plane, and the other three are at 10°, 20°, and 30° to the XZ plane respectively.

A digital level was used to adjust the flatness of the platform before the calibration. If the platform is uneven, the four screws at each corner are used for leveling. During the evaluation process, the needle was held firmly with the tracker when going through a specific hole with a corresponding incline angle (e.g., 30°) until it hit the targeting cross. The positional information of the needle was then sent to a smartphone application to display the angular reading (e.g., 29.9°). The reading was then compared to the actual inclined angle of the needle, and the accuracy of the tracker was evaluated. The typical range for acceptable accuracy is ±1°. If the performance of the tracker is outside this range, the software has a function to calibrate the tracker to an acceptable level of accuracy. For the benchtop test, 200 insertions were performed in the 3D-printed evaluation platform. Two statistical analyses were carried out to investigate the angular accuracy of the needle insertions.

(a) Side view of the evaluation platform	(b) Top view of the evaluation platform	(c) Actual review of the evaluation platform

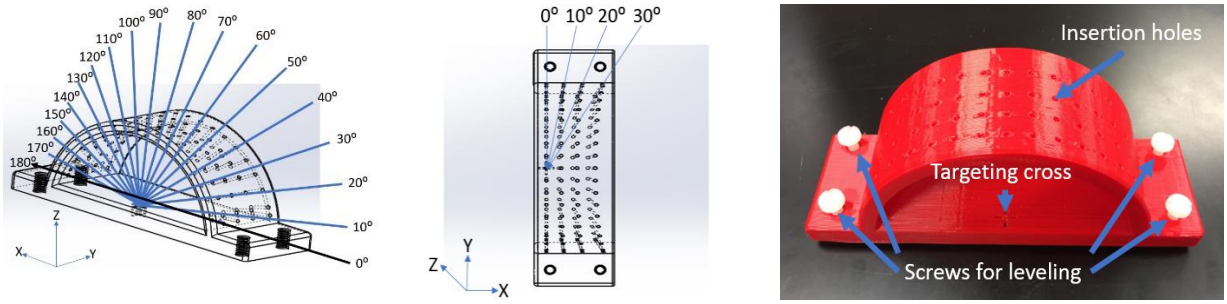

Figure 8-2: 3D printed station for calibration of the tracker reading.

7.3.3 Potential Clinical Workflow (**Figure 7-3**)

Step 1 Pre-scan preparation: The target area on the patient is sterilized. A CT-compatible, radio-opaque grid sheet is placed on the sterilized area to be used to define the skin entry point (**Figure 7-3 (a)**).

Step 2 Planning scan acquisition: Needle path planning by target and skin entry point identification.

Step 3 Needle insertion: The physician first places the needle tip on the skin entry point (based on the grid position in the CT scan). The needle is then pivoted to the planned angle using the gyroscope device and is inserted into the patient with adjustments as needed, to maintain the intended angle (via audible and visual feedback).

Step 4 Real-time needle tracking: In standard CT-guided procedures, intermediate CT evaluation is required to confirm the needle's position relative to the target. This is essential for the physician to adjust the angle of insertion accordingly, when the target moves, such as under natural respiration. The smartphone application displays the needle angular information and provides audio feedback, allowing the physician to follow both visual and auditory guidance in the procedure. Compared with the standard method, the MEMS tracker can provide real-time

measurement of the needle's orientation, which may greatly shorten procedure time and increase insertion accuracy.

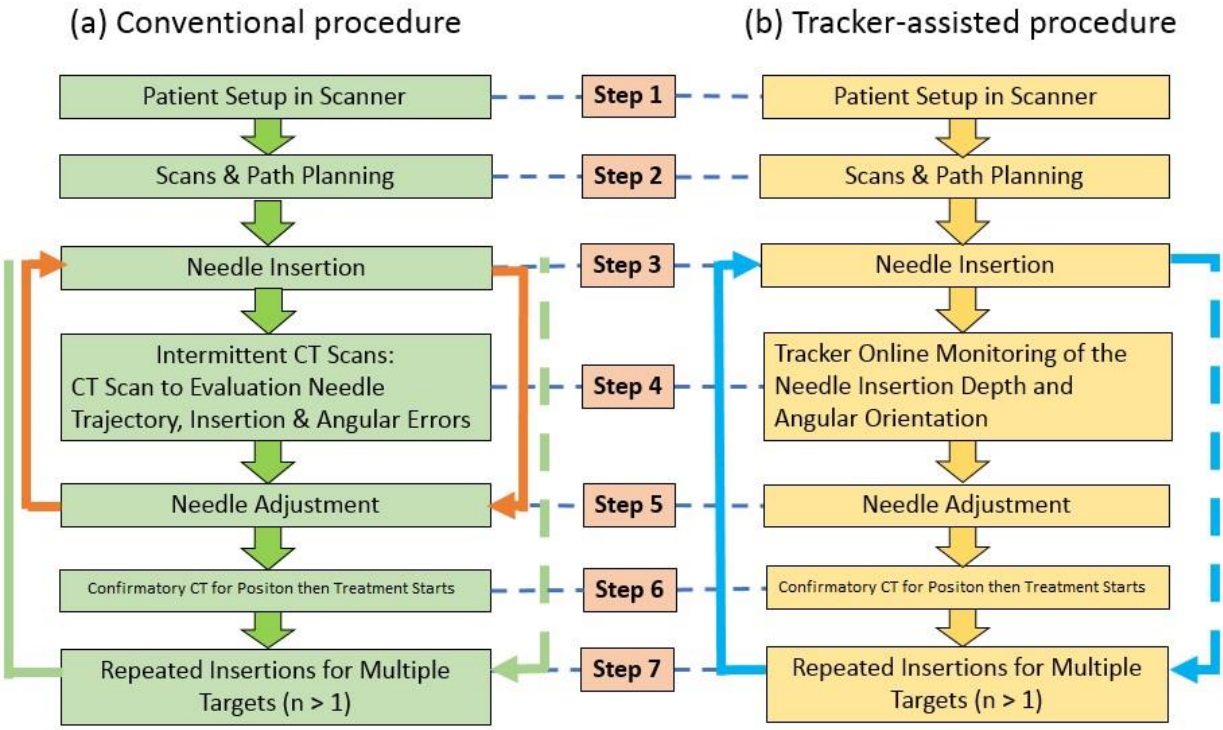

Figure 8-3: Comparison between conventional and tracker-assisted CT-guided clinical workflow. (a) shows the conventional procedure. More intermittent CT scans (steps 3–5, as shown in the orange arrows) are likely required in this workflow, lengthening the procedure. Treatments that require multiple needle insertions for multiple targets repeat steps 3–7 (green arrows). (b) Tracker-assistance shows the alternative method for step 4, in which online monitoring of needle position provides instant feedback, potentially reducing the number of confirmatory CT scans for positioning and improving the efficiency of CT in guiding needle placement.

Step 5: Needle advancement. Step 4 and Step 5 were repeated until the needle tip was reasonably close to the target. While intermediate and final CT scans are to confirm the position, the frequency of intermediate scans during needle insertion may be reduced.

Step 6: Biopsy and/or ablation.

Step 7: Repeated insertions for multiple targets. Steps 3–7 are repeated for more than one specific target.

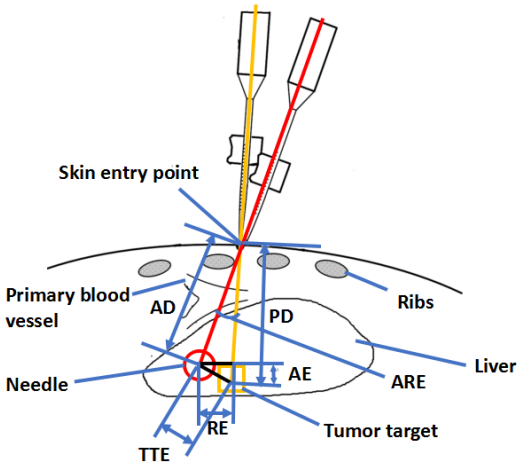

Table 8-2: Definitions of symbols

PD: planned insertion depth

AD: actual insertion depth

AE: axial insertion distance error

RE: radial insertion distance error

TTE: tip-to-target insertion distance error

ARE: angular insertion error

Figure 8-4: Interpretation of the CT image. The yellow line shows the planned pathway, and the red line shows the actual insertion pathway. The blue lines indicate each parameter.

In the results section, all the CT images are analyzed and interpreted as the way shown in **Figure 7-4**. Moreover, **Table 7-2** shows the definition of symbols for the results and discussion section. The yellow line indicates the planned insertion pathway, and the red line indicates the actual insertion pathway.

Needle advancement is an iterative process and requires a high level of physician operating skills. Step 4 is a time-consuming process because the physicians need to confirm the real-time needle location. The MEMS tracker with software navigation may shorten the operation time by giving physicians simultaneous and continuous feedback of the relative angle during insertion from the skin to the target. The MEMS tracker may reduce human errors in needle orientation and the number of needle path corrections, especially in procedures that require multiple ablations at

different locations. Finally, this method may reduce the number of unnecessary needle re-insertions by providing accurate needle targeting.

7.3.4 CT Abdominal Phantom

After the tracker passed the benchtop accuracy evaluation, the accuracy and functionality were further evaluated using an abdominal phantom (CRIS Triple Modality 3D Abdominal Phantom Model 057A) in a CT scanner (MX8000 IDT 16-Detector CT, Philips, Cleveland, OH) (**Figure 7-5 (a)**).

(a) Phantom in the CT scanner

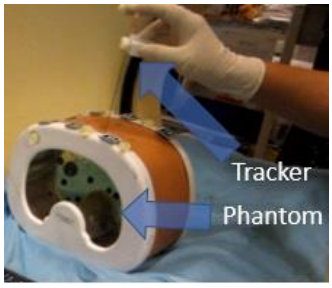

(b) CT image of insertion

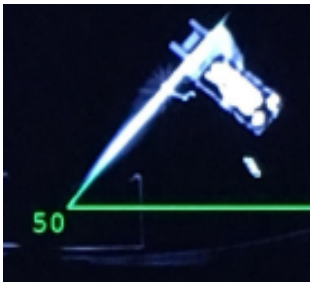

(c) Angular reading

(d) Needle alignment with the laser

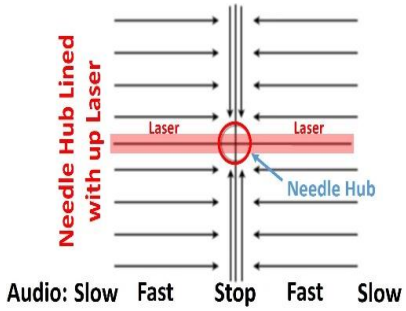

(e) Needle insertion on a template

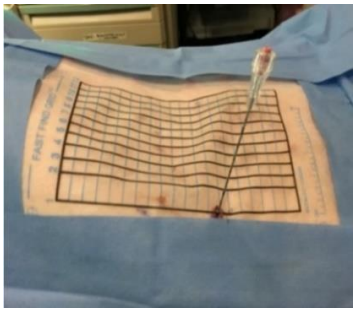

Figure 8-5: Comparison of the angular measurement (a) using the phantom, (b) In-axial plane angle measured by CT compared to (c) the smartphone application's reading. In (c), the smartphone displays: (1) X, Y, Z as angles of rotation about the roll, pitch and yaw, (2) Time function enables the creation of a needle time log/event, (3) Acceleration of the angular movement, (4) Velocity of the angular movement, (5) Output function logs out the file and data can be transferable to a computer. The schematic diagram of beeping vs. angle deviation is shown in (d), and needle alignment and insertion are shown in (e).

The CT phantom was made of silicone, and the needle can be easily inserted and held firmly. In one test, the smartphone application showed an angular reading of 50.03°, while the CT image shows the needle was positioned at 50.00° (**Figure 7-5 (b)**). The difference between these two values was hardly measure-able (~0.03°), and likely within the error of measurements. In total, there were 25 insertions performed.

7.3.5 In-vivo Study

All procedures were performed under a protocol approved by the Institutional Animal Care and Use Committee using one healthy castrated male Yorkshire domestic swine (54kg). The animal was sedated with intramuscular ketamine (25mg/kg), midazolam (0.5mg/kg), and glycopyrrolate (0.01mg/kg); anesthetized with propofol (1mg/kg IV) and then intubated and maintained under general anesthesia with isoflurane throughout the procedure. Multiple 1.5mm stainless steel balls were inserted through a needle under ultrasound imaging guidance to serve as targets. With the animal on the CT scanner table, a radiopaque grid was placed on the skin of the upper abdomen over the liver to guide skin entry point selection (**Figure 7-5 (e)**). After insertion planning, the laser line acted as a reference for in-plane insertions. The needle was maintained in the axial plane during insertion. An 18-gauge needle was used by physicians to perform the insertions, with or without tracking assistance. CT scans were obtained after each insertion for measurement of accuracy. Following the completion of the study, the animal was euthanized.

7.4 Results

There are three different tests to validate the accuracy of the handheld tracker: benchtop test, phantom test, and in-vivo study

7.4.1 Benchtop Test

A scatterplot shows the slope coefficient between the measured angle and the actual angle to be 1.0053 and R^2 as 0.9999. This defines a strong linear relationship between these two quantities. Furthermore, the Bland-Altman plot (**Figure 7-6 (a)**) shows the mean targeting accuracy of 0.01° with a maximum absolute error of 1.35° and an SD of 0.62°.

(a)Benchtop test

(1) Scatter plot

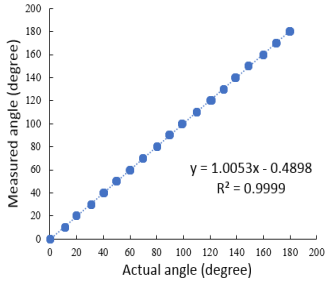

(2) Bland-Altman plot

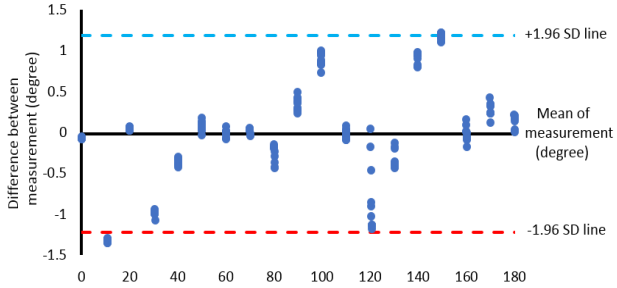

(b) Abdominal phantom study

(3) Scatter plot

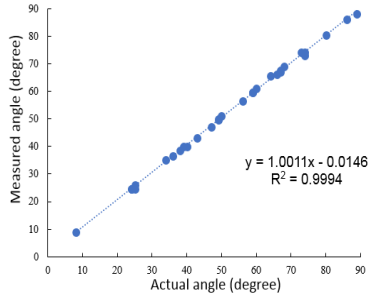

(4) Bland-Altman plot

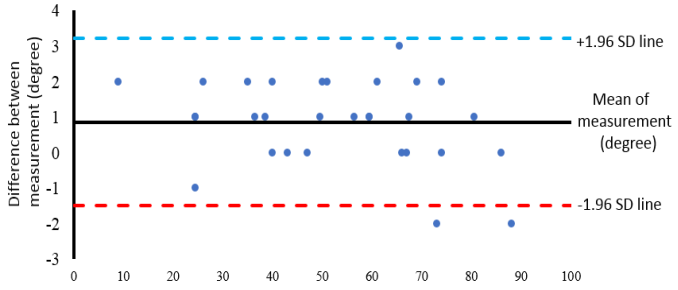

Figure 8-6: Statistical analysis between the measured angle and actual angle. (a) shows the data analysis on the benchtop test, (b) shows the data analysis on the abdominal phantom study.

7.4.2 CT Abdominal Phantom Study

Figure 7-6 (b) shows the statistical analysis of all 25 insertions. A scatterplot shows the slope coefficient between the actual angle and measured angle to be 1.0011 and R^2 as 0.9994.

This means there is a strong linear relationship between these two quantities. Furthermore, the Bland-Altman plot shows the mean angular accuracy of 0.86° with a maximum absolute error of 2° and SD of ±1.20°. Based on the analysis of the CT images (**Figure 7-7 (I)**), the mean tip-to-target distance error is 4.89 mm, with an SD of ±1.57 mm. **Figure 7-7 (I)** shows three insertion examples. The tip-to-target insertion distance errors (TTE) for three insertions are 8.6, 2.2, and 3.1 mm, respectively. The angular insertion errors (ARE) for each of the three insertions are 1.9°, 1.1°, and 1.1°, respectively. Taking the first insertion as an example, quantitative analysis shows the ARE is 1.9°, the planned insertion depth (PD) is 95.2 mm, and the actual insertion depth (AD) is 90.0 mm. The tip-to-target distance error is 8.6 mm.

7.4.3 In-vivo Study

At first, the physician followed traditional freehand cognitive guidance, and conducted insertions on four targets inside the liver, as a single pass. Second, the physician followed the tracker-assisted clinical workflow and conducted insertions on eight targets inside the liver.

Overall, a mean angular error of 6.6° (SD = ± 1.9°) and a mean tip-to-target distance error of 8.7 mm (SD = ± 3.1 mm) were achieved for in-plane insertion in 8 liver targets by tracker-assisted insertions (**Figure 7-7 (II)**). In comparison, a mean angular error of 18.6° (SD = ± 11.0°) and a mean tip-to-target distance error of 19.3 mm (SD = ± 8.0 mm) was achieved in 4 liver targets by the radiologist's freehand cognitive guidance (**Figure 7-7 (III)**).

I. CT images of the phantom study

(a) Insertion #1-approaching target

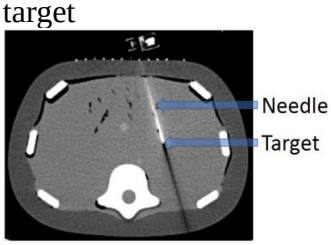

(b) Insertion #2-approaching target

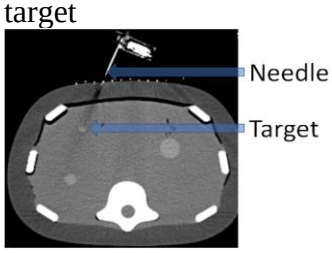

(c) Insertion #3-approaching target

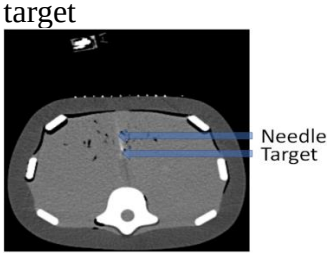

(d) Insertion #1-needle advances towards target

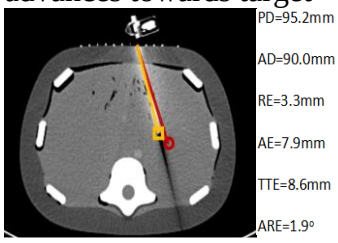

(e) Insertion #2- needle advances towards target

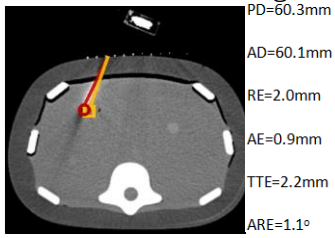

(f) Insertion #3- needle advances towards target

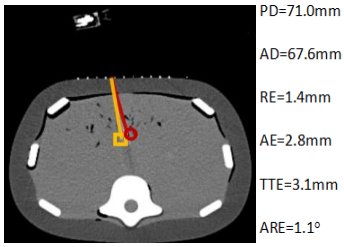

II. Tracker-assisted needle insertion

(h) Insertion #1:

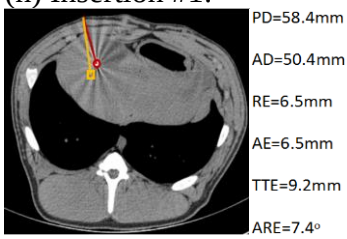

(i) Insertion #2:

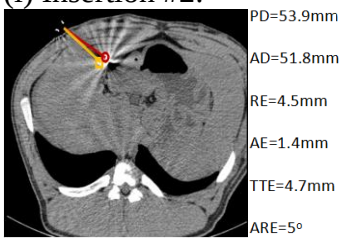

(j) Insertion #3:

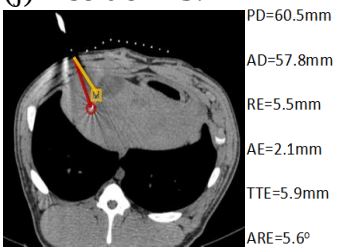

III. Cognitive guided freehand needle insertion

(k) Insertion #1:

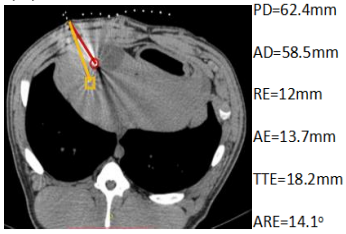

(l) Insertion #2:

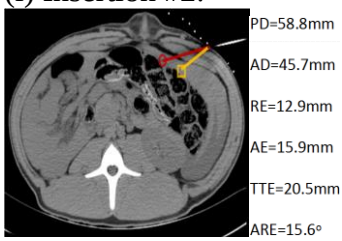

(m) Insertion #3:

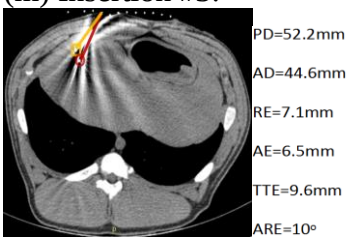

Figure 8-7: (I) shows three examples of needle insertions performed in the phantom: (a), (b), and (c) show relative positions of needles with respect to the target; (d), (e), and (f) are the quantitative analysis of needle trajectories. (II) and (III) shows the results from the tracker-assisted and cognitive guided freehand needle insertion, respectively. The yellow lines show the planned needle trajectory, and the red lines show the actual insertion pathway. The yellow squares show the position of the target, and the red circles show the position of the needle tip.

On the right-hand side of each image, the six parameters are displayed: PD, AD, RE, AE, TTE, and ARE.

The mean angular insertion error (ARE) and tip-to-target distance insertion error (TTE) were reduced by 64.4% and 54.8% during CT-guided needle procedures (**Table 7-3**).

Table 8-3: Statistical analysis between two insertion methods

Angular Error (degree)			
Insertion methods	Mean ARE (degree)	Maximum ARE (degree)	The standard deviation of ARE
MEMS tracker (a)	6.6	9.4	1.9
Free hand cognitive guidance (b)	18.6	34.8	11.0
Improvement (1-a/b) (%)	64.4	73.0	83.2
Tip-to-Target Distance Error (mm)			
Insertion methods	Mean TTE (mm)	Maximum TTE (mm)	The standard deviation of TTE
MEMS tracker (a)	8.7	14.4	3.1
Free hand cognitive guidance (b)	19.3	29.0	8.0
Improvement (1- a/b) (%)	54.8	50.3	61.2

Figure 7-8 (a) shows all eight tracker-assisted insertions. In (a), (1) shows the average planned insertion distance (PD) is 67.3 mm, which is only 1.5mm longer than the actual insertion distance (AD). (3) and (4) shows the tip-to-target insertion distance error (TTE), as well as the angular insertion error (ARE), varies in a range that is consistent with the numbers in **Table 7-3**.

7.5 Discussion

The CT abdominal phantom experiment showed a mean angular error of 0.87° (SD = ± 1.19°) while the in vivo experiment showed a mean angular error of 6.60° (SD = ± 1.9°). The errors could be attributed to the tissue deformation, respiration motion, and human deployment error.

a. Error analysis of tracker-assisted insertions in the in vivo study

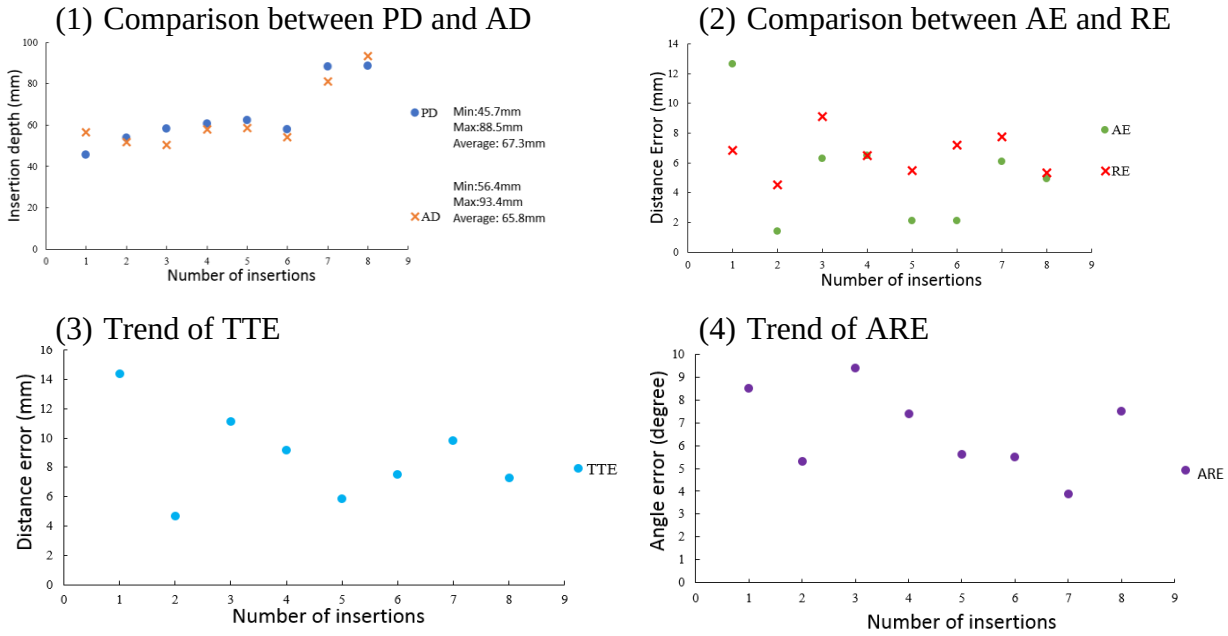

b. Comparison between the tracker-assisted and freehand procedures

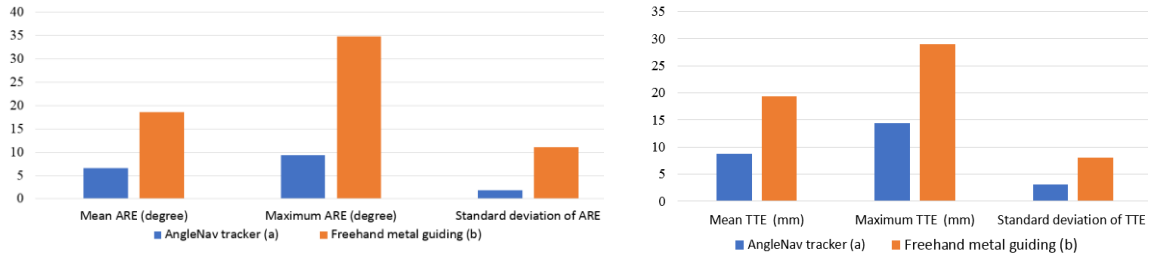

Figure 8-8: In (a), (1) shows the comparison between the PD and AD; (2) shows the comparison between the AE and RE; (3–4) show the trends of TTE and ARE. (b) shows the comparison of ARE and TTE between the tracker-assisted and freehand procedures.

However, tissue could be deformed during insertions in both phantom study and in-vivo study. After the needle was released, tissue resistance often changed the angle of the needle, resulting in much larger errors in validation CT scans. In addition, the respiration motion of the swine could cause difficulty in reaching the target. Also, with audible feedback, more attention may have been paid to keeping the needle steadily in the same plane, which might over-emphasize the improvement seen. In the animal experiment, insertions showed a mean angular error of 6.60° (SD = ± 1.9°) compared to a mean angular error of 18.6° (SD = ± 11.0°) by the radiologist's freehand insertions.

7.5.1 Comparison With Other Navigation Systems Designed for CT-Guided Interventions

In the field of CT-guided interventions, a variety of methods have been applied to improve the accuracy of the conventional freehand needle insertion. Some research has been conducted with robotic systems—for example, Mbalisike et al. proposed a novel robotic guidance system for microwave thermoablation.[356]. The study claimed that the smallest tip deviation from the target tumor was 5.3 mm. Meanwhile, the tip-to-target errors shown by other groups such as Dou et al.[357] (1.5 ± 1.7 mm), Kettenbach et al.[358] (2.3 ± 0.8 mm), and Martinez et al.[359] (1.8±1.1 mm) are smaller than our current system. However, the downside of these robotic systems is cost, complexity, workflow, and the need for repetitive needle adjustments. Moreover, these robotic systems require a lengthy registration process as well as extensive operator and staff training.

Leschka et al.[360] reported that a Cone Beam CT (CBCT)-guided procedure achieved a mean tip-to-target distance error of 2.8 mm. Another study conducted by Schulz et al.[361] had a tip-to-target error, which was less than 4.5 mm. The accuracy of those studies is comparable to our

results. However, the CBCT-guided procedure reported by Schulz et al. can only accommodate a maximum needle diameter of 15G while the presented device has no limitation on the needle size.

Some other groups have shown that a laser guidance system can be an alternative solution to improve accuracy[362]. Until now, such laser-based systems do not have complete navigation abilities such as real-time tracking of the needle movement. Moreover, these systems require patients to remain still during trajectory planning and needle placement.

Optical tracking is commonly used in surgery with high accuracy[363, 364]—a device reported by Hassfeld et al. achieved a tip-to-target distance error was less than 2mm[347]. However, the main constraint for optical systems is (1) the requirement of the line of sight between the cameras and the tracking markers mounted on the instrument, and (2) its compatibility with different needle instruments.

Electromagnetic tracking is another popular modality that can be used in biopsy and ablation procedures. In one study by Penzkofer et al.[365], 23 patients underwent image-guided interventions using EM-tracking technology with an accuracy of 3.1 ± 2.1 mm. However, the performance of electromagnetic tracking is affected by the presence of metal or other magnetic objects. EM tracking also has a limited workspace.

Finally, some navigation systems embrace the idea of fusion between several imaging modalities such as CT and ultrasound. The complex registration required for this is the main hurdle for the wide application of such systems. Registration between the pre-operative images and navigation system is often based on fiducial markers, so the whole procedure is time-consuming and may be longer than the conventional freehand intervention. Even experienced physicians must invest significant training and practice time [366].

7.6 Summary

Overall, a mean angular error of 6.6° (SD = ± 1.9°) and a mean tip-to-target distance error of 8.7 mm (SD = ± 3.1 mm) were achieved for in-plane insertion in 8 liver targets in a live swine by tracker-assisted insertions. The accuracy of angular insertion was improved by approximately 64.4%, and the accuracy of tip-to-target insertion distance was improved by 54.8%, compared to freehand cognitive guidance. The tracker-assisted CT-guided procedure provided real-time needle tracking and hence may reduce the number of intermediate scans for needle path confirmations.

CHAPTER 8

A HUMAN STUDY OF LOW-COST, SMARTPHONE-BASED AND MEMS IMU-ENABLED BODY TRACKER[6]

[6] Li, R., Jumet, B., Ren, H.L., Song, W.Z., and Tse, Z.T.H. Accepted by *Proceedings of the IMechE, Part H: Journal of Engineering in Medicine*.

Reprinted here with permission of publisher.

8.1 Abstract

The recent advancement of motion-tracking technology offers better treatment tools for conditions such as movement disorders as the outcome of the rehabilitation could be quantitatively defined. The accurate and fast angular information output of the inertial measurement unit (IMU) tracking systems enables the collection of accurate kinematic data for clinical assessment. This paper presents a study of a low-cost micro-electro-mechanical system (MEMS) IMU-based tracking system in comparison with the conventional optical tracking system (OTS). The system consists of seven MEMS IMUs, which could be mounted on the lower limbs of the subjects. For the feasibility test, ten human participants were instructed to perform three different motions: walking, running, and fencing lunging when wearing specially designed sleeves. The subjects' lower body movements were tracked using our IMU-based system and compared with the gold standard—the NDI Polaris Vega optical tracking system® (NDI). The results of the angular comparison between IMU and NDI were as follows: the average cross-correlation value was 0.85, the mean difference of joint angles was 2.00°, and the standard deviation of joint angles was ± 2.65°. The developed MEMS-based tracking system provides an alternative low-cost solution to track joint movement. Moreover, it is able to operate on an Android platform and could potentially be used to assist outdoor or home-based rehabilitation.

Keywords: Body movement, Wireless sensors, Optical tracking, Joint angles

8.2 Introduction

Movement disorders are characterized as either impaired voluntary movement or the presence of involuntary movement. Typical movement disorders are Friedreich's Ataxia [130],

Dystonia [367], Huntington's disease [132], cerebral palsy and Parkinson's disease[133, 134]. Parkinson's disease, for example, affects up to 1 million people in the US, and there are 60,000 new cases diagnosed annually [368].

Rehabilitation of movement disorders usually consists of activity-dependent and goal-directed training, where patients repeatedly move their limbs to produce functional patterns. In many cases, the patient may be incapable of completing these movements unassisted, particularly in the early stage of recovery after injury. Therapists support and move the limbs during these exercises, and regularly adjust the amount of assistance according to the needs of the patient. In recent years, robotics rehabilitation devices have been proposed as a means to complement therapists' activities [148-151]. Alternatively, in this paper, a smartphone-based microelectromechanical systems (MEMS) tracking device was developed, which is easy-to-operate and easy-to-follow and specifically designed to facilitate a better recovery procedure. This device may not only improve conventional therapy, but it may also allow the patients to carry out more challenging and effective outdoor recovery exercises. Furthermore, the device may improve the training of older or younger individuals, such as children, because it is operational in both the home and outdoors. The future plan is to further develop the device and use it for interactive training in populations with medical conditions.

Motion tracking has received extensive attention since the 1990s [369-372]. Several techniques allow for motion reconstruction based on different information sources. As one of its primary applications, motion tracking has been used for monitoring rehabilitation progress of movement disorders [373]. Movement disorders refer to a group of conditions that are related to the nervous system and cause unusual body movements. Common movement disorders include

Huntington's disease [374] and Parkinson's disease [375, 376]. As an example, Parkinson's disease is a chronic neurodegenerative disorder that has affected 1 million people in the US and 5 million people worldwide [377]. There is a specific type of rehabilitation, called neurorehabilitation, aimed at treating conditions such as movement disorders, where patients repetitively move their limbs so that functional patterns can be produced. The motion tracking could provide feedback to the patients as well as the therapist in real-time.

One of the biggest challenges in motion tracking is to obtain an accurate estimation with non-invasive sensors within a confined workspace. A mainstream solution is to use the optical tracking system (OTS). The NDI Polaris Vega® system, for example, delivers a tracking accuracy of 0.12 mm Root Mean Square (RMS) and a 95% confidence interval accuracy to 0.2 mm at a measurement rate of 60–250 Hz. The main disadvantage of the OTS is the requirement for a clear line-of-sight between the patient, the instrument trackers, and the optical cameras.

Recently, a type of inertial measurement unit (IMU) called micro-electro-mechanical systems (MEMS) IMUs has given a new surge to motion tracking research [137-140]. These systems are cost-effective for providing accurate, non-invasive, and portable motion measurements. The primary point of interest in these systems is that they can overcome the limitations of optical systems and mechanical trackers. In one of the early studies, Ren et al. used raw data from a class of miniaturized IMU—integrated system of the magnetic field, angular rate, and gravity (MARG) to estimate the orientation of a surgical instrument, this again demonstrated the IMU's ability to track movement [378].

Much research work has been published based on motion tracking using different types of IMUs, such as Xsens [379], Opal [380], and Noraxon [381]. In the area of joint movement,

Kobashi presented a method to measure knee joint angle using MARG; however, the sensor is not cost-effective[382] for the users. Müller et al. have developed a model to measure elbow angles, which introduced a concept of self-calibration [146]. Mundt et al. published a comprehensive assessment of using both IMUs and optoelectronic systems for 3D joint angles measurement [383]. However, the tasks were limited, e.g., walking and stair-step exercises. The system developed in this paper was different from existing ones as it could operate in an Android smartphone environment, as explained in the author's previous publication [384]. The smartphone application provides real-time movement tracking so that the users can carry out repetitive and straightforward rehabilitation exercises in a home or outdoor environment. Further, the kinematic data collected by the application could be upload and shared with the physical therapists for future treatment planning.

In this study, the tracking accuracy of our MEMS IMU-based tracking system was quantitatively assessed, and the results were compared with the NDI Polaris Vega® system (NDI, Ontario, Canada) for three different, typical OTS tasks: walking, running and fencing lunges. The NDI was used because it is highly accurate and easy to set up. One limitation of the study is that only 2D body movements were studied. This is because our focus was on the angular variations of the hip, knee, and ankle only within the sagittal plane. Therefore, we believe that 2D kinematic analysis is sufficient in this study. However, in the future, a 3D kinematic analysis may be carried out as it could help to reveal more movement details.

Table 8-1 highlights the differences between our system and the existing ones. First, the system offers a low-cost solution compared to the existing systems. Second, the MEMS IMU system can output acceleration reading in real-time since a built-in accelerometer was included.

In contrast, the systems like the OTS can only calculate acceleration based on the trajectories of reflective markers. With the acceleration information, the users would benefit from knowing how fast they can perform an exercise. Moreover, the MEMS IMU system was wireless and wearable by the test subject, providing a high degree of flexibility required for exercise, whereas the OTS has field-of-view and line-of-sight problems. When using the OTS, tracking errors or phantom points are generated when the reflective markers are blocked or not positioned correctly.

However, some limitations of MEMS IMU systems are that the IMU can suffer from drift due to instrumentation biases, and more affordable IMUs are prone to noisy data and a lack of precision relative to other tracking systems.

Table 9-1: Comparison of functionality between our system and existing ones

	Robotics system	VR rehabilitation	OTS system	Our system
Low-cost solution?	No, price range: $18,000-40,000[385, 386]	No, price range: $1,400—2,000[387, 388]	No, price range (passive system): $150,000—250,000[389]	Yes, the IMU modules cost $280, 3D printing material $10, Flexible bands $20. The total cost is $ 310.
Easy-to-use?	No	Yes	No	Yes
Outdoor use?	No	No	No	Yes
Exercise range limitation?	No	Yes, near a station (desktop, laptop)[390]	Yes, within the coverage area of the camera system, NDI tracking range: 2400 mm[391]	No
Portable?	No	No	No	Yes
Data logging?	Yes	Yes	Yes	Yes
Data Sharing?	No	No	No	Yes
Acceleration info?	No	No	No	Yes

8.3 Materials and Methods

The purpose of this study was to develop a new MEMS IMU-based angular tracking system that could be integrated with an Android platform to monitor human movement. Three main design criteria were addressed in this study. The first criterion was the orientation of the IMU. Since the IMUs commonly have a drift problem on the yaw angles, the orientation of the IMU was set to be vertical. Therefore, the reading of yaw angles from the Z-axis did not need to be used as the experiment consisted of two-dimensional motion analysis. The pitch and roll angles were calibrated with the gravity vector, and therefore drifting was not an issue. The second criterion was the mounting method and the positioning of the IMU. During the jogging and fencing lunge exercises, the IMU module could be easily detached from the body. The solution was to use a stretchable waist, thigh, and foot sleeves with the IMU sensors sewn on the surface. With this design, not only could the sensors be mounted more securely and adequately on the designated position, but less time was required for test preparation.

Additionally, the sleeves were more comfortable and were able to fit many different body types with no adjustment. This proper fitting also disallowed significant relative movement of the components during and in between exercises. The final criterion was the derivation of joint angles from the IMU data. As mentioned for the NDI, the pivot point was defined as the intersection between two straight lines projected from the two longitudinal markers on each sleeve, and each straight line was defined by the physical position of the IMU sensors as the markers were placed equidistant from the IMU. By positioning the IMU in the middle of the two markers, this allowed for the NDI and IMU local coordinate systems of each limb segment to have similar origins to facilitate data analysis after the experiment better.

8.3.1 Tracking Device

The system was designed to track lower limb posture with seven mountable IMU sensors. Each sensor outputs the movement angle of different parts of the leg. A therapist may evaluate the performance of the patient based on the recorded angular data. The specifications of the tracking system are shown in **Table 8-2**.

Table 9-2: Head-to-head comparison between the IMU and NDI optical tracking system		
	Specification of the IMU system	NDI Polaris Vega
Dimensions	For individual sensors: 37 mm (L) × 34 mm (W) × 19.7 mm (H)	591 mm (L) × 103 mm (W) × 106 mm (H)
Components	Switch 12 mm (L) × 2.9 mm (W) × 1.4 mm (H)	Near-infrared (IR) light
	Acceleration: ±16 g Angular speed measurement: ±2000°/s Angular measurement: ±180° Accuracy of angular reading: 0.01° Sampling rate: 50 Hz	IR sensor, sampling rate: 60 Hz
	Communicate to smartphone Valid range: 10 m	Reflective markers

Figure 8-1 (a) shows the tracking system, which consists three different parts, the waist wear, the knee wear and the foot wear. **Figure 8-1 (b)** shows the mounting locations of the sensors.

(a) Tracking system (b) Mounting instruction

Figure 9-1: (a) shows the overview of the tracking system with reflective markers, and (b) suggested mounting locations on the hip, knees, and ankles of end-users. The IMU modules were placed on the outer surface of the hip, knees, and ankles.

Figure 8-2 (a) shows the IMU sensor's internal components: a gyroscope, an accelerometer, a microprocessor, a battery, a Bluetooth module, and a switch. All the components were placed in a 3D-printed case. **Figure 8-2 (b)** shows the coordinate system of the MEMS IMU sensor. **Figure 8-2 (c)** shows the experimental set up for human trials. The blue lines on the floor is the exercise distance, and the MEMS IMU sensor was mounted on human participants. The NDI optical tracking system was placed at a detectable range to the participants.

(a) The inner structure (b) The coordinate system (c) Experimental setup

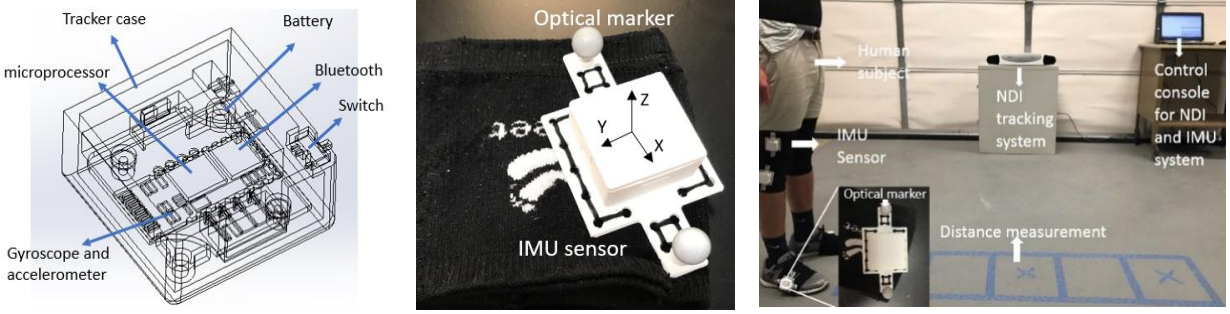

Figure 9-2: (a) shows the interior structure of the IMU sensor, which has a gyroscope, an accelerometer, a microprocessor, a battery, a Bluetooth module, and a switch. All the components were placed in a 3D-printed case, (b) shows the coordinate system of the IMU sensor, (c) shows the experimental set up for human trials. The blue lines on the floor are the measuring distance, and the IMU sensor was mounted on human participants using flexible bands. The NDI equipment was set on the table at a detectable distance to the participants. The control console was placed nearby for data recording.

8.3.2 Android System Application Design

The smartphone application was developed in the App inventor® (MIT, Cambridge, MA), which can provide real-time angle tracking when the sensor is in connection with the smartphone via Bluetooth. Moreover, the application is able to process the angular data and then translate into physical positional data, which can be displayed on the smartphone screen (**Figure 8-3**).

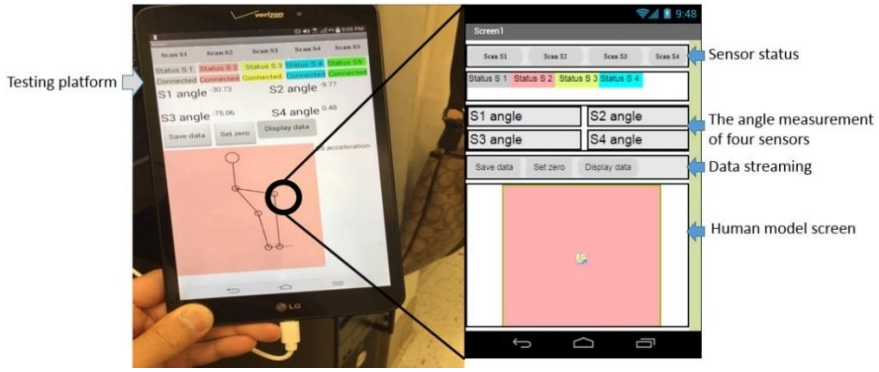

Figure 9-3: Smartphone interface

8.3.3 Application of NDI System

The experiment was set at a distance of 1.5 m from the NDI, and the walking distance was set at 2 m in order for markers to remain in the detectable range. NDI claims to have a volumetric accuracy of 0.12 mm RMS. However, three main challenges when using the NDI are the blockage of optical markers during exercise, the alignment between the optical markers, and the positioning of optical markers relating to the IMU sensors and tracking range of NDI. Additionally, the position of the NDI optical markers and IMU sensors for each wearable sleeve had to be on the same plane and centerline so that there would be the same pivot point for the calculation of angles. The calculations use a two-line angle determination as opposed to a three-vertex angle determination (**Figure 8-4**). Each limb segment had a sleeve where the IMU was sewn into place following the longitudinal axis of the pertinent segment. Two NDI markers were placed around each IMU, one superior and one inferior to the IMU along the same longitudinal axis (**Figure 8-2 (b)**). The two markers would then be able to be two points on a line that imitated the segment's position and motion. This line could then be analyzed relative to other limb segment lines for determining the angle between two segments and, thus, the joint angle. This allowed us to disregard the interpreted position of the joint determined by the NDI that would have resulted from placing one marker per segment with a median marker placed on each joint. This was preferred because joints are complex anatomical objects that do not move as consistently as limb segments due to the internal structure, causing the outer skin to move and stretch in all directions, which would make joint angle calculations less accurate.

Furthermore, the two-line determination allows for consistent data collection and interpretation across both data sets since IMUs also use a two-line determination. The body movement for a full exercise cycle was studied to ensure the kinematic equations were generalized and could be applied to different scenarios (walking, jogging, and fencing lunges). The movement cycle of a fencing lunge has five significant steps: (1) on-guard position; (2) lifting of the lead leg; (3) forward flying phase of the lead leg and push-off with the trail leg; (4) landing of the lead foot; and (5) final lunge position.

8.3.4 Overview of Kinematics Analysis

The kinematic analysis has two separate parts. The first part is to analyze and derive one set of equations describing the joint angles using the positional markers (NDI). The second part is to derive another set of equations describing the joint angles using the orientation of the IMU sensors. **Table 8-3** shows all the symbols used for kinematic analysis. For angle θ'_{ny} and θ'_{nx}, the measurements were taken directly from the gyroscope module inside the IMU and displayed on the user interface of the PC software.

Table 9-3: Variable definitions for kinematic equations

Variable	Definition
$\theta_h, \theta_k, \theta_a$	Hip, knee, and ankle joint angle for NDI
θ_n	Segment angles for NDI
x_n, y_n	X & Y coordinates from the NDI system for positional markers
$\theta'_h, \theta'_k, \theta'_a$	Hip, knee, and ankle joint angle for IMU
θ'_n	Segment angles for IMU

$\theta'_{ny}, \theta'_{nx}$	Angular readings of pitch and roll from IMU

8.3.5 Kinematics Analysis for NDI System

Figure 8-4 shows the detailed kinematics analysis for the NDI system; the optical markers have been placed on the waist, thigh, and leg sections of the human body. Three segments were used to construct the model: waist, knee, and ankle (**Figure 8-4 (b)—(c)**). The hip segment was defined as the joint region between the waist and thigh sections of the human body. The knee segment was defined as the joint region between the thigh and leg sections of the human body; the ankle segment was defined as the joint region between the thigh and foot sections of the human body.

(a) Overall kinematics (b) Hip -NDI (c) Knee -NDI (d) Ankle -NDI

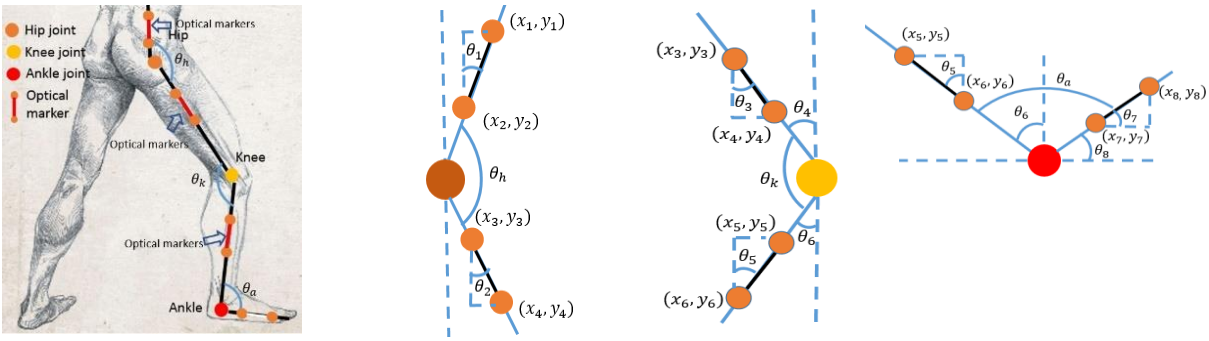

Figure 9-4: (a) shows NDI lower-limb kinematic analysis and NDI segmented kinematics analysis for each NDI marker on the (b) hip, (c) knee, and (d) ankle. Each segment was defined based on the joint region between the waist and the thigh, the thigh and the leg, the leg and the foot, respectively.

Equations 1–9 show how to calculate the hip, knee, and ankle angles based on the two pairs of reflective markers (**Table 8-4**).

Table 9-4: Motion analysis using NDI optical tracking system	
(a)Kinematic analysis for the hip section	
$\theta_1 = \text{atan}\left(\frac{x_1 - x_2}{y_1 - y_2}\right)$	(1)
$\theta_2 = \text{atan}\left(\frac{x_3 - x_4}{y_3 - y_4}\right)$	(2)
$\theta_h = 180^\circ - \theta_1 - \theta_2$	(3)
(b)Kinematic analysis for the knee section	
$\theta_4 = \theta_3 = \text{atan}\left(\frac{x_3 - x_4}{y_3 - y_4}\right)$	(4)
$\theta_6 = \theta_5 = \text{atan}\left(\frac{x_5 - x_6}{y_5 - y_6}\right)$	(5)
$\theta_k = 180^\circ - \theta_4 + \theta_6$	(6)
(c)Kinematic analysis for the ankle section	
$\theta_6 = \theta_5 = \text{atan}\left(\frac{x_5 - x_6}{y_6 - y_5}\right)$	(7)
$\theta_8 = \theta_7 = \begin{cases} 90^\circ + \text{atan}\left(\frac{x_7 - x_8}{y_7 - y_8}\right), \text{atan}\left(\frac{x_7 - x_8}{y_7 - y_8}\right) < 0 \\ -90^\circ + \text{atan}\left(\frac{x_7 - x_8}{y_7 - y_8}\right), \text{atan}\left(\frac{x_7 - x_8}{y_7 - y_8}\right) \geq 0 \end{cases}$	(8)
$\theta_a = 90^\circ + \theta_6 - \theta_8$	(9)

8.3.6 Kinematics Analysis for MEMS IMU-based Angular Tracking System

Figure 8-5 shows the detailed kinematics analysis for the IMU system.

(a) Overall kinematics (b) Hip -IMU (c) Knee -IMU (d) Ankle -IMU

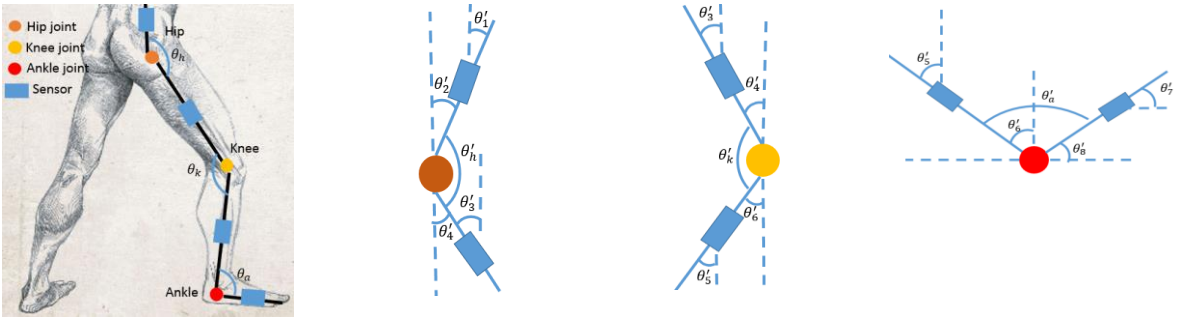

Figure 9-5: (a) shows NDI lower-limb kinematic analysis and NDI segmented kinematics analysis for each NDI marker on the (b) hip, (c) knee, and (d) ankle.

Equations 10–18 show how to calculate the hip, knee, and ankle angles based on the two IMUs (**Table 8-5**).

Table 9-5: Motion analysis using IMU tracking system	
(a)Kinematic analysis for the hip section	
$\theta_2' = \theta_1' = \begin{cases} \text{atan}((tan^2(\theta_{1x}') + tan^2(\theta_{1y}'))^{0.5}, \theta_{1y}' < 0 \\ -\text{atan}((tan^2(\theta_{1x}') + tan^2(\theta_{1y}'))^{0.5}, \theta_{1y}' \geq 0 \end{cases}$	(10)
$\theta_4' = \theta_3' = \begin{cases} \text{atan}((tan^2(\theta_{3x}') + tan^2(\theta_{3y}'))^{0.5}, \theta_{3y}' < 0 \\ -\text{atan}((tan^2(\theta_{3x}') + tan^2(\theta_{3y}'))^{0.5}, \theta_{3y}' \geq 0 \end{cases}$	(11)
$\theta_h' = 180^{\circ} + \theta_2' - \theta_4'$	(12)
(b)Kinematic analysis for the knee section	
$\theta_4' = \theta_3' = \begin{cases} \text{atan}((tan^2(\theta_{3x}') + tan^2(\theta_{3y}'))^{0.5}, \theta_{3y}' < 0 \\ -\text{atan}((tan^2(\theta_{3x}') + tan^2(\theta_{3y}'))^{0.5}, \theta_{3y}' \geq 0 \end{cases}$	(13)
$\theta_6' = \theta_5' = \begin{cases} \text{atan}((tan^2(\theta_{5x}') + tan^2(\theta_{5y}'))^{0.5}, \theta_{5y}' < 0 \\ -\text{atan}((tan^2(\theta_{5x}') + tan^2(\theta_{5y}'))^{0.5}, \theta_{5y}' \geq 0 \end{cases}$	(14)
$\theta_k' = 180^{\circ} - \theta_4' + \theta_6'$	(15)
(c)Kinematic analysis for the ankle section	
$\theta_6' = \theta_5' = \begin{cases} \text{atan}((tan^2(\theta_{5x}') + tan^2(\theta_{5y}'))^{0.5}, \theta_{5y}' < 0 \\ -\text{atan}((tan^2(\theta_{5x}') + tan^2(\theta_{5y}'))^{0.5}, \theta_{5y}' \geq 0 \end{cases}$	(16)

$\theta_7' = \theta_8' = \begin{cases} -\text{atan}((tan^2(\theta_{8x}') + tan^2(\theta_{8y}'))^{0.5}, \theta_{8y}' < 0 \\ \text{atan}((tan^2(\theta_{8x}') + tan^2(\theta_{8y}'))^{0.5}, \theta_{8y}' \geq 0 \end{cases}$	(17)
$\theta_a' = 90^{\circ} + \theta_6' - \theta_7'$	(18)

8.3.7 Planned Exercise

In this study, three different exercises were planned: walking, running, and fencing lunge. For the walking task, the average walking speed is 3.2 km/hr. For the jogging task, the average running speed is 5.1 km/hr. For the fencing lunge task, the participant was instructed to perform one lunge motion. The average speed is 4.8 km/hr. Both the IMU and NDI data were collected in the same trials.

8.3.8 Benchtop Accuracy Test

In order to determine the accuracy of the angular measurement, a benchtop test was conducted. An inclined surface of known angle measurement, verified with a protractor, was used in this test. The sensor was mounted on the top of the surface, and the results were compared to the known angle. The test aims to quantitatively evaluate the tracking accuracy of the sensors on a flat surface without considering human factors such as skin curvature.

8.3.9 Participants

Ten healthy human volunteers (sex: M/F, age: 18+, body mass: 75 ± 10 kg, height: 170 ± 10 cm) were recruited in this study. The study was carried out with approval from the University of Georgia Institutional Review Board. All participants were pre-screened by the eligibility assessment. The inclusion criteria for the study were healthy adults who exercise regularly. The exclusion criteria were knee/ankle problems, non-healing wounds, ulceration, gangrene, pain with exercise, pain at rest, claudication, arterial grafts or clots, walking impairments, or

extremity pain from other causes and cardiovascular disease. The participants gave informed consent to their inclusion in the study as required, and the work adhered to the Declaration of Helsinki. Each participant performed three different motions: walking, jogging, and fencing lunge. The overall exercise time was about 25 minutes, including preparation.

8.3.10 Pretest Calibration

The IMUs were calibrated through a method named static test, in order to reduce the tracking errors of angular measurement. In detail, each IMU module was placed on a flat surface and rotated on three axes, one at a time. The axis alignment between the IMU module and the surface was calibrated. After the calibration, another test was carried out on an inclined surface with an adjustable angle. The angular reading from the IMUs was then compared to a protractor, which was used as a reference. If the angular difference between IMUs and protractor is less than 0.05°, the IMUs were ready to use in the exercises.

8.3.11 Statistical Tool

In this study, the cross-correlation method was used to assess the similarity between two sets of data—IMU and NDI. As the sampling rate of two systems is different, in order to do cross-correlation, the raw data of each system was firstly pre-processed stage and ensure the time stamp was consistent for both data sets. The cross-correlation method allows for an angle-to-angle comparison of the angular variation between the NDI and IMU over a certain period. This pre-processing included the following processes: at first, all the collected raw data were checked and cleaned; since the NDI's sampling rate (60Hz) was different from the IMU's sampling rate (50Hz), it is important to adjust the sample sizes from both systems and make sure they are

identical. Moreover, each system's data set was aligned according to the peaks of the calculated angles.

9.4 Results

There are two different steps to validate the accuracy of the body movement tracker: benchtop test and human trial.

8.4.1 Benchtop Accuracy Test

Angular and acceleration data were recorded. The scatter plot in **Figure 8-6 (a)** shows the consistency between the angle output from the calibrated sensor and the actual angle from the protractor reading of the inclined mounting surface (R2 = 0.999). The Bland-Altman plot in **Figure 8-7 (b)** shows the close agreement between the angle measurement from the sensor and the actual angle. Both the upper and lower limit is two standard deviations from the mean. The result shows the difference is within the acceptable range. A t-test was conducted between the two sets of data, and no significant difference between the angle detected by the MEMS gyroscope and angle measured by the protractor was observed (p = 0.9997).

(a) Scatter plot (b) Bland-Altman plot

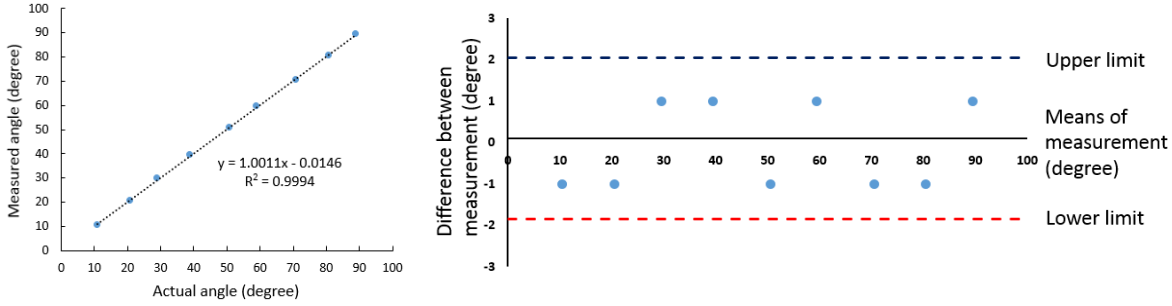

Figure 9-6: Shows the analysis of (a) scatter plot and (b) Bland-Altman plot.

8.4.2 Detailed Result of One Participant

The results of the gait analysis of one participant are shown in **Figure 8-7**. The blue line is the NDI data, and the orange line is the IMU data.

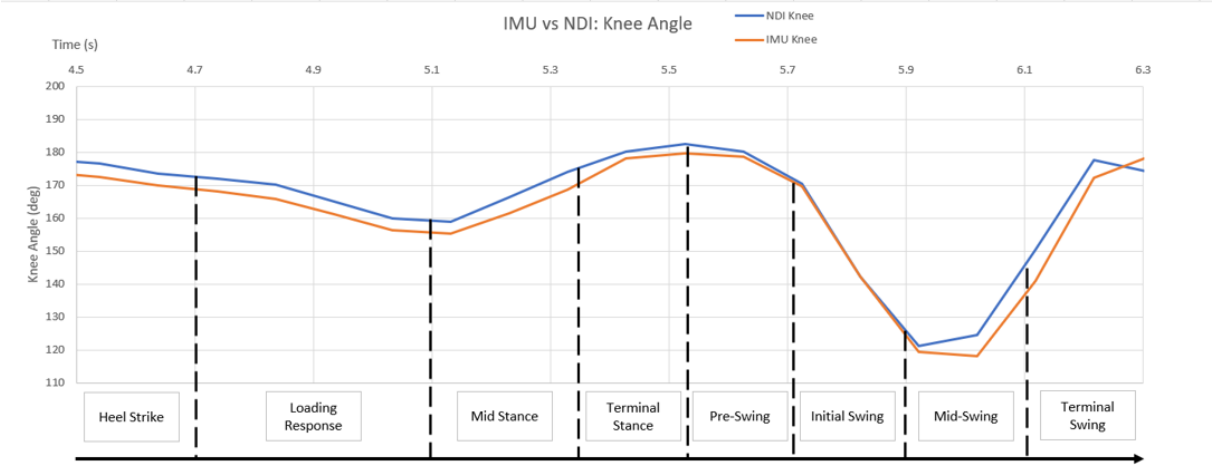

Figure 9-7: Gait comparison between the NDI optical tracking and our tracking system for one participant

8.4.3 Overall Results of Ten Participants

The angular variations of the hip, knee, and ankle during walking and jogging for all ten participants are shown in **Figure 8-8**. In each exercise, the solid line and the dashed line represents the IMU and the NDI data, respectively. The two lines were artificially separated by adding an offset of 40º for better visualization.

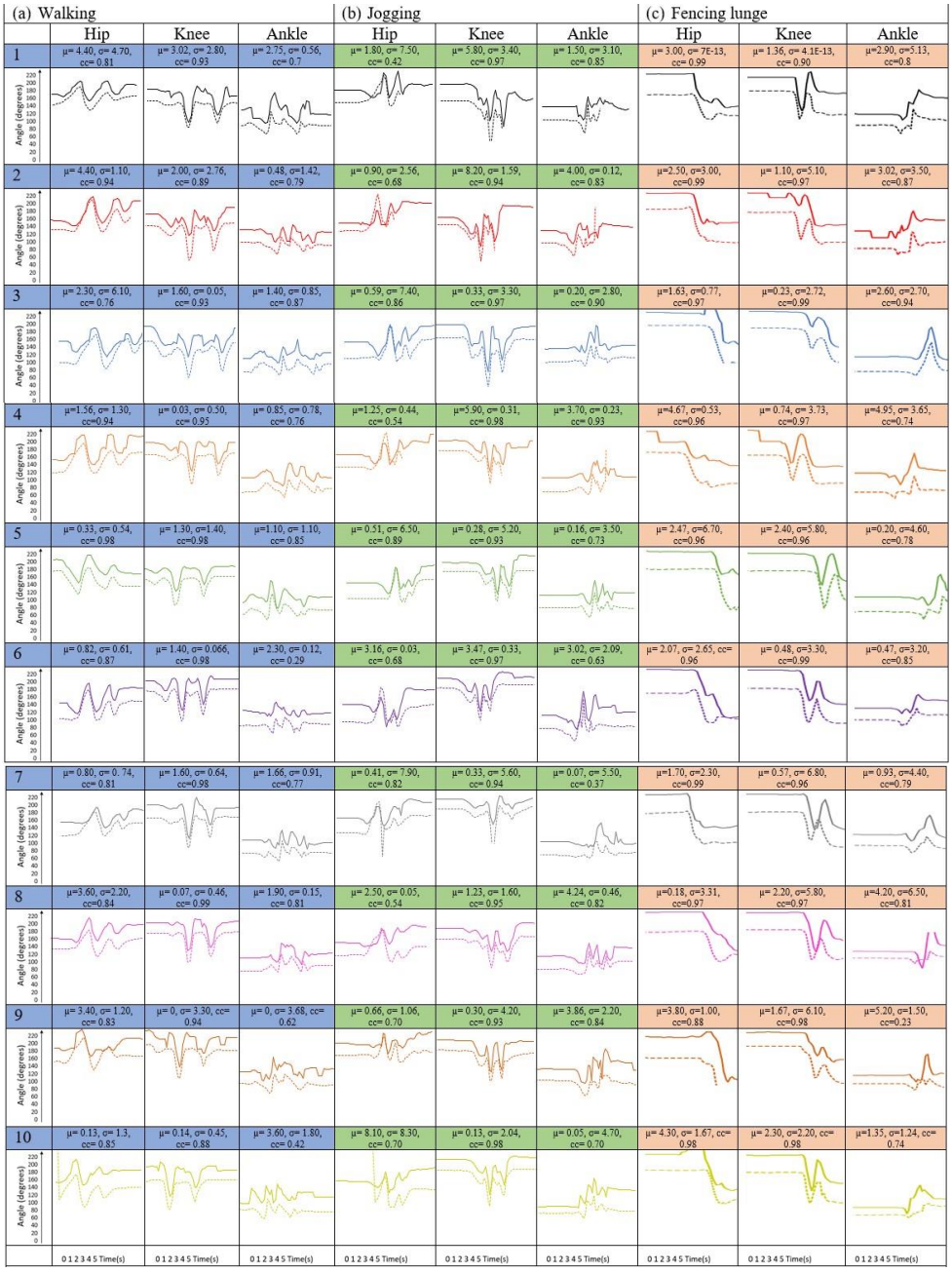

Figure 9-8: The walking, jogging, and fencing lunging results for 10 participants. The solid line is the IMU data, and the dashed line is the NDI data. Taking one graph of the hip movement of subject one as an example, μ= 4.40, σ= 4.70, cc= 0.81 means the mean of differences is 4.40º, the average standard deviation is 4.70º, and the cross-correlation is 0.81. The two lines were artificially separated from each other by adding an offset of 40º for better presentation.

A cross-correlation method was used to evaluate the difference between the results from NDI and IMU. The R-value for walking, jogging, and lunging was 0.85, 0.80, and 0.90, respectively (**Figure 8-9**).

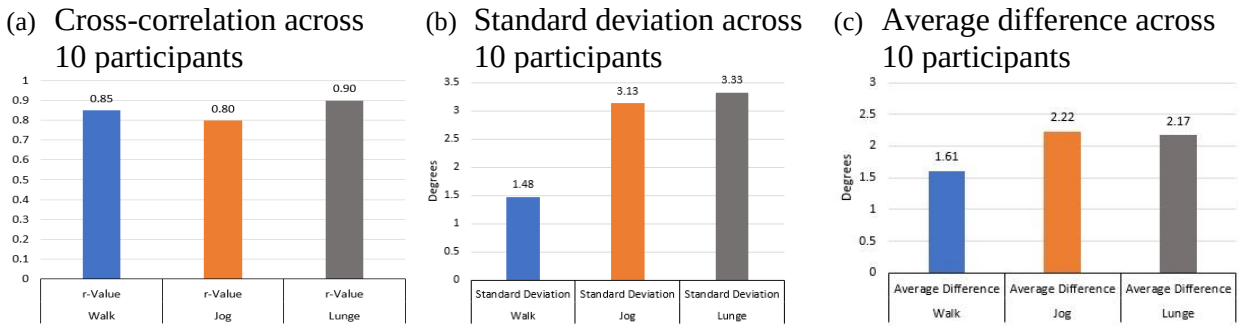

Figure 9-9: shows cross-correlation, standard deviation, and average difference for walking, jogging, and fencing lunging for 10 participants.

8.5 Discussion

The reason why three different types of motion were included is that they represent classic daily and sports exercises. The first two exercises (walking and jogging) aimed to test the IMU accuracy with greater emphasis on limb movement, whereas the exercise of fencing lunge aimed to test the IMU accuracy with greater emphasis on joint movement. All these exercises were designed to assess the IMU accuracy across a wide range of exercising speeds and limb movements.

8.5.1 Abnormalities in the Results

In **Figure 8-7**, for subject 7, the cross-correlation was only 0.37 between the IMU and NDI ankle data. The reason was when the subject was wearing the ankle sleeves. The tracking module moved off from the original position when he or she was jogging. This also happened

when subjects were wearing smaller sizes of shoes, which gave the sleeve more room to rotate. That explained why the cross-correlations were worse in the ankle angles.

8.5.2 Comparability Between NDI and IMU

The average value for cross-correlation was 0.9. These findings suggest that the MEMS-guided tracking device presented in this study is comparable to a commercially available optical tracking system. It could track real-time body motion, offering instant feedback to patients and therapists.

8.5.3 Limitations of NDI

The reflective markers were designed to be mounted on the side of the body (i.e., sagittal plane), specifically on the position of the iliotibial band of the thigh section, so that the reflective markers on both legs would not interfere with each other. The human subjects performed each exercise when one side of their body was exposed to the NDI, then turned around and performed the same exercise on the other side of the body. For brevity, only the results of the left side of the body were shown in **Figure 8-8**. The marker arrangement created a line of sight issues, such as when an arm swings down in front of the marker or a piece of clothing moves during exercise and covers the marker. This problem was solved by instructing the subjects to hold one arm above the markers when the left side of the body was facing the NDI.

8.5.4 Limitations of IMU

Generally speaking, the IMU module has a drift problem on the Z-axis. In order to mitigate the drift problem, one solution is to orientate the IMU module vertically so that the measured angle was derived only from X- and Y-axis. After that, the Euler angles of the X- and

Y-axis were used to calculate the tilt angle, which was ideal for measuring 2D movement. All the calculation has been conducted in a smartphone application. Furthermore, the human subject had to stand straight, so the orientation of the IMU sensor could be adjusted and confirmed.

8.5.5 Advantages of IMU Over NDI

From the experiments conducted, it can be seen that the IMU is more suitable in dynamic situations and environments than passive marker systems such as NDI due to the following reasons. During the experiment on the NDI, the subjects had to pay attention to the positions of markers and take actions to avoid marker blockage; this inevitably impacted the quality of exercise. In contrast, the performance of IMU was stable and did not interfere with the body posture of the subjects. For the consideration of accurate joint angle calculation, the relative position between the optical markers has to be fixed. In this study, due to the sleeve and 3D-printed mount design, this is less problematic. However, it could be a prevalent issue in many gait analyses when the reflective markers are attached with less secure options. The IMU has its own coordinate system, whereas the coordinates of NDI marker positions are dependent on the NDI emitter/receiver coordinate system. This makes the IMU an ideal option for the fabrication of a portable movement-monitoring system. The future application of the device is to aid in training a patient to carry out the repetitive activity in an outdoor environment.

8.6 Summary

The findings suggest that the MEMS-guided tracking device presented in this study could track real-time body motion, offering instant feedback to the patients and therapists. The device is low-cost, easy-to-mount, user-friendly, and portable for outdoor use. In the future, acceleration

data will be included, so more kinematic information can be integrated to generate an analysis of the repetitive rehabilitation exercise and assess the effectiveness of the exercise. Moreover, the device would detect not only movement of the lower limbs but also the movement of the upper limbs, including the movement of the fingers, after the system is scaled-down.

To sum up, in this study, a new MEMS IMU-based tracking system was developed. Ten human subjects were instructed to perform three different motions: walking, running, lunging. The same trials were then conducted together with IMU devices and the NDI Polaris Vega optical tracking system® (NDI). Comparing the IMU to the NDI, the average cross-correlation value was 0.85, the standard deviation was 2.65°, and the mean difference was 2.00°. This verified that the proposed MEMS tracking device is able to provide accurate information on joint angles and could potentially be used for outdoor or home-based rehabilitation.

CHAPTER 9

CONCLUSION AND FUTURE WORK

9.1 Conclusion

This dissertation aims to develop novel medical devices using smartphones, wireless sensors, and 3D-printing technology. Reflecting on the purpose of the study stated in Chapter 1, the conclusion begins with presenting the outcomes of six different studies, followed by suggestions for future work. The first study looked into the efficiency and limitations of one state-of-art navigation system—the NDI optical tracking system. Then the second study presented wearable medical devices for fast and accurate measurement of skin temperature. Another three studies explored the use of smartphone applications, wireless sensors, and 3D-printing technology in precision cancer diagnosis and treatment. Last, a human study was conducted to evaluate the accuracy of a real-time motion tracking system. All the developed devices were low-cost and had comparable accuracies to commercially available products.

Chapter 3 presented a thorough evaluation of one NDI tracking system in a lab setting. This detailed investigation shows the capability of current medical devices. Three potential error sources were tested: the marker orientation, the marker occlusion affected by the blood during surgery, and the environmental reflection. These experiments generated a maximum error of 2.63°, 4.88 mm, and 0.55 mm for the marker orientation, the marker occlusion, and the environmental reflection, respectively. During the reflection test, there were many phantom

points generated to make the tracking impossible. In the discussion, guidelines were suggested for using OTSs for reducing medical errors and thus improving patient safety.

Chapter 4 depicted a wearable 3D printed thermochromic device that allows people to measure skin temperature for heatstroke prevention. Combined with smartphone applications, the device was able to track real-time skin temperature and alerts the people who were vulnerable to heatstroke. The 3D printable resin developed, can change color at a specific activation temperature. The device has undergone a series of performance tests in order to optimize the color transition rate and stability of color change. The accuracy of our device was comparable to the conventional thermometer. The regression analysis shows the R-square value was 0.7599, and the average error was 1.3 ºC.

Chapter 5 illustrated a 3D-printed flexible template for image-guided therapy. The template was printed using a flexible photopolymer resin FLFLGR02 in Form 2 3D printer (Formlabs, Inc., Somerville, MA). The flexible material gave the template a unique advantage by allowing it to make close contact with human skin and provide accurate insertion with the help of the newly developed OncoNav software. At the back of the template, there was a grid comprised of circular containers filled with contrast agent. At the front of the template, the guide holes between the containers provided space and angular flexibility for needle insertion. MRI scans were initially used to identify tumor position as well as the template location. The OncoNav software then pre-selected the best guide hole for targeting a specific lesion and suggested insertion depth for the physician A phantom study of 13 insertions in a CT scanner was carried out for assessing needle placement accuracy. The mean total distance error between planned and actual insertion was 2.7 mm, the maximum error was 4.78 mm, and the standard deviation was ±

1.1 mm. The accuracy of the OncoNav-assisted and template-guided needle targeting was comparable to the robot-assisted procedure. One limitation of the study was that the accuracy test of the template has only been done in a CT scanner without inter-operative scans, which was not part of the designed clinical workflow. The results from this test can only be used as a very rough estimation of the clinical performance.

Chapter 6 focused on the development of a low-cost, smartphone-based, and patient-mounted localizer to assist the surgical operation of cancer ablation. Radiofrequency thermal ablation (RFA) is widely regarded as a non-surgical, and percutaneous way. Nowadays, RFA has been developed into a multimodal approach, which uses the images for pathway planning and applies heat to remove cancer tissues. However, image-guided RFA relied on real-time angular feedback during needle advancement. Deviated needle pathway could pose significant risks of thermal injury to essential organs. The benchtop test showed this newly developed device has an RMS error of 0.64° for angular measurement. In the live swine study, the mean tip-to-target distance error was 5.2 ± 1.3 mm. The mean tip-to-target angular error was 4.2° ± 2.6°.

Chapter 7 presented a low-cost handheld angular tracker—AngleNav as a low-cost navigation tool for image-guided therapy. It could be used to improve the accuracy, speed, and ease of CT-guided needle punctures. The AngleNav hardware included a wireless microelectromechanical (MEMS) tracker that can be attached to any standard needle. The physician defined the target, desired needle path, and skin entry point on a CT slice image. The accuracy of AngleNav was first tested in a 3D-printed calibration platform in a benchtop setting. An abdominal phantom study was then performed in a CT scanner to validate the accuracy of the device's angular measurement. Finally, an in vivo swine study was performed to guide the needle towards liver targets (n = 8). CT scans of the targets were used

to quantify the angular errors and needle tip-to-targeting distance errors between the planned needle path and the final needle position. The MEMS tracker showed a mean angular error of 0.01° with a standard deviation (SD) of ± 0.62° in the benchtop setting. The abdominal phantom test showed a mean angular error of 0.87° with an SD of ± 1.19° and a mean tip-to-target distance error of 4.89 mm with an SD of ± 1.57 mm. The animal experiment resulted in a mean angular error of 6.60° with an SD of ± 1.90° and a mean tip-to-target distance error of 8.7 mm with an SD of ± 3.1 mm. These results demonstrated the feasibility of AngleNav for CT-guided interventional workflow. The angular and distance errors were reduced by 64.4 % and 54.8 %, respectively, if using AngleNav instead of freehand insertion, with a limited number of operators. AngleNav was initially validated to assist the physicians in delivering accurate needle insertion during CT-guided intervention. The device could potentially reduce the learning curve for physicians to perform CT-guided needle targeting.

Chapter 8 demonstrated a human study of a low-cost, wireless sensor-based motion tracking system. The system consists of seven MEMS IMUs, which could be mounted on the lower limbs of the subjects. For the feasibility test, ten human participants were instructed to perform three different motions: walking, running, and fencing lunging when wearing specially designed sleeves. The subjects' lower body movements were tracked using the IMU-based system and compared with the gold standard—the NDI Polaris Vega optical tracking system® (NDI). The results of the angular comparison between IMU and NDI were as follows: the average cross-correlation value was 0.85, the mean difference of joint angles was 2.00°, and the standard deviation of joint angles was ± 2.65°. This motion tracking system provided an alternative low-cost solution to track body movement. Moreover, it was able to operate on a smartphone platform for assisting outdoor or home-based rehabilitation.

9.2 Future Work

All the presented medical devices could provide real-time positional information to the physicians without significantly modifying the existing clinical workflow. To better meet the requirements of patient-centered therapy, the devices could be more customizable based on individual patient's anatomical and physiological information. In addition, the devices could be more versatile in different clinical applications by applying the concept of modular design. In detail, the physcian could add or remove a varities of functional modules for specific surgical tasks. Last, more clinical studies should be conducted to further validate the performance of the presented medical devices.

9.2.1 A Wearable Smart Diagnostic Device for Heatstroke Prevention

Flexible resin (RS-F2-FLGR) by Formlabs (Sommerville, MA) could be used to increase the flexibility of the bracelet design. This could increase the skin contact area of the bracelet, and improve the efficiency of the heat transfer between our device and human skin. More, the color of the bracelet could be more uniform if the mixing procedure is optimized. The color detection function of the smartphone application would be further improved if the impact of the background lighting on the smartphone camera is mitigated.

In the long run, the design will be customized to individual needs by applying the deep learning method to train the device, making a more accurate diagnosis. The database will be expanded by inviting more volunteers and athletes for trials. It can be foreseen that the thermochromic principle and 3D printing technology could be applied to other applications such as food containers and indoor thermal decors.

9.2.2 Low-cost MRI-visible Flexible Template

In the percutaneous surgical procedure, one of the challenges is to stabilize the needle on a moving skin surface due to respiratory motion. In order to increase the needle stability, one of the improvements is to adjust the hole sizes of the template and allowing tight-fit features for more selection of biopsy needles. Another method to improve needle stability is to add an insertion block with different needle insertion pathways. Moreover, in order to overcome the problem of vaporization of liquid-form MRI contrast agents, an ideal alternative—Barium Sulphate power could be used to develop a new MRI-visible template.

The proposed new template design comprises two parts. One part is the flexible connection, and the other one is the needle insertion block. The template will be fabricated using Form 2 printer® (Formlabs Inc, Somerville, MA). The flexible connection will be printed using an optimal mixture of high-density Barium Sulphate and Formlabs® flexible resin (RS-F2-GPCL-04). The insertion block will be 3D-printed using the Formlabs® clear resin (RS-F2-GPCL-04); the insertion holes are designed for 17G and 18G biopsy needles. The addition of Barium Sulphate allows the template to become MRI-visible while avoiding the problem of Magnevist® leakage. The flexible connection enables close proximity to human skin. The needle insertion block made from Formlabs® clear resin has high accuracy and tolerance for the biopsy needle. The accuracy of this new stereotactic device will be evaluated in phantom and in-vivo MRI studies.

(a) Drawing (b) Template design

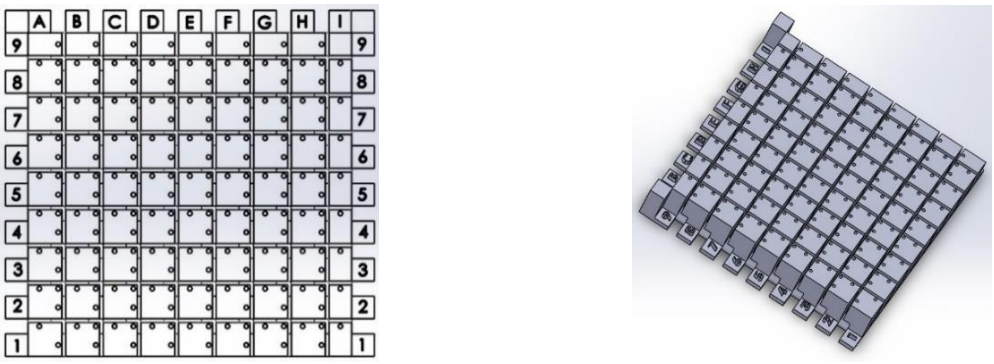

Figure 9-1: Illustration of the proposed template

9.2.3 Low-cost Patient-mounted In-plane Localizer

Currently, the device can only measure the skin insertion angle at the skin entry point. However, the needle deflection by soft tissue remains one of the top challenges for percutaneous surgeries. The needle punctures and passes through different tissue layers such as skin, muscle, fatty, and collagen[392]. There are different amounts of forces exerting on the needle tip when puncturing and cutting through the tissue layers. The extent of needle deflection varies from patient to patient. Moreover, the respiratory-induced tumor motion will create an extra layer of challenge[393]. One possible solution is to use flexible tissue along with the device. Ko et al. have demonstrated a steerable needle for soft tissue surgery[394].

9.2.4 Low-cost, Smartphone-based, and MEMS IMU-enabled Handheld Tracker

More clinical trials will be conducted for biopsy and ablation to validate the performance of the device in a real clinical environment. Although in-plane insertion covers 80% of the surgical procedures, it is still worthwhile to fully explore the potential use of the handheld tracker on the off-plane insertion. An attempt would be to place an additional MEMS IMU sensor at an orthogonal position to the existing one so that the off-plane angle can be tracked.

In order to further minimize the size and cost of the device, a concept of modular product design (MPD) could be applied. The MPD offers benefits such as a reduction in manufacturing cost, interoperability between different functional modules, shorter learning time for the users, more design flexibility, and less maintenance as well as upgrade constrains. According to MPD, the presented tracker could be divided into more function-based, scalable and reusable modules[395]. For example, the major electronic component of the tracker can be partitioned into an integrated wireless communication unit, a compact positional tracking unit, and a reusable charging unit. The major mechanical component can be divided into a handheld module and base operating module. One proposed idea is shown in **Figure 9-2**.

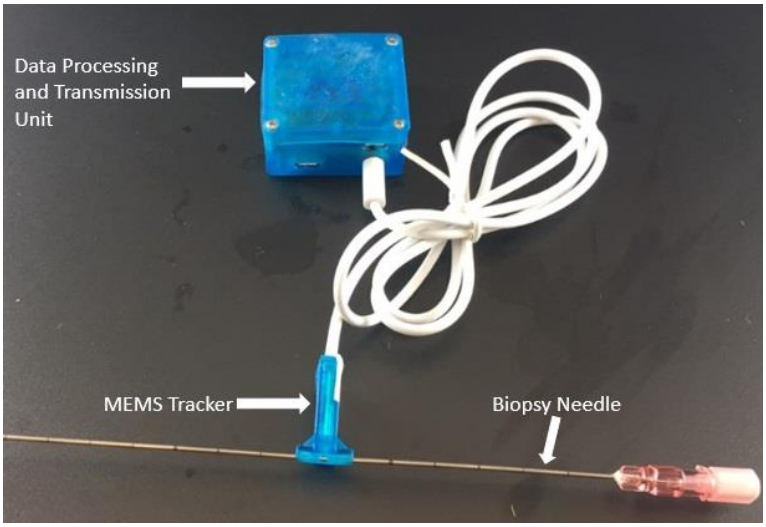

Figure 9-2: Shows a developed prototype using the MPD concept

Since both medical devices are not suitable for steam sterilization, alternative low-temperature sterilization methods would be considered, such as Ethylene Oxide Sterilization. The advantage of the EtO process is that it has high efficiency, large sterilization volume, and

non-corrosive to the 3D printed plastic material. But it is time-consuming as well as has some toxicity concerns.

9.2.5 Low-cost, Smartphone-based and MEMS Sensor-enabled Body Tracker

So far, the system could only track the joint movement of the lower limbs as the investigation was mainly focused on the lower limb recovery. For understanding more about the body locomotion, the upper limb movement would also be tracked. To better assess the patient's activities in daily life (ADL), the acceleration of limbs should also be used as another movement parameter. Moreover, the system could be upgraded to conduct a 3D kinematic analysis as it could help to reveal more movement details. As mentioned in Chapter 8, some limitations of MEMS IMU systems are that the IMU can suffer from drift due to instrumentation biases. A new way of fast pre-test calibration should be developed so that the users could instantly calibrate all the trackers when wearing them.

On the other hand, the data storage and cloud sharing function need to be further improved. The smartphone interface should be more informative and provide instant feedback and a historical review of the routine recovery exercises. This will make the system more customizable for the individual patient. Sport-related injuries greatly restricted game participation and created a large economic burden for athletes and clubs[396]. The application of a smartphone-based tracking system can identify potential risk factors and provide targeted risk-reduction training programs for players. For example, motion-tracking technology could be used in the fencing industry for coaching assistance and injury reduction. The MEMS IMU sensor

provides real-time positional and orientational data to the users, and the smartphone application will store and upload all the training data onto an online server (**Figure 9-3**).

(a) The conventional coaching (b) Common injuries (c) New proposed training

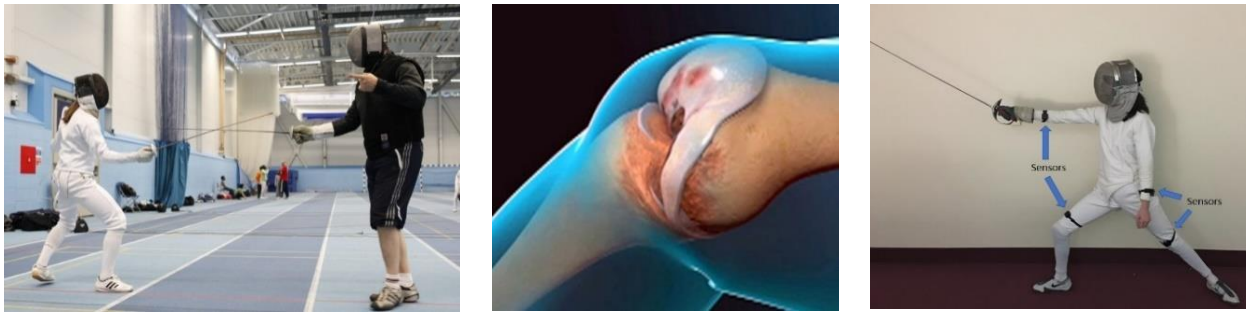

Figure 9-3: Shows a future trend for fencing analytics: (a) conventional coaching technique for fencing, (b) common fencing injuries-knee problem, (c) new training practice using sensors and smartphone application

REFERENCES

[1] A. C. Schlaerth and N. R. Abu-Rustum, "Role of minimally invasive surgery in gynecologic cancers," *Oncologist,* vol. 11, no. 8, pp. 895-901, 2006

[2] N. Aghakhani, M. Geravand, N. Shahriari, M. Vendittelli, and G. Oriolo, "Task control with remote center of motion constraint for minimally invasive robotic surgery," in *2013 IEEE International Conference on Robotics and Automation*, 6-10 May 2013 2013, pp. 5807-5812

[3] A. Biondi *et al.*, "Laparoscopic vs. open approach for colorectal cancer: evolution over time of minimal invasive surgery," *BMC surgery,* vol. 13, no. 2, p. S12, 2013

[4] M. Abdelgadir Adam *et al.*, "Minimally invasive versus open pancreaticoduodenectomy for cancer," *Annals of surgery,* vol. 262, no. 2, pp. 372-377, 2015

[5] B. a. W. s. Hospital. "What Is Image-guided Therapy?" Brigham and Women's Hospital. https://www.brighamandwomens.org/research/amigo/image-guided-therapy-at-bwh (accessed 6-1-2020, 2020).

[6] K. Cleary and T. M. Peters, "Image-Guided Interventions: Technology Review and Clinical Applications," *Annual Review of Biomedical Engineering,* vol. 12, no. 1, pp. 119-142, 2010/07/01 2010

[7] P. R. DeLucia, R. D. Mather, J. A. Griswold, and S. Mitra, "Toward the improvement of image-guided interventions for minimally invasive surgery: Three factors that affect performance," *Human factors,* vol. 48, no. 1, pp. 23-38, 2006

[8] P. Dutkiewicz, M. Kielczewski, and M. Kowalski, "Visual tracking of surgical tools for laparoscopic surgery," in *Proceedings of the Fourth International Workshop on Robot Motion and Control (IEEE Cat. No. 04EX891)*, 2004: IEEE, pp. 23-28

[9] J. Marescaux and M. Diana, "Next step in minimally invasive surgery: hybrid image-guided surgery," *Journal of Pediatric Surgery*, vol. 50, no. 1, pp. 30-36, 2015/01/01/ 2015

[10] Z. Zhou, B. Wu, J. Duan, X. Zhang, N. Zhang, and Z. Liang, "Optical surgical instrument tracking system based on the principle of stereo vision," *Journal of biomedical optics*, vol. 22, no. 6, p. 065005, 2017

[11] R. Elfring, M. de la Fuente, and K. Radermacher, "Assessment of optical localizer accuracy for computer aided surgery systems," *Computer Aided Surgery*, vol. 15, no. 1-3, pp. 1-12, 2010

[12] N. Enayati, E. D. Momi, and G. Ferrigno, "A Quaternion-Based Unscented Kalman Filter for Robust Optical/Inertial Motion Tracking in Computer-Assisted Surgery," *IEEE Transactions on Instrumentation and Measurement*, vol. 64, no. 8, pp. 2291-2301, 2015

[13] C. Nafis, V. Jensen, and M. Ron von Jako, "Method for evaluating compatibility of commercial electromagnetic (EM) microsensor tracking systems with surgical and imaging tables," in *Medical Imaging 2008: Visualization, Image-Guided Procedures, and Modeling*, 2008, vol. 6918: International Society for Optics and Photonics, p. 691820

[14] C. Hayhurst, P. Byrne, P. R. Eldridge, and C. L. Mallucci, "Application of electromagnetic technology to neuronavigation: a revolution in image-guided neurosurgery," *Journal of neurosurgery*, vol. 111, no. 6, pp. 1179-1184, 2009

[15] E. J. Hermann, H. H. Capelle, C. A. Tschan, and J. K. Krauss, "Electromagnetic-guided neuronavigation for safe placement of intraventricular catheters in pediatric neurosurgery," (in eng), *J Neurosurg Pediatr*, vol. 10, no. 4, pp. 327-33, Oct 2012

[16] J. L. McMillen, M. Vonau, and M. J. Wood, "Pinless frameless electromagnetic image-guided neuroendoscopy in children," (in eng), *Childs Nerv Syst*, vol. 26, no. 7, pp. 871-8, Jul 2010

[17] P. Maciejasz, J. Eschweiler, K. Gerlach-Hahn, A. Jansen-Troy, and S. Leonhardt, "A survey on robotic devices for upper limb rehabilitation," *Journal of NeuroEngineering and Rehabilitation*, vol. 11, no. 1, p. 3, 2014

[18] A. Vakanski, H.-P. Jun, D. Paul, and R. Baker, "A Data Set of Human Body Movements for

Physical Rehabilitation Exercises," (in eng), *Data (Basel)*, vol. 3, no. 1, p. 2, 2018

[19] G. D. Dockery, "Chapter 4 - Surgical principles," in *Lower Extremity Soft Tissue & Cutaneous Plastic Surgery (Second Edition)*, G. D. Dockery and M. E. Crawford Eds. Oxford: W.B. Saunders, 2012, pp. 23-27.

[20] M. Imbault, D. Chauvet, J.-L. Gennisson, L. Capelle, and M. Tanter, "Intraoperative functional ultrasound imaging of human brain activity," *Scientific reports*, vol. 7, no. 1, pp. 1-7, 2017

[21] K. S. Randall, J. A. Urbano, and L. A. Engle, "Ultrasound imaging systems and methods of performing ultrasound procedures," 2017.

[22] L. C. Sousa *et al.*, "Computational simulation of carotid stenosis and flow dynamics based on patient ultrasound data–A new tool for risk assessment and surgical planning," *Advances in medical sciences*, vol. 61, no. 1, pp. 32-39, 2016

[23] N. Houssami, R. M. Turner, and M. Morrow, "Meta-analysis of pre-operative magnetic resonance imaging (MRI) and surgical treatment for breast cancer," *Breast cancer research and treatment*, vol. 165, no. 2, pp. 273-283, 2017

[24] N. Wake *et al.*, "3D printed renal cancer models derived from MRI data: application in pre-surgical planning," *Abdominal Radiology*, vol. 42, no. 5, pp. 1501-1509, 2017

[25] N. Heller *et al.*, "The kits19 challenge data: 300 kidney tumor cases with clinical context, ct semantic segmentations, and surgical outcomes," *arXiv preprint arXiv:1904.00445*, 2019

[26] C. T. Yeo *et al.*, "Utility of 3D reconstruction of 2D liver computed tomography/magnetic resonance images as a surgical planning tool for residents in liver resection surgery," *Journal of surgical education*, vol. 75, no. 3, pp. 792-797, 2018

[27] N. F. Deana and N. Alves, "Cone Beam CT in diagnosis and surgical planning of dentigerous cyst," *Case reports in dentistry*, vol. 2017, 2017

[28] O. G. Avrunin *et al.*, "Principles of computer planning in the functional nasal surgery," *Przegląd Elektrotechniczny*, vol. 93, no. 3, pp. 140--143, 2017

[29] N. R. Council, *Mathematics and physics of emerging biomedical imaging*. National Academies

Press, 1996.

[30] M. C. Olson, T. D. Atwell, L. A. Mynderse, B. F. King, T. Welch, and A. H. Goenka, "CT-guided transgluteal biopsy for systematic sampling of the prostate in patients without rectal access: a 13-year single-center experience," *European Radiology,* vol. 27, no. 8, pp. 3326-3332, 2017/08/01 2017

[31] N. Lang, M. Dawood, F. Büther, O. Schober, M. Schäfers, and K. Schäfers, "Organ movement reduction in PET/CT using dual-gated listmode acquisition," *Zeitschrift für medizinische Physik,* vol. 16, no. 1, pp. 93-100, 2006

[32] G. Xu *et al.*, "Photoacoustic and ultrasound dual-modality imaging of human peripheral joints," *Journal of biomedical optics,* vol. 18, no. 1, p. 010502, 2012

[33] J. M. Koski, "Ultrasound guided injections in rheumatology," *The Journal of rheumatology,* vol. 27, no. 9, pp. 2131-2138, 2000

[34] T. Szyszko and G. Cook, "PET/CT and PET/MRI in head and neck malignancy," *Clinical radiology,* vol. 73, no. 1, pp. 60-69, 2018

[35] Philips. "CT 6000 iCT." Philips. https://www.usa.philips.com/healthcare/product/HCNOCTN194/ct-6000-ict-ct-scanner (accessed 5-17-2020, 2020).

[36] G. Healthcare. "Your standards, beyond your expectations." GE Healthcare. https://www.gehealthcare.com/products/ultrasound/voluson/voluson-s10-ultrasound (accessed 5-17-2020, 2020).

[37] D. Blog. "Siemens Avanto vs. Siemens Espree: How Do They Compare?" DMS Health. https://www.dmshealth.com/siemens-avanto-vs-siemens-espree/ (accessed 5-17-2020, 2020).

[38] R. Liao, L. Zhang, Y. Sun, S. Miao, and C. Chefd'Hotel, "A Review of Recent Advances in Registration Techniques Applied to Minimally Invasive Therapy," *IEEE Transactions on Multimedia,* vol. 15, no. 5, pp. 983-1000, 2013

[39] J. Hoffmann, C. Westendorff, C. Leitner, D. Bartz, and S. Reinert, "Validation of 3D-laser

surface registration for image-guided cranio-maxillofacial surgery," *Journal of Cranio-Maxillofacial Surgery,* vol. 33, no. 1, pp. 13-18, 2005

[40] S. Xu *et al.*, "Real-time MRI-TRUS fusion for guidance of targeted prostate biopsies," *Computer Aided Surgery,* vol. 13, no. 5, pp. 255-264, 2008/01/01 2008

[41] F. R. Khan and J. M. Henderson, "Chapter 3 - Deep brain stimulation surgical techniques," in *Handbook of Clinical Neurology*, vol. 116, A. M. Lozano and M. Hallett Eds.: Elsevier, 2013, pp. 27-37.

[42] R. A. Brown, "A stereotactic head frame for use with CT body scanners," *Investigative radiology,* vol. 14, no. 4, pp. 300-304, 1979

[43] V. Huang, J. Kamarn, R. D'Arcy, and K. Kohli, "SU-G-IeP2-02: A Proposed Solution to Accurate Delineation of External Body Contour Within CT Extended Field of View (eFOV) and the Evaluation of Dosimetric Impact from Image Distortion in EFOV," *Medical physics,* vol. 43, no. 6Part26, pp. 3655-3656, 2016

[44] N. Harada-Shoji *et al.*, "Usefulness of lesion image mapping with multidetector-row helical computed tomography using a dedicated skin marker in breast-conserving surgery," *European radiology*, vol. 19, no. 4, p. 868, 2009

[45] A. A. Khankan and M. Al-Muaikeel, "Image-guided percutaneous transthoracic biopsy in lung cancer–Emphasis on CT-guided technique," *Journal of infection and public health*, vol. 5, pp. S22-S30, 2012

[46] W. Lee, S. Chong, J. Seo, and H. Shim, "Transthoracic fine-needle aspiration biopsy of the lungs using a C-arm cone-beam CT system: diagnostic accuracy and post-procedural complications," *The British journal of radiology*, vol. 85, no. 1014, pp. e217-e222, 2012

[47] K. R. Birchard, "Transthoracic needle biopsy," in *Seminars in interventional radiology*, 2011, vol. 28, no. 01: © Thieme Medical Publishers, pp. 087-097

[48] J. Krücker *et al.*, "Clinical utility of real-time fusion guidance for biopsy and ablation," *Journal of*

vascular and interventional radiology, vol. 22, no. 4, pp. 515-524, 2011

[49] D. J. Grand, M. A. Atalay, J. J. Cronan, W. W. Mayo-Smith, and D. E. Dupuy, "CT-guided percutaneous lung biopsy: comparison of conventional CT fluoroscopy to CT fluoroscopy with electromagnetic navigation system in 60 consecutive patients," *European journal of radiology*, vol. 79, no. 2, pp. e133-e136, 2011

[50] W. Medical. "The fast find grid." Webb Medical. https://www.fastfindgrid.com/ (accessed 4-26-2020, 2020).

[51] R. Peng *et al.*, "Dosimetric analysis of 3D-printed coplanar template-assisted and CT-guided 125I seed implantation for the treatment of malignant tumors," *Chinese Journal of Radiation Oncology*, vol. 26, no. 9, pp. 1062-1066, 2017

[52] P. J. Klopotek, "Tracking system for laser surgery," ed: Google Patents, 1994.

[53] R. Khadem *et al.*, "Comparative tracking error analysis of five different optical tracking systems," *Computer Aided Surgery*, vol. 5, no. 2, pp. 98-107, 2000

[54] F. Poulin and L.-P. Amiot, "Interference during the use of an electromagnetic tracking system under OR conditions," *Journal of biomechanics*, vol. 35, no. 6, pp. 733-737, 2002

[55] N. Medical. "Aurora." NDI Medical. https://www.ndigital.com/medical/products/aurora/ (accessed 3-21-2020, 2020).

[56] N. Medical. "Polaris Spectra and Vicra." https://www.ndigital.com/medical/products/polaris-family/ (accessed 7-31-2019, 2019).

[57] D. Putzer *et al.*, "Comparison of Two Electromagnetic Navigation Systems For CT-Guided Punctures: A Phantom Study," (in eng), *Rofo*, vol. 188, no. 5, pp. 470-8, 2016

[58] T. Gruber-Rouh *et al.*, "Intervention Planning Using a Laser Navigation System for CT-Guided Interventions: A Phantom and Patient Study," *Korean J Radiol*, vol. 16, no. 4, pp. 729-735, 2015

[59] J. Engstrand, G. Toporek, P. Harbut, E. Jonas, H. Nilsson, and J. Freedman, "Stereotactic CT-Guided Percutaneous Microwave Ablation of Liver Tumors With the Use of High-Frequency Jet Ventilation: An Accuracy and Procedural Safety Study," *American Journal of Roentgenology*,

vol. 208, no. 1, pp. 193-200, 2016

[60] Y. Schwarz *et al.*, "Electromagnetic navigation during flexible bronchoscopy," *Respiration*, vol. 70, no. 5, pp. 516-522, 2003

[61] E. E. Folch *et al.*, "Electromagnetic Navigation Bronchoscopy for Peripheral Pulmonary Lesions: One-Year Results of the Prospective, Multicenter NAVIGATE Study," *Journal of Thoracic Oncology*, vol. 14, no. 3, pp. 445-458, 2019/03/01/ 2019

[62] G. Mauri *et al.*, "Real-Time US-CT/MRI Image Fusion for Guidance of Thermal Ablation of Liver Tumors Undetectable with US: Results in 295 Cases," *CardioVascular and Interventional Radiology*, vol. 38, no. 1, pp. 143-151, 2015

[63] B. J. Dixon, M. J. Daly, H. Chan, A. Vescan, I. J. Witterick, and J. C. Irish, "Augmented real-time navigation with critical structure proximity alerts for endoscopic skull base surgery," *The Laryngoscope*, vol. 124, no. 4, pp. 853-859, 2014

[64] S. Xu, V. Krishnasamy, E. Levy, M. Li, Z. T. H. Tse, and B. J. Wood, "Smartphone-Guided Needle Angle Selection During CT-Guided Procedures," *American Journal of Roentgenology*, vol. 210, no. 1, pp. 207-213, 2018/01/01 2017

[65] G. Fichtinger *et al.*, "Image overlay guidance for needle insertion in CT scanner," *IEEE Transactions on Biomedical Engineering*, vol. 52, no. 8, pp. 1415-1424, 2005

[66] M. Bovenzi, "Finger thermometry in the assessment of subjects with vibration-induced white finger," *Scandinavian journal of work, environment & health*, pp. 348-351, 1987

[67] N. Harada, "Cold-stress tests involving finger skin temperature measurement for evaluation of vascular disorders in hand-arm vibration syndrome: review of the literature," *International Archives of Occupational and Environmental Health*, vol. 75, no. 1, pp. 14-19, 2002/01/01 2002

[68] S. Begley. "Thousands of men with prostate cancer get risky treatment they don't need. New approaches could curb that." https://www.statnews.com/2017/05/04/prostate-cancer-research-psa/ (accessed July 16th 2017, 2017).

[69] S. J. Haker *et al.*, "Magnetic Resonance-guided Prostate Interventions," *Top Magn Reson*

Imaging, vol. 16, no. 5, pp. 355-368, 2005

[70] J. S. Wu, J. D. Goldsmith, P. J. Horwich, S. K. Shetty, and M. G. Hochman, "Bone and soft-tissue lesions: what factors affect diagnostic yield of image-guided core-needle biopsy?," *Radiology,* vol. 248, no. 3, pp. 962-970, 2008

[71] G. Fichtinger, A. Krieger, R. C. Susil, A. Tanacs, L. L. Whitcomb, and E. Atalar, "Transrectal prostate biopsy inside closed MRI scanner with remote actuation, under real-time image guidance," in *International Conference on Medical Image Computing and Computer-Assisted Intervention*, 2002: Springer, pp. 91-98

[72] L. A. Simmons *et al.*, "The PICTURE study: diagnostic accuracy of multiparametric MRI in men requiring a repeat prostate biopsy," *British journal of cancer,* vol. 116, no. 9, pp. 1159-1165, 2017

[73] S. D. "Problems with Transrectal Ultrasound-Guided Prostate Biopsy." Sperling Medical Group. http://sperlingprostatecenter.com/problems-with-transrectal-ultrasound-guided-prostate-biopsy/ (accessed July 27th 2017, 2017).

[74] K. M. Pondman *et al.*, "MR-guided biopsy of the prostate: an overview of techniques and a systematic review," *European urology,* vol. 54, no. 3, pp. 517-27, Sep 2008

[75] A. D'amico *et al.*, "Transperineal magnetic resonance image guided prostate biopsy," *J Urol,* vol. 164, no. 2, pp. 385-387, 2000

[76] G. Fichtinger *et al.*, "System for robotically assisted prostate biopsy and therapy with intraoperative CT guidance," *Academic radiology,* vol. 9, no. 1, pp. 60-74, Jan 2002

[77] J. Tokuda *et al.*, "Preliminary accuracy evaluation of 3T MRI-guided transperineal prostate biopsy with grid template," in *Proc Intl Soc Mag Reson Med*, 2011, pp. 7-13

[78] M. K. Samplaski and J. S. Jones, "Two centuries of cystoscopy: the development of imaging, instrumentation and synergistic technologies," (in eng), *BJU Int,* vol. 103, no. 2, pp. 154-8, Jan 2009

[79] E. v. Lima *et al.*, "Transvesical thoracoscopy: a natural orifice translumenal endoscopic approach

for thoracic surgery," *Surgical endoscopy,* vol. 21, no. 6, pp. 854-858, 2007

[80] C. H. Park, "Current application of minimally invasive surgery for gastrointestinal diseases," *The Korean journal of gastroenterology= Taehan Sohwagi Hakhoe chi,* vol. 50, no. 4, pp. 217-219, 2007

[81] F. Devernay, F. Mourgues, and È. Coste-Manière, "Towards endoscopic augmented reality for robotically assisted minimally invasive cardiac surgery," in *Proceedings International Workshop on Medical Imaging and Augmented Reality*, 2001: IEEE, pp. 16-20

[82] R. L. Witt, H. Iro, M. Koch, M. McGurk, O. Nahlieli, and J. Zenk, "Minimally invasive options for salivary calculi," *The Laryngoscope,* vol. 122, no. 6, pp. 1306-1311, 2012

[83] A. H. Wille, J. Roigas, S. Deger, M. Tüllmann, I. Türk, and S. A. Loening, "Laparoscopic radical nephrectomy: techniques, results and oncological outcome in 125 consecutive cases," *European urology,* vol. 45, no. 4, pp. 483-489, 2004

[84] P. Alison and A. McKee, "Chapter 9 - Surgery for Coronary Artery Disease," in *Cardiothoracic Critical Care*, D. Sidebotham, A. McKee, M. Gillham, and J. H. Levy Eds. Philadelphia: Butterworth-Heinemann, 2007, pp. 141-157.

[85] V. J. Miele, S. Vadera, and E. C. Benzel, "15 - Spinal Stenosis with Spondylolisthesis," in *The Comprehensive Treatment of the Aging Spine*, J. J. Yue, R. D. Guyer, J. P. Johnson, L. T. Khoo, and S. H. Hochschuler Eds. Philadelphia: W.B. Saunders, 2011, pp. 82-87.

[86] J. L. Ochsner, "Minimally invasive surgical procedures," (in eng), *Ochsner J,* vol. 2, no. 3, pp. 135-136, 2000

[87] E. Buscarini *et al.*, "Radiofrequency thermal ablation of liver tumors," *European radiology,* vol. 15, no. 5, pp. 884-894, 2005

[88] J. S. Lewin *et al.*, "Phase II clinical trial of interactive MR imaging–guided interstitial radiofrequency thermal ablation of primary kidney tumors: initial experience," *Radiology,* vol. 232, no. 3, pp. 835-845, 2004

[89] D. E. Dupuy, "Image-guided thermal ablation of lung malignancies," *Radiology,* vol. 260, no. 3,

pp. 633-655, 2011

[90] C. Pusceddu, B. Sotgia, R. M. Fele, and L. Melis, "Treatment of bone metastases with microwave thermal ablation," *Journal of Vascular and Interventional Radiology*, vol. 24, no. 2, pp. 229-233, 2013

[91] K. L. Carr and R. C. Allison, "Method and apparatus for aligning an ablation catheter and a temperature probe during an ablation procedure," 2014.

[92] J. C. Chen *et al.*, "Prostate Cancer: MR Imaging and Thermometry during Microwave Thermal Ablation-Initial Experience," *Radiology*, vol. 214, no. 1, pp. 290-297, 2000/01/01 2000

[93] V. Rieke *et al.*, "Comparison of temperature processing methods for monitoring focused ultrasound ablation in the brain," (in eng), *J Magn Reson Imaging*, vol. 38, no. 6, pp. 1462-1471, 2013

[94] P. Wang, "Evaluation of MR thermometry with proton resonance frequency method at 7T," (in eng), *Quant Imaging Med Surg*, vol. 7, no. 2, pp. 259-266, 2017

[95] E. F. Kelly and R. J. Leveillee, "Image-Guided Radiofrequency Ablation for Small Renal Masses," in *The Management of Small Renal Masses: Diagnosis and Management*, K. Ahmed, N. Raison, B. Challacombe, A. Mottrie, and P. Dasgupta Eds. Cham: Springer International Publishing, 2018, pp. 61-74.

[96] S. D. Brown, P. R. Morrison, L. Diller, and R. C. Shamberger, "CT-guided radiofrequency ablation of pediatric Wilms tumor in a solitary kidney," *Pediatric radiology*, vol. 35, no. 9, pp. 923-928, 2005

[97] B. Skjoldbye, F. Burcharth, J. Christensen, F. Moesgaard, J. Struckmann, and C. Nolsøe, "Ultrasound-guided radiofrequency ablation of malignant liver tumors," *Ugeskrift for laeger*, vol. 164, no. 40, pp. 4646-4650, 2002

[98] A. Semonche *et al.*, "MR-Guided Laser Interstitial Thermal Therapy for Treatment of Brain Tumors," in *Neurosurgical Procedures-Innovative Approaches*: IntechOpen, 2019.

[99] U. Salem *et al.*, "Neurosurgical applications of MRI guided laser interstitial thermal therapy

(LITT)," *Cancer Imaging,* vol. 19, no. 1, p. 65, 2019/10/15 2019

[100] M. S. Rao, E. L. Hargreaves, A. J. Khan, B. G. Haffty, and S. F. Danish, "Magnetic resonance-guided laser ablation improves local control for postradiosurgery recurrence and/or radiation necrosis," (in eng), *Neurosurgery,* vol. 74, no. 6, pp. 658-67; discussion 667, Jun 2014

[101] Z. Tovar-Spinoza and H. Choi, "Magnetic resonance-guided laser interstitial thermal therapy: report of a series of pediatric brain tumors," (in eng), *J Neurosurg Pediatr,* vol. 17, no. 6, pp. 723-33, Jun 2016

[102] O. Ashraf, N. V. Patel, S. Hanft, and S. F. Danish, "Laser-Induced Thermal Therapy in Neuro-Oncology: A Review," (in eng), *World Neurosurg,* vol. 112, pp. 166-177, Apr 2018

[103] K. Beccaria, M. S. Canney, and A. C. Carpentier, "Magnetic Resonance-Guided Laser Interstitial Thermal Therapy for Brain Tumors," in *Tumors of the Central Nervous System, Volume 5: Astrocytomas, Hemangioblastomas, and Gangliogliomas*, M. A. Hayat Ed. Dordrecht: Springer Netherlands, 2012, pp. 173-185.

[104] A. Kawczyk-Krupka *et al.*, "Comparison of cryotherapy and photodynamic therapy in treatment of oral leukoplakia," *Photodiagnosis and Photodynamic Therapy,* vol. 9, no. 2, pp. 148-155, 2012/06/01/ 2012

[105] J. P. Erinjeri and T. W. Clark, "Cryoablation: mechanism of action and devices," *Journal of Vascular and Interventional Radiology,* vol. 21, no. 8, pp. S187-S191, 2010

[106] M. A. A. J. van den Bosch *et al.*, "MR imaging-guided percutaneous cryoablation of the prostate in an animal model: in vivo imaging of cryoablation-induced tissue necrosis with immediate histopathologic correlation," (in eng), *Journal of vascular and interventional radiology : JVIR,* vol. 20, no. 2, pp. 252-258, 2009

[107] D. B. Rukstalis, M. Khorsandi, F. U. Garcia, D. M. Hoenig, and J. K. Cohen, "Clinical experience with open renal cryoablation," *Urology,* vol. 57, no. 1, pp. 34-39, 2001

[108] T. Ikeda, S. Yoshizawa, N. Koizumi, M. Mitsuishi, and Y. Matsumoto, "Focused Ultrasound and Lithotripsy," (in eng), *Adv Exp Med Biol,* vol. 880, pp. 113-29, 2016

[109] C. M. Tempany, E. A. Stewart, N. McDannold, B. J. Quade, F. A. Jolesz, and K. Hynynen, "MR imaging–guided focused ultrasound surgery of uterine leiomyomas: a feasibility study," *Radiology,* vol. 226, no. 3, pp. 897-905, 2003

[110] E. A. Stewart *et al.*, "Clinical outcomes of focused ultrasound surgery for the treatment of uterine fibroids," *Fertility and sterility,* vol. 85, no. 1, pp. 22-29, 2006

[111] J. E. Kennedy, G. Ter Haar, and D. Cranston, "High intensity focused ultrasound: surgery of the future?," *The British journal of radiology,* vol. 76, no. 909, pp. 590-599, 2003

[112] M. Nakai *et al.*, "Radiofrequency Ablation Assisted by Real-Time Virtual Sonography and CT for Hepatocellular Carcinoma Undetectable by Conventional Sonography," *CardioVascular and Interventional Radiology,* vol. 32, no. 1, pp. 62-69, 2009/01/01 2009

[113] D. L. Stippel, S. Böhm, T. K. Beckurts, H. G. Brochhagen, and A. H. Hölscher, "Experimental evaluation of accuracy of radiofrequency ablation using conventional ultrasound or a third-dimension navigation tool," *Langenbeck's Archives of Surgery,* vol. 387, no. 7, pp. 303-308, 2002/11/01 2002

[114] F. Di Vece, P. Tombesi, F. Ermili, C. Maraldi, and S. Sartori, "Coagulation Areas Produced by Cool-Tip Radiofrequency Ablation and Microwave Ablation Using a Device to Decrease Back-Heating Effects: A Prospective Pilot Study," *CardioVascular and Interventional Radiology,* vol. 37, no. 3, pp. 723-729, 2014/06/01 2014

[115] S. J. Graham *et al.*, "Quantifying tissue damage due to focused ultrasound heating observed by MRI," *Magnetic Resonance in Medicine,* vol. 41, no. 2, pp. 321-328, 1999

[116] G. Hubens, H. Coveliers, L. Balliu, M. Ruppert, and W. Vaneerdeweg, "A performance study comparing manual and robotically assisted laparoscopic surgery using the da Vinci system," *Surgical Endoscopy And Other Interventional Techniques,* vol. 17, no. 10, pp. 1595-1599, 2003/10/01 2003

[117] B. J. Park, R. M. Flores, and V. W. Rusch, "Robotic assistance for video-assisted thoracic surgical lobectomy: Technique and initial results," *The Journal of Thoracic and Cardiovascular*

Surgery, vol. 131, no. 1, pp. 54-59, 2006/01/01/ 2006

[118] Q. H. Li, L. Zamorano, A. Pandya, R. Perez, J. Gong, and F. Diaz, "The application accuracy of the NeuroMate robot--A quantitative comparison with frameless and frame-based surgical localization systems," (in eng), *Comput Aided Surg,* vol. 7, no. 2, pp. 90-8, 2002

[119] M. S. Eljamel, "Robotic neurological surgery applications: accuracy and consistency or pure fantasy?," (in eng), *Stereotact Funct Neurosurg,* vol. 87, no. 2, pp. 88-93, 2009

[120] H. J. Kim, W. I. Jung, B. S. Chang, C. K. Lee, K. T. Kang, and J. S. Yeom, "A prospective, randomized, controlled trial of robot-assisted vs freehand pedicle screw fixation in spine surgery," (in eng), *Int J Med Robot,* vol. 13, no. 3, Sep 2017

[121] M. H. L. Liow, P. L. Chin, H. N. Pang, D. K.-J. Tay, and S.-J. Yeo, "THINK surgical TSolution-One(®) (Robodoc) total knee arthroplasty," (in eng), *SICOT J,* vol. 3, pp. 63-63, 2017

[122] S. W. Bell, I. Anthony, B. Jones, A. MacLean, P. Rowe, and M. Blyth, "Improved Accuracy of Component Positioning with Robotic-Assisted Unicompartmental Knee Arthroplasty: Data from a Prospective, Randomized Controlled Study," (in eng), *J Bone Joint Surg Am,* vol. 98, no. 8, pp. 627-35, Apr 20 2016

[123] J. Huang, J. Li, H. Li, H. Lin, P. Lu, and Q. Luo, "Continuous 389 cases of Da Vinci robot-assisted thoracoscopic lobectomy in treatment of non-small cell lung cancer: experience in Shanghai Chest Hospital," (in eng), *J Thorac Dis,* vol. 10, no. 6, pp. 3776-3782, 2018

[124] B. Yi *et al.*, "The first clinical use of domestically produced Chinese minimally invasive surgical robot system “Micro Hand S”," *Surgical endoscopy,* vol. 30, no. 6, pp. 2649-2655, 2016

[125] M. Remacle, M. N. P. V, G. Lawson, L. Plisson, V. Bachy, and S. Van der Vorst, "Transoral robotic surgery (TORS) with the Medrobotics Flex System: first surgical application on humans," (in eng), *Eur Arch Otorhinolaryngol,* vol. 272, no. 6, pp. 1451-5, Jun 2015

[126] B. Seeliger, M. Diana, J. P. Ruurda, K. M. Konstantinidis, J. Marescaux, and L. L. Swanström, "Enabling single-site laparoscopy: the SPORT platform," *Surgical Endoscopy,* vol. 33, no. 11, pp. 3696-3703, 2019/11/01 2019

[127] K. D. Chang, A. Abdel Raheem, Y. D. Choi, B. H. Chung, and K. H. Rha, "Retzius-sparing robot-assisted radical prostatectomy using the Revo-i robotic surgical system: surgical technique and results of the first human trial," *BJU international,* vol. 122, no. 3, pp. 441-448, 2018

[128] C. M. Kang *et al.*, "Robotic cholecystectomy using the newly developed Korean robotic surgical system, Revo-i: a preclinical experiment in a porcine model," *Yonsei medical journal,* vol. 58, no. 5, pp. 1075-1077, 2017

[129] F. Fanfani *et al.*, "The new robotic TELELAP ALF-X in gynecological surgery: single-center experience," *Surgical Endoscopy,* vol. 30, no. 1, pp. 215-221, 2016/01/01 2016

[130] J. M. Cooper and A. H. V. Schapira, "Friedreich's Ataxia: Disease mechanisms, antioxidant and Coenzyme Q10 therapy," *Biofactors,* vol. 18, no. 1-4, pp. 163-171, 2003

[131] J. Chan, M. F. Brin, and S. J. M. d. o. j. o. t. M. D. S. Fahn, "Idiopathic cervical dystonia: clinical characteristics," vol. 6, no. 2, pp. 119-126, 1991

[132] R. A. C. Roos, "Huntington's disease: a clinical review," *Orphanet journal of rare diseases,* vol. 5, pp. 40-40, 2010

[133] G. DeMaagd and A. Philip, "Parkinson's Disease and Its Management: Part 1: Disease Entity, Risk Factors, Pathophysiology, Clinical Presentation, and Diagnosis," *P & T : a peer-reviewed journal for formulary management,* vol. 40, no. 8, pp. 504-532, 2015

[134] C. Frank, G. Pari, and J. P. Rossiter, "Approach to diagnosis of Parkinson disease," *Canadian family physician Medecin de famille canadien,* vol. 52, no. 7, pp. 862-868, 2006

[135] A. E. Lang and A. M. Lozano, "Parkinson's disease," *J New England Journal of Medicine,* vol. 339, no. 16, pp. 1130-1143, 1998

[136] D. Tarsy, "Treatment of Parkinson Disease: A 64-Year-Old Man With Motor Complications of Advanced Parkinson DiseaseMotor Complications in Advanced Parkinson Disease," *JAMA,* vol. 307, no. 21, pp. 2305-2314, 2012

[137] Y. Tian, X. Meng, D. Tao, D. Liu, and C. Feng, "Upper limb motion tracking with the integration

of IMU and Kinect," *Neurocomputing*, vol. 159, pp. 207-218, 2015

[138] J. A. Corrales, F. Candelas, and F. Torres, "Hybrid tracking of human operators using IMU/UWB data fusion by a Kalman filter," in *2008 3rd ACM/IEEE International Conference on Human-Robot Interaction (HRI)*, 2008: IEEE, pp. 193-200

[139] Q. Yuan and I.-M. Chen, "Localization and velocity tracking of human via 3 IMU sensors," *Sensors and Actuators A: Physical*, vol. 212, pp. 25-33, 2014

[140] H. Zhou, T. Stone, H. Hu, and N. Harris, "Use of multiple wearable inertial sensors in upper limb motion tracking," *Medical engineering & physics*, vol. 30, no. 1, pp. 123-133, 2008

[141] S. Yang and Q. Li, "IMU-based ambulatory walking speed estimation in constrained treadmill and overground walking," *Computer Methods in Biomechanics and Biomedical Engineering*, vol. 15, no. 3, pp. 313-322, 2012/03/01 2012

[142] W. Teufl, M. Lorenz, M. Miezal, B. Taetz, M. Fröhlich, and G. Bleser, "Towards Inertial Sensor Based Mobile Gait Analysis: Event-Detection and Spatio-Temporal Parameters," (in eng), *Sensors (Basel)*, vol. 19, no. 1, p. 38, 2018

[143] W. Kong *et al.*, "Development of a real-time IMU-based motion capture system for gait rehabilitation," in *2013 IEEE International Conference on Robotics and Biomimetics (ROBIO)*, 12-14 Dec. 2013 2013, pp. 2100-2105

[144] H. T. Chang, L. A. Cheng, and J. J. Chang, "Development of IMU-based angle measurement system for finger rehabilitation," in *23rd International Conference on Mechatronics and Machine Vision in Practice (M2VIP)*, 28-30 Nov. 2016 2016, pp. 1-6

[145] D. Roetenberg, H. Luinge, and P. Slycke, "Xsens MVN: Full 6DOF human motion tracking using miniature inertial sensors," *Xsens Motion Technologies BV, Tech. Rep*, vol. 1, 2009

[146] P. Müller, M. Bégin, T. Schauer, and T. Seel, "Alignment-Free, Self-Calibrating Elbow Angles Measurement Using Inertial Sensors," *IEEE Journal of Biomedical and Health Informatics*, vol. 21, no. 2, pp. 312-319, 2017

[147] S. Bakhshi, M. H. Mahoor, and B. S. Davidson, "Development of a body joint angle

measurement system using IMU sensors," in *2011 Annual International Conference of the IEEE Engineering in Medicine and Biology Society*, 30 Aug.-3 Sept. 2011 2011, pp. 6923-6926

[148] A. Frisoli, M. Bergamasco, M. C. Carboncini, and B. Rossi, "Robotic assisted rehabilitation in virtual reality with the L-EXOS," *J Stud Health Technol Inform,* vol. 145, pp. 40-54, 2009

[149] G. Kwakkel, B. J. Kollen, and H. I. Krebs, "Effects of robot-assisted therapy on upper limb recovery after stroke: a systematic review," *J Neurorehabilitation and neural repair,* vol. 22, no. 2, pp. 111-121, 2008

[150] A. Montagner *et al.*, "A pilot clinical study on robotic assisted rehabilitation in VR with an arm exoskeleton device," in *Virtual Rehabilitation, 2007*, 2007: IEEE, pp. 57-64

[151] S. Masiero, A. Celia, G. Rosati, M. Armani, and rehabilitation, "Robotic-assisted rehabilitation of the upper limb after acute stroke," *J Archives of physical medicine,* vol. 88, no. 2, pp. 142-149, 2007

[152] G. Abbruzzese, R. Marchese, L. Avanzino, and E. Pelosin, "Rehabilitation for Parkinson's disease: Current outlook and future challenges," *Parkinsonism & Related Disorders,* vol. 22, pp. S60-S64, 2016/01/01/ 2016

[153] A. Meyer-Heim and H. J. van Hedel, "Robot-assisted and computer-enhanced therapies for children with cerebral palsy: current state and clinical implementation," (in eng), *Semin Pediatr Neurol,* vol. 20, no. 2, pp. 139-45, Jun 2013

[154] X. Tu *et al.*, "Upper Limb Rehabilitation Robot Powered by PAMs Cooperates with FES Arrays to Realize Reach-to-Grasp Trainings," (in eng), *J Healthc Eng,* vol. 2017, pp. 1282934-1282934, 2017

[155] R. Nijland, G. Kwakkel, J. Bakers, and E. van Wegen, "Constraint-induced movement therapy for the upper paretic limb in acute or sub-acute stroke: a systematic review," (in eng), *Int J Stroke,* vol. 6, no. 5, pp. 425-33, Oct 2011

[156] A. A. Blank, J. A. French, A. U. Pehlivan, and M. K. O'Malley, "Current Trends in Robot-Assisted Upper-Limb Stroke Rehabilitation: Promoting Patient Engagement in Therapy," (in

eng), *Curr Phys Med Rehabil Rep,* vol. 2, no. 3, pp. 184-195, 2014

[157] A. Jackson *et al.*, "Initial patient testing of iPAM - a robotic system for Stroke rehabilitation," in *2007 IEEE 10th International Conference on Rehabilitation Robotics*, 13-15 June 2007 2007, pp. 250-256

[158] D. J. Reinkensmeyer, E. T. Wolbrecht, V. Chan, C. Chou, S. C. Cramer, and J. E. Bobrow, "Comparison of three-dimensional, assist-as-needed robotic arm/hand movement training provided with Pneu-WREX to conventional tabletop therapy after chronic stroke," (in eng), *Am J Phys Med Rehabil,* vol. 91, no. 11 Suppl 3, pp. S232-S241, 2012

[159] G. Zeilig, H. Weingarden, M. Zwecker, I. Dudkiewicz, A. Bloch, and A. Esquenazi, "Safety and tolerance of the ReWalk™ exoskeleton suit for ambulation by people with complete spinal cord injury: a pilot study," *The journal of spinal cord medicine,* vol. 35, no. 2, pp. 96-101, 2012

[160] H. Kawamoto, S. Lee, S. Kanbe, and Y. Sankai, "Power assist method for HAL-3 using EMG-based feedback controller," in *SMC'03 Conference Proceedings. 2003 IEEE International Conference on Systems, Man and Cybernetics. Conference Theme-System Security and Assurance (Cat. No. 03CH37483)*, 2003, vol. 2: IEEE, pp. 1648-1653

[161] S. K. Banala, S. H. Kim, S. K. Agrawal, and J. P. Scholz, "Robot assisted gait training with active leg exoskeleton (ALEX)," *IEEE transactions on neural systems and rehabilitation engineering,* vol. 17, no. 1, pp. 2-8, 2008

[162] M. Topping, "An Overview of the Development of Handy 1, a Rehabilitation Robot to Assist the Severely Disabled," *Journal of Intelligent and Robotic Systems,* vol. 34, no. 3, pp. 253-263, 2002/07/01 2002

[163] M. Hillman, "2 rehabilitation robotics from past to present–a historical perspective," in *Advances in Rehabilitation Robotics*: Springer, 2004, pp. 25-44.

[164] A. Campeau-Lecours *et al.*, "Jaco assistive robotic device: Empowering people with disabilities through innovative algorithms," in *RESNA/NCART 2016,* Arlington, VA, 2016,

[165] J. M. McBean and K. N. Narendran, "Powered orthotic device and method of using same," ed:

Google Patents, 2015.

[166] L. Ferreira dos Santos, O. Christ, K. Mate, H. Schmidt, J. Krüger, and C. Dohle, "Movement visualisation in virtual reality rehabilitation of the lower limb: a systematic review," *BioMedical Engineering OnLine,* vol. 15, no. 3, p. 144, 2016/12/19 2016

[167] D. Jack *et al.*, "Virtual reality-enhanced stroke rehabilitation," *IEEE transactions on neural systems and rehabilitation engineering,* vol. 9, no. 3, pp. 308-318, 2001

[168] D. T. Reid, "Benefits of a virtual play rehabilitation environment for children with cerebral palsy on perceptions of self-efficacy: a pilot study," *Pediatric rehabilitation,* vol. 5, no. 3, pp. 141-148, 2002

[169] K. Dockx *et al.*, "Virtual reality for rehabilitation in Parkinson's disease," *Cochrane Database of Systematic Reviews,* no. 12, 2016

[170] A. S. Rizzo and G. J. Kim, "A SWOT analysis of the field of virtual reality rehabilitation and therapy," *Presence: Teleoperators & Virtual Environments,* vol. 14, no. 2, pp. 119-146, 2005

[171] H. Sveistrup, "Motor rehabilitation using virtual reality," *Journal of NeuroEngineering and Rehabilitation,* vol. 1, no. 1, p. 10, 2004/12/10 2004

[172] M. Slater, V. Linakis, M. Usoh, and R. Kooper, "Immersion, presence and performance in virtual environments: An experiment with tri-dimensional chess," in *Proceedings of the ACM symposium on virtual reality software and technology*, 1996, pp. 163-172

[173] S. K. Subramanian and M. F. Levin, "Viewing medium affects arm motor performance in 3D virtual environments," *Journal of neuroengineering and rehabilitation,* vol. 8, no. 1, p. 36, 2011

[174] S. M. Slobounov, W. Ray, B. Johnson, E. Slobounov, and K. M. Newell, "Modulation of cortical activity in 2D versus 3D virtual reality environments: an EEG study," *International Journal of Psychophysiology,* vol. 95, no. 3, pp. 254-260, 2015

[175] R. Lloréns, C. Colomer-Font, M. Alcaniz, and E. Noé-Sebastián, "BioTrak virtual reality system: effectiveness and satisfaction analysis for balance rehabilitation in patients with brain injury," *Neurología (English Edition),* vol. 28, no. 5, pp. 268-275, 2013

[176] T. Rose, C. S. Nam, and K. B. Chen, "Immersion of virtual reality for rehabilitation-Review," *Applied ergonomics,* vol. 69, pp. 153-161, 2018

[177] A. Gokeler *et al.*, "Immersive virtual reality improves movement patterns in patients after ACL reconstruction: implications for enhanced criteria-based return-to-sport rehabilitation," *Knee Surgery, Sports Traumatology, Arthroscopy,* vol. 24, no. 7, pp. 2280-2286, 2016

[178] M. F. Yanik, H. Cinar, H. N. Cinar, A. D. Chisholm, Y. Jin, and A. Ben-Yakar, "Neurosurgery: functional regeneration after laser axotomy," *Nature,* vol. 432, no. 7019, p. 822, 2004

[179] A. A. Cohen-Gadol, D. G. Piepgras, S. Krishnamurthy, and R. D. Fessler, "Resident duty hours reform: results of a national survey of the program directors and residents in neurosurgery training programs," *Neurosurgery,* vol. 56, no. 2, pp. 398-403, 2005

[180] A. R. Cohen, S. Lohani, S. Manjila, S. Natsupakpong, N. Brown, and M. C. Cavusoglu, "Virtual reality simulation: basic concepts and use in endoscopic neurosurgery training," *Child's Nervous System,* vol. 29, no. 8, pp. 1235-1244, 2013

[181] T. A. B. o. N. Surgery. "Training requirement." https://www.abns.org/training-requirements/ (accessed 7-14-2019, 2019).

[182] W. C. Newman, Y.-F. Chang, and L. D. Lunsford, "Professionalism and performance issues during neurosurgical training and job satisfaction after training: a single training center 50-year experience," *Journal of neurosurgery,* vol. 131, no. 1, pp. 245-251, 2018

[183] A. Nabavi *et al.*, "Surgical navigation in the open MRI," in *Intraoperative Imaging in Neurosurgery*: Springer, 2003, pp. 121-125.

[184] U. Herwig *et al.*, "The navigation of transcranial magnetic stimulation," vol. 108, no. 2, pp. 123-131, 2001

[185] T. N. Hernes, S. Ommedal, T. Lie, F. Lindseth, T. Langø, and G. J. m.-M. I. N. Unsgaard, "Stereoscopic navigation-controlled display of preoperative MRI and intraoperative 3D ultrasound in planning and guidance of neurosurgery: new technology for minimally invasive image-guided surgery approaches," vol. 46, no. 03, pp. 129-137, 2003

[186] A. Meola, F. Cutolo, M. Carbone, F. Cagnazzo, M. Ferrari, and V. J. N. r. Ferrari, "Augmented reality in neurosurgery: a systematic review," vol. 40, no. 4, pp. 537-548, 2017

[187] K. Cai *et al.*, "Synchronization design and error analysis of near-infrared cameras in surgical navigation," *Journal of medical systems*, vol. 40, no. 1, p. 7, 2016

[188] S. Engelhardt *et al.*, "Accuracy evaluation of a mitral valve surgery assistance system based on optical tracking," *International journal of computer assisted radiology and surgery*, vol. 11, no. 10, pp. 1891-1904, 2016

[189] A. D. Wiles, D. G. Thompson, and D. D. Frantz, "Accuracy assessment and interpretation for optical tracking systems," in *Medical Imaging 2004: Visualization, Image-Guided Procedures, and Display*, 2004, vol. 5367: International Society for Optics and Photonics, pp. 421-432

[190] M. Ribo, A. Pinz, and A. L. Fuhrmann, "A new optical tracking system for virtual and augmented reality applications," in *IMTC 2001. Proceedings of the 18th IEEE Instrumentation and Measurement Technology Conference. Rediscovering Measurement in the Age of Informatics (Cat. No. 01CH 37188)*, 2001, vol. 3: IEEE, pp. 1932-1936

[191] L. A. Groves, P. Carnahan, D. R. Allen, R. Adam, T. M. Peters, and E. C. Chen, "Accuracy assessment for the co-registration between optical and VIVE head-mounted display tracking," *International journal of computer assisted radiology and surgery*, vol. 14, no. 7, pp. 1207-1215, 2019

[192] R. Elfring, M. de la Fuente, and K. Radermacher, "Assessment of optical localizer accuracy for computer aided surgery systems," (in eng), *Comput Aided Surg*, vol. 15, no. 1-3, pp. 1-12, 2010

[193] N. Medical. "NDI Polaris Vega." https://www.ndigital.com/medical/products/polaris-vega/ (accessed 7-31-2019, 2019).

[194] NDI. "Optotrak Certus." NDI. https://wigi725ylkk16hjts2tbfo9i-wpengine.netdna-ssl.com/msci/wp-content/uploads/sites/17/2014/02/8300324_rev001_optotrak_Certus.pdf (accessed 5-12-2020, 2020).

[195] NDI. "Optotrak Certus HD." NDI. https://www.ndigital.com/msci/products/certus-hd/ (accessed

5-12-2020, 2020).

[196] ClaroNav. "Microntracker specifications." https://www.claronav.com/microntracker/microntracker-specifications/ (accessed 5-12-2020, 2020).

[197] Atracsys. "FusionTrack 500." Atracsys. https://www.atracsys-measurement.com/wp-content/documents/fTk500-datasheet.pdf (accessed 5-12-2020, 2020).

[198] D. F. Abawi, J. Bienwald, and R. Dorner, "Accuracy in optical tracking with fiducial markers: an accuracy function for ARToolKit," in *Proceedings of the 3rd IEEE/ACM International Symposium on Mixed and Augmented Reality*, 2004: IEEE Computer Society, pp. 260-261

[199] P. Haggard and A. M. Wing, "Assessing and reporting the accuracy of position measurements made with optical tracking systems," *Journal of Motor Behavior*, vol. 22, no. 2, pp. 315-321, 1990

[200] R. D. Ferguson, D. X. Hammer, L. A. Paunescu, S. Beaton, and J. S. Schuman, "Tracking optical coherence tomography," *Optics letters*, vol. 29, no. 18, pp. 2139-2141, 2004

[201] C. R. Mascott, "In vivo accuracy of image guidance performed using optical tracking and optimized registration," *Journal of neurosurgery*, vol. 105, no. 4, pp. 561-567, 2006

[202] L. Qin *et al.*, "Prospective head-movement correction for high-resolution MRI using an in-bore optical tracking system," *Magnetic Resonance in Medicine: An Official Journal of the International Society for Magnetic Resonance in Medicine*, vol. 62, no. 4, pp. 924-934, 2009

[203] A. E. Kedgley, T. Birmingham, and T. R. Jenkyn, "Comparative accuracy of radiostereometric and optical tracking systems," *Journal of biomechanics*, vol. 42, no. 9, pp. 1350-1354, 2009

[204] B. J. Lopresti *et al.*, "Implementation and performance of an optical motion tracking system for high resolution brain PET imaging," *IEEE Transactions on Nuclear Science*, vol. 46, no. 6, pp. 2059-2067, 1999

[205] J. Schmidt, D. R. Berg, H.-L. Ploeg, and L. Ploeg, "Precision, repeatability and accuracy of

Optotrak® optical motion tracking systems," *International Journal of Experimental and Computational Biomechanics,* vol. 1, no. 1, pp. 114-127, 2009

[206] W. Birkfellner, F. Watzinger, F. Wanschitz, R. Ewers, and H. Bergmann, "Calibration of tracking systems in a surgical environment," *IEEE Transactions on Medical Imaging,* vol. 17, no. 5, pp. 737-742, 1998

[207] S. Lee, H. Lee, H. Choi, S. Jeon, and J. Hong, "Effective calibration of an endoscope to an optical tracking system for medical augmented reality," *Cogent Engineering,* vol. 4, no. 1, p. 1359955, 2017

[208] S. Ma and Z. Zhao, "A New Method of Surgical Tracking System Based on Fiducial Marker," in *Medical Image Understanding and Analysis*, Cham, M. Valdés Hernández and V. González-Castro, Eds., 2017// 2017: Springer International Publishing, pp. 886-896

[209] F. Kral, E. J. Puschban, H. Riechelmann, and W. Freysinger, "Comparison of optical and electromagnetic tracking for navigated lateral skull base surgery," *The International Journal of Medical Robotics and Computer Assisted Surgery,* vol. 9, no. 2, pp. 247-252, 2013

[210] N. Medical, *Polaris Tool Design Guide*. Ontario, Canada: NDI Medical 2018.

[211] A. Bouchama and J. P. Knochel, "Heat stroke," *New England Journal of Medicine,* vol. 346, no. 25, pp. 1978-1988, 2002

[212] E. Choudhary and A. Vaidyanathan, "Heat stress illness hospitalizations—Environmental public health tracking program, 20 states, 2001–2010," *Morbidity and Mortality Weekly Report: Surveillance Summaries,* vol. 63, no. 13, pp. 1-10, 2014

[213] P. Larsen and T. Mousel, "Radio-Frequency Based Detection of Unattended Children to Reduce In-Vehicle Heat Stroke Fatalities," in *IRCOBI Conference Proceedings*, 2017,

[214] E. Lawton, G. Gabb, and H. Pearce, "Environmental heat stroke and long-term clinical neurological outcomes: a literature review of case reports and case series 2000–2016," *Internal Medicine Journal,* vol. 47, no. S3, pp. 20-20, 2017

[215] L. R. Leon and B. G. Helwig, "Heat stroke: role of the systemic inflammatory response," *Journal of applied physiology,* vol. 109, no. 6, pp. 1980-1988, 2010

[216] A. S. Ogbomo, C. J. Gronlund, M. S. O'Neill, T. Konen, L. Cameron, and R. Wahl, "Vulnerability to extreme-heat-associated hospitalization in three counties in Michigan, USA, 2000–2009," *International journal of biometeorology,* vol. 61, no. 5, pp. 833-843, 2017

[217] A. N. Peiris, S. Jaroudi, and R. Noor, "Heat Stroke," *Jama,* vol. 318, no. 24, pp. 2503-2503, 2017

[218] S. Shibolet, M. C. Lancaster, and Y. Danon, "Heat stroke: a review," *Aviation, space, and environmental medicine,* vol. 47, no. 3, pp. 280-301, 1976

[219] B. C. Davis *et al.*, "Heat stroke leading to acute liver injury & failure: A case series from the Acute Liver Failure Study Group," *Liver International,* vol. 37, no. 4, pp. 509-513, 2017

[220] R. Katch *et al.*, "Cold Water Immersion in the Treatment of Exertional Heat Stroke Remains the Gold Standard at the Falmouth Road Race," *Journal of Athletic Training,* vol. 52, no. 6, p. S313, 2017

[221] M. A. King, M. D. Ward, C. H. Gabrial, G. N. Audet, B. Adams, and L. R. Leon, "Prior Infection and Prior Heat Illness as Risk Factors for Exertional Heat Stroke," *The FASEB Journal,* vol. 31, no. 1 Supplement, pp. 1018.4-1018.4, 2017

[222] N. Knight, J. Parkin, R. Smith, and C. Kipps, "The Incidence Of Exertional Heat Stroke During Mass-participation Triathlon Races: Optimising Athlete Safety," *Br J Sports Med,* vol. 51, no. 4, pp. 344-345, 2017

[223] K. C. Schellhase, J. Plant, and S. M. Mazerolle, "Athletic Trainers' Attitudes and Perceptions Regarding Exertional Heat Stroke Before and After an Educational Intervention," *Athletic Training Education Journal,* vol. 12, no. 3, pp. 179-187, 2017

[224] T. T. Truxton and K. C. Miller, "Can Temperate-Water Immersion Effectively Reduce Rectal Temperature in Exertional Heat Stroke? A Critically Appraised Topic," *Journal of sport rehabilitation,* vol. 26, no. 5, pp. 447-451, 2017

[225] D. J. Casa, Y. Hosokawa, L. N. Belval, W. M. Adams, and R. L. Stearns, "Preventing death from

exertional heat stroke—The long road from evidence to policy," *Kinesiology Review,* vol. 6, no. 1, pp. 99-109, 2017

[226] C. Chang, M. Lin, and K. Niu, "Reduction of neurological injury by hyperbaric oxygen in exertional heat stroke rats," *Journal of the Neurological Sciences,* vol. 381, p. 751, 2017

[227] Jesse. "Three Common Misconceptions About Infrared Thermometers." ThermoWorks. https://blog.thermoworks.com/2012/03/infrared-thermometry/ (accessed 2018-4-8, 2018).

[228] Y.-F. Lin, T.-T. Liu, C.-H. Hu, C.-C. Chen, and J.-Y. Wang, "Expressions of chemokines and their receptors in the brain after heat stroke-induced cortical damage," *Journal of neuroimmunology,* 2018

[229] C. Mora, C. W. Counsell, C. R. Bielecki, and L. V. Louis, "Twenty-Seven Ways a Heat Wave Can Kill You:: Deadly Heat in the Era of Climate Change," *Circulation: Cardiovascular Quality and Outcomes,* vol. 10, no. 11, p. e004233, 2017

[230] S.-F. Hsu, K.-C. Niu, C.-L. Lin, and M.-T. Lin, "Brain cooling causes attenuation of cerebral oxidative stress, systemic inflammation, activated coagulation, and tissue ischemia/injury during heatstroke," *Shock,* vol. 26, no. 2, pp. 210-220, 2006

[231] J. González-Alonso, C. Teller, S. L. Andersen, F. B. Jensen, T. Hyldig, and B. Nielsen, "Influence of body temperature on the development of fatigue during prolonged exercise in the heat," vol. 86, no. 3, pp. 1032-1039, 1999

[232] G. M. Varghese, G. John, K. Thomas, O. C. Abraham, and D. Mathai, "Predictors of multi-organ dysfunction in heatstroke," *Emergency Medicine Journal,* vol. 22, no. 3, p. 185, 2005

[233] L. R. Leon and B. G. Helwig, "Heat stroke: Role of the systemic inflammatory response," vol. 109, no. 6, pp. 1980-1988, 2010

[234] A. Uchiyama, T. Hamatani, and T. Higashino, "Estimation of core temperature based on a human thermal model using a wearable sensor," in *2015 IEEE 4th Global Conference on Consumer Electronics (GCCE)*, 27-30 Oct. 2015 2015, pp. 605-609

[235] H. Brinnel and M. J. J. o. T. B. Cabanac, "Tympanic temperature is a core temperature in

humans," vol. 14, no. 1, pp. 47-53, 1989

[236] Y. Epstein, W. J. S. j. o. m. Roberts, and s. i. sports, "The pathopysiology of heat stroke: an integrative view of the final common pathway," vol. 21, no. 6, pp. 742-748, 2011

[237] J. Kravchenko, A. P. Abernethy, M. Fawzy, and H. K. J. A. j. o. p. m. Lyerly, "Minimization of heatwave morbidity and mortality," vol. 44, no. 3, pp. 274-282, 2013

[238] F. Matos *et al.*, "The use of thermal imaging to monitoring skin temperature during cryotherapy: a systematic review," vol. 73, pp. 194-203, 2015

[239] R. R. Pryor, D. J. Casa, J. C. Holschen, F. G. O'Connor, and L. W. J. C. P. E. M. Vandermark, "Exertional heat stroke: strategies for prevention and treatment from the sports field to the emergency department," vol. 14, no. 4, pp. 267-278, 2013

[240] T. Q. Trung, S. Ramasundaram, B. U. Hwang, and N. E. J. A. M. Lee, "An all-elastomeric transparent and stretchable temperature sensor for body-attachable wearable electronics," vol. 28, no. 3, pp. 502-509, 2016

[241] J. Stivoric *et al.*, "Non-invasive temperature monitoring device," ed: Google Patents, 2014.

[242] H. Lee *et al.*, "A graphene-based electrochemical device with thermoresponsive microneedles for diabetes monitoring and therapy," vol. 11, no. 6, p. 566, 2016

[243] S. Amendola, G. Bovesecchi, P. Coppa, and G. Marrocco, "Thermal characterization of epidermal RFID sensor for skin temperature measurements," in *Antennas and Propagation (APSURSI), 2016 IEEE International Symposium on*, 2016: IEEE, pp. 461-462

[244] A. Farzana. "The Physics Factbook." https://hypertextbook.com/facts/2001/AbantyFarzana.shtml (accessed 2-5-2019, 2019).

[245] S.-H. Kim, H.-J. Suh, J.-Z. Cui, Y.-S. Gal, S.-H. Jin, and K. Koh, "Crystalline-state photochromism and thermochromism of new spiroxazine," *Dyes and Pigments*, vol. 53, no. 3, pp. 251-256, 2002/06/01/ 2002

[246] F. Azizian, A. J. Field, and B. M. Heron, "Reductive alkylation of aminofluorans: A simple route

to intrinsically thermochromic fluorans," *Dyes and Pigments,* vol. 99, no. 2, pp. 432-439, 2013/11/01/ 2013

[247] L. C. Glover and E. F. Lopez, "Method for coating a polymeric article with a thermochromic paint," ed: Google Patents, 1980.

[248] K. Senga, K. Fujita, and S. Koide, "Thermally color-developing reversibly thermochromic pigment," ed: Google Patents, 2008.

[249] L. C. Glover and E. F. Lopez, "Thermochromic paint for use on plastic substrates," ed: Google Patents, 1978.

[250] A. S. University. "Facts About Your Skin - Temperatures in and on the human body." http://www.healthyheating.com/Definitions/facts_about_skin.htm#.XBcoQttKiM8 (accessed 2018-12-16, 2018).

[251] A. Jemal, R. Siegel, J. Xu, and E. Ward, "Cancer statistics, 2010," (in eng), *CA: a cancer journal for clinicians,* vol. 60, no. 5, pp. 277-300, Sep-Oct 2010

[252] S. Xu *et al.*, "Real-time MRI-TRUS fusion for guidance of targeted prostate biopsies," *Comput Aided Surg,* vol. 13, no. 5, pp. 255-264, 2008

[253] A. R. Rastinehad *et al.*, "Improving detection of clinically significant prostate cancer: magnetic resonance imaging/transrectal ultrasound fusion guided prostate biopsy," *J Urol,* vol. 191, no. 6, pp. 1749-1754, 2014

[254] P. Pepe, A. Garufi, G. Priolo, and M. Pennisi, "Can MRI/TRUS fusion targeted biopsy replace saturation prostate biopsy in the re-evaluation of men in active surveillance?," *World J Urol,* vol. 34, no. 9, pp. 1249-1253, 2016

[255] G. Reusz, P. Sarkany, J. Gal, and A. Csomos, "Needle-related ultrasound artifacts and their importance in anaesthetic practice," *Br J Anaesth,* vol. 112, no. 5, pp. 794-802, 2014

[256] Y. Chen, S. Zhang, F. Gao, Y. Chen, J. He, and T. Qi, "TRUS/MRI Fusion-Guided Prostate Biopsy Based on Improved Intracavitary Markers," in *Proceedings of the International Conference on Bioinformatics and Computational Intelligence*, 2017: ACM, pp. 6-10

[257] W. Venderink, T. M. Govers, M. de Rooij, J. J. Fütterer, and J. M. Sedelaar, "Cost-effectiveness comparison of imaging-guided prostate biopsy techniques: systematic transrectal ultrasound, direct in-bore MRI, and image fusion," *AJR Am J Roentgenol,* vol. 208, no. 5, pp. 1058-1063, 2017

[258] C. Arsov *et al.*, "Prospective randomized trial comparing magnetic resonance imaging (MRI)-guided in-bore biopsy to MRI-ultrasound fusion and transrectal ultrasound-guided prostate biopsy in patients with prior negative biopsies," *European urology,* vol. 68, no. 4, pp. 713-720, 2015

[259] F. Cornud *et al.*, "Precision Matters in MR Imaging–targeted Prostate Biopsies: Evidence from a Prospective Study of Cognitive and Elastic Fusion Registration Transrectal Biopsies," *Radiology,* vol. 287, no. 2, pp. 534-542, 2018

[260] D. Hausmann *et al.*, "Prostate cancer detection among readers with different degree of experience using ultra-high b-value diffusion-weighted Imaging: Is a non-contrast protocol sufficient to detect significant cancer?," *Eur Radiol,* journal article vol. 28, no. 2, pp. 869-876, February 01 2018

[261] V. Kasivisvanathan *et al.*, "MRI-Targeted or Standard Biopsy for Prostate-Cancer Diagnosis," *N Engl J Med,* vol. 378, no. 19, pp. 1767-1777, 2018

[262] K. Engelhard, H. P. Hollenbach, B. Kiefer, A. Winkel, K. Goeb, and D. Engehausen, "Prostate biopsy in the supine position in a standard 1.5-T scanner under real time MR-imaging control using a MR-compatible endorectal biopsy device," (in eng), *Eur Radiol,* vol. 16, no. 6, pp. 1237-43, Jun 2006

[263] D. Beyersdorff, A. Winkel, B. Hamm, S. Lenk, S. A. Loening, and M. Taupitz, "MR Imaging–guided Prostate Biopsy with a Closed MR Unit at 1.5 T: Initial Results," *Radiology,* vol. 234, no. 2, pp. 576-581, 2005

[264] A. G. Anastasiadis *et al.*, "MRI-guided biopsy of the prostate increases diagnostic performance in men with elevated or increasing PSA levels after previous negative TRUS biopsies," (in eng), *European urology,* vol. 50, no. 4, pp. 738-48; discussion 748-9, Oct 2006

[265] G. Fichtinger, A. Krieger, R. C. Susil, A. Tanacs, L. L. Whitcomb, and E. Atalar, "Transrectal Prostate Biopsy Inside Closed MRI Scanner with Remote Actuation, under Real-Time Image Guidance," in *Medical Image Computing and Computer-Assisted Intervention — MICCAI 2002: 5th International Conference Tokyo, Japan, September 25–28, 2002 Proceedings, Part I*, T. Dohi and R. Kikinis Eds. Berlin, Heidelberg: Springer Berlin Heidelberg, 2002, pp. 91-98.

[266] A. Krieger *et al.*, "Design of a novel MRI compatible manipulator for image guided prostate interventions," (in eng), *IEEE transactions on bio-medical engineering,* vol. 52, no. 2, pp. 306-13, Feb 2005

[267] R. C. Susil *et al.*, "Transrectal Prostate Biopsy and Fiducial Marker Placement in a Standard 1.5T Magnetic Resonance Imaging Scanner," *J Urol,* vol. 175, no. 1, pp. 113-120, 2006

[268] S. P. DiMaio *et al.*, "A System for MRI-guided Prostate Interventions," in *The First IEEE/RAS-EMBS International Conference on Biomedical Robotics and Biomechatronics*, 20-22 Feb. 2006 2006, pp. 68-73

[269] S. P. DiMaio *et al.*, "Robot-assisted needle placement in open MRI: system architecture, integration and validation," (in eng), *Comput Aided Surg,* vol. 12, no. 1, pp. 15-24, Jan 2007

[270] N. Hata *et al.*, "MR Imaging-guided Prostate Biopsy with Surgical Navigation Software: Device Validation and Feasibility," *Radiology,* vol. 220, no. 1, pp. 263-268, 2001

[271] D. M. Pinkstaff, T. C. Igel, S. P. Petrou, G. A. Broderick, M. J. Wehle, and P. R. Young, "Systematic transperineal ultrasound-guided template biopsy of the prostate: three-year experience," *Urology,* vol. 65, no. 4, pp. 735-739, 2005

[272] B. E. Ayres *et al.*, "The role of transperineal template prostate biopsies in restaging men with prostate cancer managed by active surveillance," *BJU int,* vol. 109, no. 8, pp. 1170-1176, 2012

[273] Civco. "Disposable Template Grids." Civco medical solutions. http://civco.com/mmi/ultrasound/positioning/brachytherapy/disposable-template-grids-PID5150.htm (accessed 5-1-2018, 2018).

[274] Noras. "Biopsy Unit for GE 8-Channel Breast Coil." Noras MRI products.

http://www.noras.de/en/mri-accessories/biopsy-units/bu-for-ge-8-ch-breast-coil/ (accessed sept 6, 2017).

[275] Webb. "THE FAST FIND GRID." Webb medical. http://www.fastfindgrid.com/ (accessed 10-3-2018, 2018).

[276] G. P. Haas, N. Delongchamps, O. W. Brawley, C. Y. Wang, and G. de la Roza, "The worldwide epidemiology of prostate cancer: perspectives from autopsy studies," (in eng), *The Canadian journal of urology*, vol. 15, no. 1, pp. 3866-71, Feb 2008

[277] P. Pepe, A. Garufi, G. D. Priolo, A. Galia, F. Fraggetta, and M. Pennisi, "Is it time to perform only MRI targeted cores? Our experience in 1032 men submitted to prostate biopsy," *J Urol*, vol. 200, no. 4, pp. 774-778, 2018

[278] F. Cornud, J. Bomers, J. Futterer, S. Ghai, J. Reijnen, and C. Tempany, "MR imaging-guided prostate interventional imaging: Ready for a clinical use?," *Diagn Interv Imaging*, 2018

[279] S. Pahwa, N. K. Schiltz, L. E. Ponsky, Z. Lu, M. A. Griswold, and V. Gulani, "Cost-effectiveness of MR imaging–guided strategies for detection of prostate cancer in biopsy-naive men," *Radiology*, vol. 285, no. 1, pp. 157-166, 2017

[280] T. H. Kuru *et al.*, "How to Perform Image-guided Prostate Biopsy: In-bore and Fusion Approaches," *Eur Urol Focus*, vol. 2, no. 2, p. 151, 2016

[281] A. Sciarra *et al.*, "Value of magnetic resonance spectroscopy imaging and dynamic contrast-enhanced imaging for detecting prostate cancer foci in men with prior negative biopsy," *Clin Cancer Res*, pp. 1078-0432. CCR-09-2195, 2010

[282] S. Vourganti *et al.*, "Multiparametric magnetic resonance imaging and ultrasound fusion biopsy detect prostate cancer in patients with prior negative transrectal ultrasound biopsies," *J Urol*, vol. 188, no. 6, pp. 2152-2157, 2012

[283] A. V. Taira *et al.*, "Performance of transperineal template-guided mapping biopsy in detecting prostate cancer in the initial and repeat biopsy setting," *Prostate Cancer Prostatic Dis*, Original Article vol. 13, p. 71, 09/29/online 2009

[284] P. Moreira *et al.*, "The MIRIAM Robot: a novel robotic system for MR-guided needle insertion in the prostate," *J Med Robot Res,* vol. 2, no. 04, p. 1750006, 2017

[285] G. Srimathveeravalli *et al.*, "MRI‐safe robot for targeted transrectal prostate biopsy: animal experiments," *BJU int,* vol. 113, no. 6, pp. 977-985, 2014

[286] D. Sia, A. Villanueva, S. L. Friedman, and J. M. Llovet, "Liver cancer cell of origin, molecular class, and effects on patient prognosis," *Gastroenterology,* vol. 152, no. 4, pp. 745-761, 2017

[287] H. Takahashi, B. Kahramangil, E. Kose, and E. Berber, "A comparison of microwave thermosphere versus radiofrequency thermal ablation in the treatment of colorectal liver metastases," *HPB,* vol. 20, no. 12, pp. 1157-1162, 2018

[288] A. M. Dietzek, R. Ahmad, and M. N. Richard, "Radiofrequency Thermal Ablation: Current Data," in *Atlas of Endovascular Venous Surgery*: Elsevier, 2019, pp. 215-231.

[289] I. Roberto *et al.*, "Radiofrequency thermal ablation of renal graft neoplasms: A literature review," *Transplantation Reviews,* 2019

[290] M. J. Norton and N. D. Ischy, "Apparatus and method for minimally invasive surgery," ed: Google Patents, 2017.

[291] T. T. Kim, J. P. Johnson, R. Pashman, and D. Drazin, "Minimally invasive spinal surgery with intraoperative image-guided navigation," *BioMed research international,* vol. 2016, 2016

[292] Y. Wang *et al.*, "Mandibular reconstruction with the vascularized fibula flap: comparison of virtual planning surgery and conventional surgery," *International journal of oral and maxillofacial surgery,* vol. 45, no. 11, pp. 1400-1405, 2016

[293] P. Lu *et al.*, "Systemic chemotherapy and survival in patients with metastatic low‐grade appendiceal mucinous adenocarcinoma," *Journal of Surgical Oncology,* vol. 120, no. 3, pp. 446-451, 2019

[294] W. U. Shipley *et al.*, "Radiation with or without antiandrogen therapy in recurrent prostate cancer," *New England Journal of Medicine,* vol. 376, no. 5, pp. 417-428, 2017

[295] B. Zhou *et al.*, "PEGylated polyethylenimine-entrapped gold nanoparticles modified with folic acid for targeted tumor CT imaging," *Colloids and Surfaces B: Biointerfaces,* vol. 140, pp. 489-496, 2016

[296] Y. Zhao *et al.*, "Tumor-targeted and clearable human protein-based MRI nanoprobes," *Nano letters,* vol. 17, no. 7, pp. 4096-4100, 2017

[297] M. Ahmed *et al.*, "Hepatic Radiofrequency Ablation-induced Stimulation of Distant Tumor Growth Is Suppressed by c-Met Inhibition," (in eng), *Radiology,* vol. 279, no. 1, pp. 103-117, 2016

[298] J. Izaaryene *et al.*, "Pathological effects of lung radiofrequency ablation that contribute to pneumothorax, using a porcine model," (in eng), *Int J Hyperthermia,* vol. 33, no. 7, pp. 713-716, Nov 2017

[299] S. P. DiMaio and S. E. Salcudean, "Needle steering and motion planning in soft tissues," *IEEE Transactions on Biomedical Engineering,* vol. 52, no. 6, pp. 965-974, 2005

[300] K. Cleary *et al.*, "Precision placement of instruments for minimally invasive procedures using a “needle driver” robot," *The International Journal of Medical Robotics and Computer Assisted Surgery,* vol. 1, no. 2, pp. 40-47, 2005

[301] E. Ben-David, M. Shochat, I. Roth, I. Nissenbaum, J. Sosna, and S. N. Goldberg, "Evaluation of a CT-Guided Robotic System for Precise Percutaneous Needle Insertion," *Journal of Vascular and Interventional Radiology,* vol. 29, no. 10, pp. 1440-1446, 2018/10/01/ 2018

[302] P. Bruners *et al.*, "Electromagnetic tracking for CT-guided spine interventions: phantom, ex-vivo and in-vivo results," *European Radiology,* vol. 19, no. 4, pp. 990-994, 2009/04/01 2009

[303] Civco. "VirtuTRAX™ Instrument Navigator." Civco. https://www.civco.com/catalog/fusion-tracking-technology/virtutrax-instrument-navigator/ (accessed 2-18-2020, 2020).

[304] NeoRad. "SimpliCT." NeoRad. https://www.neorad.no/products/simplict-for-ct-and-pet-ct (accessed 2-18-2020, 2020).

[305] M. Abayazid, T. Kato, S. G. Silverman, and N. Hata, "Using needle orientation sensing as

surrogate signal for respiratory motion estimation in percutaneous interventions," (in eng), *International journal of computer assisted radiology and surgery,* vol. 13, no. 1, pp. 125-133, 2018

[306] E. Basafa, M. Hoßbach, and P. J. Stolka, "Fast, Intuitive, Vision-Based: Performance Metrics for Visual Registration, Instrument Guidance, and Image Fusion," in *Clinical Image-Based Procedures. Translational Research in Medical Imaging*, Cham, R. Shekhar *et al.*, Eds., 2016// 2016: Springer International Publishing, pp. 9-17

[307] Y. Koethe, S. Xu, G. Velusamy, B. J. Wood, and A. M. Venkatesan, "Accuracy and efficacy of percutaneous biopsy and ablation using robotic assistance under computed tomography guidance: a phantom study," *European Radiology*, vol. 24, no. 3, pp. 723-730, 2014/03/01 2014

[308] L. Appelbaum, L. Solbiati, J. Sosna, Y. Nissenbaum, N. Greenbaum, and S. N. Goldberg, "Evaluation of an Electromagnetic Image-Fusion Navigation System for Biopsy of Small Lesions: Assessment of Accuracy in an In Vivo Swine Model," *Academic radiology,* vol. 20, no. 2, pp. 209-217, 2013/02/01/ 2013

[309] C. Roberts, W. Morrison, D. Deely, A. Zoga, G. Koulouris, and C. Winalski, "Use of a novel percutaneous biopsy localization device: initial musculoskeletal experience," *Skeletal radiology,* vol. 36, no. 1, pp. 53-57, 2007

[310] A. Magnusson, E. Radecka, M. Lönnemark, and H. Raland, "Computed-tomography-guided punctures using a new guidance device," *Acta Radiologica*, vol. 46, no. 5, pp. 505-509, 2005/08/01 2005

[311] A. Behneke, M. Burwinkel, and N. Behneke, "Factors influencing transfer accuracy of cone beam CT-derived template-based implant placement," *Clinical oral implants research,* vol. 23, no. 4, pp. 416-423, 2012

[312] G. Widmann, R. Widmann, E. Widmann, W. Jaschke, and R. Bale, "Use of a surgical navigation system for CT-guided template production," *International Journal of Oral & Maxillofacial*

Implants, vol. 22, no. 1, 2007

[313] G. Eggers, J. Mühling, and R. Marmulla, "Template-Based Registration for Image-Guided Maxillofacial Surgery," *Journal of Oral and Maxillofacial Surgery,* vol. 63, no. 9, pp. 1330-1336, 2005/09/01/ 2005

[314] W. G. Campbell, M. Miften, and B. L. Jones, "Automated target tracking in kilovoltage images using dynamic templates of fiducial marker clusters," *Medical physics,* vol. 44, no. 2, pp. 364-374, 2017

[315] M. V. Wyawahare, P. M. Patil, and H. K. Abhyankar, "Image registration techniques: an overview," *International Journal of Signal Processing, Image Processing and Pattern Recognition,* vol. 2, no. 3, pp. 11-28, 2009

[316] M. C. Bernardes, B. V. Adorno, P. Poignet, and G. A. Borges, "Robot-assisted automatic insertion of steerable needles with closed-loop imaging feedback and intraoperative trajectory replanning," *Mechatronics,* vol. 23, no. 6, pp. 630-645, 2013/09/01/ 2013

[317] J. R. Haaga and R. J. Alfidi, "Precise biopsy localization by computer tomography," *Radiology,* vol. 118, no. 3, pp. 603-7, 1976

[318] J. R. Haaga, R. J. Alfidi, T. R. Havrilla, A. M. Cooperman, F. E. Seidelmann, and N. E. Reich, "CT detection and aspiration of abdominal abscesses," *AJR,* vol. 128, no. 3, pp. 465-74, 1977

[319] G. E. Wile, J. R. Leyendecker, K. A. Krehbiel, R. B. Dyer, and R. J. Zagoria, "CT and MR imaging after imaging-guided thermal ablation of renal neoplasms," *Radiographics,* vol. 27, no. 2, pp. 325-39, 2007

[320] A. Gupta *et al.,* "Computerized tomography guided percutaneous renal cryoablation with the patient under conscious sedation: initial clinical experience," *The Journal of urology,* vol. 175, no. 2, pp. 447-453, 2006

[321] F. J. Wolf, D. J. Grand, J. T. Machan, T. A. DiPetrillo, W. W. Mayo-Smith, and D. E. Dupuy, "Microwave Ablation of Lung Malignancies: Effectiveness, CT Findings, and Safety in 50 Patients," *Radiology,* vol. 247, no. 3, pp. 871-879, 2008

[322] Z. Amin *et al.*, "Hepatic metastases: interstitial laser photocoagulation with real-time US monitoring and dynamic CT evaluation of treatment," *Radiology,* vol. 187, no. 2, pp. 339-347, 1993

[323] E. R. Ryan *et al.*, "Split-Dose Technique for FDG PET/CT–guided Percutaneous Ablation: A Method to Facilitate Lesion Targeting and to Provide Immediate Assessment of Treatment Effectiveness," *Radiology,* vol. 268, no. 1, pp. 288-295, 2013

[324] J. J. Froelich, B. Saar, M. Hoppe, N. Ishaque, E. M. Walthers, and J. Regn, "Real-time Ct-fluoroscopy for guidance of percutaneous drainage procedures," *J Vasc Interv Radiol,* vol. 9, no. 5, pp. 735-40, 1998

[325] S. G. Silverman, K. Tuncali, D. F. Adams, R. D. Nawfel, K. H. Zou, and P. F. Judy, "CT fluoroscopy-guided abdominal interventions: techniques, results, and radiation exposure," *Radiology,* vol. 212, no. 3, pp. 673-81, 1999

[326] B. Daly and P. A. Templeton, "Real-time CT fluoroscopy: evolution of an interventional tool," *Radiology,* vol. 211, no. 2, pp. 309-15, 1999

[327] L. Tselikas *et al.*, "Percutaneous Bone Biopsies: Comparison between Flat-Panel Cone-Beam CT and CT-Scan Guidance," *CardioVascular and Interventional Radiology,* journal article vol. 38, no. 1, pp. 167-176, February 01 2015

[328] K. T. Brown, G. I. Getrajdman, and J. F. Botet, "Clinical trial of the Bard CT guide system," (in eng), *J Vasc Interv Radiol,* vol. 6, no. 3, pp. 405-10, May-Jun 1995

[329] P. R. Frederick, T. H. Brown, M. H. Miller, A. L. Bahr, and K. H. Taylor, "A light-guidance system to be used for CT-guided biopsy," (in eng), *Radiology,* vol. 154, no. 2, pp. 535-6, Feb 1985

[330] A. Gangi, B. Kastler, J. M. Arhan, A. Klinkert, J. M. Grampp, and J. L. Dietemann, "A compact laser beam guidance system for interventional CT," (in eng), *Journal of computer assisted tomography,* vol. 18, no. 2, pp. 326-8, Mar-Apr 1994

[331] W. Hruby and H. Muschik, "Belt device for simplified CT-guided puncture and biopsy: a

technical note," (in eng), *Cardiovasc Intervent Radiol,* vol. 10, no. 5, pp. 301-2, 1987

[332] V. Jacobi, A. Thalhammer, and J. Kirchner, "Value of a laser guidance system for CT interventions: a phantom study," (in eng), *Eur Radiol,* vol. 9, no. 1, pp. 137-40, 1999

[333] R. Kloeppel, T. Weisse, F. Deckert, W. Wilke, and S. Pecher, "CT-guided intervention using a patient laser marker system," (in eng), *Eur Radiol,* vol. 10, no. 6, pp. 1010-4, 2000

[334] Y. Miaux *et al.*, "Laser guidance system for CT-guided procedures," (in eng), *Radiology,* vol. 194, no. 1, pp. 282-4, Jan 1995

[335] C. Ozdoba, K. Voigt, and F. Nusslin, "New device for CT-targeted percutaneous punctures," (in eng), *Radiology,* vol. 180, no. 2, pp. 576-8, Aug 1991

[336] F. S. Pereles, M. Baker, R. Baldwin, E. Krupinski, and E. C. Unger, "Accuracy of CT biopsy: laser guidance versus conventional freehand techniques," (in eng), *Academic radiology,* vol. 5, no. 11, pp. 766-70, Nov 1998

[337] F. Wunschik, M. Georgi, and O. Pastyr, "Stereotactic biopsy using computed tomography," (in eng), *Journal of computer assisted tomography,* vol. 8, no. 1, pp. 32-7, Feb 1984

[338] G. Fichtinger *et al.*, "Robotic assistance for ultrasound-guided prostate brachytherapy," (in eng), *Medical image analysis,* vol. 12, no. 5, pp. 535-45, Oct 2008

[339] N. Abolhassani, R. V. Patel, and F. Ayazi, "Minimization of needle deflection in robot-assisted percutaneous therapy," (in eng), *Int J Med Robot,* vol. 3, no. 2, pp. 140-8, Jun 2007

[340] A. Chellathurai, S. Kanhirat, K. Chokkappan, T. S. Swaminathan, and N. Kulasekaran, "Technical note: CT-guided biopsy of lung masses using an automated guiding apparatus," (in eng), *The Indian journal of radiology & imaging,* vol. 19, no. 3, pp. 206-7, Jul-Sep 2009

[341] G. Onik *et al.*, "CT body stereotaxis: an aid for CT-guided biopsies," (in eng), *AJR Am J Roentgenol,* vol. 146, no. 1, pp. 163-8, Jan 1986

[342] G. Onik *et al.*, "CT-guided aspirations for the body: comparison of hand guidance with stereotaxis," (in eng), *Radiology,* vol. 166, no. 2, pp. 389-94, Feb 1988

[343] A. M. Palestrant, "Comprehensive approach to CT-guided procedures with a hand-held guidance

device," (in eng), *Radiology,* vol. 174, no. 1, pp. 270-2, Jan 1990

[344] G. D. Reyes, "A guidance device for CT-guided procedures," (in eng), *Radiology,* vol. 176, no. 3, pp. 863-4, Sep 1990

[345] M. H. Howard and R. C. Nelson, "An electronic device for needle placement during sonographically guided percutaneous intervention," *Radiology,* vol. 218, no. 3, pp. 905-911, 2001

[346] G. A. Krombach and A. Mahnken, "US-guided nephrostomy with the aid of a magnetic field-based navigation device in the porcine pelvicaliceal system," *J Vasc Interv Radiol,* vol. 12, no. 5, pp. 623-628, 2001

[347] S. Hassfeld and J. Mühling, "Comparative examination of the accuracy of a mechanical and an optical system in CT and MRT based instrument navigation," *International Journal of Oral and Maxillofacial Surgery,* vol. 29, no. 6, pp. 400-407,

[348] M. Jakopec, F. y. Baena, and S. J. Harris, "The hands-on orthopaedic robot "Acrobot": Early clinical trials of total knee replacement surgery," *IEEE Transactions on Robotics,* vol. 19, no. 5, 2003

[349] J. Cobb, J. Henckel, P. Gomes, and S. Harris, "Hands-on robotic unicompartmental knee replacement," *Bone & Joint,* 2006

[350] S. Bartling, M. Kachelrieß, J. Kuntz, R. Gupta, C. Walsh, and I. S. Wang, *CT-Guided Interventions: Current Practice and Future Directions*. 2014.

[351] NeoRad. "SimpliCT." http://neorad.no/products_1/simplict_for_ct_and_pet_ct/ (accessed 10/16/2017, 2017).

[352] A. S. T. S. GmbH. "Quick and uncomplicated CT-guided interventions on the highest level with 3D-LNS!" http://www.amedo-gmbh.com/index.php/en/ (accessed 10/16/2017, 2017).

[353] CAScination. "CAS-ONE Liver." http://www.cascination.com/products/cas-one-liver/ (accessed 10/16/2017, 2017).

[354] P. H. P. Ltd. "MAXIO is a USFDA 510(k) approved device." http://www.perfinthealthcare.com/MaxioOverview.asp (accessed 10/16/2017, 2017).

[355] K. P. N.V. "EPIQ PercuNav." https://www.philips.co.in/healthcare/product/HCNOCTN150/epiq-percunav-premium-fusion-and-navigation (accessed 10/16/2017, 2017).

[356] E. C. Mbalisike, T. J. Vogl, S. Zangos, K. Eichler, P. Balakrishnan, and J. Paul, "Image-guided microwave thermoablation of hepatic tumours using novel robotic guidance: an early experience," (in eng), *Eur Radiol*, vol. 25, no. 2, pp. 454-62, Feb 2015

[357] H. Dou, S. Jiang, Z. Yang, L. Sun, X. Ma, and B. Huo, "Design and validation of a CT-guided robotic system for lung cancer brachytherapy," (in eng), *Medical physics*, vol. 44, no. 9, pp. 4828-4837, Sep 2017

[358] J. Kettenbach, L. Kara, G. Toporek, M. Fuerst, and G. Kronreif, "A robotic needle-positioning and guidance system for CT-guided puncture: Ex vivo results," (in eng), *Minimally invasive therapy & allied technologies : MITAT : official journal of the Society for Minimally Invasive Therapy*, vol. 23, no. 5, pp. 271-8, Oct 2014

[359] R. M. Martinez *et al.*, "CT-Guided, Minimally Invasive, Postmortem Needle Biopsy Using the B-Rob II Needle-Positioning Robot," *Journal of Forensic Sciences*, vol. 59, no. 2, pp. 517-521, 2014

[360] S. C. Leschka, D. Babic, S. El Shikh, C. Wossmann, M. Schumacher, and C. A. Taschner, "C-arm cone beam computed tomography needle path overlay for image-guided procedures of the spine and pelvis," (in eng), *Neuroradiology*, vol. 54, no. 3, pp. 215-23, Mar 2012

[361] B. Schulz *et al.*, "Accuracy and speed of robotic assisted needle interventions using a modern cone beam computed tomography intervention suite: a phantom study," *European Radiology*, journal article vol. 23, no. 1, pp. 198-204, January 01 2013

[362] C. Moser, J. Becker, M. Deli, M. Busch, M. Boehme, and D. H. W. Groenemeyer, "A novel Laser Navigation System reduces radiation exposure and improves accuracy and workflow of CT-guided spinal interventions: A prospective, randomized, controlled, clinical trial in comparison to conventional freehand puncture," *European Journal of Radiology*, vol. 82, no. 4, pp. 627-632, 2013/04/01/ 2013

[363] R. F. Grasso *et al.*, "Percutaneous lung biopsy: comparison between an augmented reality CT navigation system and standard CT-guided technique," *International Journal of Computer Assisted Radiology and Surgery,* journal article vol. 8, no. 5, pp. 837-848, September 01 2013

[364] N. D. Glossop, "Advantages of Optical Compared with Electromagnetic Tracking," *JBJS,* vol. 91, no. Supplement_1, pp. 23-28, 2009

[365] T. Penzkofer *et al.*, "Free-hand CT-based electromagnetically guided interventions: accuracy, efficiency and dose usage," (in eng), *Minimally invasive therapy & allied technologies : MITAT : official journal of the Society for Minimally Invasive Therapy,* vol. 20, no. 4, pp. 226-33, Jul 2011

[366] E. Kim, T. J. Ward, R. S. Patel, A. M. Fischman, S. Nowakowski, and R. A. Lookstein, "CT-guided liver biopsy with electromagnetic tracking: results from a single-center prospective randomized controlled trial," (in eng), *AJR Am J Roentgenol,* vol. 203, no. 6, pp. W715-23, Dec 2014

[367] M. Hallett, "The neurophysiology of dystonia," *Archives of Neurology,* vol. 55, no. 5, pp. 601-603, 1998

[368] G. Gex, J. A. Pralong, C. Combescure, L. Seijo, T. Rochat, and P. M. Soccal, "Diagnostic Yield and Safety of Electromagnetic Navigation Bronchoscopy for Lung Nodules: A Systematic Review and Meta-Analysis," *Respiration,* vol. 87, no. 2, pp. 165-176, 2014

[369] E. Machida, M. Cao, T. Murao, and H. Hashimoto, "Human motion tracking of mobile robot with Kinect 3D sensor," in *2012 Proceedings of SICE Annual Conference (SICE)*, 2012: IEEE, pp. 2207-2211

[370] D. Murray and A. Basu, "Motion tracking with an active camera," *IEEE transactions on pattern analysis and machine intelligence,* vol. 16, no. 5, pp. 449-459, 1994

[371] J.-H. Zhang, P. Li, C.-C. Jin, W.-A. Zhang, and S. Liu, "A Novel Adaptive Kalman Filtering Approach to Human Motion Tracking with Magnetic-Inertial Sensors," *IEEE Transactions on Industrial Electronics,* 2019

[372] C.-Y. Chang *et al.*, "Towards pervasive physical rehabilitation using Microsoft Kinect," in *2012*

6th international conference on pervasive computing technologies for healthcare (PervasiveHealth) and workshops, 2012: IEEE, pp. 159-162

[373] W. Zhao, M. A. Reinthal, D. D. Espy, and X. Luo, "Rule-based human motion tracking for rehabilitation exercises: Realtime assessment, feedback, and guidance," *IEEE Access,* vol. 5, pp. 21382-21394, 2017

[374] M. R. Hayden, *Huntington's chorea*. Springer Science & Business Media, 2012.

[375] A. E. Lang and A. M. Lozano, "Parkinson's disease," *New England Journal of Medicine,* vol. 339, no. 16, pp. 1130-1143, 1998

[376] D. L. Radder, I. H. Sturkenboom, M. van Nimwegen, S. H. Keus, B. R. Bloem, and N. M. de Vries, "Physical therapy and occupational therapy in Parkinson's disease," *International Journal of Neuroscience,* vol. 127, no. 10, pp. 930-943, 2017

[377] D. Tarsy, "Treatment of Parkinson disease: a 64-year-old man with motor complications of advanced Parkinson disease," (in eng), *The Journal of the American Medical Association,* vol. 307, no. 21, pp. 2305-14, Jun 6 2012

[378] H. Ren and P. Kazanzides, "Investigation of Attitude Tracking Using an Integrated Inertial and Magnetic Navigation System for Hand-Held Surgical Instruments," *IEEE/ASME Transactions on Mechatronics,* vol. 17, no. 2, pp. 210-217, 2012

[379] H. Guo, M. Uradzinski, H. Yin, and M. Yu, "Indoor positioning based on foot-mounted IMU," *Bulletin of the Polish Academy of Sciences Technical Sciences,* vol. 63, no. 3, pp. 629-634, 2015

[380] R. Sun, R. G. Aldunate, and J. J. Sosnoff, "The Validity of a Mixed Reality-Based Automated Functional Mobility Assessment," *Sensors,* vol. 19, no. 9, p. 2183, 2019

[381] T. Miyatake *et al.*, "Biomechanical analysis and inertial sensing of ankle joint while stepping on an unanticipated bump," in *Wearable Robotics: Challenges and Trends*: Springer, 2017, pp. 343-347.

[382] S. Kobashi, Y. Tsumori, S. Imawaki, S. Yoshiya, and Y. Hata, "Wearable knee kinematics monitoring system of MARG sensor and pressure sensor systems," in *2009 IEEE International*

Conference on System of Systems Engineering (SoSE), 2009: IEEE, pp. 1-6

[383] M. Mundt *et al.*, "Assessment of the measurement accuracy of inertial sensors during different tasks of daily living," *Journal of Biomechanics*, vol. 84, pp. 81-86, 2019/02/14/ 2019

[384] R. Li, C. M. Modlesky, and Z. T. H. Tse, "Smartphone-enabled Trackers for Lower-body Monitoring," in *2019 International Symposium on Medical Robotics (ISMR)*, 3-5 April 2019 2019, pp. 1-5

[385] W. Roush. "an Tibion's Bionic Leg Rewire Stroke Victims' Brains?" Xconomy. https://xconomy.com/san-francisco/2010/12/13/can-tibions-bionic-leg-rewire-stroke-victims-brains/ (accessed 3-8-2020, 2020).

[386] V. Wiwanitkit, "Rehabilitation Robotics: Cost Effectiveness Issue," *Journal of Rehabilitation Robotics*, vol. 4, p. 1, 2016

[387] R. Lloréns, E. Noé, C. Colomer, and M. Alcañiz, "Effectiveness, usability, and cost-benefit of a virtual reality–based telerehabilitation program for balance recovery after stroke: A randomized controlled trial," *Archives of physical medicine and rehabilitation*, vol. 96, no. 3, pp. 418-425. e2, 2015

[388] C. Zirbel, X. Zhang, and C. Hughes, "The VRehab System: A Low-Cost Mobile Virtual Reality System for Post-Stroke Upper Limb Rehabilitation for Medically Underserved Populations," in *2018 IEEE Global Humanitarian Technology Conference (GHTC)*, 2018: IEEE, pp. 1-8

[389] M. motion. "Optical Motion Capture Systems." META motion. https://metamotion.com/motion-capture/optical-motion-capture-1.htm (accessed 3-8-2020, 2020).

[390] H. Morse, L. Biggart, V. Pomeroy, and S. Rossit, "Virtual reality telerehabilitation for spatial neglect post-stroke: perspectives from stroke survivors, carers and clinicians," *medRxiv*, p. 2020.01.07.20016782, 2020

[391] NDI. "Polaris optical tracking systems." NDI. http://www.ndigital.com/medical/wp-content/uploads/sites/4/2013/12/Polaris.pdf (accessed 3-8-2020, 2020).

[392] N. Abolhassani, R. Patel, and M. Moallem, "Needle insertion into soft tissue: A survey," *Medical*

Engineering & Physics, vol. 29, no. 4, pp. 413-431, 2007/05/01/ 2007

[393] S. A. Yoganathan, K. J. Maria Das, A. Agarwal, and S. Kumar, "Magnitude, Impact, and Management of Respiration-induced Target Motion in Radiotherapy Treatment: A Comprehensive Review," (in eng), *J Med Phys*, vol. 42, no. 3, pp. 101-115, Jul-Sep 2017

[394] S. Y. Ko and F. R. y. Baena, "Toward a Miniaturized Needle Steering System With Path Planning for Obstacle Avoidance," *IEEE Transactions on Biomedical Engineering*, vol. 60, no. 4, pp. 910-917, 2013

[395] J. Ma and G. E. Okudan Kremer, "A Modular Product Design Approach With Key Components Consideration to Improve Sustainability," 2014. [Online]. Available: https://doi.org/10.1115/DETC2014-35091.

[396] S. Polinder, J. Haagsma, M. Panneman, A. Scholten, M. Brugmans, and E. Van Beeck, "The economic burden of injury: Health care and productivity costs of injuries in the Netherlands," *Accident Analysis & Prevention*, vol. 93, pp. 92-100, 2016/08/01/ 2016

APPENDIX

LIST OF PUBLICATIONS

A. Journal Papers (published)

1. Rui Li, Sheng Xu, William F Pritchard, John W Karanian, Venkatesh P Krishnasamy, Bradford J Wood, Zion Tsz Ho Tse, "AngleNav: MEMS Tracker to Facilitate CT-Guided Puncture", Annals of Biomedical Engineering, Volume 46, pages 452-463, March 2018.
2. Rui Li, Sheng Xu, Ivane Bakhutashvili, Ismail B Turkbey, Peter L Choyke, Peter A Pinto, Bradford Wood, Zion Tsz Ho Tse, "Template for MR visualization and needle targeting", Annals of Biomedical Engineering, Volume 46, Page 1-13, December 2018.
3. Rui Li, Aaron Smith, Harshitha Tadinada, Hovet Sierra, Zion Tsz Ho Tse, "Heatguard: An Ultra-low-cost 3D-printed Sensor for Skin Temperature Alert & Reporting System", Proceedings of the IMechE, Part H: Journal of Engineering in Medicine.
4. Rui Li, Barclay Jumet, Zion Tse, "A Smartphone-based IMU Tracking System for Body Movement in Comparison with Optical Tracking", Proceedings of the IMechE, Part H: Journal of Engineering in Medicine.

B. Journal Papers (under review)

1. Rui Li, Barclay Jumet, Zion Tse, "Common Errors of Optical Tracking in Clinical Environment", Proceedings of the IMechE, Part H: Journal of Engineering in Medicine.
2. Rui Li, Austin Taylor, Zion Tse, "Rapid Prototyping of Custom Radiocontrast Agent Markers for CT-guided Procedures", Proceedings of the IMechE, Part H: Journal of Engineering in Medicine.

3. Zhuo Zhao, Rui Li, Zion Tse, “A low-cost Angular Tracker for CT Applications”, International Journal of Computer Assisted Radiology and Surgery.

C. Journal Articles (in preparation)

1. Rui Li, Julian Moore, Sheng Xu, Bradford Wood, Hongliang Ren, Zion Tse, A Feasibility Study of Using Thermochromic Material for Radiofrequency Ablation Phantom.

D. Conference Publications

1. Rui Li, Sheng Xu, Bradford Wood, John Oshinski, Zion Tsz Ho Tse, “Towards Precise Freehand MRI-guided Cellular Therapeutic Targeting for Amyotrophic Lateral Sclerosis”, 9th National IGT Workshop, Bethesda, March 2017.
2. Rui Li, Sheng Xu, Bradford Wood, Zion Tsz Ho Tse, “3D-printed MRI Grid for Guiding Transperineal Prostate Focal Laser Ablation”, 9th National IGT Workshop, Bethesda, March 2017.
3. Rui Li, Aaron A Smith, Harshitha S Tadinada, Zion Tsz Ho Tse, “Heatguard: An Ultra-Low-Cost 3D Printed Sensor for Body Temperature Alert and Reporting System”, 2018 Design of Medical Devices Conference, ASME, Pages V001T10A008-V001T10A008, Minneapolis, April 2018.
4. Rui Li, Ivane Bakhutashvili, Sheng Xu, Bradford Wood, Zion Tsz Ho Tse, “Flexible Template to Assist MRI-Guided Biopsy on Prostate Cancer”, 2018 Design of Medical Devices Conference, ASME, pages V001T04A002-V001T04A002, Minneapolis, April 2018.
5. Ivane Bakhutashvili, Sheng Xu, Rui Li, Zion Tsz Ho Tse, Ismail Turkbey, Peter Choyke, Peter Pinto, Bradford Wood, “Software Assisted MRI-visible Grid for Transperineal MR-

guided Prostate Needle Interventions", Society of Interventional Oncology, Boston, June 2018.

6. Aaron Smith, Rui Li, Zion Tsz Ho Tse "AirCure: a 2in1 System for 3D SLA Prints and Medical Applications", BMES annual meeting, Atlanta, October 2018.
7. Sheng Xu, Zion Tse, Rui Li, Quirina De Ruiter, Braford Wood, "Virtual bronchoscopy navigation using a wireless gyroscope", Journal of Vascular and Interventional Radiology 30 (3), S227, March 2019.
8. Noah Scott, Rui Li, Zion Tse, "MobileGyro: Android Application for Bluetooth Gyroscope Tracking With Potential for Impact in Rehabilitative Processes", 2019 Design of Medical Devices Conference, ASME, pages V001T04A001-V001T04A001, Minneapolis, April 2019.